Data Analysis in the Direct Dark Matter Search Experiment CRESST and Calculation of the corresponding Limit on the Cross Section of Dark Matter

Dissertation

der Mathematisch-Naturwissenschaftlichen Fakultät
der Eberhard Karls Universität Tübingen
zur Erlangung des Grades eines
Doktors der Naturwissenschaften
(Dr. rer. nat.)

vorgelegt von
Marcel Kimmerle
aus Heidenheim

Tübingen
2010

Tag der mündlichen Qualifikation:	04.02.2011
Dekan:	Prof. Dr. Wolfgang Rosenstiel
1. Berichterstatter:	Prof. Dr. Josef Jochum
2. Berichterstatter:	Prof. Dr. Peter Grabmayr

Abstract

The nature of Dark Matter is one of the most important unsolved questions in astronomy and particle physics. It is proven by different observations and based on different experimental techniques that there is matter in the universe which is not like anything we know from particle physics. The motion of observable matter deviates from the expectation of gravity. Either it could be explained by the introduction of new particles or a modification of the theory of the field of gravitation. This work describes the measurement efforts to be done to detect the hypothetical new particles.

To learn more about this mystery of the universe, dedicated experiments were performed to search for direct or indirect signatures of Dark Matter. A leading one is the CRESST (**C**ryogenic **R**are **E**vent **S**earch with **S**uperconducting **T**hermometers) experiment. This thesis focusses on the installation and calibration of the muon veto and the following first analysis of a CRESST Dark Matter run taking the muon veto data into account.

In part III a special method to analyse the data from a low rate experiment is developed. With its help it is possible to compare the results of all direct Dark Matter experiments as objective as possible. For the first time a comparison of different implementations of this analysis method within different background models is done in a 2–dimensional parameter space. Only with this knowledge it is possible to find the best upper limit in presence of an unknown background which is, for example, time and energy dependent.

Contents

Abstract **v**

I Introduction 3

1 Astrophysical Motivation **5**
1.1 Direct Gravitational Hints for Dark Matter 5
1.1.1 Pioneer Anomaly 5
1.1.2 Rotation Curves of Galaxies 6
1.1.3 The Collision of Galaxy Clusters 8
1.2 The Standard Cosmology 15
1.2.1 Supernovae Ia 15
1.2.2 Cosmic Microwave Background (CMB) 22

2 Possible Modifications of Gravity **27**
2.1 General Relativity 27
2.2 Parameterized Post-Newtonian Formalism 28
2.3 Modified Newtonian Dynamics (MOND) 29

3 Particle Physics Candidates **33**
3.1 Introduction to the Standard Model 33
3.2 Candidates for Dark Matter 39
3.3 Big-Bang Nucleosynthesis 41
3.4 Evidences 42

4 Summary I **47**

II Muon veto of CRESST 49

5 The CRESST Experiment **51**
5.1 CRESST-II 52

6 The Muon Veto **59**
6.1 The Veto System 59
6.1.1 Cabling Scheme 61
6.1.2 Trigger Scheme 61
6.2 Calibration of the Veto Panels 64
6.2.1 Measurement 64
6.2.2 Simulation 65
6.2.3 Summary of the Calibration Measurement 65

7 Data Analysis **71**
7.1 Muon Veto Analysis 71
7.1.1 Event Categories 71
7.1.2 Determination of Efficiency 77
7.1.3 Time Stability of the Muon Veto 78
7.1.4 Summary of the Muon Veto Analysis 80
7.2 Particle Events 84
7.2.1 Cuts and Tools to Ensure the Longterm Stability . . . 84
7.2.2 Calibration Process of the Cryogenic Detectors 85
7.2.3 Neutron Calibration 86
7.3 Muon Correlated Particle Events 94
7.3.1 Comparison of Muon induced Recoil Rates 95

8 Summary II **99**

III The Dark Matter Limits **101**

9 Expected Signal **103**
9.1 Model of the Expected Energy Spectrum 103
9.1.1 Velocity Distribution 106
9.1.2 Nuclear Form Factor 107
9.2 Calculated Recoil Spectrum 108
9.2.1 Inelastic Dark Matter Recoil Spectrum 110
9.3 Limit Calculation 113

10 Methods for Data Analysis **115**
10.1 Poisson Distribution 115
10.2 Erlang Distribution 120

11 Yellin Method **125**
11.1 Transformation of the Variable . . . 125
11.2 Maximum Gap Method . . . 127
11.2.1 Largest Gap Spectra . . . 127
11.2.2 Gap Distribution for a known True Value . . . 128
11.2.3 Confidence Level and Lookup Table . . . 131
11.3 Optimum Gap Method . . . 134
11.3.1 Calculation of the Spectra . . . 134
11.3.2 Choosing the Optimum LT Branch . . . 134
11.3.3 Calculation of the CL Function . . . 135
11.3.4 Final Optimum Gap Method LT . . . 137
11.3.5 Software Check . . . 139
11.4 Combining Different Results . . . 139

12 Extension to More Dimensions **143**
12.1 Best of x and y 1D-Limit (B-1D) . . . 144
12.2 Patch Method (P-2D) . . . 144
12.3 Corner Method (C-2D) . . . 146
12.4 Comparison of the 2D Methods . . . 147

13 Study of new 2D Methods **153**
13.1 The Background Models . . . 153
13.1.1 Signal-like Distributed Background (SDB) . . . 154
13.1.2 One Quarter Background (OQB) . . . 155
13.1.3 Circular Leakage Background (CLB) . . . 156
13.2 Comparison of the 2D Methods . . . 159
13.2.1 The Comparison Procedure . . . 159
13.2.2 Statistical Performance of Pure Signal (SDB) . . . 159
13.2.3 Statistical Performance Test with OQB . . . 161
13.2.4 Realistic CRESST-like Test with CLB . . . 163
13.2.5 Spread of the Statistical Methods . . . 166
13.2.6 Result of the Statistical Tests . . . 167

14 Summary III **171**

IV Appendix **173**

A Circuit Diagram of FIFO **175**

B Muon Veto Data **177**

C Landau Function **185**

D Shell-Code **187**
D.1 Coldtrap . . . 187
D.2 Data Quality Monitoring . . . 187
D.3 Gnuplot Fitting of the Quenching Factor . . . 187
D.4 Calculation of the Quenching Factor and its Error . . . 188

E Perl-Code **189**
E.1 Mixing.pl . . . 189
E.2 Extract.pl . . . 189

F C-Code **191**
F.1 SimLight: Border Definition . . . 191
F.2 SimLight: Source Positioning . . . 191

G C++-Code **193**
G.1 Data Analysis Part . . . 193
G.1.1 Muon Veto Calibration . . . 193
G.1.2 Muon Analysis Root-Macro . . . 193
G.1.3 Landau Integral . . . 194
G.1.4 Time Difference Root-Macro . . . 194
G.2 Limit Calculation . . . 194
G.2.1 Dark Matter Cross Section ROOT-Macro . . . 194
G.2.2 Yellin Method ROOT-Macro . . . 194

List of figures **199**

List of tables **201**

Literature **228**

Part I

Introduction

The concept of Dark Matter was introduced to explain several astronomical measurements where the contribution of gravity is much higher than one would expect from the observed matter. Some powerful examples of those measurements are introduced in the first chapter. A chapter about the constrains to the theory of gravity follows, as a modification of the law of gravity would be a natural solution to the Dark Matter problem. Since increasingly more experiments exclude a simple modification of gravity alternative solutions become more likely. Particle physics provides in every extention of the well proven Standard Model of particles a broad variety of candidates. Each of them could have exact the right properties to be the Dark Matter particle. A short overview is given in the third chapter.

Chapter 1

Astrophysical Motivation for Dark Matter

What we can see through satellites in space and telescopes on earth is not always providing a consistent picture. The observations of the dynamics of galaxies, the distribution of the cosmic microwave background or the behavior of the light from far supernova explosions cannot be explained with known physics. Therefore, some Dark Matter which interacts only gravitationally (and maybe via some very weak force) with ordinary matter is often introduced as a solution. First some measurements will be presented.

1.1 Direct Gravitational Hints for Dark Matter

The Newtonian Theory of gravity as well as Einsteins Theory of General Relativity is experimentally proven with high accuracy as it is shown in chapter 2. Every deviation is therefore astonishing and will be investigated. In the following sections the best–known examples of such deviations in astronomy are presented.

1.1.1 Pioneer Anomaly

There is the phenomenon that man–made spacecrafts receive an additional acceleration towards the sun in the order of $a_P = (8.74 \pm 1.33) \times 10^{-10} m/s^2$. It is called after the Pioneer spacecrafts (Fig. 1.1 shows Pioneer 10) were this effect was observed first. Meanwhile it was seen with other vehicles like Galileo or Ulysses, but due to their simpler geometry the most precise numbers for the effect still come from the eponym of the anomaly. Other sources of this tiny additional acceleration were considered [1] and seem very

unlikely. The possibility of a hint for new physic is not excluded but it could be interpreted as an evidence of Dark Matter in the solar system.

The acceleration of the Pioneer spacecrafts was consistently observed in both missions, 10 and 11. The radio–metric tracking data shows a small, anomalous Doppler frequency drift which can be interpreted as a small acceleration. Sources like the recoil from the heat radiation of the nuclear power plant on board or interaction with the interstellar gas are not expected to have such an influence on the flight [2]. So it might be that the law of gravitation is slightly different on earth and on distances between 20 and 70 AU[1] or there is an unconsidered source of gravitation. The additional mass to explain the Pioneer anomaly would correspond to 3×10^{-4} times the solar mass within 50 AU [2]. Such a mass contribution to the solar system would influence the ephemerides of the planets and can therefore be excluded in the Standard theory of gravity. A modification of the standard theory as mentioned in chapter 2.3 seems to be natural.

1.1.2 Rotation Curves of Galaxies

The rotation velocity of many galaxies, mainly of spiral type like shown in Fig. 1.2, were measured and the most of them exhibit no decrease in the rotation velocity as one expects from simple assumptions: If the luminous mass would be all of the gravitating mass the centripetal and gravitational force should be in equilibrium:

$$\frac{m_{test} v_{rot}^2}{r} = \frac{G_N M_{gal} m_{test}}{r^2} \tag{1.1}$$

and therefore the rotation velocity v_{rot} should behave like

$$v_{rot} = \sqrt{G_N M_{gal}/r} \tag{1.2}$$

where G_N is the Newtonian constant of gravity and r is the distance between the test particle and the galactic center. M_{gal} is the galactic mass inside r. Though the rotation velocity of a test particle of mass m_{test} outside the luminous disk should decrease, a nearly constant velocity is observed in most systems. A typical example for such rotation curves is shown in the lower part of figure 1.3.

The explanation could be the existence of a almost spherical halo of Dark Matter. Different kinds of ordinary Dark Matter like Brown Dwarf stars or Black Holes were search for in many experiments. A massive compact object, called MACHO, would focus the light of a background star and the

[1] 1 AU is the distance between the sun and the earth, which is about 149.598.000 km

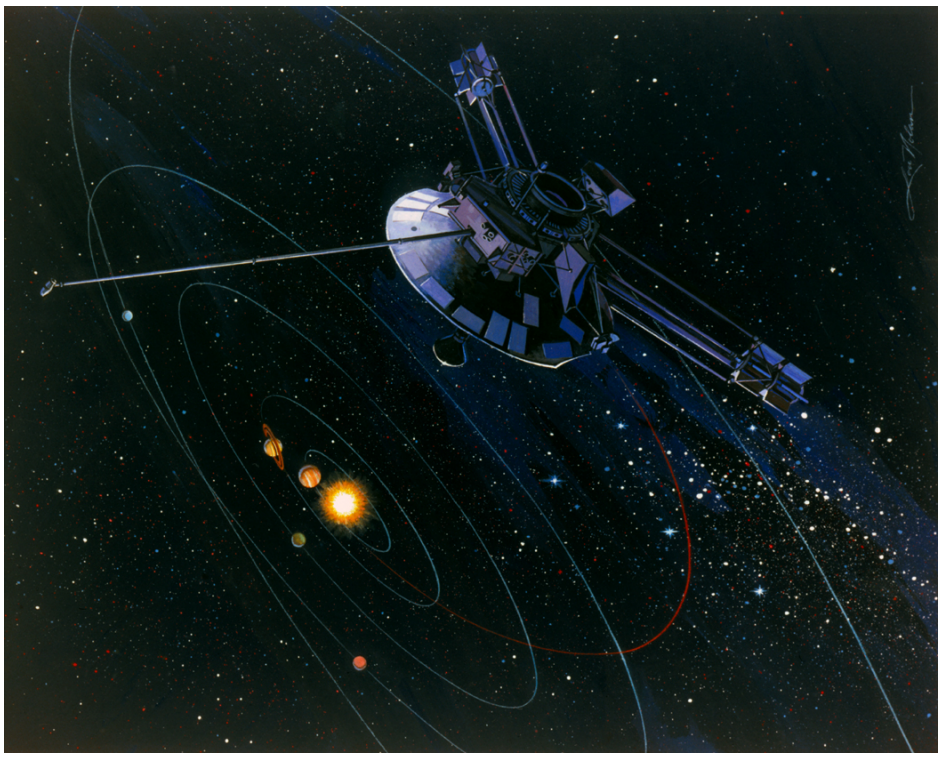

Figure 1.1: An artists view of the Pioneer 10 spacecraft on its ways to the system of Aldebaran [3] is shown. An unexpected and not understood deviation from the calculated track is still under investigation. It could be an effect of Dark Matter or a hint for a modified law of gravitation.

background star for a short period of time seems to be brighter than usual. The experiments searched for a short variation in the brightness of the stars in the Large Magellanic Cloud and our Milky Way galaxy with a high resolution CCD–camera. Some events caused by gravitational lensing could be found, but they are far to rare to explain the Dark Matter with such objects alone [4]. Therefore the explanation for the shape of the rotation curves is an open question until today. It could be solved with an unknown type of matter as well as a modification of gravity.

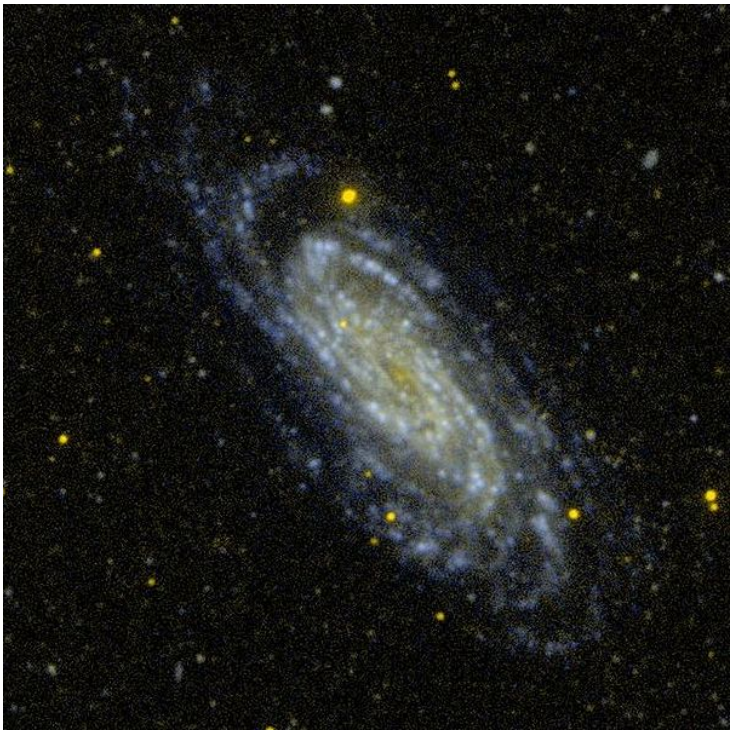

Figure 1.2: The galaxy NGC 3198 is one of the best examples for an unexpected velocity distribution of spiral galaxies (from Ref. [5]). Our own galaxy, the Milky Way, is also a spiral galaxy, but here the rotation velocity of the member stars is far more difficult to determine as our solar system moves within the frame of the Milky Way.

1.1.3 The Collision of Galaxy Clusters

The collision of galaxy clusters gives the unique possibility to study the dynamical behavior of the cluster components in non–equilibrium situations. The gas components measured with X–Ray telescopes interact with each other

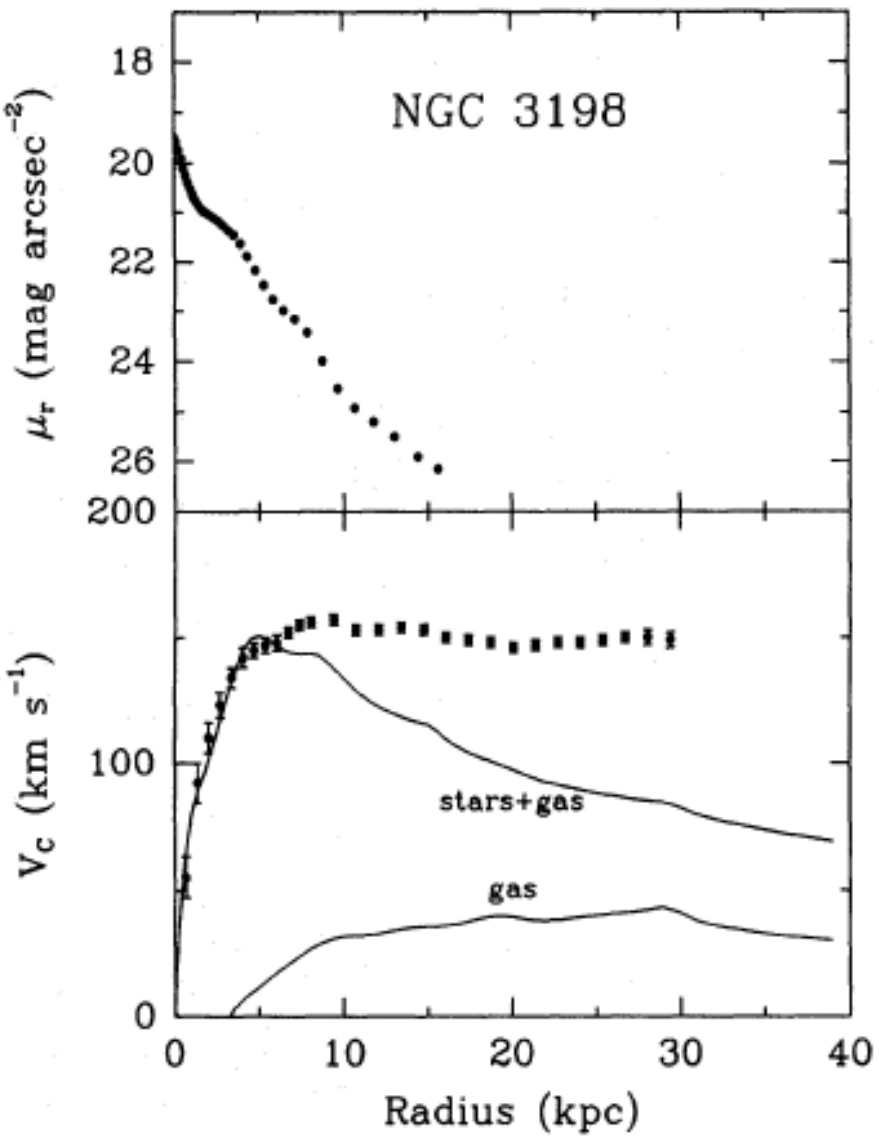

Figure 1.3: Upper part: The density of luminosity from NGC3198 — compare Fig 1.2 — is shown on a logarithmic scale. In the classical picture, luminosity is assumed to be directly proportional to the mass. Lower part: Far beyond the visible radius of NGC 3198 the velocity distribution was measured with help of the 21 cm–line of Hydrogen. There was no decrease of the rotation velocity found [6]. This points towards a halo of Dark Matter which is large compared to the luminous disk.

in a hydrodynamic way, similar to a fluid. The luminous component made out of galaxies is like dust and almost collisionless within such a merger. These different behaviors allow to separate the components of a galaxy cluster and study their properties individually. In addition a gravity map of the whole cluster is made via the weak–lensing effect. Every deviation of the gravity center from an optical counterpart is a strong hint for Dark Matter.

Bullet Cluster

One of the seldom events of a cluster merger happens in the Bullet Cluster [7]. The gas component is expected to be much heavier than the galaxy component. Therefore, one would expect that the center of gravitation would have a similar behavior like the gas part. As one sees in the upper part of figure 1.4 this is in contradiction to the observation. The mass center follows apparently more the collisionless component in the cluster as the lower part of 1.4 illustrates. But after a closer look, the center of gravity is not found near the point of the brightest galaxy as one would expect if the luminous component made up the mass. There is an $8\,\sigma$ deviation between those two spots (for the east and the west cloud each). This result favors again Dark Matter as the main component of gravitation in a galaxy cluster and its interaction should be very weak. The interaction of Dark Matter probably also can be described as dust–like due to the properties in a cluster merger.

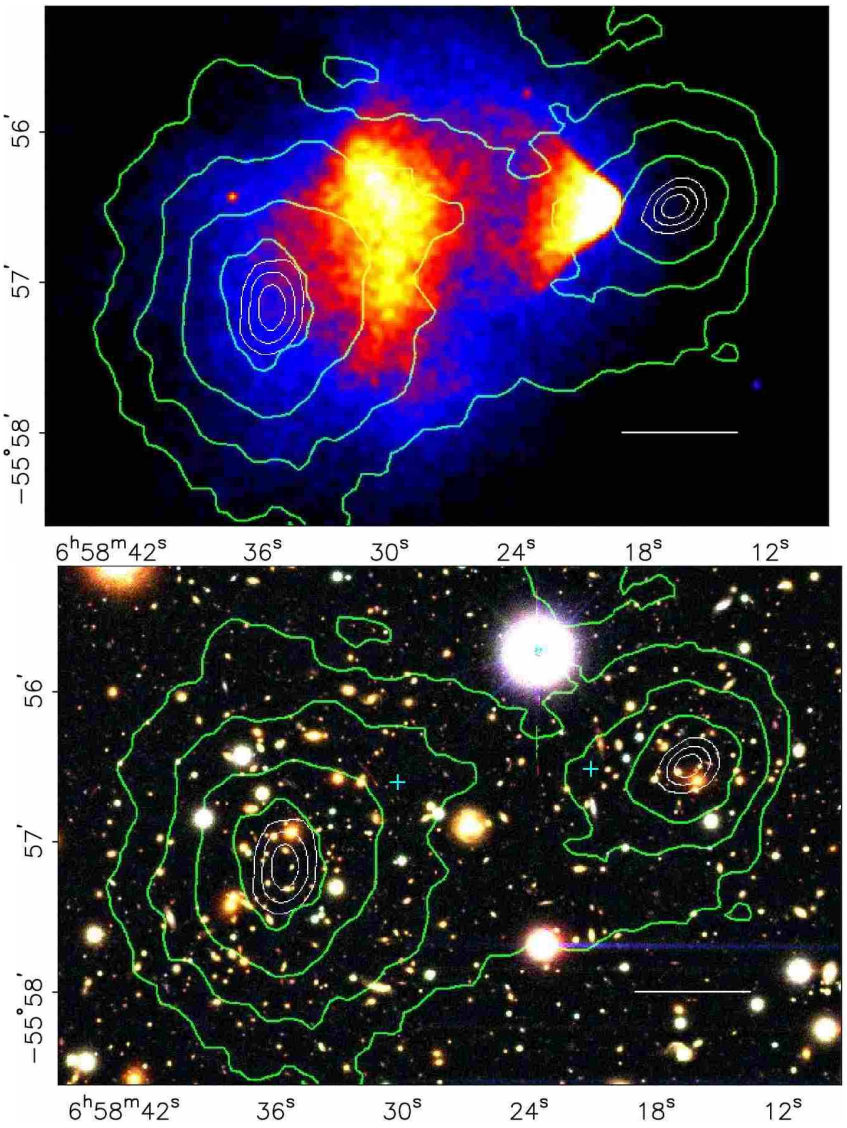

Figure 1.4: The cluster merger from reference [7] is one of the most powerful hints for a Dark Matter contribution to galaxies. Upper figure: The green contour lines indicate the mass distribution as it is expected from weak gravitational lensing effect. The superimposed color picture is the cluster in X–Ray light coming from enclosing gas. The shape of the gas cloud shows that the clusters hit recently. The distribution tells that gas is not the main gravitational source if it is compared to the contour shape. Lower figure: The same contour lines as in the upper figure are shown. This time superimposed with the optical picture. In the two gravitational centers, there is not sufficient mass visible in the optical picture. Dark Matter is often introduced to explain this observation.

Cluster MS1054–0321

The collision of the Bullet Cluster of the previous section is perhaps the most impressive example, but there are more clusters where the gravitational centers are not conclusive within the General Relativity Theory (Sec. 2.1). One of these clusters is MS1054–0321 [8]. Though one recognizes in figure 1.5 multiple maxima in the contour line plot as centers for gravitation, it is assumed that this galaxy cluster is also in the phase of rearrangement after a collision. The X–Ray distribution in the mentioned figure again does not match very well with gravity contours and, more important, there are islands of gravitation without an X–Ray counterpart. The assumption that there the source of gravitation is visible in the optical range is tested with Fig. 1.6. The quantitative analysis of Ref. [8] results in a mismatch greater than $8\,\sigma$ of the statistical error. That supports consistently with the Bullet Cluster the need for a Dark Matter component.

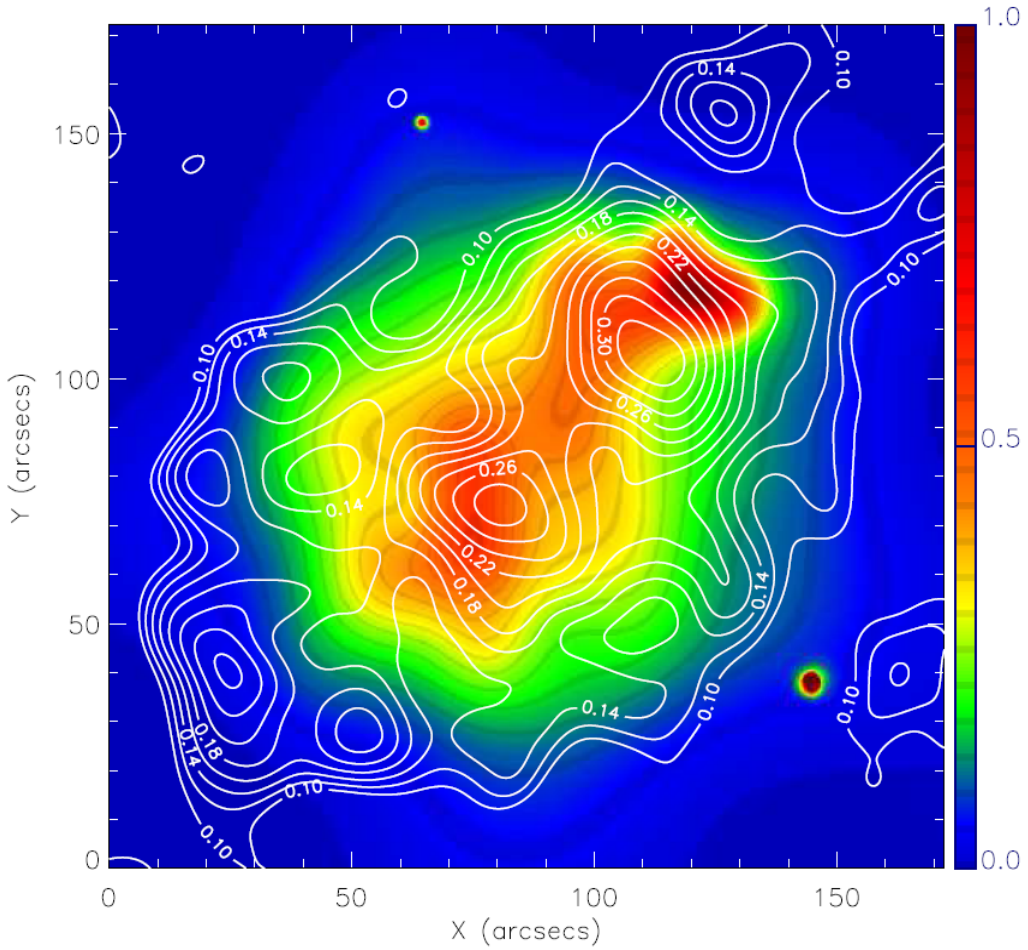

Figure 1.5: The cluster merger from MS1054–0321 [8] is another hint for a Dark Matter contribution to galaxies. The contour lines indicate the gravitational centers as they are derived from the weak gravitational lensing. Color coded is the intensity of X–Rays which is a direct signal of the gas distribution and thus the majority of the visible mass. There is only a loose relation between those distributions. Some "islands" of gravitation cannot be explained.

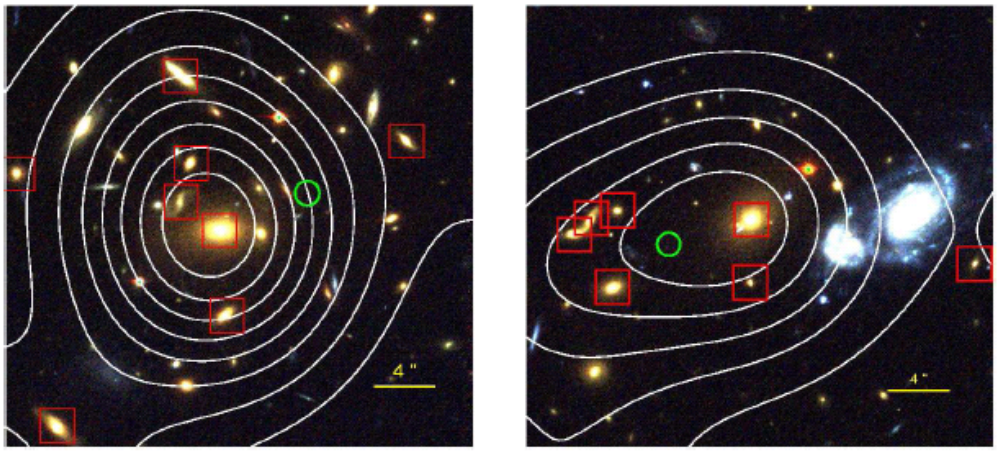

Figure 1.6: The two main gravitational centers of MS1054–0321 are shown as green circles. The contour lines quantify the optical brightness and center around the brightest galaxy within 1″ for the left or 2″ for the right one. The red squares mark spectroscopically confirmed members of the cluster. One would assume the brightest galaxy to be the main gravitational center. The green indicators are far more than the measurement uncertainties away from the brightest galaxy nearby. Either the law of gravitation (and with it the law of gravitational lensing) must be modified or some invisible matter has to be added in our models to bring all the results into agreement [8].

1.2 The Standard Cosmology - ΛCDM Model

In the early 20th century it was observed that most of the nebulae (today known as galaxies) have a redshifted spectrum. Edwin Hubble measured the distance of these objects and found a proportionality between the degree of redshift and the distance. Today this relation is named Hubble Law in his honor. The redshift is interpreted as a Doppler shift of the spectrum due to the velocity of the galaxies moving away from us. With the assumption of homogeneity one comes to the conclusion that the universe expands. Alexander Friedmann found a solution for the evolution of the universe in time within the framework of the General Relativity Theory. Looking backward in time the universe started in a very dense, hot and small region to expand afterwards like an explosion (often referred to as Big Bang). Studying the dynamics of the expansion provides information of the properties of the matter content.

1.2.1 Supernovae Ia

In cosmology one of the crucial issues is the measurement of distances. Beginning in a closer region one can use a simple geometrical effect called parallax measurement. Here, the virtual motion of a close object, like the nearest neighbor stars compared to very far objects, is measured during the earth circling around the sun. This direct method has a very limited range of up to 10^8 AU[9]. At larger distances one has to rely on indirect effects like the above mentioned Hubble Law. A unique possibility are so–called standard candles. That are objects from which we know how bright they are or at least that different objects of that kind are always of the same luminosity.

Due to the understood explosion mechanism of a Supernova type Ia, illustrated in Fig. 1.7, they are the ideal choice. The event is very bright therefore one can see Supernovae over large distances. A Supernova Ia always occurs in a binary system. The heavier star burnes faster and becomes a Red Giant. The envelope of the giant star is blown into space leaving behind the core in the form of a White Dwarf within the binary system. When the companion becomes older it grows in diameter and a part of its envelope is collected by the White Dwarf which grows heavier and heavier. A key property of White Dwarfs is that they are stable only below a critical value, called Chandrasekhar–mass ($M_C \approx 1.4\,M_\odot$). When the star collected enough mass it becomes unstable and explodes [10]. The calibration of the absolute magnitude of the explosion is still under improvement[11], but as there are always the same fixed boundary conditions and enough events of this kind, the type Ia Supernovae becomes a powerful tool for the astronomers.

The Hubble Law can be very accurately verified with the help of supernova

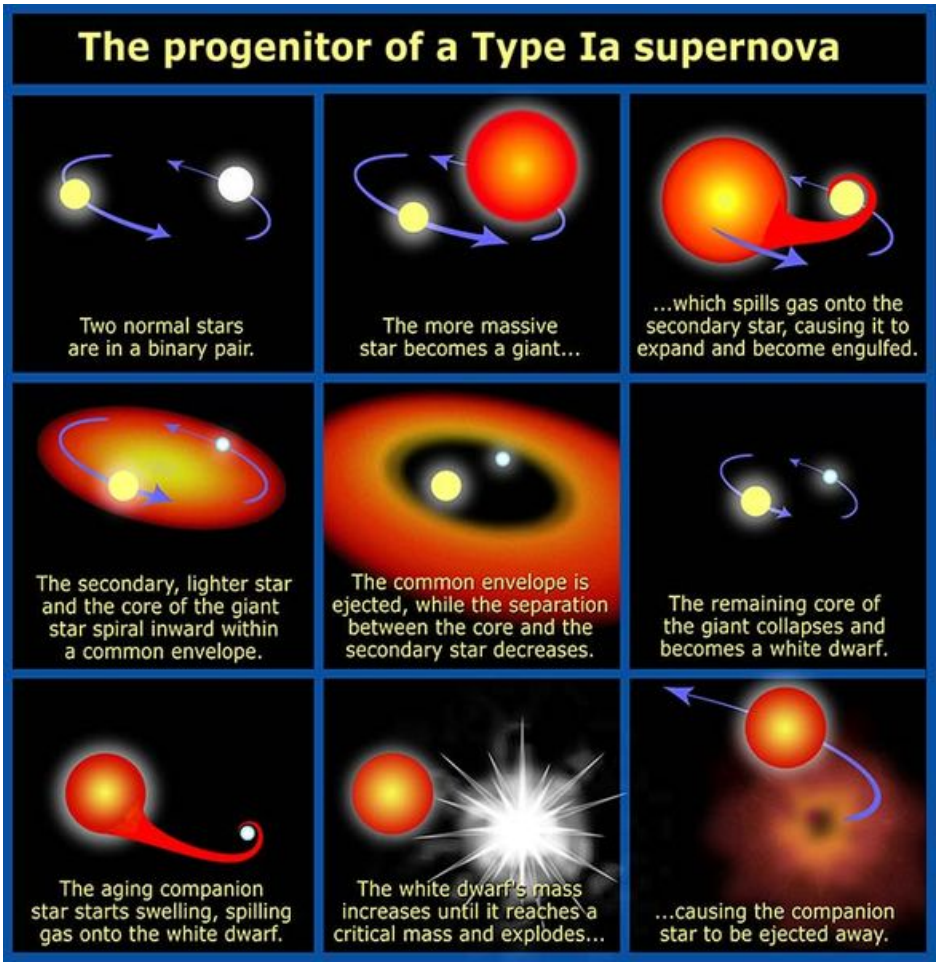

Figure 1.7: The explosion mechanism of a Supernova Ia is very well understood [10]. And more important, the boundary conditions are always the same: A White Dwarf star in a binary system accretates matter from the partner until it reaches the Chandrasekhar–mass. Then the pressure in the White Dwarf gets too high and the core explodes in a nuclear reaction. The picture is taken from reference [5]

brightness as figure 1.8 shows. The measured brightness is an indirect measure for the distance as we know that all events are equal in absolute brightness. The Redshift is given in z, which is defined as

$$z = \frac{\lambda_{\text{obsv}} - \lambda_{\text{emit}}}{\lambda_{\text{emit}}} \tag{1.3}$$

where λ_{emit} is the wavelength as it is emitted and λ_{obsv} is the wavelength observed on earth. The emitted wavelength can only be assumed, but it is very probable that e.g. Hydrogen has the same emitted wavelength everywhere in the universe.

In the Friedmann model of the universe z has an additional meaning:

$$1 + z = \frac{a_{\text{now}}}{a_{\text{then}}} \tag{1.4}$$

where $a(t)$ is the time dependent scaling parameter of the spacial components in the metric

$$-c^2 \mathrm{d}\tau^2 = -c^2 \mathrm{d}t^2 + a(t)^2 \mathrm{d}\mathbf{\Sigma}^2 \tag{1.5}$$

and $\mathbf{\Sigma}$ ranges over a 3–dimensional space of uniform curvature and is independent of time. All time dependence is in $a(t)$. The explanation for the Redshift in the Friedmann model is the expansion of space itself:

$$1 + z = \frac{a_{\text{now}}}{a_{\text{then}}} = \frac{\lambda_{\text{obsv}}}{\lambda_{\text{emit}}} \tag{1.6}$$

The Redshift in that sense is also a measurement of time and if one looks into the past, the development of the Redshift contains information about the dynamics of the Big Bang which is influenced by the energy and matter content of the universe. The energy and matter contents are given in form of the density parameter Ω, which is the ratio of the averaged density for that specific type to the critical density ρ_{c} of the universe. The critical density is the value, where the universe is flat. It is given by the formula

$$\rho_{\text{c}} = \frac{3H_0^2}{8\pi G_N} \tag{1.7}$$

where G_N is again the Newtonian constant of gravity and H_0 is the Hubble constant[2].

Precise measurements were made to see a deviation of the linear Hubble Law. A deviation could be found [12] and was later confirmed by an independent data set of supernovae of even higher z [13]. In figure 1.9 the brightness

[2]Strictly speaking the Hubble constant is not constant. Its value is time dependent following $H(t) = \frac{\dot{a}(t)}{a(t)}$. H_0 is the value of $H(t)$ today.

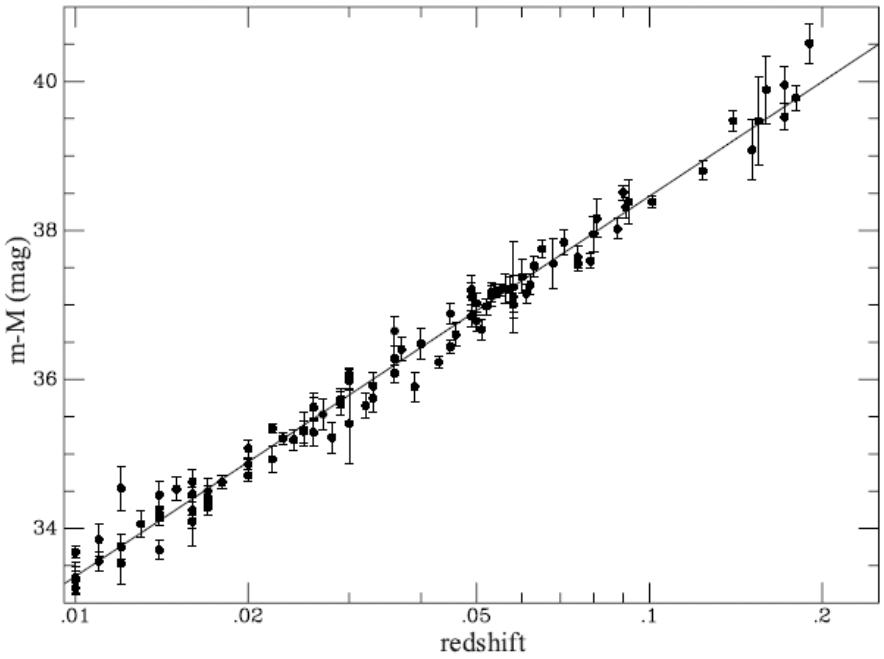

Figure 1.8: Due to their common explosion mechanism the Supernovae of type Ia are fixed in the absolute brightness. If they seem to be darker then they have to be further away from us. The parameter (m-M) is the difference between the observed and the calculated brightness and quantifies the "darkness" of an object on a logarithmic scale. Remarkably the redshift of Supernova spectra, measured in z, gets higher and higher as they are further away [12]. This experimental fact leads to the Hubble Law, that the redshift *is* a measure for distance.

is plotted versus the Redshift in z for a wider range of z than in figure 1.8, so the deviation from the linear Hubble Law for large values of z becomes visible. The values for the cosmological parameters of the Matter content $\Omega_M = 0.3$ and the Energy content $\Omega_\Lambda = 0.7$ fit the data best. The Energy content Ω_Λ is ascribed to the Dark Energy, which occurs in cosmological models, for example in form of the Cosmological constant Λ, but the origin remains unknown. A probability map of the whole allowed region in the parameter range of Ω_M and Ω_Λ is shown in Fig. 1.10. The mentioned values are not the preferred ones from this measurement alone, but with the boundary condition that $\Omega_M + \Omega_\Lambda = \Omega_{tot} = 1$, which corresponds to a flat universe, it is the likeliest combination. This value for Ω_{tot} comes from measurements of the Cosmic Microwave Background as shown in the next section.

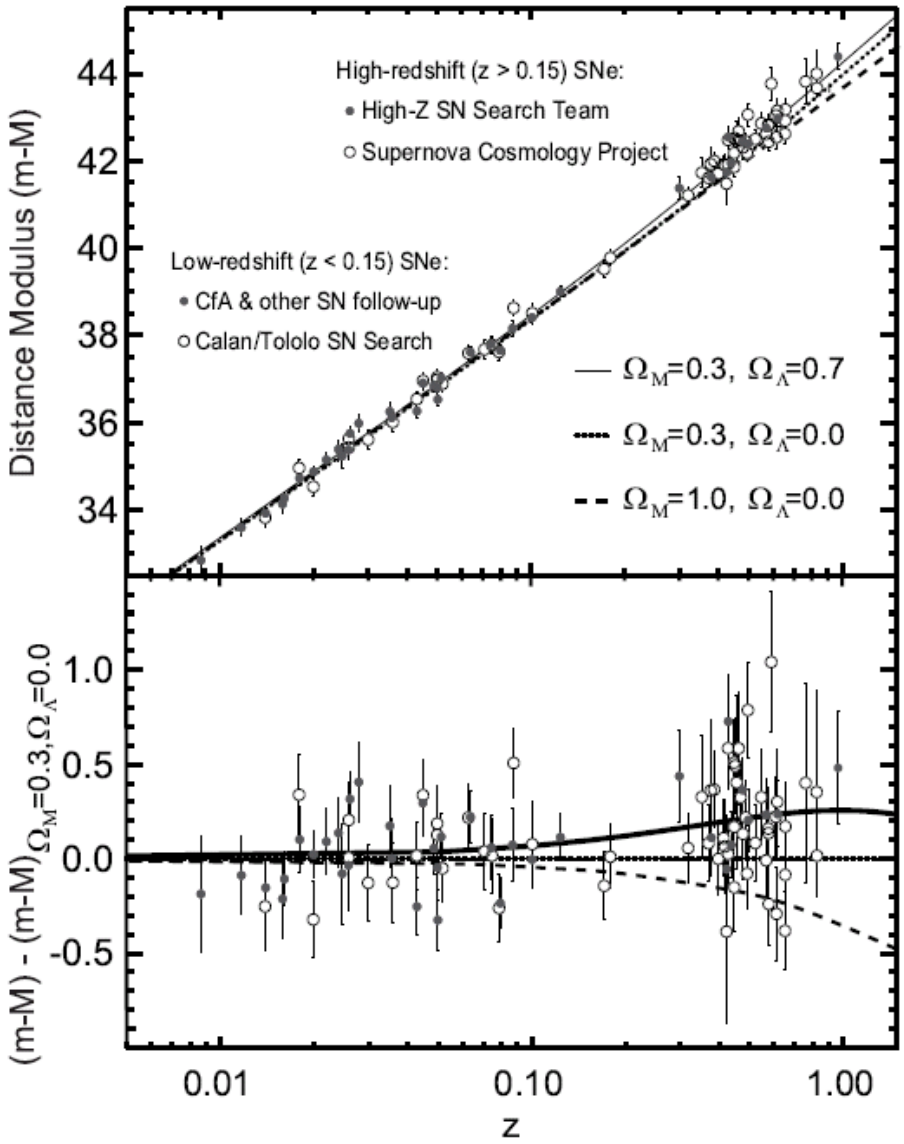

Figure 1.9: Upper picture: The distance modulus versus the redshift z is plotted like in figure 1.8. For large values of z a small deviation from the Hubble Law is observed which is an expected phenomenon of cosmology. Lower picture: The difference of the distance modulus with respect to a model with $(\Omega_M = 0.3; \Omega_\Lambda = 0.0)$ is plotted and the combination of $(\Omega_M = 0.3; \Omega_\Lambda = 0.7)$ seems to fit the data best [12].

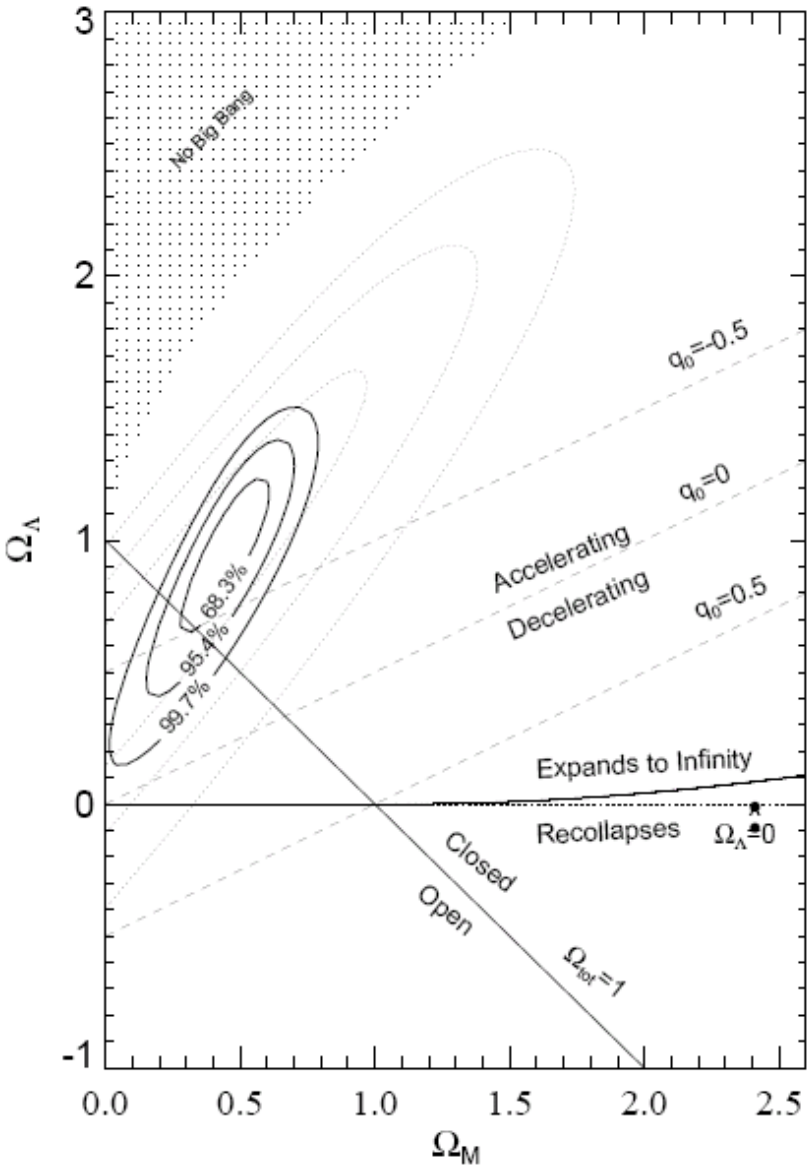

Figure 1.10: The fit of all parameter combinations to the data leads to this probability map. Indicated with the black contour lines is the preferred region of parameters [13]. The grey shaded probability contours come from an older measurement with less supernovae of high Redshift. The paper suggests a model with an accelerated expansion today which was a deceleration at the beginning shortly after the Big Bang. To learn more about the evolution of the expansion a bigger dataset of high z supernovae would be useful.

1.2.2 Cosmic Microwave Background (CMB)

The Cosmic Microwave Background is the earliest radiation which was set free to travel through the universe. At the beginning of the universe it was too hot to build neutral atoms and so the radiation was in thermal equilibrium with the charged particles. But as the temperature decreases, atoms were formed at roughly 3000 K and the radiation decoupled from matter. Therefore, a thermal distributed spectrum is expected to reach us from all directions. The spectrum is heavily redshifted as it happened in an early stage of the universe and today the temperature of the CMB is 2.725 Kelvin. This radiation was accidentally detected in 1964 by Arno Penzias and Robert Woodrow Wilson.

Precise measurements of the temperature of the CMB with satellites like COBE, WMAP or Planck found a variation in the order of 10^{-5} over the hemisphere (see Fig. 1.11). This map is the earliest angle–dependent information of our universe. The detailed analysis of that map provides us exact values of the cosmological properties. The total density is $\Omega_{tot} = 1$ and suggests a flat space. The matter density is $\Omega_M = 0.23$ as can be calculated from the depth of the gravitational potentials, but baryonic matter which interacts with electro–magnetic radiation makes up only 4%. The difference between these numbers is explained with the contribution of Dark Matter. All the rest of Ω_{tot} is either in the energy density Ω_Λ or, to a very tiny amount, radiation. The values can be extracted from the so called power spectrum (Fig. 1.12) as shown in Ref. [14].

The ΛCDM Model seems overwhelmingly consistent as it predicts the CMB with the right temperature and the model prefers a tiny angular dependency of the temperature of the radiation due to the presence of Dark Matter. The Supernova data from the previous section can be described with the same parameters. Also the development over the time of the universe is modeled and leads to a consistent picture shown in figure 1.13. However, small issues like the outlying first point of the power–spectrum give reason to the theoretical community to improve the model. For example Steiner [15] suggests a limited sized universe with the geometry of a 3–dimensional torus to bring the model in a better agreement with the data.

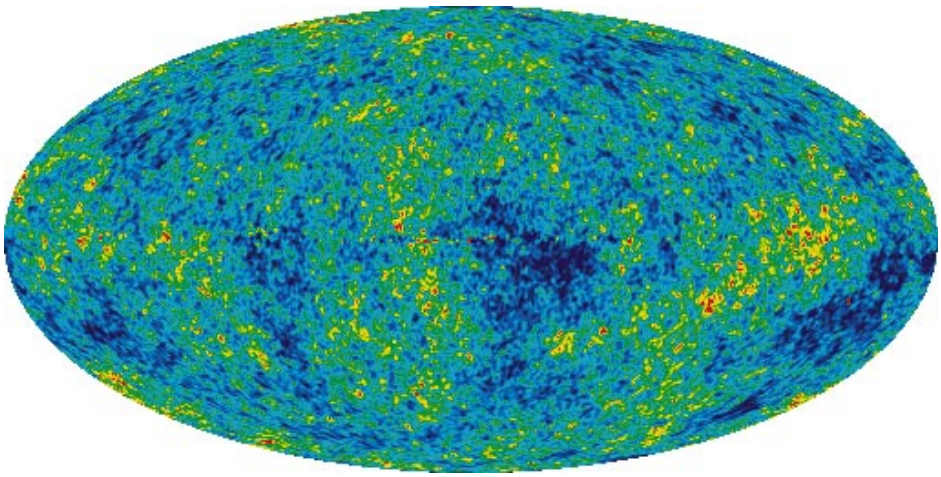

Figure 1.11: The CMB after correction for the earth motion and subtraction of the galactic plane. The map has a tiny fluctuation in the order of 10^{-5} in its temperature which points towards a breaking of the homogeneity of the universe. The cooler regions have consumed some energy as the radiation started in a stronger gravitational field. This contains useful informations about the distribution and properties of matter [16].

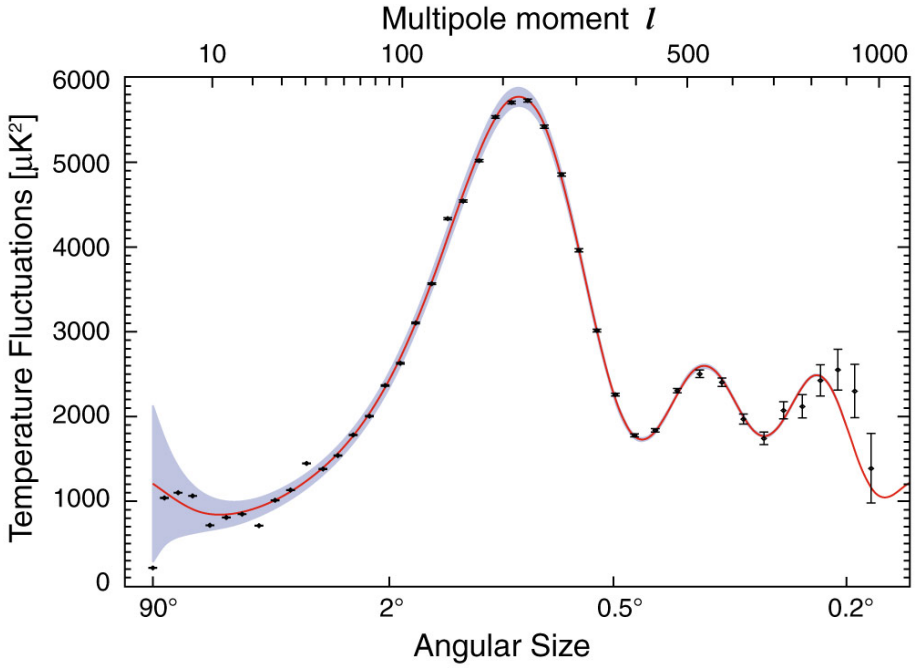

Figure 1.12: The fluctuations shown in Fig. 1.11 are analyzed in reference [16] and sorted by the strength of their multipole order. The positions and relative heights of the peaks give very precise information — within the ΛCDM model — about the Dark Matter content of the universe, which is calculated to be $\Omega_M = 0.23$. However, the baryonic matter like stars, galaxies and all ordinary matter make up only $\Omega_B = 0.04$. The question for the nature of all other matter content remains unsolved.

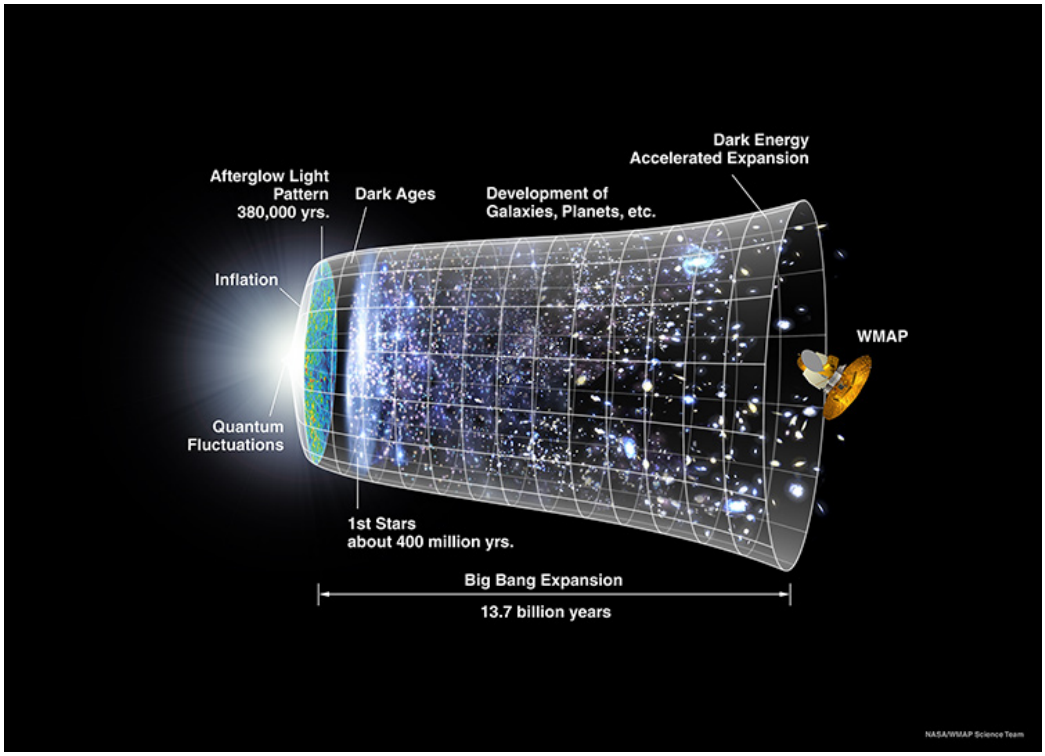

Figure 1.13: The picture illustrates the evolution of the universe as it is imagined today [16]. The WMAP satellite observes nowadays the first signal after the decoupling of radiation and matter. The ΛCDM model fits the measured radiation distribution being a perfect thermal blackbody spectrum with a corresponding temperature of 2.725 Kelvin.

Chapter 2

Possible Modifications of the Gravitational Force

Einsteins General Relativity Theory (GRT) describes our present knowledge of the gravitation best. It is very well tested by experiments and up to now there was no modification needed. The evidences for Dark Matter rely in particular on the present form of the GRT. This way, a modification of GRT has obviously to be taken into account as a possible solution of the Dark Matter problem. There are theories which vary some new parameter in the allowed region and provide surprisingly reasonable explanations. In this chapter, first a short introduction to the GRT is given and then possible modifications will be introduced. Except for section 2.3 about MOND, this chapter is based on the review by S. Turyshev [17].

2.1 General Relativity

General Relativity is a tensor field theory of gravitation with universal coupling to the particles and fields of the Standard Model (Sec.3.1). It describes gravity as a universal deformation of the flat space–time Minkowski metric, γ_{mn}:

$$g_{mn}\left(x^k\right) = \gamma_{mn} + h_{mn}\left(x^k\right) \tag{2.1}$$

Alternatively, it can also be defined as the unique, consistent, local theory of a massless spin–2 field h_{mn} , whose source is the total, conserved energy–momentum tensor (see [18] and references therein).

Classically (see [19]), general theory of relativity is defined by two postulates. One of the postulates states that the action describing the propagation

and self–interaction of the gravitational field is given by

$$S_G\left[g_{mn}\right] = \frac{c^4}{16\pi G_N}\int d^4x\sqrt{-g}R \tag{2.2}$$

where G_N is the Newton's universal gravitational constant, g^{mn} is the matrix inverse of g_{mn} , and $g = \det g_{mn}$, R is the Ricci scalar given as $R = g^{mn}R_{mn}$ with the quantity $R_{mn} = \partial_k\Gamma^k_{mn} - \partial_m\Gamma^k_{nk} + \Gamma^k_{mn}\Gamma^l_{kl} - \Gamma^k_{ml}\Gamma^l_{nk}$being the Ricci tensor and $\Gamma^k_{mn} = \frac{1}{2}g^{kp}\left(\partial_m g_{pn} + \partial_n g_{pm} - \partial_p g_{mn}\right)$ are the Christoffel symbols.

The second postulate states that g_{mn} couples universally, and minimally, to all the fields of the Standard Model by replacing everywhere the Minkowski metric. After applying the variational principle to the total action one obtains the well–known field equations of general theory of relativity,

$$R_{mn} - \frac{1}{2}g_{mn}R + \Lambda g_{mn} = \frac{8\pi G_N}{c^4}T_{mn} \tag{2.3}$$

where $T_{mn} = g_{mk}g_{nl}T^{kl}$ with $T_{mn} = 2/\sqrt{-g}\delta L_{SM}/\delta g_{mn}$ being the (symmetric) energy–momentum tensor of the matter as described by the Standard Model with the Lagrangian density L_{SM}. With the value for the vacuum energy density $\rho_{vac} \approx (2.3 \times 10^{-3}eV)^4$, as measured by recent cosmological observations, the cosmological constant $\Lambda = 8\pi G_N\rho_{vac}$ [20] is too small to be observed by solar system experiments, but is clearly important on larger scales.

Einsteins equations Eq. 2.3 link the geometry of a four–dimensional, Riemannian manifold representing space–time with the energy–momentum contained in that space–time. Phenomena that, in classical mechanics, are ascribed to the action of the force of gravity (such as free–fall, orbital motion, and spacecraft trajectories), correspond to inertial motion within a curved geometry of space–time in general relativity.

2.2 Parameterized Post–Newtonian Formalism

By introducing new degrees of freedom to the standard GRT a possible deviation can be quantified. The parameterized post–Newtonian formalism (PPN) is a phenomenological parameterization of the gravitational metric tensor field $g^{PPN}_{mn} = g^{GR}_{mn} + \delta g^{PPN}_{mn}$. Measurements can give this way constrains to the extra parameters, which should be all exactly zero, if no modification of GRT is realized in nature.

One can calculate for this ansatz the PPN–perturbative acceleration between two bodies with the masses m_i, respectively m_j, on the positions $\mathbf{r_i}$,

respectively $\mathbf{r_j}$:

$$\begin{aligned}
\delta\ddot{\mathbf{r}}_i^{PPN} &= \sum_{j\neq i} \frac{\mu_i\left(\mathbf{r_j}-\mathbf{r_i}\right)}{r_{ij}^3}\left\{\left(\left[\frac{m_G}{m_I}\right]_i - 1\right) + \frac{\dot{G}}{G}\cdot(t-t_0)\right. \\
&- \left.\frac{2\left(\bar{\beta}+\bar{\gamma}\right)}{c^2}\sum_{l\neq i}\frac{\mu_l}{r_{il}} - \frac{2\bar{\beta}}{c^2}\sum_{k\neq j}\frac{\mu_k}{r_{jk}} + \frac{\bar{\gamma}}{c^2}\left(\dot{\mathbf{r}}_\mathbf{i}-\dot{\mathbf{r}}_\mathbf{j}\right)^2\right\} \\
&+ \frac{2\bar{\gamma}}{c^2}\sum_{j\neq i}\frac{\mu_j}{r_{ij}^3}\left\{\left(\mathbf{r_i}-\mathbf{r_j}\right)\cdot\left(\dot{\mathbf{r}}_\mathbf{i}-\dot{\mathbf{r}}_\mathbf{j}\right)\right\}\left(\dot{\mathbf{r}}_\mathbf{i}-\dot{\mathbf{r}}_\mathbf{j}\right) \\
&+ \frac{2\bar{\gamma}}{c^2}\sum_{j\neq i}\frac{\mu_j\ddot{\mathbf{r}}_\mathbf{j}}{r_{ij}} + \mathcal{O}\left(c^{-4}\right)
\end{aligned} \tag{2.4}$$

with $\mu_j = G_N m_j$, G_N the Newtonian constant of gravity and c equal to the light velocity in vacuum. Eq. 2.4 provides a useful framework for testing the gravitation theory, because besides the terms with the renormalized Parameters $\bar{\gamma}$ and $\bar{\beta}$ it contains a term for the temporal evolution of the gravitation constant $\dot{G}/G$. Maybe even more important, it provides a handle to test for the Equivalence Principle, *the* implicit assumption of most standard gravitation theories. Roughly speaking, this is the assumption that the mass m_G being the source of the gravitational field and the mass m_I being the source of inertia are identical. A non–zero first term in the above equation would violate that principle. The parameter $\bar{\gamma}$ is a measure of the violation of the unit curvature. The parameter $\bar{\beta}$ is interpreted as the violation of the non-linearity of the law of gravitation.

Multiple measurements on astronomical scales provide upper limits for the parameters $\bar{\gamma}$ and $\bar{\beta}$. In Figure 2.1 an overview over the experiments and their measured limits is given. The microwave tracking of the Cassini spacecraft on its approach to Saturn in the year 2003 improved the experimental accuracy of the parameter $\bar{\gamma}$ to $\bar{\gamma} = (2.1 \pm 2.3) \times 10^{-5}$. The Lunar Laser Ranging (LLR) is a continuing legacy of the Apollo program. It provides improved constraints on the combination of parameters $4\bar{\beta} - \bar{\gamma} = (4.0 \pm 4.3) \times 10^{-4}$ via precision measurements of the lunar orbit. These results together leave only very little parameter space for alternative theories to explain Dark Matter with a modified theory of gravity.

2.3 Modified Newtonian Dynamics (MOND)

An empirical ansatz to explain the flat rotation curves of spiral galaxies was suggested in 1983 by M. Milgrom. It rests on the idea that one modifies Newton's law of gravitation for large distances in that way that one achieves

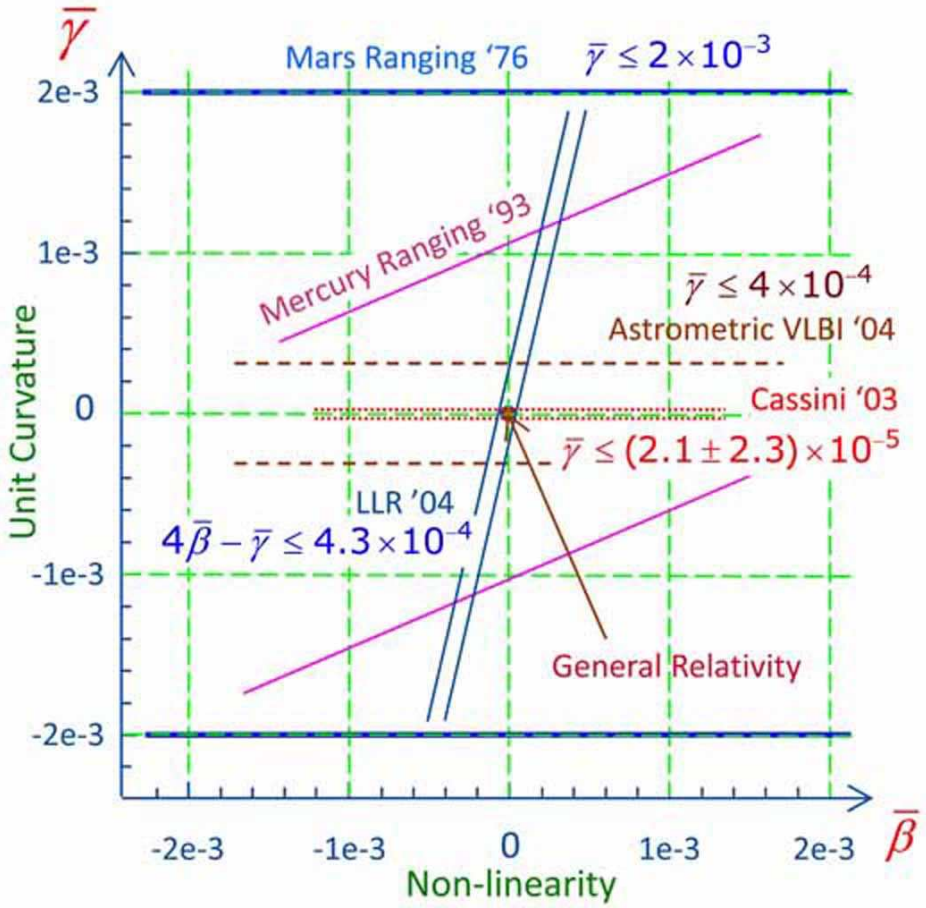

Figure 2.1: Different experiments proved the accuracy of the GRT. The resulting limits are displayed in the picture above [17]. Due to the kind of the measurement principle they are sensitive to $\bar{\gamma}$ or a combination of $\bar{\beta}$ and $\bar{\gamma}$. A big violation of GRT is excluded, at least for length scales of the order of our Solar System.

flat rotation curves. Thus, the gravitation becomes proportional to the distance exactly like the Centrifugal Force. The most simple ansatz is

$$F = \frac{GM}{r^2} f(r/r_0) \tag{2.5}$$

The distance r_0 is a constant in the order of a few kpc. The function f(x) is defined such that $f(x) = x$ when $x \gg 1$ and $f(x) = 1$ for $x \ll 1$. Soon after publication it was realized that this ansatz implies an asymptotic velocity $v^2 \propto M$, whereas the empirically found Tully Fisher Law predicts a relation $v^4 \propto L \propto M$

To satisfy also the Tully Fisher Law one chooses not to modify Newton's Law of gravitation but his second law of motion $F \propto ma$ in a similar way:

$$ma\mu(a/a_0) = F \tag{2.6}$$

with $\mu(x) = x$ when $x \ll 1$ and $\mu(x) = 1$ for $x \gg 1$.

A value for the parameter a_0 is proposed to be around $10^{-10} m/s^2$ (page 41 in Ref. [21]). With that value many different rotation curves can be explained very well with only the mass–to–light ratio as free parameter. The value seems also to explain consistently the Pioneer anomaly from section 1.1.1. But despite its success in astronomy on the scale of galaxies it is in clear contradiction to some gravity experiments in laboratories on earth, which tested the second law of Newton down toward accelerations around $10^{-12} m/s^2$ as shown in Fig 2.2. Therefore a promising theory should predict a MOND–like behavior only on astronomical scales.

The solution to the Dark Matter problem by modifying the gravitation is followed up in various references, for example Ref. [22],[23] and [24]. But an explanation for the curious dynamics of colliding galaxy clusters (see Sec. 1.1.3) seem to be unlikely within this framework. Therefore, an alternative from particle physics is favored at the moment and will be introduced in the next chapter.

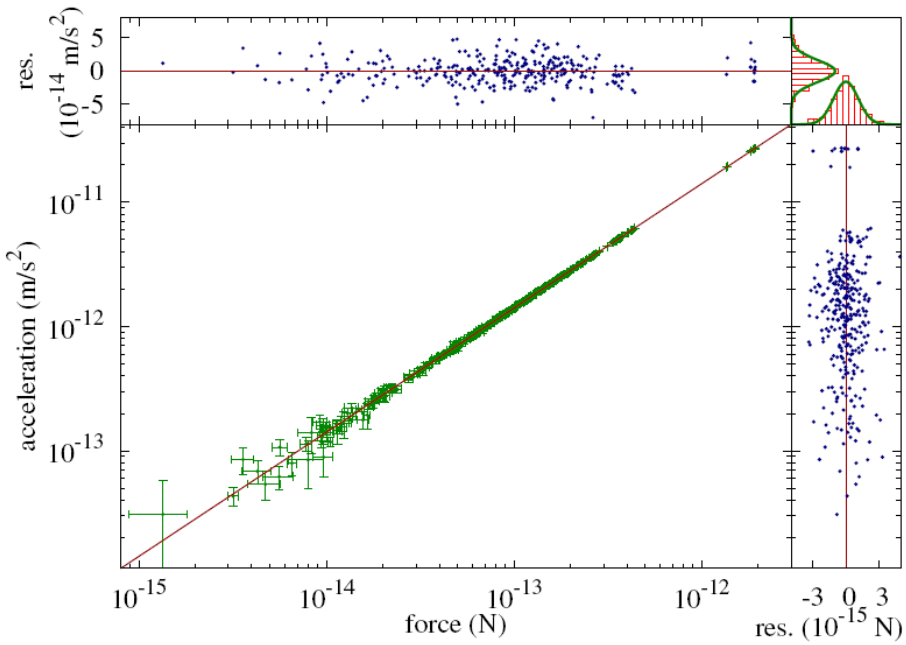

Figure 2.2: The measured force versus the measured acceleration of a classical torsion balance experiment. The solid line is the best fit for acceleration a, being exactly proportional to force F. The data agrees very well with the curve. The insets on the right and the top of the main graph give the residuals of the data to the fitted line. The picture is taken from [25].

Chapter 3

Possible Particle Physics Candidates for the Dark Matter

In the 1980s a theoretical model was developed which could explain all the different aspects of the particle zoo found at high energy accelerators. This model is called the Standard Model today and is briefly presented in section 3.1. An extension of the Standard Model is Supersymmetry, discussed in section 3.2. Some additional particles appear and are candidates of being the Dark Matter particles. The last part of this chapter introduces two leading experiments which search directly for Dark Matter consisting of a yet unknown particle.

3.1 Introduction to the Standard Model

In everyday life our surrounding consists of different chemical elements. But if one takes a closer look, the broad variety in chemistry boils down to the table of elements (Fig. 3.1) with a handful different pieces. The quantity which changes from one element to the next is the proton number of the nucleus of the atom. If this changes the negatively charged atomic shell also has to change accordingly the number of electrons to achieve the atom to be as whole electrically neutral. Often there are multiple realizations of the core of an atom, namely the number of neutrons can vary without changing the chemical properties. So the table of isotopes in figure 3.2 shows the full variety of isotopes found on earth.

With only three particles (proton, neutron and electron) this simple model explains nicely our surrounding world. But if we look at high energetic collisions in accelerators or the decay products of cosmic rays or even the kinematics of a β decay it gets obvious that we need more ingredients for a

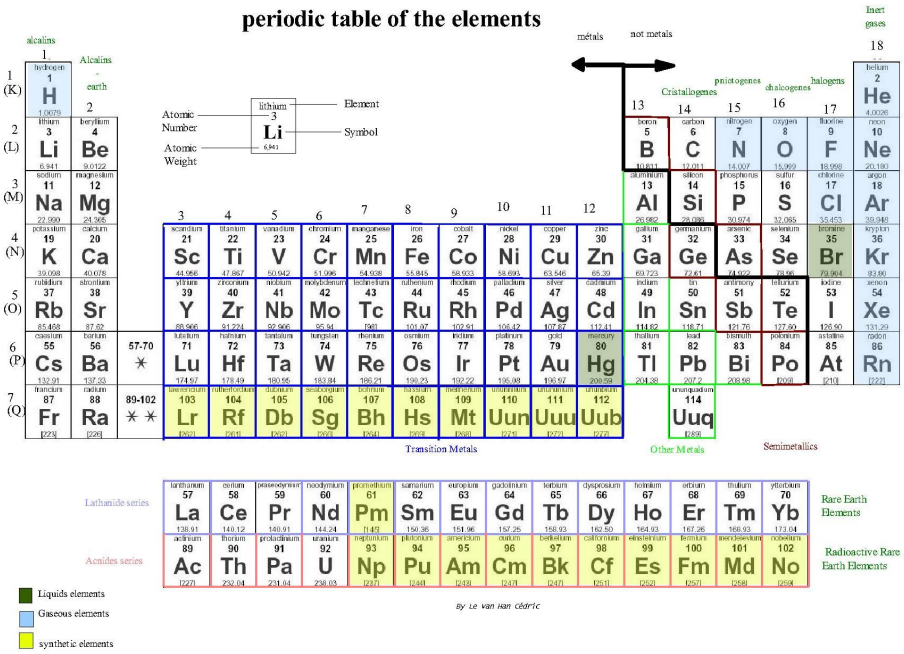

Figure 3.1: The Table of Elements: Proposed by the Russian scientist Mendeleyev in 1869 as an ordering scheme for the chemical Elements. At this time only 63 (Ref. [26]) of the about 110 elements we know today were known and the ones discovered later all fit perfectly into his scheme. Picture from [5].

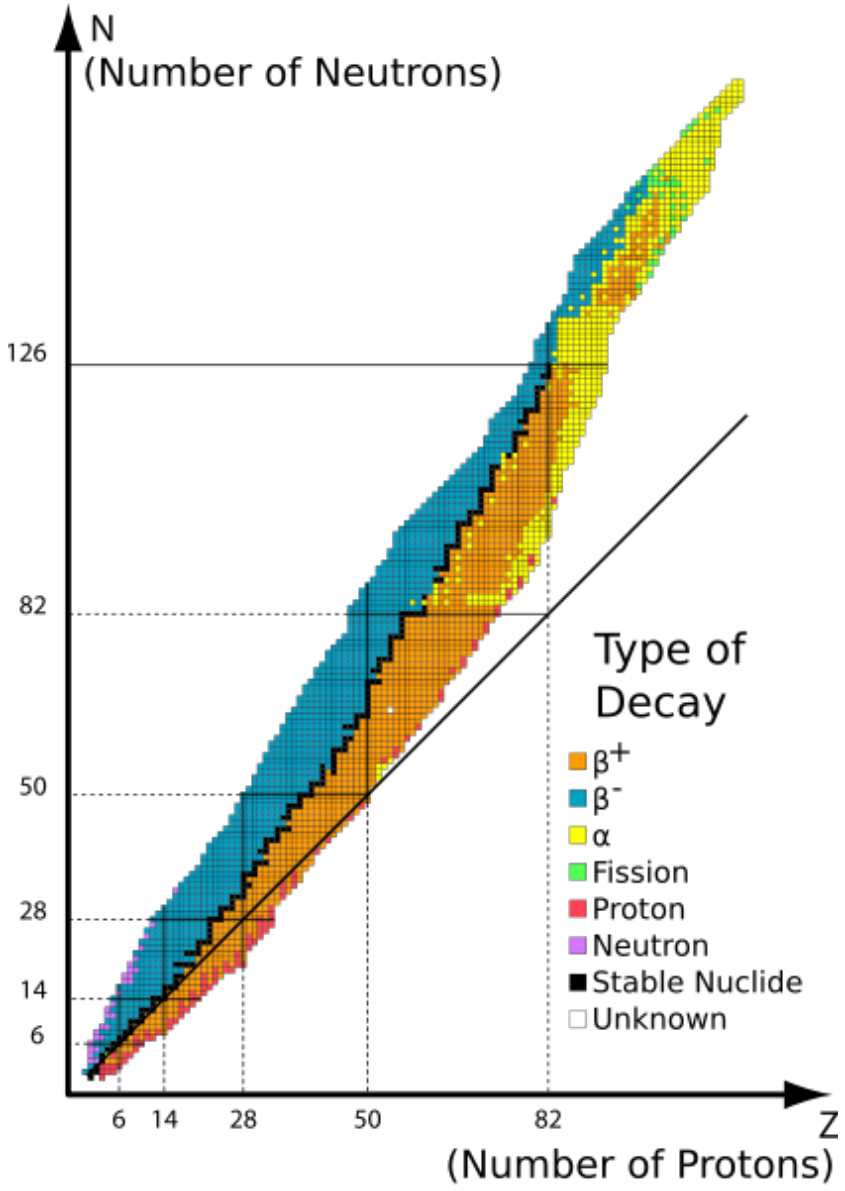

Figure 3.2: The Table of Isotopes: You see all known isotopes found on earth represented with a small rectangle. Color–coded is the decay–property of the nucleus, so one sees on a first look, whether it is stable or which decay mode (like α, β^- or β^+) is existent. Picture from [5].

full description.

In the year 1930 Wolfgang Pauli proposed one should extent the group of particles to resolve the problem in the kinematics of the β decay. The β–spectrum is a continuous electron energy spectrum measured, which would violate the conservation of energy and momentum if only two particles were involved in the decay. Thus Pauli suggested a third particle, which was electrically neutral and had an extremely weak interaction rate so it could not be measured with the usual methods at that time. This particle later was called Neutrino and nowadays it is measurable with large detectors. A lot of neutrinos are produced in the fusion reaction in the sun or at man–made reactors therefore the properties are well measured and partly understood. But the mass of this particle is not known. All we know is, that it is nonzero[1] and there is an upper value of 1.8 eV/c^2 which can be derived from astronomical constrains, like in [27].

Later, in the year 1936, Carl D. Anderson discovered in cosmic rays a particle with the properties of an electron but about 200 times heavier. Due to its intermediate mass between electrons and protons it was first given the name "mesotron", what seems inconvenient as more and more particles of that mass range were discovered. Today this particle is called muon. The lifetime of muons is $2.2 \times 10^{-6}\,s$ but as they travel near the speed of light after they are produced in the upper part of the atmosphere, they have a much longer lifetime in the rest frame of the earth. A muon interacts via the electro–magnetic force and the weak force (and of course gravitation). Its decay is dominated by the weak interaction process via a W^- like shown schematically in figure 3.3. In all interactions observed in nature the sum of the participating muon and muon neutrinos or the sum of the electrons and electron neutrinos remains constant. In muon decay this observation means that a muon neutrino has to occur as the muon disappears and an electron anti–neutrino occurs together with an electron as the W^- disappears. The anti–neutrino is the anti–particle of the neutrino with the same quantum numbers, each with the opposite sign. The exact separation between electron and muon sector is accounted for as they are sorted to different "generations" in table 3.1.

A third generation was found in 1975 at the Stanford Linear Accelerator Center [28]. The new particles were named tauon. All these particles are possible decay modes for heavier particles and with the help of this property it was shown that there are not more than three generations[2]. The Z^0 particle was produced in large numbers at the Large Electron Positron (LEP) collider

[1] at least in two of the three particle generations

[2] at least up to the mass scale of the Z^0 which is around $90\,GeV$

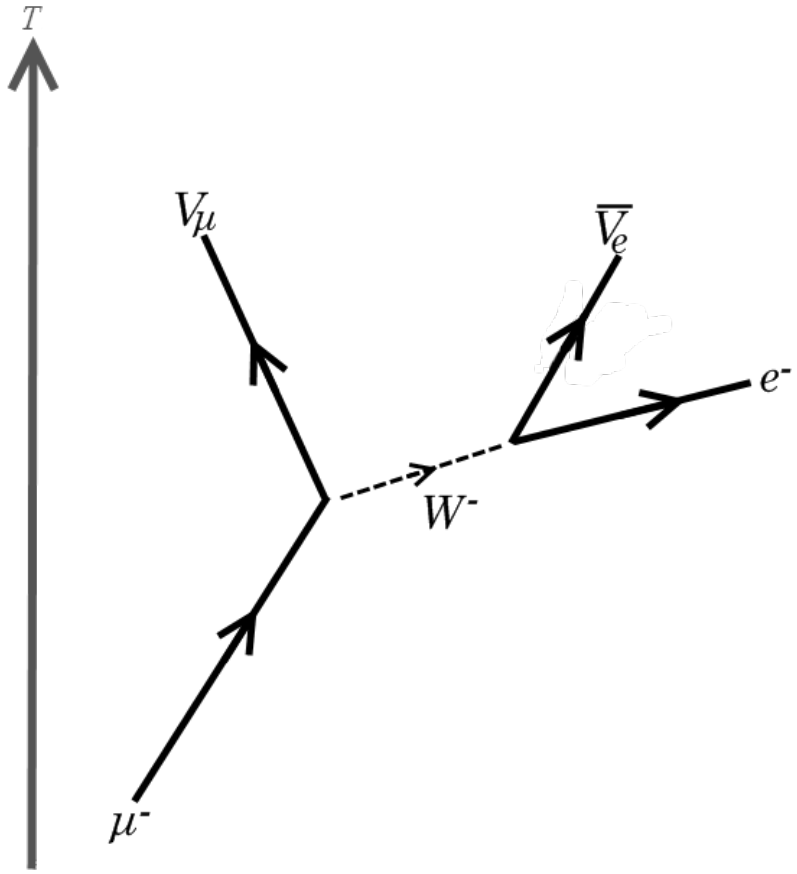

Figure 3.3: The muon decay is displayed in form of a Feynman–graph. The time runs from the bottom to the top. At first the muon decays into a real muon neutrino and a virtual W^- Boson. The virtual particle has only a very limited range because the energy to generate it is not available and can only be "borrowed" extreme briefly from the vacuum. Afterwards the boson decays into two real particles, namely an electron and an anti–electron neutrino (Picture based on [5]).

of CERN and its production cross section was measured precisely at various energies [29]. In figure 3.4 the shape of the theoretical expectation is calculated for two, three and four generations, but the data clearly prefers the three generation model.

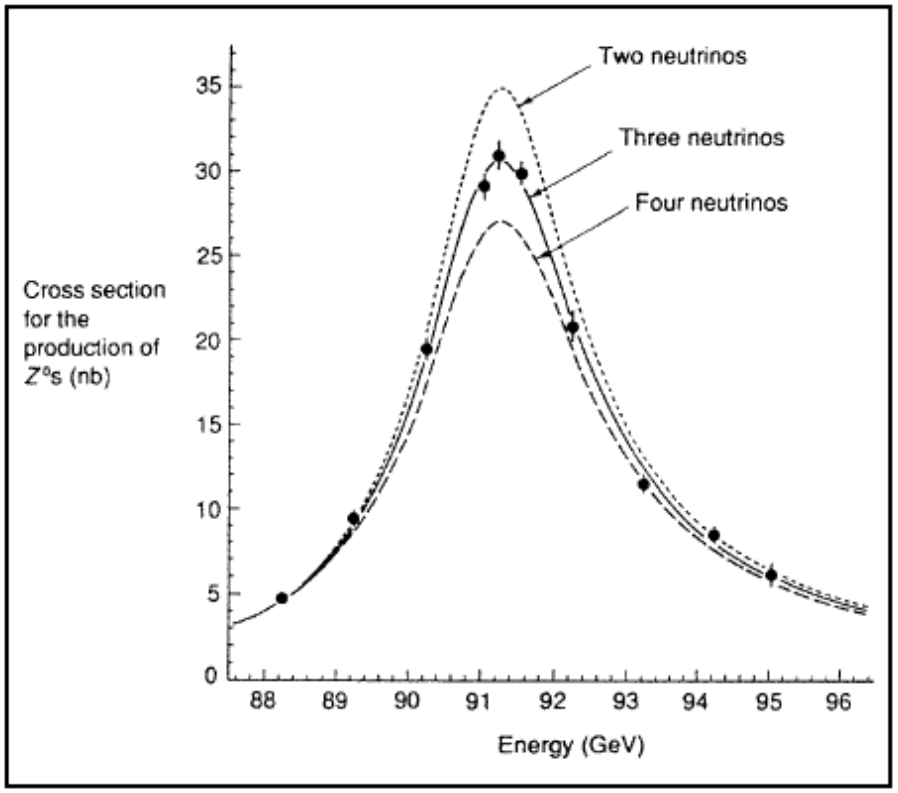

Figure 3.4: The Large Electron Positron collider of CERN, LEP, measured the production rate of the Z^0 particle precisely at multiple energies. In the conversion rate from electron/positron to Z^0 enters the number of possibilities how this conversion can be done. This way the number of neutrinos can be extracted. The measurement clearly prefers a three family model. A fourth family is therefore unlikely as its neutrino would have to weight at least half the Z^0 mass of about 45 GeV [29].

Within the quark sector the predicted new constituents were also found. The first one of the second generation was the strange or s quark. It received its name as the kaon particle was discovered in the cosmic radiation and showed a strangely long lifetime of about 10 ns. The explanation for the unusual long lifetime is that the decay is suppressed as the Strong Interaction only interacts within a family. The decay has to be realized via the Weak

Interaction.

The Standard Model provides also an exact picture about the forces between the fermions. The bosons, having a spin with an integer number, are the carrier of the forces. The electro–magnetic interaction has one carrier called γ, whereas the Strong and Weak force have multiple carriers. A list of them is provided in table 3.2. It is worth mentioning that at higher energy scales the forces can be unified. First the electro–magnetic and the Weak force become unified at energies around 100 GeV. The Strong force is expected to integrate at energies around 10^{16} GeV, but that is far beyond the energies which can artificially be produced on earth. But an unstable proton would be the consequence of the Grand Unification Theory (GUT). Until now it was not measured.

An integration of gravity into the Standard Model with the interaction particle graviton would give a whole description of our surrounding world. However, a verification is far beyond our technical possibilities today.

3.2 Candidates for Dark Matter

Despite the Standard Model is in agreement with all experimental results, it is appealing from the theoretical point of view to extend it with additional symmetries to solve some issues like the fine–tuning problem in the CP–violation or to get quite naturally to a unification of all forces at very high energies around $E_{GUT} = 10^{16} GeV$, the scale of the Grand Unified Theories. The advantage for the Dark Matter search is that in such extensions there are many well motivated particle candidates which have the right properties to be the WIMP. A WIMP is a weakly interacting massive particle. In the first step, before a positive measurement signal is received, it is not so much of importance, which exactly is the WIMP, but the fact that there are reasonable candidates.

The Standard Model can be extended with additional symmetries. The best motivated candidates for such additional symmetries are the Peccei–Quinn symmetry, Supersymmetry or a combination of these. A review from F. Steffen [30] on possible tests and upper boundaries from cosmology for the new particles coming with these new symmetries is summarized here. A quick overview about the theoretical candidates is highlighted in table 3.3.

The Peccei–Quinn symmetry was introduced to solve the contradiction between the predicted CP–violation from QCD and the observation of no such violation. If CP–symmetry would be violated there should be an electric dipole moment of the neutron, which is excluded to a level of $|d_n| < 2.9 \times 10^{-26}$ ecm [31]. However, that problem were non–existent, if at least one of

Fermions	First generation		Second generation		Third generation	
Lepton	Electron	e^-	Muon	μ^-	Tau	τ^-
	e–neutrino	ν_e	μ–neutrino	ν_μ	τ–neutrino	ν_τ
Quark	Up	u	Charm	c	Top	t
(Baryon)	Down	d	Strange	s	Bottom	b

Table 3.1: Fermion like particles of the Standard Model. The particles are arranged in three families. All charged particles are also realized as anti–particles with opposite charge. Whether the neutrino is its own anti–particle is still an outstanding question. In all observed reactions the number of baryons and leptons is conserved individually.

Bosons	
Interaction	Particle
Electro–magnetic	γ
Weak Force	W^-, W^+, Z^0
Strong Force	Gluons
Gravitation	graviton ?

Table 3.2: Boson like particles of the Standard Model. These particles carry the interaction forces between the fermions. The electro–magnetic and weak force become unified at higher energies in the order of 100 GeV. The gluons of the strong force have a very short range as they carry the so–called color charge. This property causes a gluon to be confined within the surrounding of other colored particles like a quark or another gluon. Whether a graviton exists is not clear yet as there is no commonly accepted quantum description of gravity nor an experimental proof.

the quarks would be massless. Another solution with three massive quarks is the introduction of a new U(1) symmetry by Peccei and Quinn. This symmetry would have to be spontaneously broken and provides the axion a as Nambu–Goldstone boson for a Dark Matter candidate.

The super–symmetric extension of the Standard Model (SUSY), where every fermionic/bosonic particle gets a supersymmetric bosonic/fermionic particle as a partner, has some appealing properties. It provides solutions to the hierarchy and the gauge coupling problem as well as it naturally includes gravity. But as no super–partners have been observed, they must be either very heavy or interact very weakly. In most SUSY theories the multiplicative quantum number

$$R = (-1)^{3B+L+2S} \tag{3.1}$$

where B is the Baryon number, L the Lepton number and S the spin, is assumed to be conserved. The super–partners with $R = -1$ can only decay in pairs to Standard Model particles. The lightest supersymmetric particle (LSP) is therefore stable, even if it is heavy. An LSP being electrically and color neutral would be a promising candidate for Dark Matter. The neutralino $\tilde{\chi}_1^0$ or the gravitino $\tilde{G}$ would have such properties.

If the Peccei–Quinn symmetry together with SUSY is applied to the Standard Model, an additional candidate appears as super–partner of the axion: The axino $\tilde{a}$. With respect to upper boundaries from cosmology the axino and the gravitino are expected to be very heavy, compared to the Standard Model particles, if they were the LSP. Only upcoming collider experiments like the LHC from CERN are able to produce them and study their decay. An axion is expected to couple to electro–magnetic field and there are chances to measure it in microwave cavities.

The highest potential to be discovered has the neutralino. Its predicted properties are in a range where future collider experiments together with direct and indirect astroparticle experiments could investigate and give in combination precise values for the cross section and the mass of the Dark Matter particle.

For a more detailed introduction the original paper of Steffen [30] or the review article [32] are good starting points.

3.3 Big–Bang Nucleosynthesis

The measured composition of the light elements gives very stringent constraints to every variation of the Standard Model. These elements were formed directly after the Big–Bang at a time before the radiation decoupled and made the

Candidate	Identity	Experiment
a	axion	direct search with microwave cavities
$\tilde{\chi}_1^0$ LSP	lightest neutralino	(in–)direct or collider searches
$\tilde{G}$ LSP	gravitino	collider decay analysis
$\tilde{a}$ LSP	axino	collider decay analysis

Table 3.3: Possible candidates for a Dark Matter particle. Each candidate X could fulfill $\Omega_X = \Omega_{DM}$ on its own. The table is adapted from reference [30].

Cosmic Microwave Background (CMB) mentioned in Sec. 1.2.2. At that time the very high temperatures did not allow the formation of composite isotopes. Only the proton and the neutron could exist without getting destroyed shortly after. The high temperature provides energies higher than the mass difference between proton and neutron of $Q = 1.3\,MeV$. As the temperature dropped, the equilibrium was broken and neutrons and protons became decoupled. At this point the neutron to proton ratio was $n/p = 1/6$. The neutrons were now free to β^-–decay into the lighter protons. The universe was further cooling and stable isotopes could then be formed.

The prediction for the light element abundance from known nuclear cross sections are calculated as a function of the baryon–to–photon ratio η. They vary over a wide range in number ratios. The predicted values scatter from ${}^4He/H \sim 0.08$ down to ${}^7Li/H \sim 10^{-10}$. The comparison of that ratios with measured values results in a well overall agreement [33]. In Fig. 3.5 the yellow boxes indicate the 2σ statistically allowed areas from measurements of the abundance of the isotopes ${}^4He$, D and ${}^7Li$. The bigger grey boxes take the systematical error into account. Therefore the red vertical region is the range of the baryon to photon ratio η preferred by BBN. Values from the CMB encourage the result as indicated with the blue vertical band.

Thus BBN provides constraints on new physics beyond the Standard Model of particle physics or cosmology. By changing for example the number of relativistic particles (e.g. with another neutrino flavor) one modifies automatically the expansion rate of the early universe. This way also the value of the freeze–out temperature, which is linked to the BBN, is varied. Every new theory like the Supersymmetry has to fulfill these strict boundary conditions.

3.4 Evidences

Two Dark Matter experiments nowadays have promising results. First of all the DAMA Collaboration measured an annual fluctuation of the rate with

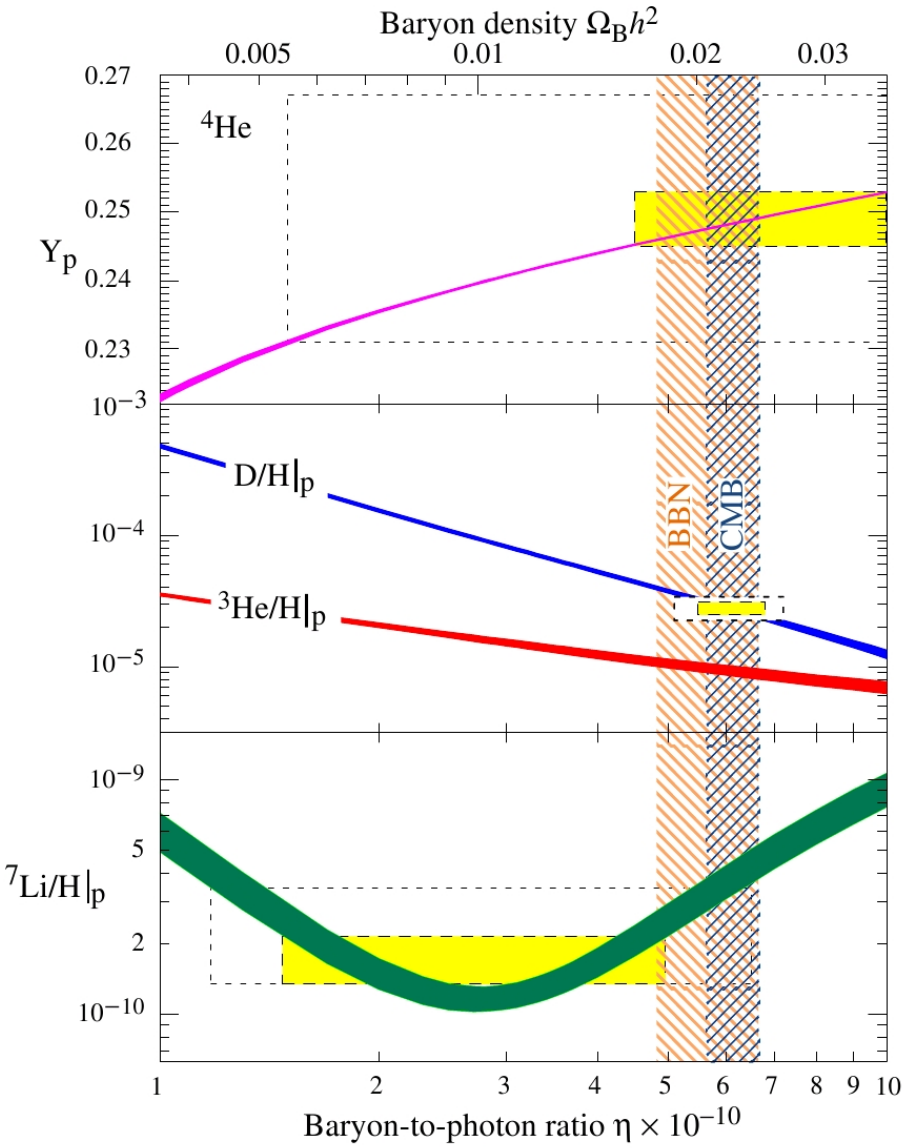

Figure 3.5: The abundances of ^4He, D, ^3He and ^7Li as calculated in the standard model of Big–Bang nucleosynthesis as a function of the baryon–to–photon ratio η. Boxes indicate the observed light element abundances (smaller boxes: 2σ statistical errors; larger boxes: $\pm 2\sigma$ statistical and systematic errors). The narrow vertical band indicates the CMB measure of the cosmic baryon density [33].

scintillating NaI crystals at room temperature. According to their interpretation it is a model independent hint for a variation of the flux of Dark Matter particles due to the earth motion around the sun. With increased detector mass they confirmed their detection far beyond the statistical error [34] (Fig. 3.6). The Dark Matter particle is expected to scatter off the nucleus and not off the atomic shell. But the DAMA Experiment is not able to distinguish between those interactions. The non–existing discrimination of DAMA between nuclear recoils and electro–magnetic interactions remains the focus of criticism. It is possible that another annual effect causes the fluctuation on the 2 % level of their signal at low energies. The phase of the fluctuations is in excellent agreement with the expectation from astronomical observations. But many parameters remain uncertain and a variety of interpretations are still possible [35].

One the other hand, the presently most sensitive direct Dark Matter search experiment CDMS–II has published a new result [36]. They found in their blind analysis two events which are not likely to be background (compare Fig. 3.7). Statistically they expected 0.9 background counts in their region of interest for Dark Matter search. So the measured event rate is with some probability an accidental accumulation of background. An upgrade of the detector mass will check in a future experiment whether the CDMS–II events are a signal or not.

In the meantime the problem remains that the DAMA experiment claims to have found Dark Matter and all other direct detection experiments found nothing compatible with the Dark Matter explanation of the DAMA result. However every modell for interaction with Dark Matter particles has the freedom to couple either with the whole nucleus (spin–independent) or only the difference between neutron and proton number (spin–dependent). An overview of the allowed regions within spin–dependent or spin–independent scattering is given in the review of the combined data analysis [37]. It favors the spin–dependent, inelastic scattering to fulfill all boundary conditions from the experiments.

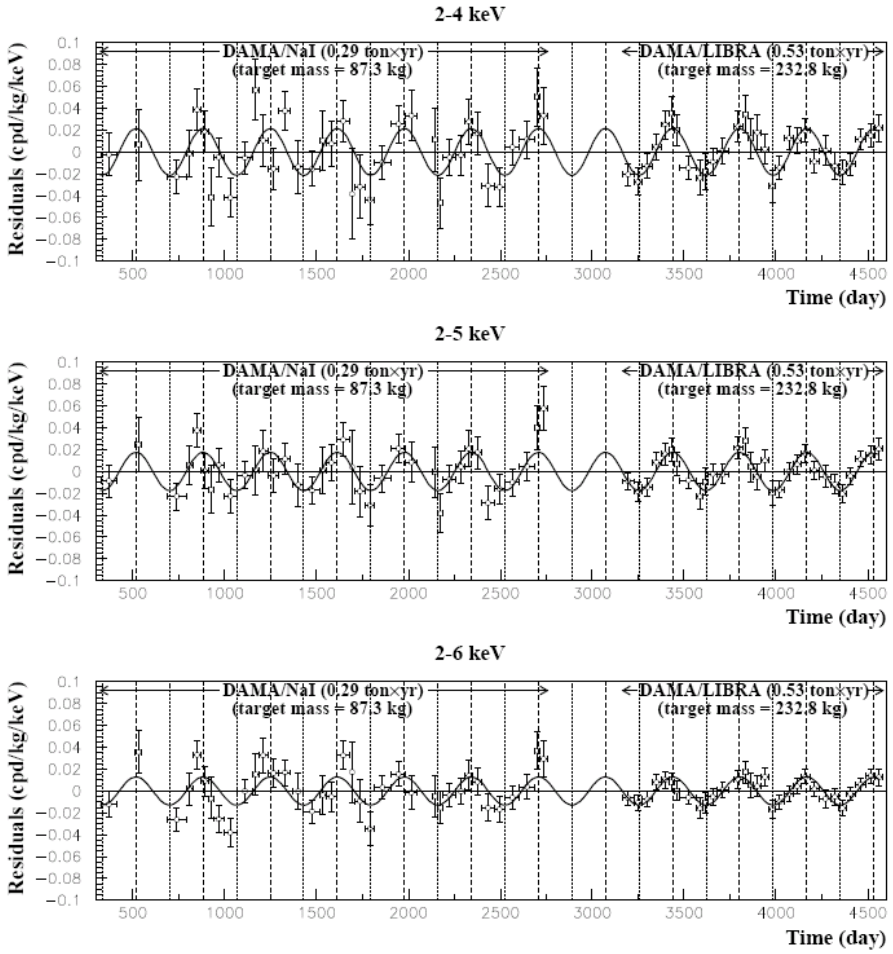

Figure 3.6: The result of the DAMA experiment displayed [34]. In the very low energy region an annual fluctuation of the rate in the order of 2 % of the absolute rate is measured. It is explained with the earth motion around the sun which modifies the relative motion of the Dark Matter particles. This fluctuation is expected purely due to kinematics and not to a property of the scattering nucleus. In that sense the interpretation is model independent.

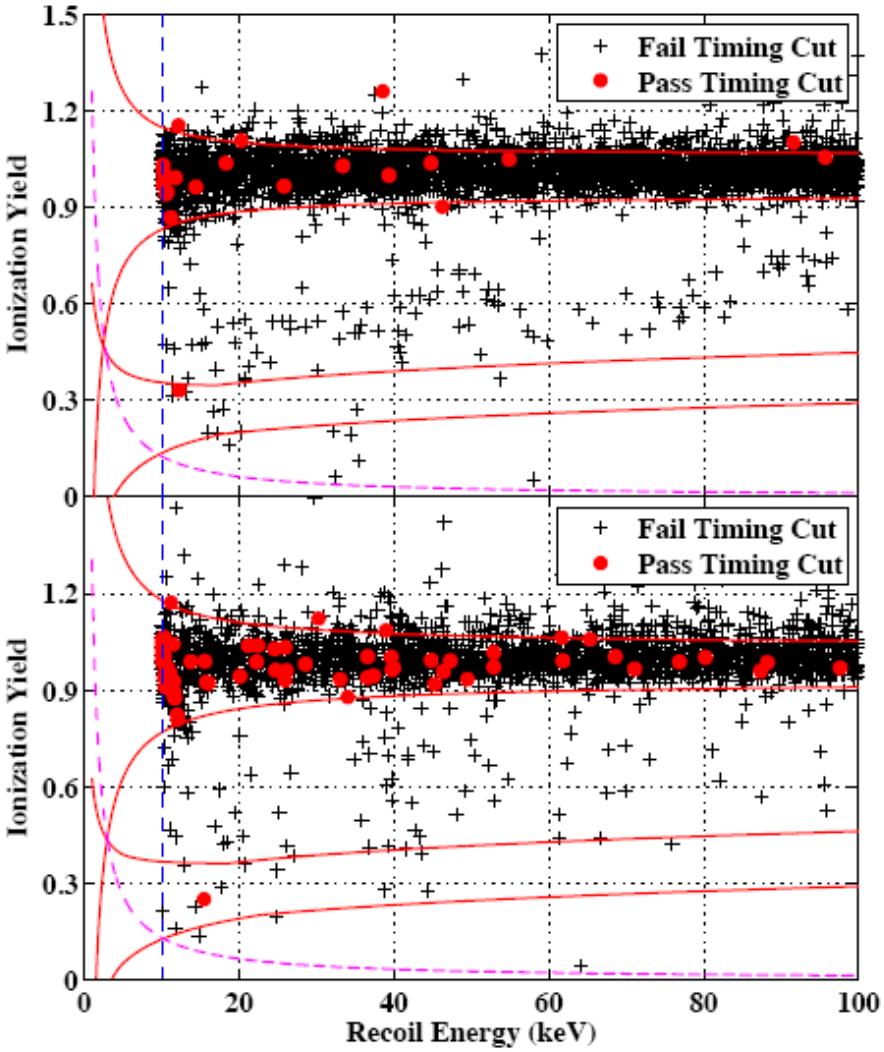

Figure 3.7: The Cryogenic Dark Matter Search (CDMS) experiment with germanium based detector is able to discriminate event–by–event between an electro–magnetic interaction and a nuclear recoil. After the timing cut, which removes events located on the surface of the detector module, two events in different detector modules remain (upper and lower part of the figure). This result from [36] might be a first direct hint for Dark Matter.

Chapter 4

Summary of Part I

The precise astronomical observations presented in chapter 1 make it absolutely necessary either to modify the law of gravity or accept the fact that there is unidentified Dark Matter in our universe. It seems easier to adjust the law of gravity on large scales. On the scale of the solar system it is confirmed through measurements with high accuracy. There are several ideas for possible modifications which could correctly describe the rotation curves of galaxies and also some tiny deviations of the track of space crafts.

But to successfully explain the unexpected behavior of galaxy clusters with a theory of gravity is unlikely. Observations support strongly the theory that Dark Matter is made of particles which interact very weakly. Theoretical particle physics provides a broad variety of possible candidates with the right properties to be abundant enough for the whole Dark Matter content of the universe. Some candidates would also have an interaction probability to produce a significant signal in the latest low background detectors and maybe the first experiments start to detect a signal. Part II describes the challenge of measuring a signal that has never been unambiguously detected before with the most sensitive detectors ever built.

Part II

CRESST with special focus on the Muon Veto

The CRESST (**C**ryogenic **R**are **E**vent **S**earch with **S**uperconducting **T**hermometers) project is one of the leading experiments in direct Dark Matter search. It tries to detect the hypothetical Dark Matter Particle, often called WIMP — **W**eakly **I**nteracting **M**assive **P**article. A very low count rate is expected and makes a very good shielding against any disturbance essential. In addition to the existing shielding of the experiment, an active muon veto system was installed in the framework of this thesis. The first combined analysis of the cryogenic Dark Matter detectors together with the muon veto will be presented in the following chapters.

Chapter 5

The CRESST Experiment

The CRESST (**C**ryogenic **R**are **E**vent **S**earch with **S**uperconducting **T**hermometers) experiment is designed to investigate the question if the Dark Matter in our universe consists of a yet unknown new particle. There are two ways to go: Either one builds bigger accelerators to reach the energy scale of that new physics and then looks for the creation of new particles[1] or one tries to detect them in nature – direct or indirect. The CRESST experiment investigates the possibility of direct detection. The challenge is to reach the very high level of sensitivity in rate, because CRESST[38] and other experiments like XENON [39] or CDMS [36, 40] have already shown that one has to detect a few events per year and ton of detector material within all the background events from natural radioactivity.

Therefore CRESST is located in a very low background environment deep underground in the Laboratori Nazionali del Gran Sasso (LNGS) of the Instituto Nazionale di Fisca Nucleare (INFN), shown in Fig. 5.1. This laboratory is shielded well from the muons, a very penetrating component of the cosmic radiation. The muon rate at the LNGS is reduced by a factor of about a million compared to the surface (Fig 5.2). Muons could cause a signal via an intermediate neutron, which is hard to discriminate against a Dark Matter signal.

CRESST had two phases. In phase I CRESST had no muon veto and no possibility of discriminating electro–magnetic background. Both were implemented in phase II, starting in the year 2006.

The first phase of the CRESST experiment, where the detector modules were made of sapphire (Al_2O_3), ended in December 2003. The sapphire detectors did provide only an energy signal and could not distinguish between

[1] Strictly speaking, an accelerator experiment would only be able to prove the existence of a new particle. That Dark Matter is made of this particle has to be confirmed by direct or indirect measurements.

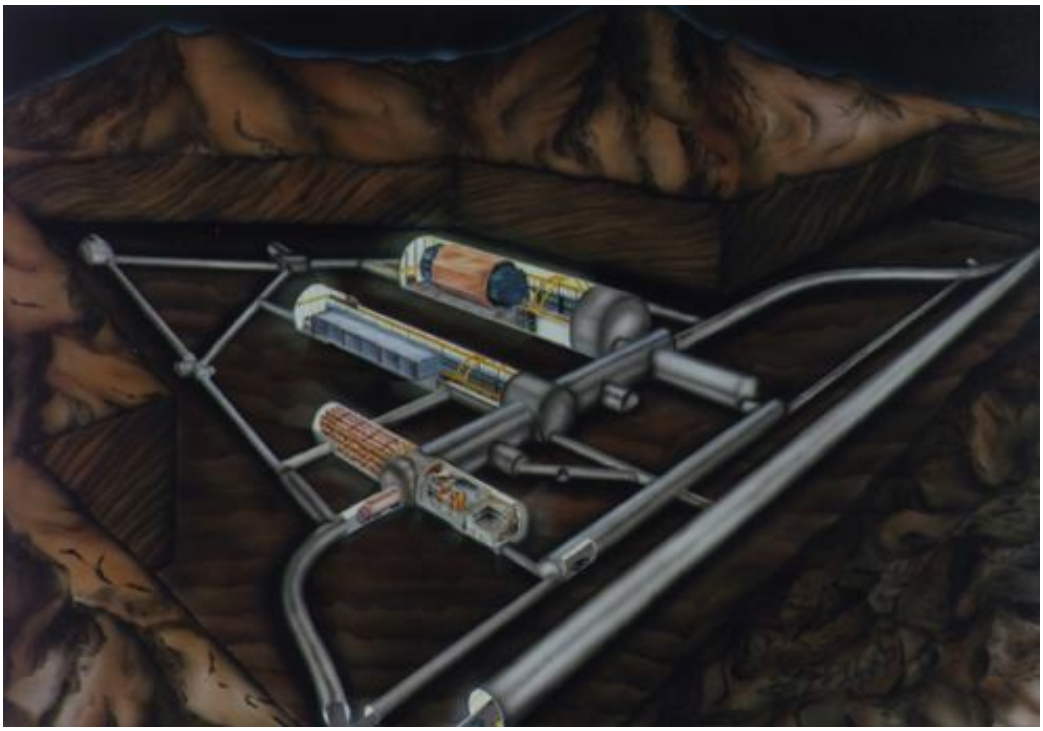

Figure 5.1: The CRESST experiment is located in the Italian national laboratory under the Gran Sasso mountain (LNGS). The experimental setup is in the smallest cave, cave A, which is the most front one in the picture [42]. All caves can be reached by car via a bypass of the Rome–Teramo highway in the Gran Sasso tunnel. The whole laboratory is shielded by the mountain against cosmic radiation.

nuclear recoils and electro–magnetic interaction. So it was not possible to identify Dark Matter without any doubt. But until today one of the best limits for spin–dependent Dark Matter and for very light WIMPs comes from that period [41].

5.1 CRESST–II

The CRESST Experiment was upgraded and phase II started in 2006. As the focus went to heavier WIMP masses, a heavier target nucleus was needed, leading to the use of the new material calcium–tungstate ($CaWO_4$), which is a scintillator. This provides a unique possibility to discriminate electro–magnetic interactions from nuclear recoils, because the scintillation output is different for γ (or electron) and nuclear induced recoils [44]. During the

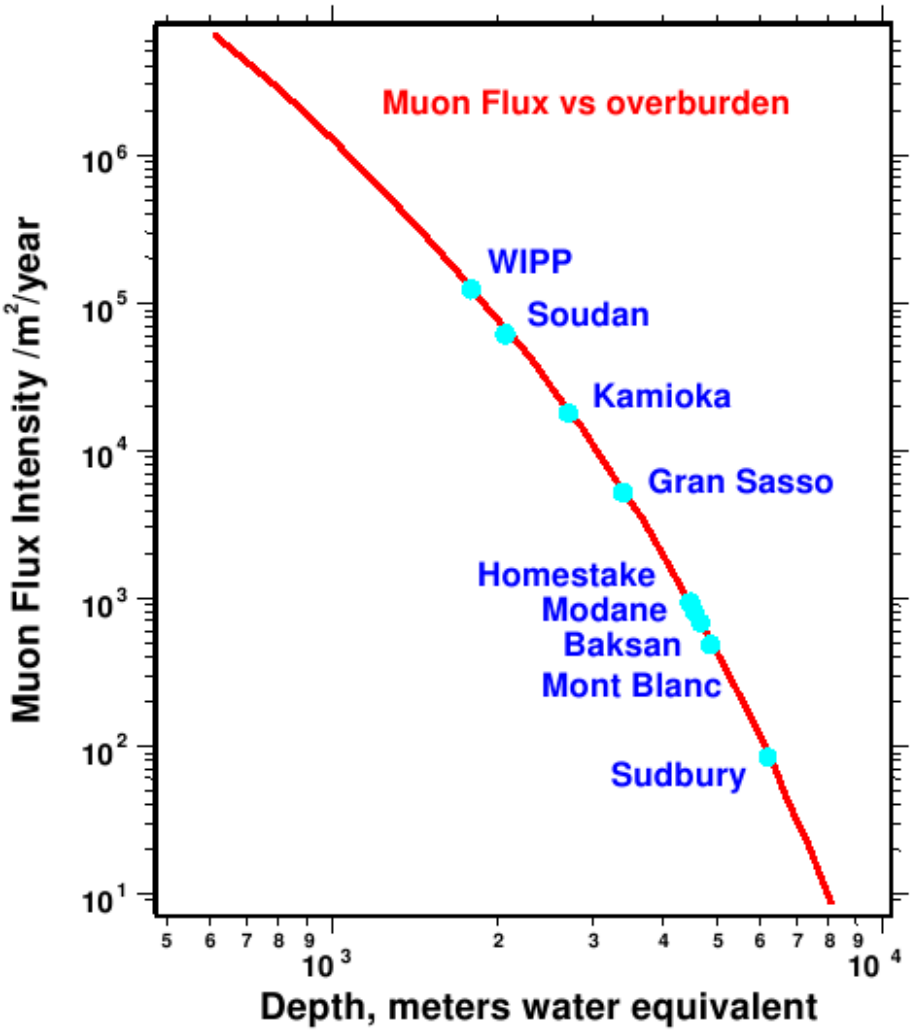

Figure 5.2: The muon flux, a very penetrating part of cosmic radiation, on several experimental sites is shown. The red line shows the theoretical prediction for the muon flux in different depths under ground (Data are taken from the review [43] on Dark Matter). In the Gran Sasso laboratory a muon flux of about a 0.5 muons per hour and square meter is measured.

upgrade phase a neutron shield made of polyethylene (PE) and a muon veto were installed. The cryostat was upgraded to house 33 detector modules. 66 channels, two per module, can be read out via a SQUID[2] electronic [45].

The detectors itself are shielded with very radio–pure lead and copper in an onion–like shielding as one sees in Fig. 5.3. The detector crystals are built only of materials of preselected ingredients to reduce the contamination of the radioactive isotopes from the natural Uranium– and Thorium–chains. After all this passive shielding the suppression of events which are close in time — or "coincident" — to a muon event remains as a task to increase the potential of CRESST. The detailed procedure of discriminating muon coincident events will be described in chapter 7.3.

The detectors are cooled inside a special cryostat whose cold–finger and temperature–shields are made out of low radioactive copper. A new housing structure was installed for the second phase to make it possible to increase the detector mass up to 10 kg. Each detector module like in Fig. 5.4 has a crystal of about 300 g. A tungsten film is evaporated directly onto the crystal and acts as a transition edge thermometer [46]. With focus on a future ton scale experiment made out of CRESST–type detectors a glueing technique is developed and presently under commissioning [47]. The film is evaporated on a small holder crystal and the holder crystal is glued onto the large detector crystal. With the help of the glueing it should be possible to mass–produce the detector modules with constant quality.

For the suppression of the electro–magnetic background CRESST has the possibility to discriminate via the light output between interactions in the electron shell and interactions directly with the nucleus. The light output is significantly reduced in interaction processes without contribution of electrons. How much it is reduced depends on the nucleus it scatters off and is described by a so–called "quenching factor". Due to the separation in nuclear recoil and electro–magnetic interaction via the scintillation light the neutron background is the only dangerous background for the WIMP detection. This source is significantly reduced with the new neutron shielding made of PE [48], but the remaining background events can be suppressed when knowing the exact quenching factor for the scintillation light. One expects neutrons below 1 MeV to scatter more off light nuclei like oxygen or calcium and heavy particles like a hypothetical WIMP more likely scatters off tungsten. For the quenching factor measurement at Milli–Kelvin temperatures a dedicated setup was built in the accelerator laboratory at TU Munich [49]. For the first time quenching could also be measured during the neutron calibration in the CRESST setup

[2]Superconducting quantum interference devices are very sensitive magnetometers used to measure extremely weak magnetic fields

(Sec. 7.2.3). Together with an enhanced light detection efficiency it would be possible to remove the only remaining dangerous background. If one could identify these events without any doubt, CRESST would have the unique possibility to measure WIMPs background free. The detection technique is in addition easy to adopt to new materials which scintillate and CRESST could confirm its detection with other isotopes to exclude a specific effect of the detector material.

The first test of the upgraded setup, the so–called commissioning run, was performed in 2007. All data analyzed here are from the period of June 22nd till July 18th within that commissioning phase.

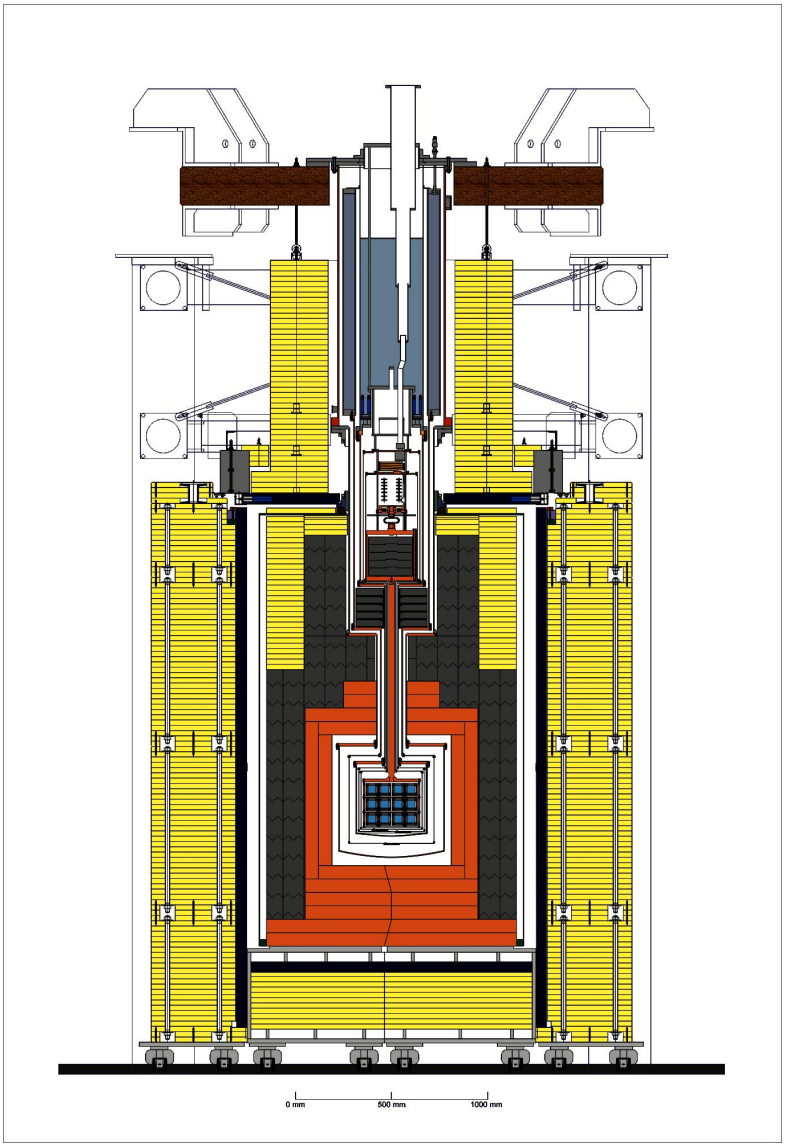

Figure 5.3: The setup of the CRESST experiment in the second phase: The detector modules are housed in the cryostat which provides the operating temperature of about 15 mK. The cryostat is hanging from top on a wooden plate which is decoupled from ground vibrations via air dumpers. Around the detectors is an onion–like shielding beginning from inside with copper (red) and lead (dark gray) in the inner part. The black layer is the muon veto surrounded by the yellow colored Polyethylene shielding against the ambient neutrons.

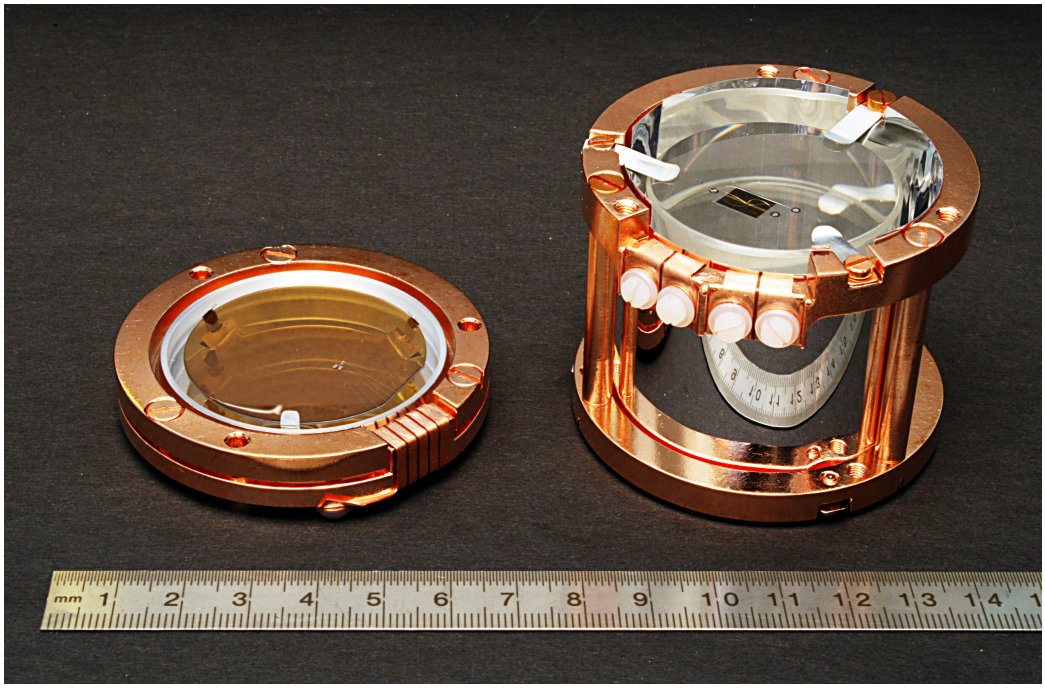

Figure 5.4: The two parts of a CRESST II detector module. On the left one sees the very thin silicon wafer which detects the scintillation light. On the right there is a $CaWO_4$ detector module in its housing of copper. All sides except the top are covered by a reflecting foil to collect the scintillation light. On top of the crystal the thermometer film can be seen.

Chapter 6

The Muon Veto

One major change during the upgrade to the second phase of the CRESST Experiment was the installation of a muon veto. It is located as an additional layer between the PE–shield and the lead–shield. The muon veto consists of twenty panels of solid plastic scintillator each read out by a photomultiplier (PM). The data acquiring system (DAQ) is described in the first section. Afterwards the calibration of the muon veto is presented.

6.1 The Veto System

The veto system consists of twenty panels of three different shapes. All are 5 cm thick and made out of plastic scintillator (Bicron BC–408) with an attenuation length for scintillation light of 210 cm. The scintillation light produced in the panel due to electro–magnetic interaction is read out with a small photomultiplier tube type 9900B from Electron Tubes. There are three different shapes of the panel, given in table 6.1, depending on which position of the veto system they are installed. There are 16 side panels, four on each of the four side walls and additionally two on the top and two on the bottom as shown in figure 6.1. They are arranged in a cube–shaped way around the detector holder of the cryostat. The hole in the top panels is needed to feed–through the hanging cryostat. It leaves about four percent of the solid angle uncovered. But muons entering here can also be detected in the bottom as they travel very likely through the whole experimental setup.

The muon veto was installed in the LNGS laboratory by the end of 2005 by the Tübingen group of the CRESST collaboration. Ref. [50] contains all relevant information regarding the muon veto. It is intended as a reference in case of future problems.

Panel type	position of PM	nr. of panels	dimensions [mm]
Bottom Panel	center of the long edge	2	1430 × 720
Top Panel	long edge,	2	1620 × 800
	opposite to the circle		a half circle
			of 295 mm radius
Side Panel	center of the short edge	16	1350 × 770

Table 6.1: Geometry of the different shapes of panels in the CRESST muon veto

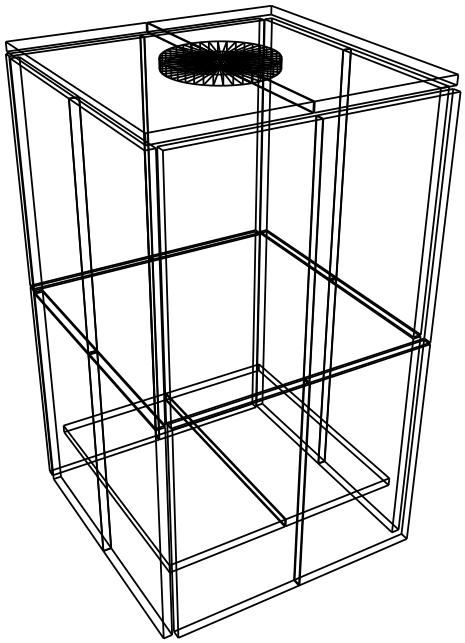

Figure 6.1: The muon veto of CRESST consists of 20 panels in a cube–shaped arrangement. There are 16 side–panels, four on each side, and additionally two on both the top and the bottom. There is a circular hole cut out of the two top panels to feed through the cryostat.

6.1.1 Cabling Scheme

The high voltage (HV) source for the PMs is installed outside the Faraday cage of the CRESST setup to minimize the risk of inducing electrical high frequency noise to the cryogenic detectors. Via a frequency filter the HV is fed with its own electrical ground into the Faraday cage. There it is split up in twenty different channels and each of them can be varied individually with a potentiometer to provide the exact HV for each PM. The optimal HV required by the PM of each panel is determined by the position of the Landau distribution in the spectrum of muon energy deposition. The position of the Landau peak can be adjusted by varying the HV and thus the gain of the PM. It should be at the same channel number for all panels. A twenty meter long cable transfers the HV to a connector station, which is needed because most of the panels have to be disconnected for dismounting to allow maintenance work on the experiment. A five meter long cable from the connector station, which is fixed to the neutron shielding, provides the HV to the photomultiplier of the panel.

The signal cable from the photomultiplier runs the same way. The length of the signal cable for all panels is the same and one does not induce a time shift between the signals of different panels. The electrical analog signal is fed into the Optical Analog Transmitter, which converts the electrical signal into a light signal with a corresponding amplitude. The optical signal is guided out of the Faraday cage by fibers to decouple the electrical ground of the data acquisition from the Faraday cage ground. Outside the optical signal is converted back to an electrical output with the Optical Analog Receiver.

6.1.2 Trigger Scheme

The trigger defines the condition which combination of values in the different signal–channels has to occur to start the data acquisition of an event. The veto system is designed in a way, that every single panel or the sum of all channels could start a trigger. During the commissioning run only the trigger on the sum was activated and this proved to be sufficient.

A problem of the veto system is that there is no clear pulse height maximum for the γ radiation. In the pulse height spectrum this population overlaps with the muon events, which have on average a higher pulse height. But as it is absolutely necessary to detect all muons the pulse height threshold has to be reasonably low. For a single panel this problem is harder than for a group of panels, because muons are likely to hit more than one panel in contrast to a γ event. In our setup in the Gran Sasso laboratory a typical muon hits two panels, one at the upper part when entering and one in the lower part when

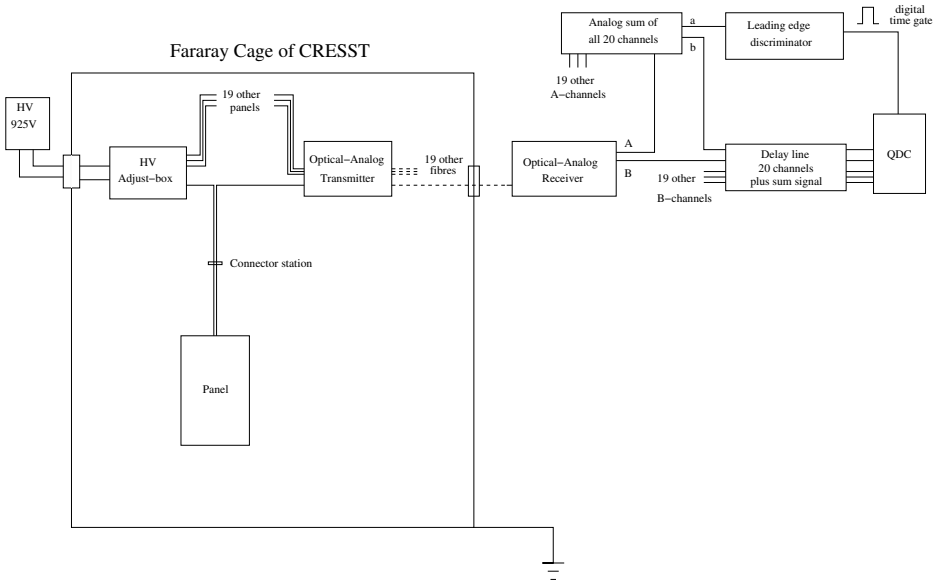

Figure 6.2: Scheme of the cabling of the muon veto: Shown on the left a single voltage source provides a differential high voltage into the Faraday cage of the experimental setup. For each panel this voltage is adjusted individually with potentiometers. The photomultiplier signal is converted into a light signal. This light signal leaves the Faraday cage via an optical fiber and is converted back to an electrical signal outside the Faraday cage. The electrical signal is split into two channels, A and B. All A channels are summed up and treated afterwards as an additional signal channel of the muon veto system. If the sum pulse rises above a certain level the discrimination electronics (LED) opens a digital gate and all 21 signal heights are converted to a digital signal in the QDC module.

it leaves the system. This property makes a muon signal in the sum signal higher than one caused by γ radiation which typically happens in only one panel at a time.

One of the optical receiver outputs of each channel is connected to a delay line to allow the trigger logic to build the trigger signal. The analog sum of the whole veto system is built from the second optical receiver output of all twenty channels in a very fast FanIn–FanOut (FIFO). The FIFO was built especially for this purpose (see figure A.1). The practically non–existent delay, smaller than 1 ns, offers the treatment of the sum signal like an additional muon veto panel. Thus one output of the FIFO is fed into channel 21 of the data acquisition and the other output is directed to a Leading Edge Discriminator (LED). This sum signal determines the trigger condition as soon as it exceeds a predefined value. The fulfilled condition opens a digital gate which enables the Charge–to–Digital–Converter (QDC) to collect for about 100 ns the charges from the 21 signal channels.

The QDC module digitizes only channels, which exceed a typical value for the baseline noise. With this so–called readout suppression[2] only channels containing a signal are taken into account. The number of channels which are digitized is later referred to as multiplicity. The raw data is stored on hard disk and analyzed later as will be shown in section 7.1.

The intention of the trigger scheme is to fire on the sum at a relatively low threshold. By the low threshold it is ensured that no muon is missed, not even the muons which hit only one panel. This is possible if they entered for example through the hole in the top of the veto system. Off line the processes are analyzed in more detail. The exact muon distribution of the individual panels are fixed and a threshold is given. This individual energy threshold identifies the lower border of the muon population. In combination with the knowledge of the number of panels which showed a signal this is a very precise method for the identification of muon events. The single panel hits remain the problematic issue as they contain in addition to the many γ events also some muon hits which have to be identified or at least one has to quantify how many muons are below the energy threshold. To take simply all events of that kind is not an option as it would be too many signals. Every signal in the veto system introduces dead–time to the cryogenic detector system. The time stamp of a cryogenic event can only be given with a uncertainty of a few ms. Depending on the kind of analysis it is between 4 and 10 ms. The trigger rate of single events in the veto system is about the trigger rate of the whole system, which is about 5 events per second. Without any

[2]The noise level can be defined via the readout–suppression parameter individually for each channel.

special treatment the single events would introduce about 5 % deadtime in the cryogenic detectors.

6.2 Calibration of the Veto Panels

The space for the muon veto is very limited as can be seen in Fig. 5.3. Therefore the photomultipliers have to be inside the panels. That induces a dead volume in the scintillator, because the photomultiplier itself does not scintillate. Minimization of the dead volume mandates the installation of only one very small PMT. But as one can expect, that makes the response of such panels very inhomogeneous and a detailed study of all three shapes of panels was needed.

6.2.1 Measurement

A calibration scheme was developed to measure the position dependency of the light output. In the frame of a "tesi di laurea" the system was later automatized. This work can be found online via reference [51]. The data presented here is for one panel of each type. In Ref. [51] the flow chart of the data analysis is described in great detail and only a summary is given here.

First of all, one provides a sufficient voltage of about 850 V to the photomultiplier of the panel and then measures the background signals for about half an hour coming from natural sources like cosmic rays or the Uranium–Thorium-decay chain. In a second measurement a collimated ^{228}Th source is placed on a fixed position over the panel and a second energy spectrum is measured. This has to be done for many positions. Afterwards the background spectrum is subtracted from the spectrum with the source on a certain panel position and the location of the Compton-Edge[3] is determined by a fit. Due to the chemical composition of organic material our scintillator provides not a photo–peak in the spectrum and one has to extract the calibration from the Compton–Edge. The positions of the Compton–Edges for all positions are normalized to the average value of the panel. As a result we have the relative signal height as a function of position within the panel. These maps can be plotted with the script displayed in appendix G.1.1.

[3]The main interaction of γ radiation with the panel material is Compton scattering. The scattered γ takes away a certain amount of energy depending on its scattering angle. The maximum energy transfer to an electron happens in the backscattering under 180 degrees. The exact shape of the energy distribution of the scattered electrons is described with the Klein–Nishina formula, which can in first order be approximated with a box–like shape.

The results for the top panel, the side panel and the bottom panel (Fig. 6.3(b), 6.4(b) and 6.5(b)) can be found in the summary section including discussion and comparison to the simulation.

6.2.2 Simulation

As a cross check of the results a simulation of the light output was performed with the program SimLight[52]. This software simulates the propagation of optical photons in a two dimensional slab. The panels of the CRESST muon veto are much smaller in height than in all other dimensions, so the assumption of a flat scintillator is very realistic. The input parameters of the reflection coefficient on the edges and the attenuation length of the scintillating material were given by the manufacturer. No variation of these parameters was needed, as the simulated result agrees well with the measurement.

The SimLight framework needs two kinds of input files. First the "border files": Here the properties such as degree of reflection and geometry of the panel are defined[4]. For the CRESST panels one file for the sensitive area, the PM, and a second for the reflective side borders is needed (App. F.1).

The second kind of input file is the source definition. Here a small C–Code (App. F.2) helps to position the sources which start a certain number of γ's in randomly selected directions. Though all panels are symmetric around the PM axis, the sources are placed only in one side of the panel and the result is later copied to the other one.

After running the simulation with 50 000 γ–events per source a Perl–Script (App. E.2) extracts the number of registered photons in the PM. The result can then be displayed via the ROOT macro (App. G.1.1). For the top–panel, the side–panel and the bottom–panel (Fig. 6.3(a), 6.4(a)) and 6.5(a)) it can be found in the summary section.

6.2.3 Summary of the Calibration Measurement

As previously expected the light response in the panel is strongly dependent on the location. Directly in front of a photomultiplier it is enhanced by a factor of about two compared to the average. This effect is expected and seen in the measurement of all panels. On the top panels (Fig. 6.3) the effect is most dominant, due to the geometrical shape with the circular cut near the PM. The side panels (Fig. 6.4) have the disadvantage that the PM is mounted on the short edge, so the light has longer ways on average and is therefore more affected by attenuation in the scintillation material. The smoothest

[4] In the top–panel border file the round shape of the half circle is defined as a poly–line.

response map is found in the bottom panel (Fig. 6.5) where the enhancement factor directly in front of the PM is only around 1.5.

The measured maps are the input for the simulation performed in sec. 7.1.2 to give some predictions about the efficiency of the whole muon veto system in the Gran Sasso laboratory. This is later discussed in chapter 7.1.2.

To emphasize once more the importance of the calibration a comparison between the muon and the γ population is made. The data is taken from the simulated map of the bottom panel and is plotted now in a one dimensional histogram (Fig. 6.6). The red population illustrates the simulated average response of the panel to γ background. The response function to a muons most probable energy deposition in a panel of that thickness is plotted in green. The value 2.5 for the muon–factor is an experimentally found approximation. It is the ratio between the average energy deposite of a muon in the 5 cm thick panel and the energy deposit of the γ events of the calibration source. The red and the green populations are not separated clearly which is a problem if one reminds that we want to tag muons but the γ population deep underground is at least by three orders of magnitude higher in comparison to the muon rate.

There will be an additional dead time of the experiment, simply because some γ events will be mistakenly tagged as muons and the corresponding cryogenic particle events are thrown away. For future muon vetos a double layer structure should be taken into account, because this type of detector has the intrinsic possibility to identify minimal ionizing particles such as muons.

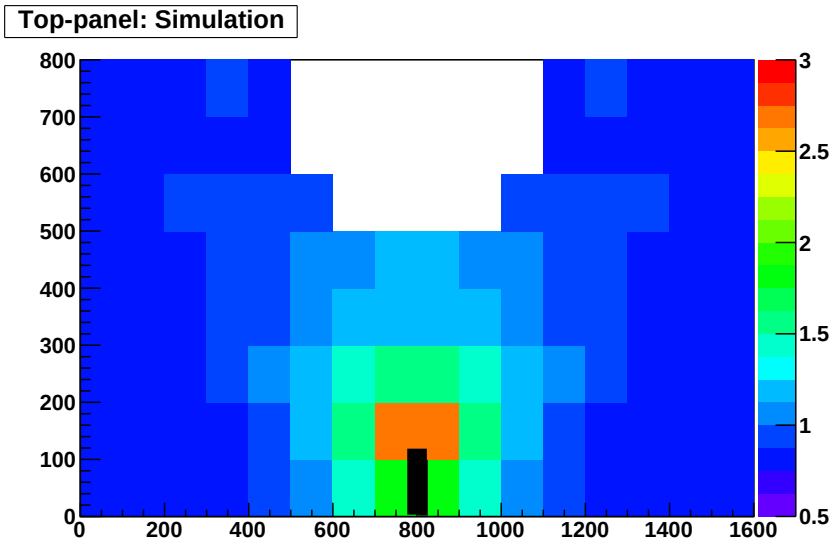

(a) Simulated light response (Top)

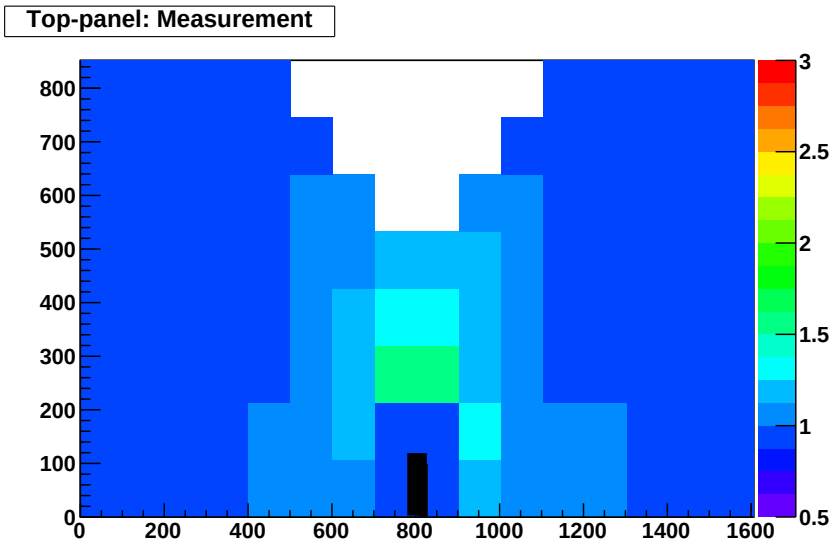

(b) Measured light response (Top)

Figure 6.3: The simulated map of a CRESST top panel from the muon veto in comparison to the measurement. The average output of the panel is normalized to one. Both show the enhancement near the PM location, which is marked with a black rectangle. The white pixels opposite to the PMs are part of the circular feed–through for the cryostat.

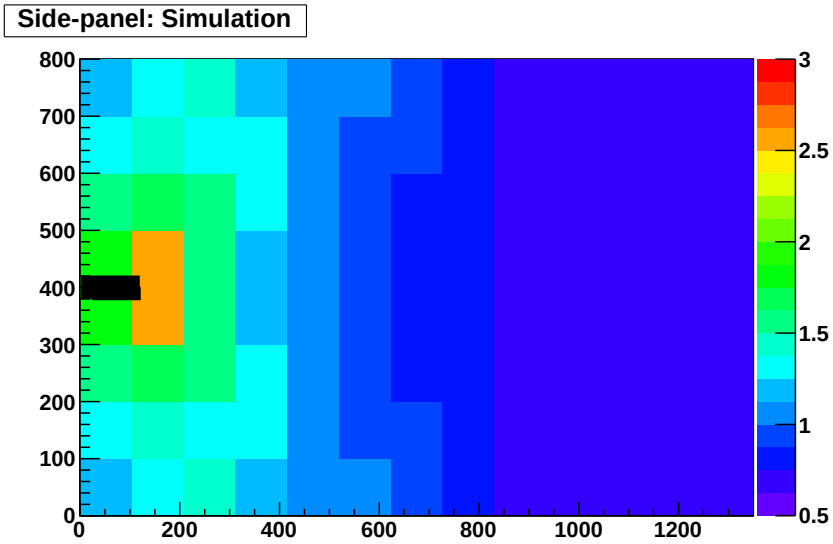

(a) Simulated light response (Side)

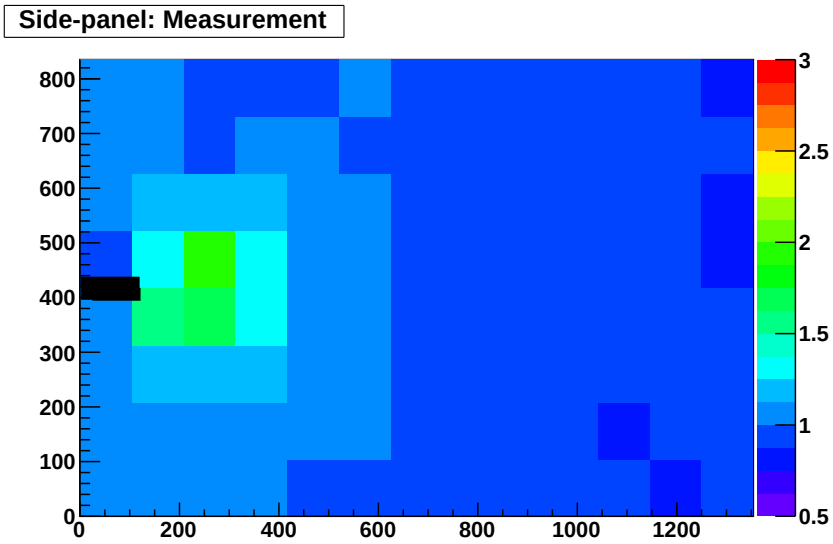

(b) Measured light response (Side)

Figure 6.4: The simulated map of a CRESST side panel from the muon veto in comparison to the measurement. The average output of the panel is normalized to one. Directly in front of the photomultiplier (black box) the response is very strongly enhanced.

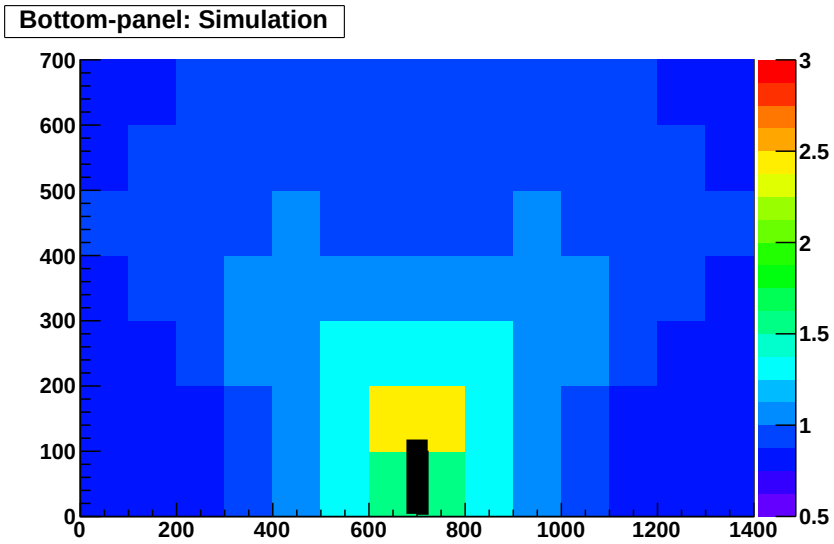

(a) Simulated light response (Bottom)

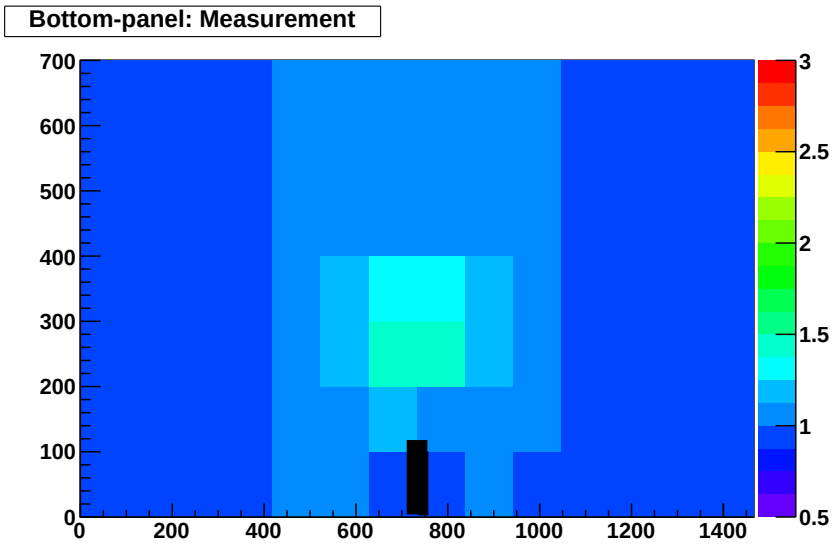

(b) Measured light response (Bottom)

Figure 6.5: The simulated map of a CRESST bottom panel from the muon veto in comparison to the measurement. The average output of the panel is normalized to one. Directly in front of the photomultiplier (black box) the response is enhanced, although the bottom panel is the most homogenous one.

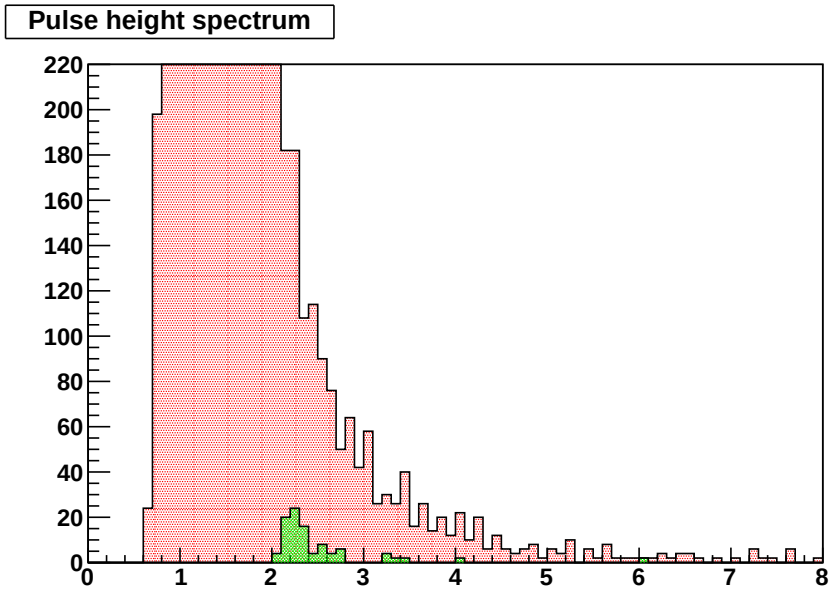

Figure 6.6: The simulated pulse–height spectrum of the bottom muon veto panel. The simulated distribution shown in red represents the response to a γ event at different positions. The green population is the gamma population stretched by a factor of 2.5 in order to take the higher muon energy deposition into account. The value 2.5 was found experimentally as an approximation to the muon signals by comparing the energy deposites of the γ calibration source and the average of the cosmic muon energy deposition.
Both populations overlap in this simulation and so it is not possible to select only, but all muons in a panel by a simple pulse height cut. Finally one has to find the green muon population as good as possible to not produce unnecessary dead time. The red one is calculated with a finer grid to result in about thousand times more data points. This approximates the ambient γ to muon ratio of the LNGS.

Chapter 7

Data Analysis

An example of the full data analysis process of CRESST is given in this following chapter. This analysis focuses on the identification of the muon coincident events in the cryogenic particle detectors. For the first time such a combined analysis is performed. The data used for that purpose is a subset from the commissioning run (Run30) [38] with a live–time of about 550 hours before cuts. In the first section the Muon Veto itself is analyzed and afterwards the data analysis of the cryogenic particle detectors is explained in the second section. In the last section the results are combined and the muon coincident particle events are studied.

7.1 Muon Veto Analysis

The analysis is split into three parts: At first it is describes how the data of the Muon Veto is handled and how the cuts are defined for an optimized recognition of as many as possible muon events without introducing too much dead time by the γ events. In the next section a value for the veto efficiency is extracted out of the data combined with a simulation. The last section defines some parameters which allow to check easily the data quality of the muon veto on large time scales.

7.1.1 Event Categories

The trigger scheme of the muon veto, described in the previous section 6.1.2, is a rather conservative one, which means that many of the recorded events are not caused by a muon. Most of the events are caused by ambient γ radiation, but their signal is not easily distinguishable from muons. To discriminate between gamma and muon events it is convenient to define the following

groups:

All Recorded Events (ARE)

An event in this group contains up to 21 single signal channels. Twenty channels provide a direct information of the energy entry in the respective panel. One channel is the sum of all twenty analog signals. If the sum exceeds the threshold signal height, all other panel signals are read out if they are above the noise level. The "Multiplicity"–parameter is equal to the number of panels which had a signal above the noise level. A special case is that no panel on its own was above noise level, but the sum signal passed the threshold value and the multiplicity then is equal to zero.

Clear Muon Events (CME)

The most probable scenario for a muon crossing the detector array is an event with multiplicity equal to two. One panel gets hit by the penetration into the array and the second muon panel is hit while leaving the system. The high voltage of the photomultipliers in the single panels is adjusted in a calibration measurement. The maximum of the muon signal height distribution is adjusted in the center of the dynamic range of the DAQ. If two panels are hit simultaneously by a muon the sum signal is likely to be above the upper end of the dynamic range. This class of events is collected in the so–called overflow, the last entry of a spectrum. These events are marked in Fig. 7.1. All these events are members of the CME group.

This event group is designed to learn about the distribution of the muon events in the single panels. Later in the coincidence measurements with the cryogenic detectors it is a good indicator how muons influence the result. The CME group indeed contains mainly muons, but not all of the muons. Therefore another group is needed with a less restrictive criterion of being a muon event. But that unavoidably induces a γ contamination. The CME group contains more than half the muon events.

Dangerous Veto Events (DVE)

The "Clear Muon" Events are now sorted in histograms for each single panels. From the physics of minimal ionizing particles — like the muon — one expects a Landau distribution[1] of the deposited energy. This distribution can clearly

[1]The Landau distribution is described in detail in App. C. In the Vavilov approximation it can be written as:
$vav(sig, MPV, x) = \sqrt{\exp\left[-\frac{x-MPV}{sig} - \exp\left(-\frac{x-MPV}{sig}\right)\right]}$

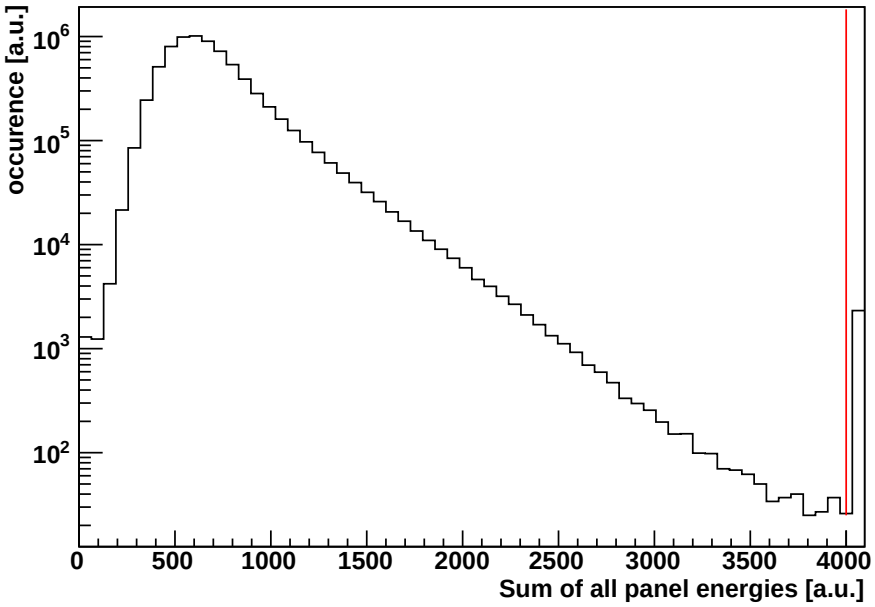

Figure 7.1: The energy spectrum of the sum signal of **a**ll **r**ecorded **e**vents (ARE) is displayed in a logarithmic scale. The high voltage of the single panels is adjusted in the way that in the likely muon scenario of a hit in two panels the sum signal is in the overflow. However, for a single γ event it is very unlikely to deposit that much energy in a panel. Therefore a cut at the position of the red line is applied to define an event group, which consists mainly of muon induced ones. This group is further referred to as "Clear Muon" events (CME) which are display in red for an easier comparison.

be seen in the example spectrum of the panel "Left Top Near" (LTN) in Fig. 7.2. The histograms are fitted to determine the individual parameters of the Landau distribution of each panel. This is automatically done by a macro (G.1.2). For about 550 hours of data taking during the commissioning run the parameters of table 7.1 were found. From the calibration in principle the peak position of all panels is expected to be on the same position. After the installation of the panels in the Gran Sasso laboratory this was obviously not the case and the HV is going to be re–adjusted.

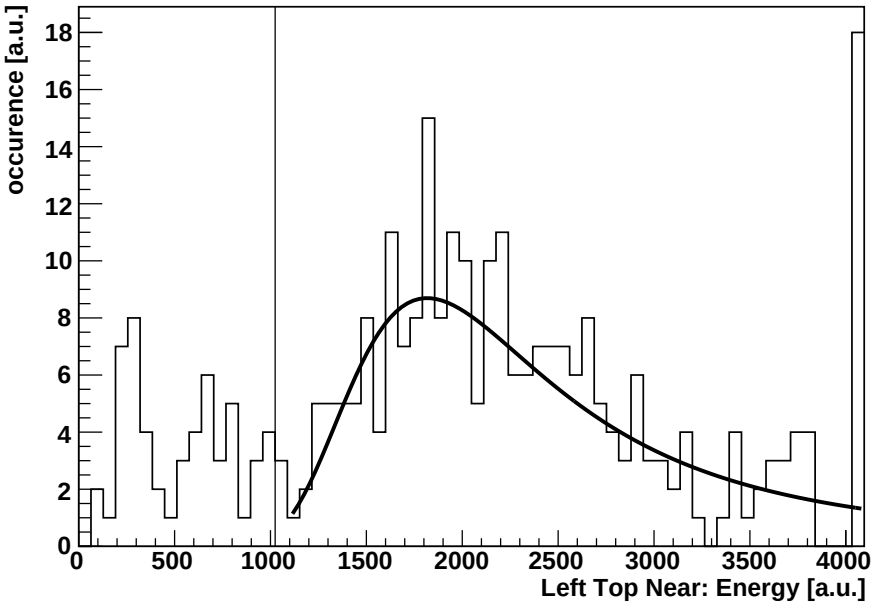

Figure 7.2: The energy spectrum of the CME population is shown for the panel "Left Top Near" (LTN). A Landau distribution is clearly visible. The parameters of the fit to the Landau distributions define the thresholds of table 7.1. The vertical line marks the value $2.5\,\sigma$ lower than the maximum. A muon event is very unlikely to deposit energy less than this value. All members of the DVE group have to exceed in at least one of the panels this energy threshold.

The definition for the DVE events is dependent on their multiplicity. For all events of multiplicity of two or higher the threshold value of table 7.1 is applied. Nothing special about the multiplicity equal to zero cases can be said (due to the missing single panel information) and their number is rather small. All of these events are therefore simply included in the DVE group. The multiplicity equal to one events would dramatically increase the dead

Panel name	Pre–factor	Peak Position (MPV)	σ	threshold for muon events
Ceiling Left	104	2154	237	1561
Ceiling Right	99	2970	282	2265
Floor Left	130	2121	226	1555
Floor Right	130	1881	232	1299
Front Top Right	30	2307	480	1106
Front Top Left	28	2756	616	1214
Front Bottom Right	19	2515	743	656
Front Bottom Left	19	2677	747	807
Right Top Far	41	2082	397	1088
Right Top Near	31	2672	619	1124
Right Bottom Far	38	2034	276	1343
Right Bottom Near	39	2347	324	1535
Back Top Left	24	2615	641	1012
Back Top Right	23	2479	633	896
Back Bottom Left	24	2405	550	1029
Back Bottom Right	33	1677	309	904
Left Top Near	48	1894	348	1024
Left Top Far	18	2052	542	695
Left Bottom Near	38	1931	358	1034
Left Bottom Far	23	1536	551	158

Table 7.1: The parameter values obtained for a dataset of the commissioning run in the LNGS. It was created by the *muon_analysis*() script of App. G.1.2. Out of the Peak Position and the value of σ a threshold parameter is calculated. Below this value it is very unlikely for an event to be caused by a muon.

time if one would apply the same threshold as for the higher multiplicities. Beside that, it is much more likely for them to be an event caused by a single γ and not by a crossing muon so it was decided to set the threshold in this work to the peak maximum of the muon distribution. By doing this one still gets most of the muons (compare Sec. 7.1.2) and not too many γ events. For all panels the plot of the Landau fit and the histograms after the different cuts are given in App. B to prove the stability of the method.

Comparison of the Event Groups

In figure 7.3 a signal height histogram of the previously defined event groups are shown. In yellow one can see the ARE, in red the CME and in black the DVE. The DVE group contains almost all muon events, a number is calculated in section 7.1.2, and the dead–time induced by the misidentified γ events to the experiment is reasonably low.

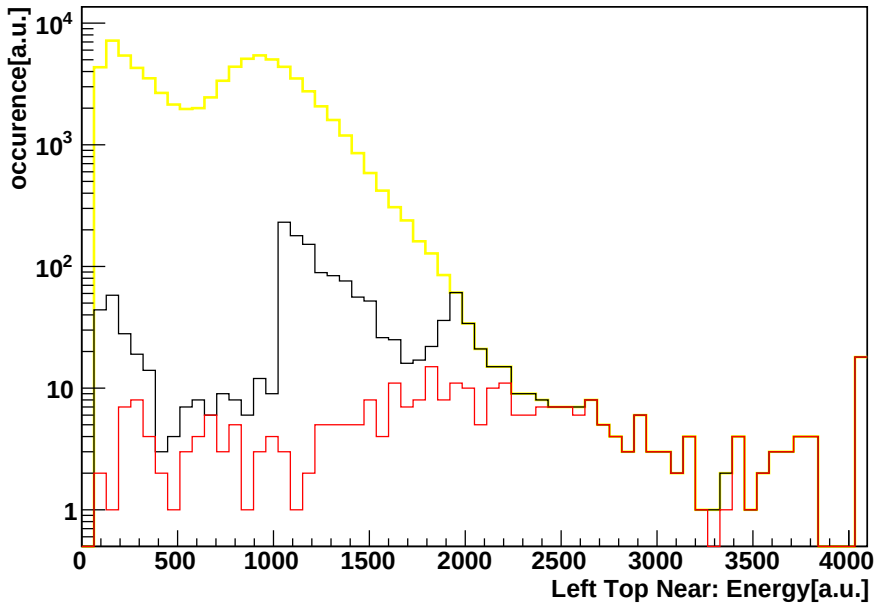

Figure 7.3: The energy spectrum of the same panel as in Fig. 7.2 is displayed for the different groups on a logarithmic scale. The ARE is plotted in yellow, the CME in red and the DVE in black. The DVE group has to be handled as "muon candidates" in further studies.

7.1.2 Determination of Efficiency

Efficiency is an important parameter for further studies to the muon coincident particle events. It gives the probability that a muon crossing the veto detector array is recognized as such by the veto system. This probability cannot be obtained without the help of a simulation to formulate an expectation, because one has to know for example the fraction of muons which gives no signal at all due to the geometrical arrangement of the veto panels. An direct measurement is not possible as there are no portable muon sources.

The inhomogeneous response maps of the calibration measurements in section 6.2.3 were the input to a simulation of the muon veto array, done in Ref. [53]. About 25 years of measuring time were simulated. The muon flux in the Gran Sasso laboratory is about 0.5 muons per square–meter and hour [43]. An average energy deposit of 1.8 MeV/cm was assumed. The corresponding light signal of the photomultiplier (PM) is a function of the deposited energy and the location of the event in the panel. With this geometrical input from the panel maps and the muon distribution for the Gran Sasso laboratory the simulation was done. Multiplicity equal to zero means, that the event hit none of the 20 panels. That is for example possible for a muon entering through the hole in the top of the setup and leaving through the tiny non–scintillating gap between the two bottom panels.

With an integration (App. G.1.3) over the Landau distribution for realistic values (see table 7.1) one can estimate the fraction of muons below the energy threshold in a single panel to be 0.2 %. Accounting the statistical nature of the energy loss of muons the probability for not identifying a muon has to be taken with the power of the multiplicity of the event. The probability for identifying the muon in events with a multiplicity higher than one is therefore

$$P(id_{muon}) = 1 - (0.002)^{multiplicity} \geq 99.999\,\%. \tag{7.1}$$

This class can obviously be assumed as identified.

The events with the multiplicity equal to one are treated separately, as in the cut procedure a different threshold is applied. If one would apply the same low threshold than for higher multiplicities, one would end up with many single hits of γ–events in the DVE group which induces more dead time to the cryogenic detector array. The value taken for this group of events is the peak position of table 7.1. At the peak position about 30 % of the muons are not visible. From the simulation it is known that about 5 % of the muons cause a multiplicity equal to one and therefore this class remains as the major source of unidentified muons. 30 % of this 5 % of the total muon flux are 1.5 % of the total muon flux.

The muon veto has an efficiency higher than 98 % with the cuts proposed in this work, what is sufficient for the CRESST–II setup, but for future experiments with an active plastic scintillator much more efficiency could be achieved by using a double layer structure for the panel, so that one panel on its own could discriminate between muons and γ–background. This way the dominant leakage for the muon veto, the γ events which cause an event with a multiplicity of one with sufficient energy, would by largely reduced.

The comparison of multiplicities up to three from the simulation and from the measured result in Fig. 7.4 shows a good consistency. The colors of the measured result are chosen in the same way than in the section before. The ratios between the multiplicities from simulation are in agreement with the measurement if one takes into account that the 'pure' muon contribution to the measurement is somewhere between the red and the black population. The higher multiplicities occur more frequent in the data than expected from the simulation. This can be explained by cosmic showers, where many muons are produced at the same time and the muon veto then is hit by several muons at once. However in the simulation the muons are started individually.

DAQ Induced Dead–Time

An independent source of dead–time, which lowers practically the efficiency, is the DAQ induced dead–time. After each event recorded in the muon veto there is a conversion time for the digitization process. During that time of about $8\,\mu s$ the DAQ is not able to record new events. The problem is that events in the ARE group are followed by a time period where the muon veto is "blind" and there a disturbing muon could cross which is not recorded. The loss of muon events can be estimated by the trigger rate of the ARE group multiplied by the dead time.

For the commissioning run the numbers are 7.5 million events in 550 hours of measurement time which corresponds to less than $3.8\,s^{-1}$. That leads to an additional dead–time of $3.8\,s^{-1} \times 8\,\mu s \simeq 0.003\,\%$. The corresponding lifetime of 99.997 % would have to be multiplied with the efficiency of the muon identification (98 %), but for all practical purposes this contribution is absolutely negligible. This knowledge leads to a total efficiency of 98 % for the whole muon veto system during the commissioning run. The DAQ dead–time has no impact to the overall efficiency.

7.1.3 Time Stability of the Muon Veto

The longterm stability of the muon veto is an issue which has to be checked on a regular basis, because a change in the data quality may result in

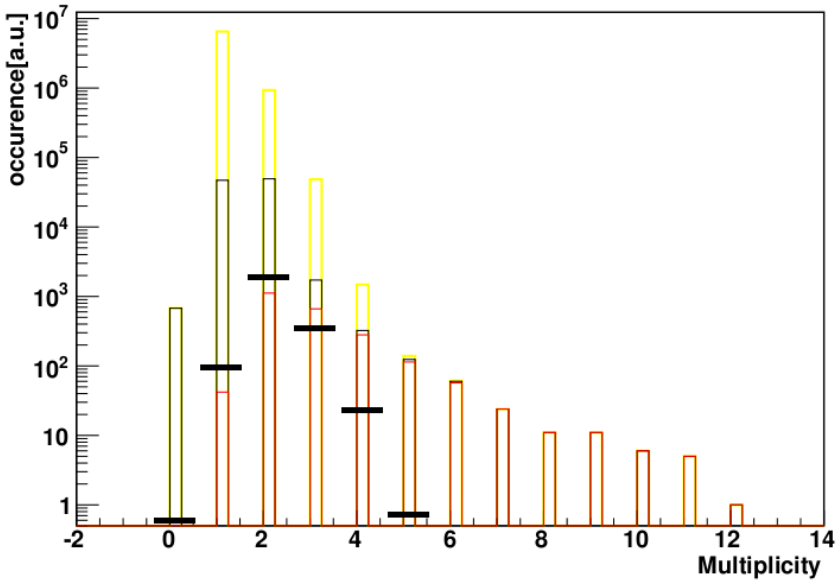

Figure 7.4: A comparison between the measured and the simulated result reveals a good consistency for the lower multiplicities up to three. Not only in the correct ratios between the multiplicities but even the total count rate is in good agreement. The black DVE group of measured events contains 98 % of the muons which cross the veto array. This value can be determined with the help of the simulation.

an unidentified muon and in an unrecognized coincidence to the cryogenic detectors. As one has to be sure on an event–by–event decision whether an event was muon induced or not the veto has to work all the times and its performance has to be monitored. The tools for the monitoring are scripts running on a regular basis (An example given in Sec. 7.2.1). Changes in the behaviour of the veto can such be detected as soon as possible. If the data is taken it is advisable to double–check the quality. In figure 7.5(a) the rate of the CME group is plotted versus time and one can see that it behaves quite constant within the statistical fluctuations. To quantify the fluctuation a histogram of the measured rate is shown in figure 7.5(b). It agrees very well with the expected Poissonian behavior of low event rates. To guide the eyes the best fit to the data is also plotted. The high entry number in the first bin is related to the downtime of the muon veto array at the beginning of this section of the commissioning Run and the stop of the DAQ system during the refilling of the cryostat. The peak position at a value of five events per hour is comparable to the expected muon flux in the Gran Sasso laboratory, which is 0.5 muons per hour and square meter. The effective area of the veto array for passing muons is about 6 m^2, so the rate in the CME group seems to have a small additional component.

A very sensitive parameter for a noise–level check on the veto system has proven to be the rate of the multiplicity equal to zero events. These events are above the threshold of the sum trigger, but each panel on its own is below the readout threshold. If the uncorrelated noise in all panels increases this class of events is more likely and contributes to the DVE group as zero multiplicities are kept in the DVE class. This way one can easily check the stability of the noise conditions in the DAQ system. At the end of the data set shown there was a time period where this conditions varied a lot as can be seen in figure 7.6.

7.1.4 Summary of the Muon Veto Analysis

Two event–groups, the "clear muon events" (CME) and the "dangerous veto events" (DVE), are considered for further coincidence analyses with the cryogenic detectors. The CME group contains almost no disturbing γ events (but only about half of the muons, compared to the theoretical expectation) and is therefore appropriate to study the behavior of muon induced events without other influences. In the DVE group are over 98 % of the passing muons, but many γ's as well. The DVE group is designed for the coincidence analysis of a Dark Matter run with an optimized "detected muons" to "dead time of the DAQ" ratio.

The veto system proved to have a good longterm stability. The rate of

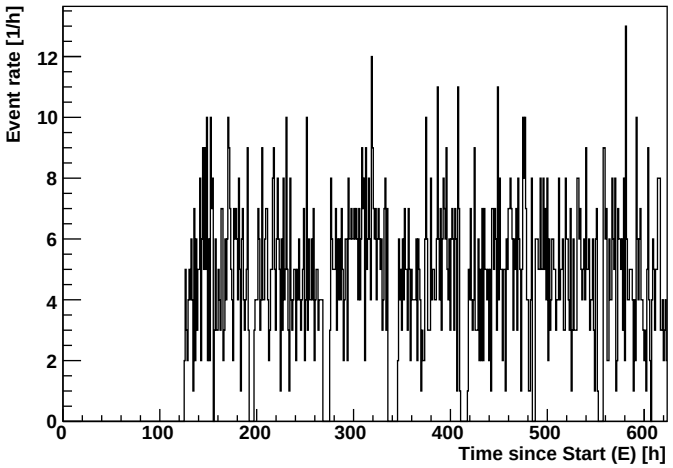

(a) The time evolution of the rate of the events in the CME group in the commissioning run is shown.

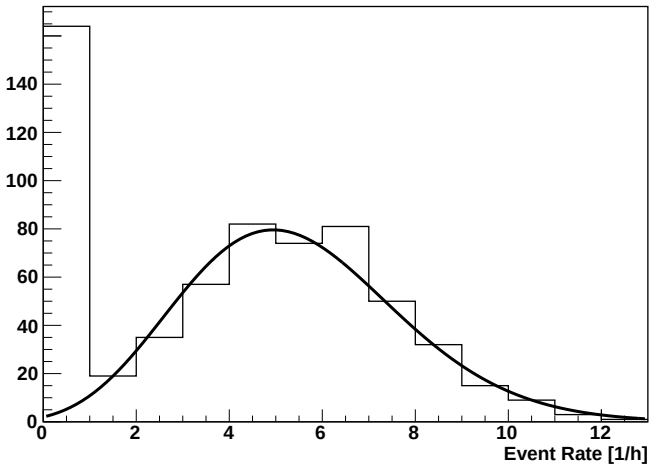

(b) The event rates from the upper picture are histogrammed and a Poisson distribution is found.

Figure 7.5: The Event group of the CME is displayed. In the upper picture one sees the rate over time. Within statistical fluctuations that is fully comparable to a Poisson process as the lower picture indicates. The mean value of about 5 events per hour is about twice the expectation. Probably some misidentified γ–events contribute to that higher rate. The stability of the rate over time proves the good long–term stability of the veto system.

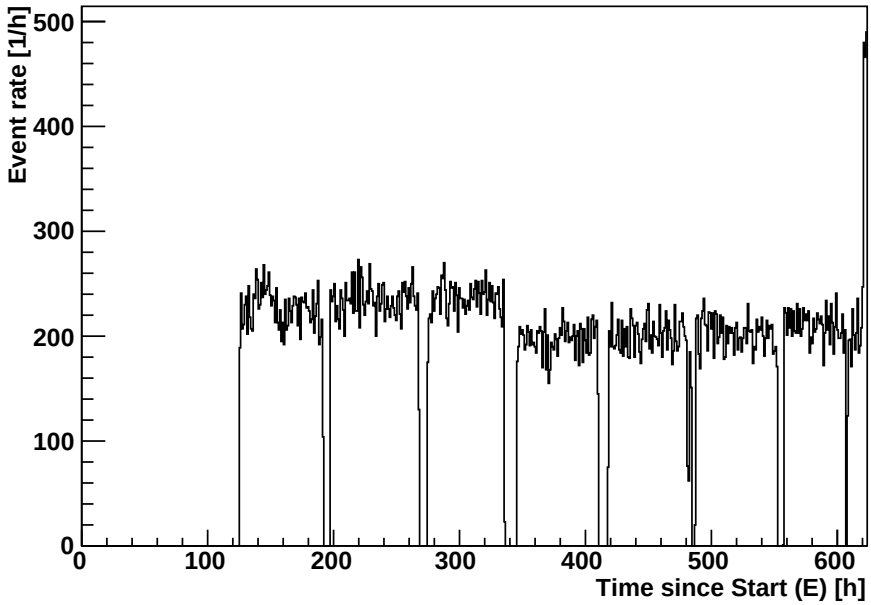

Figure 7.6: The rate of the DVE group as a function of time is shown. A huge burst of events with multiplicity equal zero at the end of the data set occurred. After fixing the noise level the veto system behaved as usual again. So this parameter is a valid candidate in future runs to check for the noise level in the veto system. The reduction in rate after $\sim$350 hours is due to a slight modification of the supplied voltage to the panels, which lowered the pulse heights and therefore the trigger rate.

physical events in the CME group is stable at a rate of about 5 events per hour. This is consistent with the expected muon rate for this detector in the Gran Sasso laboratory. It was shown that the rate of DVE group is a good indicator for a change of the veto system like a change in the HV supplied or the noise level of the DAQ. It should be monitored on a regular basis to react to a change of the running conditions.

In the next section the cryogenic particle detectors are discussed. After this brief overview about the particle detectors, both systems, the muon veto and the cryogenic detectors, are used for a combined coincidence analysis.

7.2 Particle Events

Events in the cryogenic detectors are furtheron called particle events. They differ in the amount of scintillation light according to the interaction. The electron and γ induced events have the highest light output [44]. Alpha events have an intermediate light output. Neutrons and other nuclear recoils have a very low one. This changing of light output is called quenching. Work is in progress [49] to discriminate with CRESST–like detectors even from different recoiling nuclei.

In this section, first the long term stability of CRESST particle detectors is described. Contributions to this first level data check were developed in this work. The next step is the energy calibration. In the last section, the data analysis of the neutron calibration of the commissioning run is presented. For the first time a hint for the discrimination of different recoiling nuclei was found in–situ in the CRESST setup.

7.2.1 Cuts and Tools to Ensure the Longterm Stability

To run such a complex experiment like CRESST at milli–Kelvin temperatures over a long time one has to check the data quality on a regular basis. Therefore a three–leveled procedure has been established:

- Cryostat checks: A maintenance crew at the Gran Sasso laboratory takes care about the regular refills of liquid nitrogen and helium to cool the setup and about all other work around the experiment. The extremely risky issues for the continuation of a measurement like for example the plugging of the coldtrap of the $^3He/^4He$–circuit of the cryostat, which would result in a warm up of the detectors within hours, are checked on a regular basis. In App. D.1 an example script for this purpose is shown. It sends an email and a text message to the responsible team of shifters in case of a critical parameter, like the pressure of the coldtrap, leaves the range of being safe. Thereupon the shifter can react on very short notice.

- First level data check: More subtle issues like a change in the noise conditions or a hardware problem in the DAQ system can be checked only on the basis of the data taken. The reaction time therefore is a little bit longer, in the order of days. A script for this purpose was also developed and can be run remotely as it is shown in App. D.2.

- Second level data check: There are artificial Control Pulses injected every few seconds directly into the thermometer of the detectors. Via

the height of the resulting pulses it can be checked if the detector was in the correct bias condition directly at the moment before and after an event. Times, where the response to the Control Pulses were not in a narrow range around the norm value, are cut as unstable periods of the detector. These periods mainly occur due to a small disturbance of the whole setup, such as small earth quakes or construction works around the experimental site[2].

7.2.2 Calibration Process of the Cryogenic Detectors

For each measurement period, a so–called "run", a calibration with a ^{57}Co source is performed for a few days. As the photons of 122 keV energy cannot penetrate through the shielding and an opening of the shielding destabilizes the detectors, due to the high rate from ambient γ–radiation, a source lift was installed. With its help the source can be positioned at every angular position around the cryostat without opening the shielding. In Fig. 7.7(a) a pulse–height spectrum from such a calibration can be seen. The events within the red markers belong to the 122 keV line. The shoulder on the low energy side of the peak is due to Compton scattering in the thermal shielding of the cryostat. Other spectral features are described in Ref. [54].

To define precisely the height of the particle pulses a Standard Pulse is fitted to all particle pulses. The Standard Pulse is obtained from averaging many pulses. This way the Standard Pulse is a model for the optimal pulse shape without disturbing influences. The height of the fitted Standard Pulse is a measure for the corresponding energy and is only very little influenced by the noise of the signal. The maximum of the signal is more subject to fluctuations and therefore less precise. The shape of the Standard Pulse is an individual detector property and can hardly be predicted, thus it has to be determined by the calibration measurement, too.

At first an averaged pulse for the light– and the phonon–detector is built from the 122 keV events. This first attempt of a Standard Pulse is fitted back to the events it was built from, so outliers with respect to various parameters, such as the root–mean–square (RMS) of the individual pulse fit or a mis–reconstructed pulse height, can be removed. From this cleaned list again an averaged pulse for the heat and for the light signal is built as it is shown in Fig. 7.7(b). With this pair of pulses all pulses in the Dark Matter Run will be fitted with only 5 free parameters, namely the pulse height of light and phonon channel, baseline of light and phonon channel and the time

[2]The stability cut and the correct live–time calculation was done in this thesis by a routine provided by S. Pfister and J. Schmaler.

offset. The time difference between the light and the phonon channel is not a variable parameter as it is fixed by the Standard Pulse pair.

To avoid the influence of a non–linear behavior of the superconducting film — a saturation effect at higher energies where the thermometer is not fully superconducting anymore — the fit is truncated at a level well below the non–linear part of the signal. Only the "foot" of the pulse is fitted and the region around the higher levels of the particle pulse, where a non–linearity first takes effect, is not included.

To achieve the long term stability of the energy calibration there are Test Pulses of different amplitudes (see Fig. 7.8) which are constant over the period of a run. A certain energy is periodically injected via a heater to the thermometer, which mimics a particle pulse. As the input in form of the Test Pulses is constant, one can correct for every difference in the reconstructed pulse amplitude.

For Test Pulses the Standard Pulse is built in a similar way. One additional feature is considered: From the DAQ it is known when a test pulse is injected. If there is a trigger delay between the injected and the reconstructed pulse the pulse is discarded. This effect happens mainly when a bigger real signal arrives close to the Test Pulse.

To reconstruct the detector response for every point in time the pulse heights of Test Pulses of one injected energy are interpolated with a spline of appropriate stiffness. From the calibration measurement one takes the reconstructed amplitude of a peak of known energy and calculates the calibration factor with the help of the two nearest test pulses. The calibration–ladder of different Test Pulse–heights guarantees the long term stability of the calibration over a wide energy range from zero up to about 600 keV. The upper limit in the calibrated energy range is a detector specific property. The region of interest for the Dark Matter search is up to 100 keV and in every detector within the linear range.

7.2.3 Neutron Calibration

A neutron calibration was performed for the commissioning run to verify the response to recoils of the detector modules in the WIMP–sensitive region. The detector modules were therfore exposed to a neutron source for about 150 hours. About 3.4 kg·days (kgd) of calibration data with the two detector modules "Zora" and "Verena" were acquired. Both modules were located next to each other in the top position of a tower.

In the data of the neutron calibration there are two bands of events in the scattering plot of light yield over energy visible (Fig. 7.9). The band with the slope equal to one (by definition) is caused by electro–magnetic interactions.

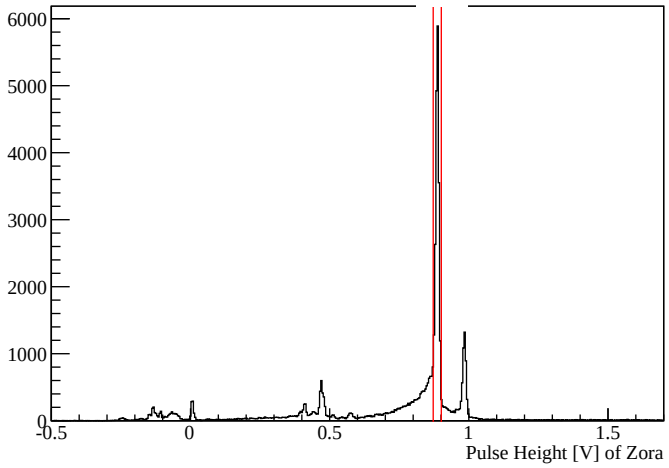

(a) A raw pulse height spectrum from the calibration run of the detector module Zora is shown. The Standard Pulse is built from the pulses in the red marked area of the 122 keV events.

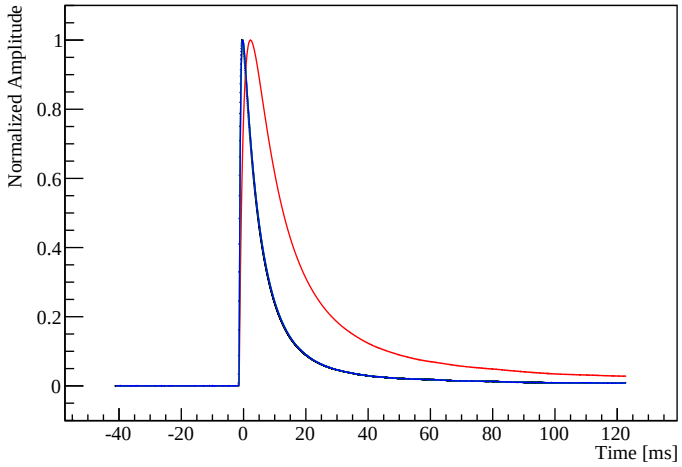

(b) A pair of Standard Pulses for the detector Zora is plotted. The blue pulse with the faster rise time is the light–pulse, the red one is for the phonon chanel. Due to the averaging of many real pulses the Standard Pulse is free of electronic noise. This pulse is later fitted to all events in the Dark Matter run and is responsible for the precise energy reconstruction of CRESST [54].

Figure 7.7: The Standard Pulses are built by the average of many real particle pulses of similar energy.

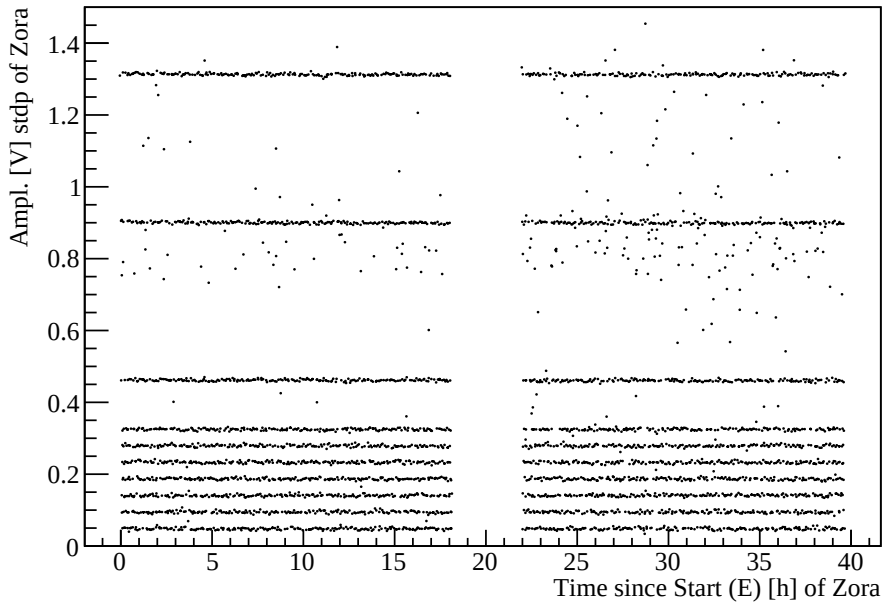

Figure 7.8: The pattern of Test Pulse amplitudes is shown over time. It guarantees a precise transfer of the energy calibration to a pulse which may be acquired months later. The non–linearity behavior between the Test Pulse amplitudes is interpolated with a polynomial of third order. All outliers in the amplitudes here can be safely removed as they come from accidental coincidences with the calibration source.

The events having roughly ten times less light–output are neutron scattering events off oxygen, which is the most likely scattering partner. The light yield is the ratio between the light output of a given scattering event normalized to an event with the same deposited energy of a γ recoil. Even electrons from a β–decay have a slightly different light yield [55]. The quenching factor is the inverse of the light yield.

Determination of the Quenching Factors

By the precise knowledge of the quenching factor one can suppress neutron background in the CRESST data analysis. In the energy range up to 40 keV WIMPs would scatter mainly off tungsten whereas neutrons unlikely scatter off tungsten. A precise tungsten recoil identification would remove a possible neutron background.

But the quenching factor at milli-Kelvin temperature is not easy to measure. The absolute light output has to be measured inside a cryogenic setup. During the neutron calibration the two detector modules "Zora" and "Verena" were mounted close together. This geometry allows for an attempt to suppress the dominant electro–magnetic background. This background overlaps with the nuclear recoil band at low energies. A double scattering in both detector modules selects very efficiently the neutron events.

In the class of double scattered events the interesting tungsten scattering events are largely suppressed by kinematics. To find the tungsten events an energy window from zero to 30 keV is defined, where most of the recoil events from tungsten are, whereas the calcium and oxygen events are distributed up to a few MeV. By cutting only the first 30 keV they are suppressed and the tungsten events become relatively enriched. It turns out that the suppression of calcium and oxygen gets even better if one requires in both detectors the energy window to be from zero to 30 keV. Probably the geometry of the setup prefers the double scattering off tungsten in this energy range, but that has to be confirmed by detailed Monte Carlo simulations.

Thus, for the determination of the quenching factor with the coincident events in both detectors a window for a light yield from zero to 0.2 and an energy range from zero to 30 keV is selected. In figure 7.10 one can see the light yield of this event group. For a larger statistical basis the histograms of both modules were combined. The best fit of the three population (tungsten, calcium and oxygen) with three individual Gaussians is shown. Due to the nature of the cuts, no background rate is expected. The only constrain applied to the fit is a relation of the widths of each of the single Gaussian. The smaller the light yield, the smaller the width of the Gaussian. Due to the statistical nature of the reduction, the width decreases only with the square–root. This

condition is motivated by statistics, but in a CRESST data analysis it was positively checked. More details about the algorithm are shown in App. D.3 for the fit itself and in App. D.4 for the related error calculation. The obtained result is displayed in Tab. 7.2.

A comparison with the results obtained at the accelerator laboratory at the TU Munich shows a rather good agreement as highlighted in Fig. 7.11. The special focus was on precise confirmation of the tungsten quenching factor. The result of both measurements at mK temperature are consistent. This work could determine the quenching factor directly with the CRESST setup for the first time to be $31.7^{+16.9}_{-8.2}$ (vgl. Tab. 7.2). The error bars are asymmetric due to the fact that the inverse property, the light yield, is measured. During the transformation of the measured light yield to the quenching factor the error bar becomes asymmetric.

The potential to discriminate even an possibly remaining neutron background from the WIMP recoils is visible via the different quenching factor of oxygen, calcium and tungsten. Therefore CRESST has the unique possibility to discover Dark Matter without any doubt, as a WIMP is supposed to scatter mainly off tungsten, due to the higher mass.

[3] g.e.: γ equivalent

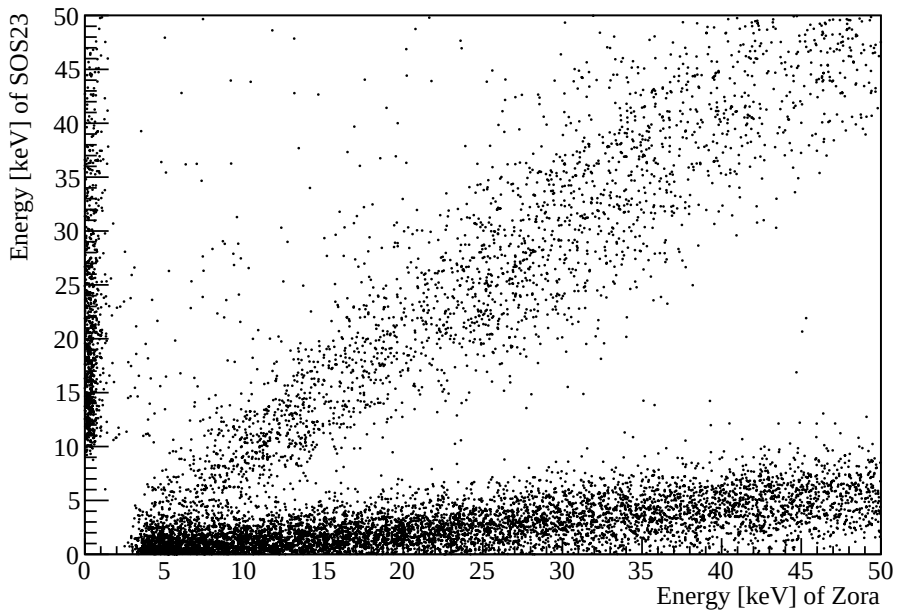

Figure 7.9: The measured energy of the light detector over the total energy in $keV_{g.e.}$[3]is shown for every event during the neutron calibration. The data of the detector "Zora" clearly discriminates between the upper electro–magnetic band and the lower neutron recoil band. The slope of this two bands are in first order not energy dependent and so the light output, relative to a gamma event of the same energy, is taken as a discrimination parameter called light yield. The events of detector "Zora" below 2 keV are single hits of the light detector. Furtheron they are not taken into account.

Element	Quenching factor	Minus	Plus
Oxygen	7.20	-.98	1.35
Calcium	12.3	-2.1	3.25
Tungstun	31.7	-8.2	16.9

Table 7.2: The results of the fit shown in figure 7.10 are displayed. The fit is obtained which the gnuplot script in App. D.3. The calculation of the quenching factor and its errors determination is described in App. D.4. It is technically extremely challenging to measure quenching factors at milli–Kelvin and therefore the values in literature are mostly from room temperature measurements. The given result suffers obviously from the very low statistic, but it is encouraging that it is consistent with the sophisticated measurements of the scattering experiment at the MLL laboratory [49] as one sees in figure 7.11.

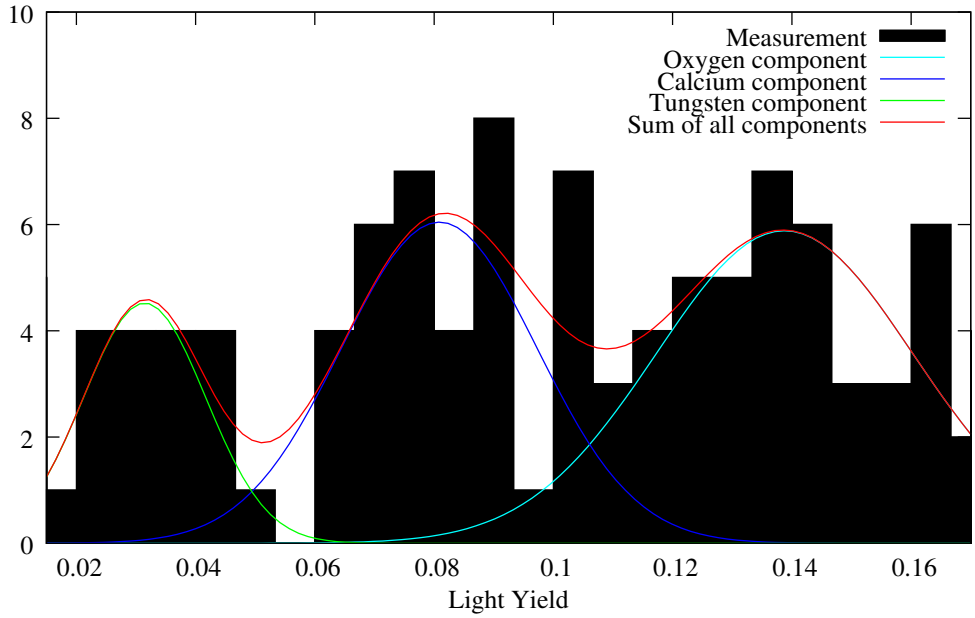

Figure 7.10: The light yield, or inverse quenching factor, from the events surviving the cuts mentioned in the text is plotted. The light and dark blue components refer to the oxygen, respectively the calcium, contribution. Whereas green is the tungsten component which is important for the Dark Matter search. Due to the clear discrimination CRESST has a unique possibility to suppress neutron background in region of interest by orders of magnitude.

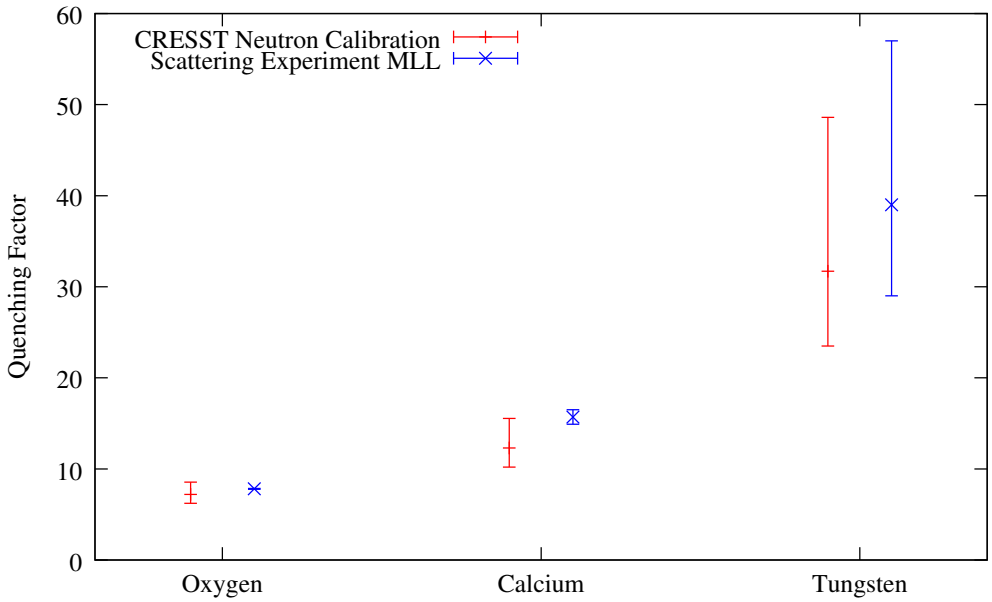

Figure 7.11: The measured quenching factors of this work in red are compared with the result of the measurement at the TU Munich [49] in blue. They are consistent within the errors. The plotted error bars are the combined error from statistics and from the fit uncertanty. For the first time the quenching factor of tungsten could be measured directly in the CRESST setup.

7.3 Muon correlated Particle Events

Within the measurement time of 550 hours the detector "Zora" acquired 6.4 kgd of data after the stability cut. The stability cut removes measurement periods where the detector might not have worked properly. During the first 110 hours of data–taking the muon veto was not active. Leaving 5.2 kgd of data for a coincidence analysis. The muons are identified as described in Sec. 7.1.1 with an automatic selection process by a software described in more detail in App. G.1.2.

The coincidence analysis requires a link between the time stamps of the particle events and the muon veto system. Both systems use a common clock to build the time stamps. The trigger is built independently for both systems.

In this work two additional particle parameters are introduced. The difference between both time stamps, from every particle detector event to the closest veto event, is saved in the first parameter $\bar{DT}$. The data acquisition system uses a Leading Edge Trigger (LED) to determine the time of a particle event. If the energy deposit rises over a certain level the LED builds the trigger. However, this method introduces a dependence of the trigger time on the pulse height. To correct for this so–called 'walk' the second new parameter DT takes the time shift from the event time of the data acquisition against the reconstructed event time from the Standard Pulse fit into account (see App G.1.4). With the help of this two new parameters the time difference is independent of the energy of the particle event.

Figure 7.12 provides a histogram of the corrected time difference DT from every particle event in the "Zora" detector to its closest muon veto event. All muon veto events of the DVE group are displayed in black. The red histogram is the time difference to veto events of the CME group. Within the red selection a cluster of coincidences between zero and two milliseconds is noticed. At this position in the black histogram also a clustering can be found. These events can be assumed to have the same physical origin.

If these events would be direct hits from muons or muon induced particle showers in the particle detector there should be an occurrence of high energy events at that time. This hypothesis is verified in Fig. 7.13. One can see the reconstructed pulse hights from detector "Zora" versus the time difference to the next muon of the CME group. The events clustering around zero milliseconds time difference show on average a very high energy. A Dark Matter signal is expected to have only very low energy (see chapter 9). So only one "dangerous" event with an energy lower than 0.25 V, which corresponds to about 35 keV, could possibly fake a Dark Matter signal. This event is marked with a circle in the corresponding figure.

The cut proposed for a future Dark Matter run analysis is to reject all

particle events within a ±5 millisecond time window around the reconstructed particle time stamp. It has been shown that within that time the muon population produces a clustering of particle events and it is also enough for all muon induced neutrons to lose their energy via scattering. Afterwards they are no longer able to deposit a sufficient amount of energy in the region of interest for the Dark Matter search.

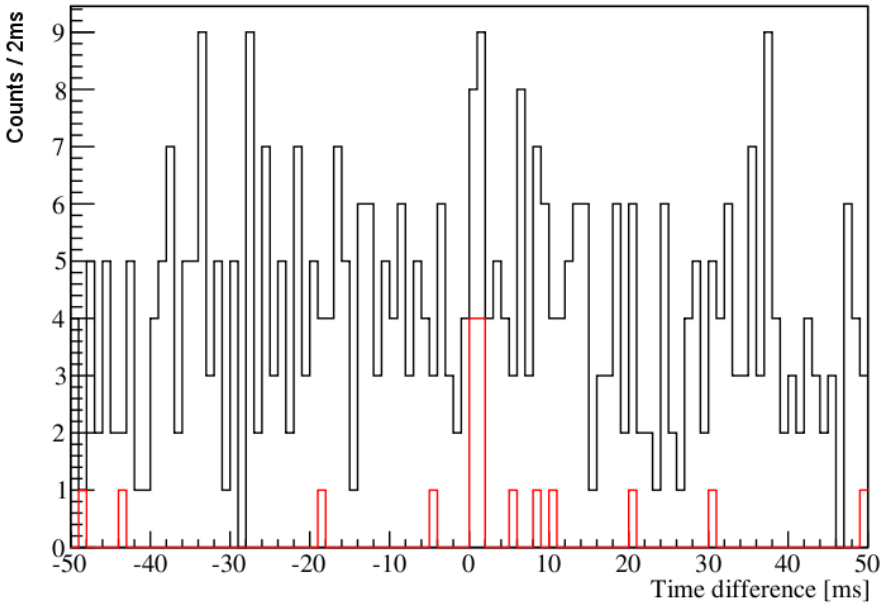

Figure 7.12: The time difference *DT* between all particle events and their nearest muon veto partner is shown. The red population takes only muon candidates of the CME group into account. The black distribution includes DVE members. A clustering from zero to two milliseconds is an indicator for muon induced events. Accidental coincidences from miss–identified gammas in the muon veto causing the other ones.

7.3.1 Comparison of Muon induced Recoil Rates

It is planned to integrate the CRESST technology into the future experiment EURECA at the Modane laboratory. Therefore the rate of muon induced events is compared to the partner experiment EDELWEISS, which is already located at Modane and also an estimation of the expected coincident rate of the EURECA experiment is given.

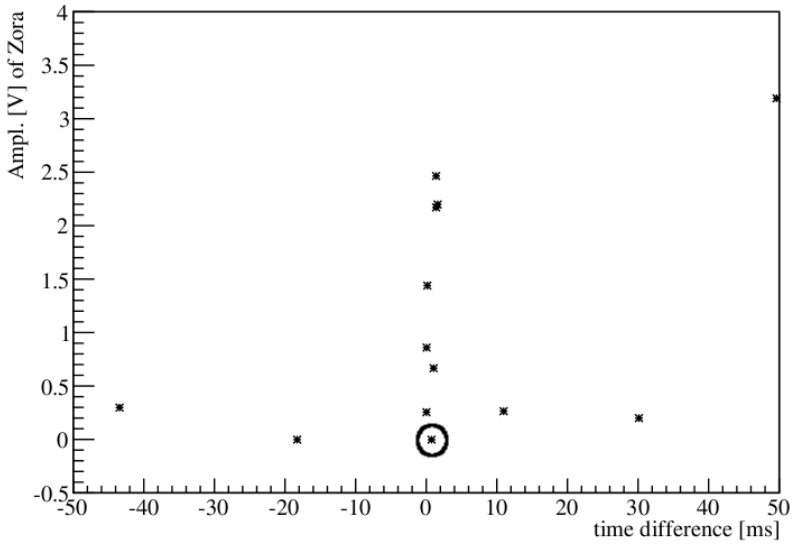

Figure 7.13: For the red CME population from Fig 7.12 the reconstructed pulse amplitude in the cryogenic detector versus the time difference DT is displayed. The amplitude is an uncalibrated measure for the deposited energy. The events accumulated around a time difference of zero show an unusual high energy entry as it is expected for muon induced events. The muon is a minimal ionizing particle and deposits therefore a large amount of energy in the detector module in case of a direct hit. Only one dangerous event with very low energy could fake a Dark Matter signal.

The EDELWEISS experiment has a muon coincident rate of $0.04\,ev/kgd$ [56] detected in its Germanium detectors. Events up to a deposited energy of 250 keV were included. Due the heavier target nucleus the events of CRESST are included only up to 150 keV, which corresponds to about 1 V in Fig. 7.13. There are four events in the whole measurement time of 5.2 kgd, which corresponds to a rate of $0.77\,ev/kgd$. The muon flux is about six times less in Modane compared to the LNGS. So the rate normalized to the muon flux of Modane is for CRESST $0.12\,ev/kgd$. Taking into account the low statistical basis and the resulting large uncertainties of a factor of 2, these numbers are harmonious.

Thinking of the future EURECA experiment which is planned to be equipped up to the mass of one ton detector material one has to take care very well about muon induced events. Assuming an average rate of $0.1\,ev/kgd$, there could be up to 100 events per days in the region of interest. With a muon veto efficiency of "only" 99 % that would result in one event per day take fakes a WIMP recoil. That is not sufficient and therefore the muon veto efficiency has to be at least higher than 99.99 %.

Chapter 8

Summary of Part II

The CRESST experiment successfully performed a commissioning run in the year 2007. This was the first possibility to check the setup altogether after the upgrade to phase two in 2006. The calculation of the efficiency of the muon veto and a detailed analysis of the muon event identification were done in this work for the first time. The efficiency of the veto system itself could be determined to be 98 %. The optimal muon identification procedure is important as the ambient γ radiation is detected by the veto system as well and has to be suppressed by at least three orders of magnitude. Otherwise too less life time of the cryogenic detector system survives on which a meaningful Dark Matter analysis can be applied. The analysis of the muon veto system together with the cryogenic detector system in this work proves that the cut procedure is ready to be used in a dedicated Dark Matter run like the recently ongoing one.

To analyze the result of a rare event search, a detailed study of, e.g. the energy spectrum of the few remaining (background) events is required. This is the subject of the following chapters.

Part III

The Dark Matter Limits

The present Dark Matter search experiments suffer from a very low event rate in the order of one event per day and per hundred kilograms of detector mass. With this low statistical basis it is challenging to find the correct best upper limit on the measured rate, which one can exclude to a certain Confidence Level (CL). Especially if one takes into account, that these experiments fight against an unknown background. There has never been a possibility to measure the background for these experiments up to now.
In the first chapter it is shown how the expected WIMP recoil spectrum is calculated. After an introduction to analytical methods of statistics, the state–of–the–art method to treat the different experiments in a fair and comparable way is described. This method created by S. Yellin [57] suppresses the influence of background events of unknown origin via the expected shape of the recoil energy spectrum. An even more effective suppression is expected in a two dimensional parameter space. For example the second parameter could be the time or light yield. There are several ways for extending the spectrum based method. Three possibilities are investigated here and prepared for the use in the upcoming data analysis. Finally examples of applications of the Yellin method in two dimensions with various kinds of backgrounds are presented.

Chapter 9

Expected Signal

Besides the counting statistics itself which is presented in the following chapters, the expectation of the energy spectrum plays a significant role in Dark Matter data analysis. This expectation is based on a theoretical model with several parameters, e.g. the galactic escape velocity of WIMPs or the nuclear form factor for the target nucleus. In a more advanced analysis even the information of the shape of the modeled spectrum is taken into account. This way one becomes less sensitive to any unknown background with a different spectrum.

9.1 Model of the expected Energy Spectrum

It seems natural that the prediction of the properties of a particle which has never been observed has huge uncertainties. But to compare different results one must try to develop a common model and, more important, agree on common values of the unknown parameters. Otherwise it is not possible to evaluate results within a community of different experiments using different techniques and detector materials. This section introduces the calculations for the expected WIMP induced recoil spectrum and will point out some features.

In Ref. [58] it is motivated why we expect a recoil spectrum of an exponential shape like

$$\frac{dR}{dE_R} = \frac{R_0}{E_0 r} e^{-E_R/E_0 r} \tag{9.1}$$

where E_R is the recoil energy of the target nucleus, E_0 the most probable recoil energy and R_0 the total recoil rate. r is a kinematic factor taking into account the different masses M_W and M_T of the WIMP and the detector

(target) nucleus:

$$r = \frac{4M_W M_T}{(M_W + M_T)^2} \tag{9.2}$$

The total event rate R_0 is given by

$$R_0 = \frac{2}{\sqrt{\pi}} \frac{N_0}{A} \frac{\rho_W}{M_W} \sigma_0 v_0 \tag{9.3}$$

where N_0 is the Avogadro number ($6.02 \cdot 10^{23} mol^{-1}$), σ_0 an assumed cross section, A the atomic mass of the detector material, ρ_W the mass density of WIMPs in the galactic halo and v_0 a typical WIMP velocity. To calculate the expected spectrum, e.g. the example spectrum of Fig. 9.1, a software is used, which is listed in App. G.2.1.

In literature (i.e. Ref. [59]) it is pointed out that the nuclear form factor $F(q)$, which models the finite extension of the target nucleus, and the WIMP velocity distribution $f(\vec{v})$ should be taken into account like the following:

$$\frac{dR}{dE_R} = \frac{N_0}{A} \frac{\rho_W}{M_W} \int d\vec{v} f(\vec{v}) v \frac{d\sigma}{dE_R}(v, E_R) \tag{9.4}$$

$$\frac{dR}{dE_R} = \frac{N_0}{A} \frac{\rho_W}{M_W} \int d\vec{v} f(\vec{v}) v \frac{\sigma_0}{E_R^{max}} F^2 \left(q\left(E_R\right)\right) \tag{9.5}$$

where

$$q(E_R) = |\overrightarrow{q}| = \sqrt{2M_T E_R} = \sqrt{2M_{red}^2 v^2 \left(1 - \cos\Theta\left(v, E_R\right)\right)} \tag{9.6}$$

is the momentum transfer. $M_{red} = M_T M_W / (M_T + M_W)$ is the reduced mass and $\Theta\left(v, E_R\right)$ is the scattering angle in the WIMP–nucleus center–of–mass frame. Θ is determined by kinematics via the WIMP velocity v and the recoil energy E_R. The formula 9.5 corresponds to the differential cross section of two point–like particles, $\frac{d\sigma}{dE_R} = \frac{\sigma_0}{E_R^{max}}$, multiplied with the form factor $F^2(q)$ for extended objects.

For comparison between experiments with different target nuclei the presented exclusions for the cross section are normalized to the cross section for a proton–WIMP scatter. The normalization for spin–independent (or scalar) scattering takes the kinematics and the A^2 behavior of the cross section into account (compare Ref. [59]):

$$\sigma_{0\,T} = \sigma_{0\,prot} \left(\frac{M_{red,\,T}}{M_{red,\,prot}} \times A_T \right)^2 \tag{9.7}$$

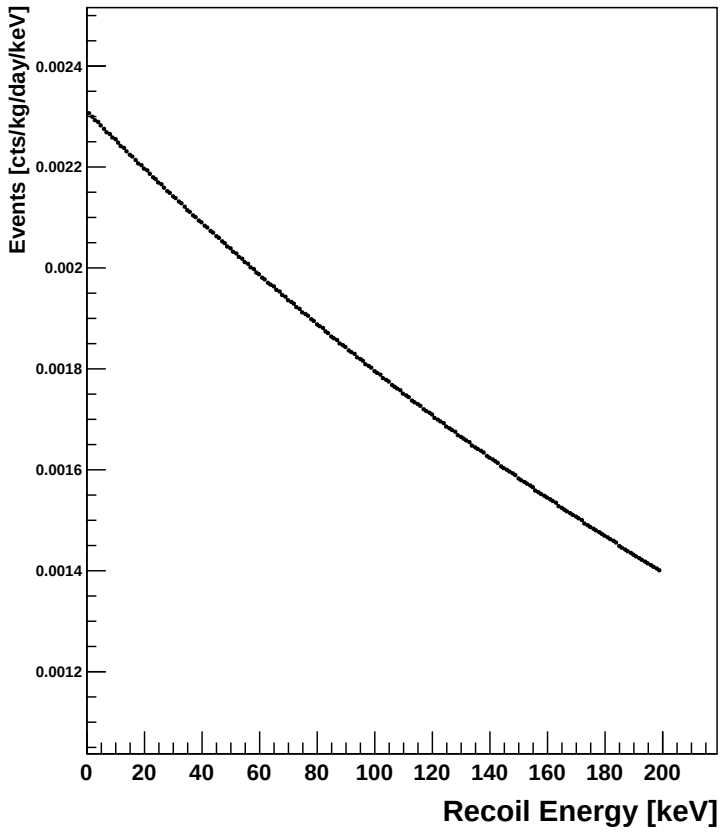

Figure 9.1: A WIMP recoil spectrum following the simple model from reference [58]. It is calculated for WIMP–proton cross section of $10^{-7}pb$ with a target nucleus with $A = 180$ and a WIMP mass of $M_\chi = 200GeV/c^2$. The program for the calculation of the spectrum is shown in App. G.2.1. In the given example about half a count is expected within the whole energy range in one day and one kilogram of detector material.

9.1.1 Velocity Distribution

The velocity distribution of WIMPs in the halo of our galaxy is unknown. With an assumed dust–like behavior of WIMPs in our galaxy one expects these particles with an isothermal velocity distribution with a cutoff velocity equal to the galactic escape velocity. This value is in a range within $498km/s < v_{esc} < 608km/s$ as a recent measurement concludes [60]. The calculation done in this thesis takes the distribution function from the micromegas software [61]. This velocity distribution is given by

$$f(u) = c_{norm}\left\{\exp\left(-\frac{\min^2(u-v_1, v_{esc})}{v_0^2}\right) - \exp\left(-\frac{\min^2(u+v_1, v_{esc})}{v_0^2}\right)\right\} \tag{9.8}$$

where c_{norm} is defined as

$$c_{norm} = \frac{1}{\int_0^\infty f(u)\mathrm{d}u}. \tag{9.9}$$

The values of v_0 and v_1 are taken to be $v_0 = (220 \pm 20)km/s$ and $v_1 = v_0 + 5km/s \pm v_{earth}$. The motion of the earth v_{earth} can cause an annual modulation in the recoil spectrum. Here it is set to zero.

Direct detection experiments are able to measure the recoil energy E_R of the detector nucleus. For a given E_R the form factor $F(q)$ is a constant. The integral of formula 9.5 over all velocities, which can cause a specific E_R, splits up in the constant prefactor $F^2(q)$ and the pure velocity distribution multiplied by a factor $v/E_R^{max} \propto v/v^2 \propto 1/v$. The integration starts at the minimum velocity v_{min} needed in a central collision to cause E_R. Generally the upper integral bound is taken to be the escape velocity of our galaxy.

The first minimum–function of Eq. 9.8 is built–in to be able to describe also models (like inelastic Dark Matter in Sec. 9.2.1), where $v_{min} - v_1 > v_{esc}$ can occur. Other references, for example [62], are taking a WIMP velocity distribution different to Eq. 9.8. The isothermal halo model is taken in this work for further calculations, but it has to be classified as a theoretical motivated assumption.

An interesting model–independent ansatz to determine the WIMP mass and cross section by comparing the recoil spectra is presented in Ref. [63]. As soon as at least two experiments measure around 50 events each, the WIMP mass and its cross section could be determined without assumptions on the velocity distribution. The experiments should have different target nuclei. The error of the result increases rapidly if the WIMP mass would be higher than the heavier target nucleus.

9.1.2 Nuclear Form Factor

The previous subsection points out that there is a certain freedom in the choice of the parameters for the velocity distribution, which is an astronomical input and hard to measure. However, the form factor, a parameter from nuclear physics, is often meant to be exactly determined. This section points out, that the form factor used for Dark Matter Search analysis, generally the Helm form factor (Ref. [64]), has also some uncertainty.

The Helm form factor is given by:

$$|F^{SI}(q)|^2 = \left(\frac{3j_1(qR_0)}{qR_0}\right)^2 \exp(-q^2 s^2) \tag{9.10}$$

where q is the momentum transfer in units of [1/fm]. The conversion factor into units of 1/fm can be found for example in reference [65]. s is the soft skin thickness around the hard core with radius R_0. In literature there are different approximations for R_0. Three of them are listed in table 9.1. The function j_1 is the spherical Bessel function of the first kind. The normalization is chosen in a way that the form factors fulfill the condition $F(q) = 1$ for $q \to 0$.

The issues of this Helm ansatz are the following:

- In general the Helm parameterization from Eq. 9.10 for the form factor is taken, i.e. Ref. [58]. This analytic expression is available for all isotopes and easy to calculate. However, strictly speaking it is the form factor for the charge distribution, but it is assumed today that the interaction of a WIMP couples to the whole nucleus in the spin–independent case, so one should take the mass form factor. In scattering experiments with an electrical neutral particle of the strong interaction, like the photoproduction of π^0, this kind of form factor can be measured. For a few isotopes this was done, compare Ref. [66], and the mass form factor and the charge form factor agree on the level of about one percent. This result gives confidence in the Helm form factor, but it needs to be checked for the nuclei used in direct Dark Matter search.

- In reference [65] the Helm form factor is compared with the Fourier–Bessel charge form factor which is known to describe the individual nuclei better. For light nuclei both form factors differ less than 10 %, but for heavy nuclei like tungsten or Xenon they vary about a factor of two at recoil energies of 100 keV, which results directly in an uncertainty of the upper limit in the same order obtained in a WIMP search experiment.

- Similar to the previous issue the form factor of a given model is very sensitive to the radius for heavy nuclei (compare Fig. 9.2). If the first

minimum of the form factor is in the region of interest below 100 keV, small variations of the radius or the soft skin parameter change the result up to a factor of five.

R_0	r	s	reference
$\sqrt{r^2 - 5s^2}$	$1.2A^{1/3}$	1	Chang, et al. [67] Donato, et al. [59]
$\sqrt{r^2 + 7/3\pi^2 \cdot 0.52^2 - 5s^2}$	$1.23A^{1/3} - 0.6$	0.9	Duda and Kemper [65] or Smith and Lewin [58]
$\sqrt{r^2 - 5s^2}$	$0.91A^{1/3} + 0.3$	1	Dark Matter tool [68]

Table 9.1: The radius parameterization in the Helm form factor function is not unique in literature. Three examples of different parameterizations are given in this table. The radius determines the position of the first minimum of the form factor function.

One can conclude that the form factor is an unknown parameter which can only be approximated. Usually this is done with the Helm model, especially for heavy nuclei. Since it is an unknown parameter it could also be very different from the Helm form factor. This fact is used in some references [69] to explain otherwise contradictory results by large (and otherwise unmotivated) modifications of the form factor.

9.2 Calculated Recoil Spectrum

In the previous section the focus was on possible issues of the model as many uncertain parameters enter the formula for the recoil spectrum. In this work the new ansatz for calculating the WIMP recoil spectrum is done via an averaging approach: The spectrum is calculated for the whole allowed range of the most critical parameters. The averaged result is displayed as the mean value. The highest result value is displayed as maximum of the error bar and the lowest value is treated as minimum of the error bar.

The calculation is done for the following parameter variation:

- the escape velocity of the galaxy (500 and 600 km/s)
- the velocity of the sun in the galactic frame (200, 220 and 240 km/s)
- skin thickness of the nucleus (0.9 and 1.0 fm)

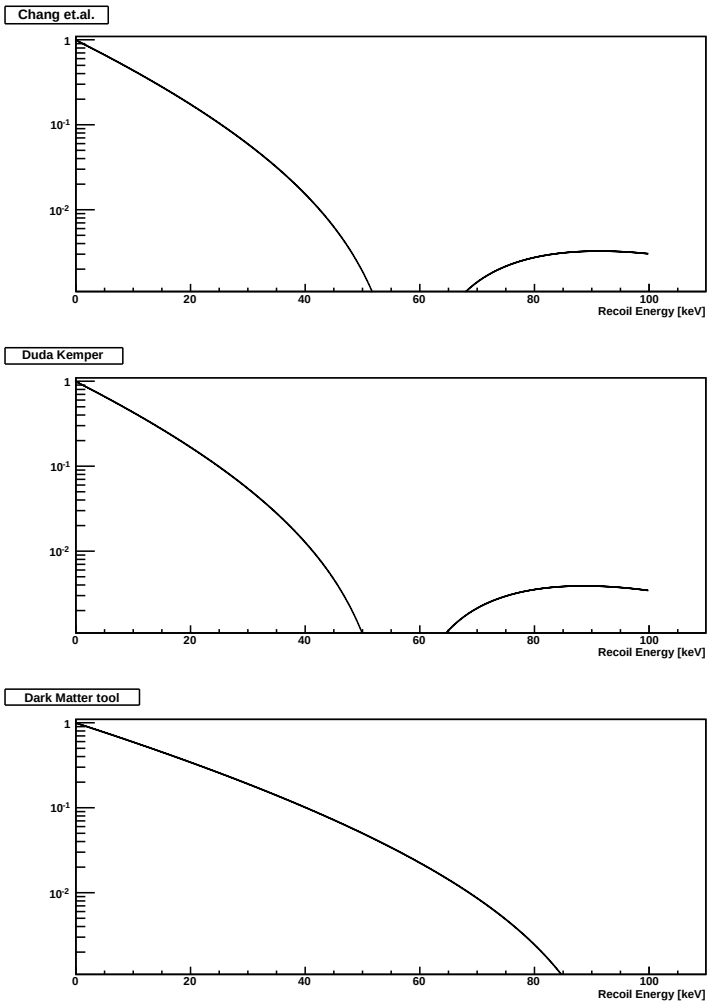

Figure 9.2: The values for three parameterizations of the Helm form factor of tungsten is shown for recoil energies up to 100 keV. In all advanced models of the Dark Matter recoil spectrum the form factor of the scattered nucleus is taken into account. Commonly the Helm parameterization of the form factor from Eq. 9.10 is used. The figure is generated with the software presented in App. G.2.1 for different parameterizations of the radius of the nucleus. The position of the first minimum of the form factor is connected to the radius parameter. This position varies significantly in the different parameterizations form 55 keV in the upper figure to about 100 keV in the last figure.

- the three parameterization alternatives for the form factor of Tab. 9.1

The program *Rate_vary* of App. G.2.1 calculates the output spectra with this set of input parameters. The mean of all solutions is taken as the result. The lowest and the highest value is shown to illustrate the range of the predicted values. The prefactor of the whole spectrum is directly proportional to the density of Dark Matter at the position of the earth. It is set to $\rho_{DM} = 0.3\,GeV/cm^3$ and will not be modified here.

The result of an example calculation is shown in Fig. 9.3 for the case of a WIMP with a mass of $80\,GeV$ which scatters elastically off tungsten. Despite the large astronomical and nuclear physics uncertainties the error bars from the minimum to the maximum count rate are small. At low energies the uncertainty is for example $\pm 8\%$. For energies above the first minimum in the form factor the relative uncertainty of the count rate becomes higher (up to a decade), but the contribution to the total count rate is negligible.

This introduction to the calculation of WIMP recoil spectra shows that the expectation for a Dark Matter experiment is not that fixed and leaves freedom for new ideas and speculations.

9.2.1 Calculated Recoil Spectrum for inelastic DM

To bring the results of all experiments into agreement, especially the two evidences mentioned in section 3.4 and CRESST, a further assumption is made in the iDM modell: The scattering process needs a certain amount of energy δ for example due to an excitation of the WIMP. This energy "loss" causes a higher minimum velocity v_{min} of the WIMP than it is calculated for pure kinematic and therefore the recoil spectrum is suppressed at low energies due to momentum conservation. Eliminating events beneath the experimental threshold, gives all experiments a higher detection efficiency. In the model of inelastic Dark Matter (iDM) scattering [67] the expected recoil spectrum is very sensitive to astronomical parameters.

The additional energy effort for the inelastic scattering process results directly in a higher minimum WIMP velocity needed to make the process possible. If this minimum required velocity is higher than the v_{esc} parameter the expected count rate is zero. This results in huge uncertainties at low energies of the recoil spectrum as shown in Fig. 9.4. There are parameter combinations where the total count rate for lighter WIMPs is allowed to be exactly zero. On the other hand the model provides a new parameter to become more sensitive to the motion of the earth around the sun.

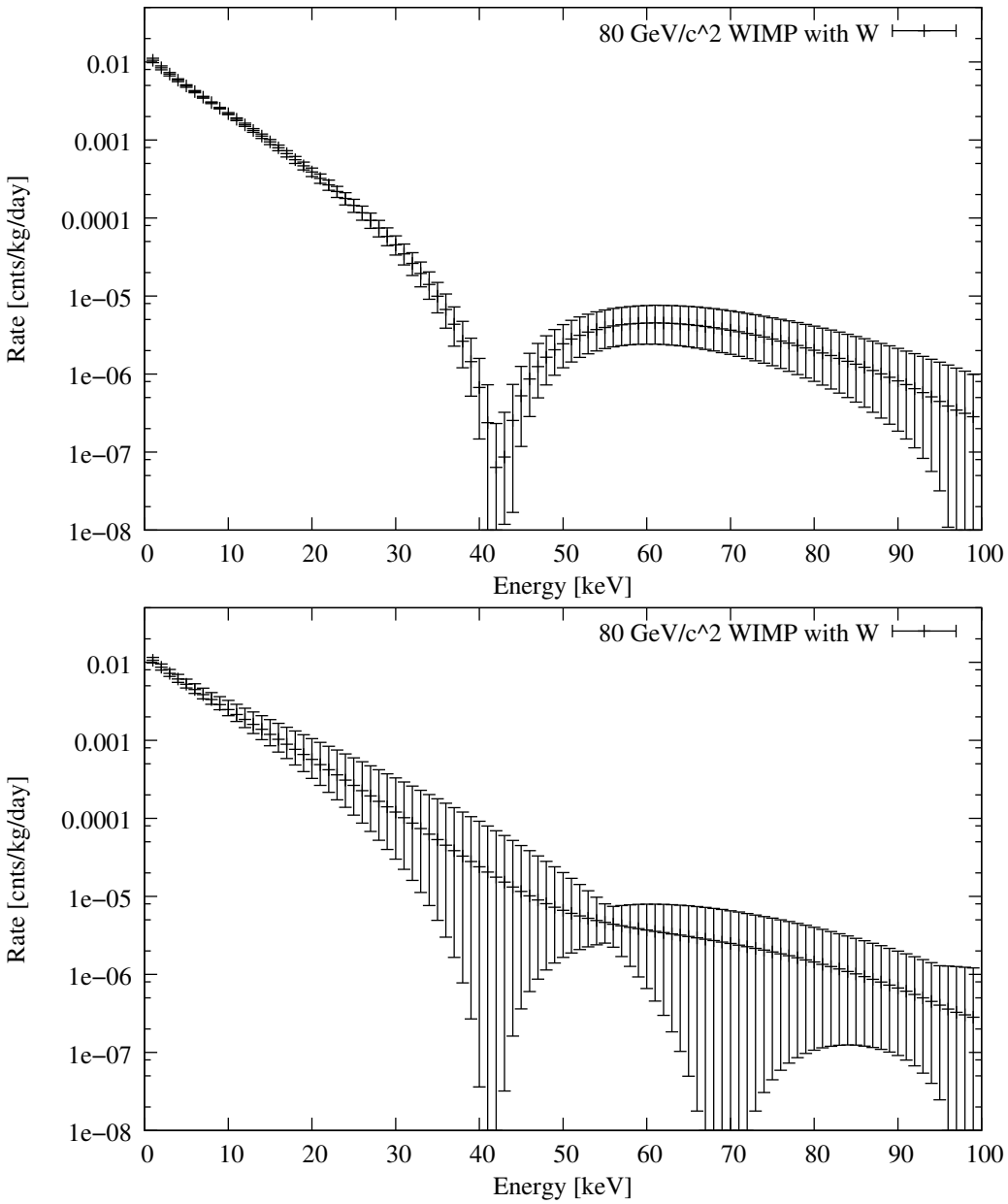

Figure 9.3: Recoil spectra of elastic scattering from WIMPs of the mass $M_W = 80\,GeV$ off tungsten. All combinations of the allowed parameters were calculated and averaged. The minimum and maximum values mark the possible range of the fluctuation. In the upper figure only the form factor parameterizations of Chang [67] and Duda [65] are taken into account. In the lower figure also the form factor of Ref. [68] is included and causes a second minimum at 70 keV.

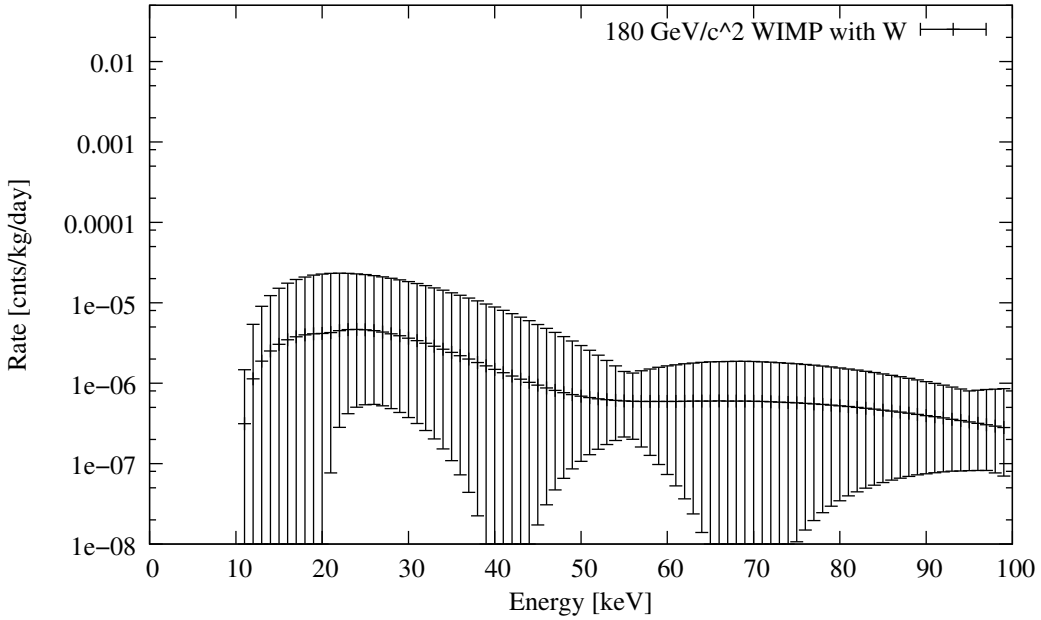

Figure 9.4: Recoil spectrum of inelastic scattering from WIMPs of the mass of $180\,GeV$ off tungsten. The energy splitting here is $\delta = 100\,keV$. The expected spectrum is empty in the very low energy range. Therefore no expected event is below a typically experimental threshold of 10 keV. Such experiments seems to become more sensible in the iDM model as they could detect all expected events.

9.3 Limit Calculation

The excluded rate of a Dark Matter search experiment can be transformed into an upper limit to the WIMP–proton cross section via the equation 9.5. The present situation for some leading experiments with their excluded cross section is shown in Fig 9.5. In such plots the comparison of experiments with each other or with the theoretical expectations are made. To account for the unknown WIMP mass a scan over the possible mass range is done. The target mass of an experiment defines the most sensible mass region.

Besides the dependency of the scattering rate on the mass of the WIMP the rate is only dependent on the assumed cross section σ_{ass} (if one neglects for a moment the previously discussed uncertainties of the astronomical and nuclear physics parameters). As the rate is proportional to the cross section the experimentally excluded cross section σ_{obs} is:

$$\sigma_{obs} = \sigma_{ass} \frac{R_{obs}}{R_{calc}} \tag{9.11}$$

where R_{obs} is the observed rate and R_{calc} the calculated rate under the assumption of $\sigma_0 = \sigma_{ass}$. From the experimental point of view, the parameter R_{obs} is the only one, which can be improved. The measuring time or the detector mass are therefore the best choice for improvements in case of a background free measurement. A third method of optimization is presented in the following sections: The idea is to use in addition to the measured rate R_{obs} the measured event distribution. The distribution can be compared to the expectation of the event distribution in energy, time or other parameter. Such a parameter would be in the CRESST case the discrimination parameter, called light yield.

For example an experiment measures four events at the high energetic part of the recoil spectrum. It is much more likely for the modeled WIMP to deposit less energy and therefore it seems natural that this experiment ends up with a lower limit on σ_{obs} than one with the counts exactly where they are expected for that WIMP.

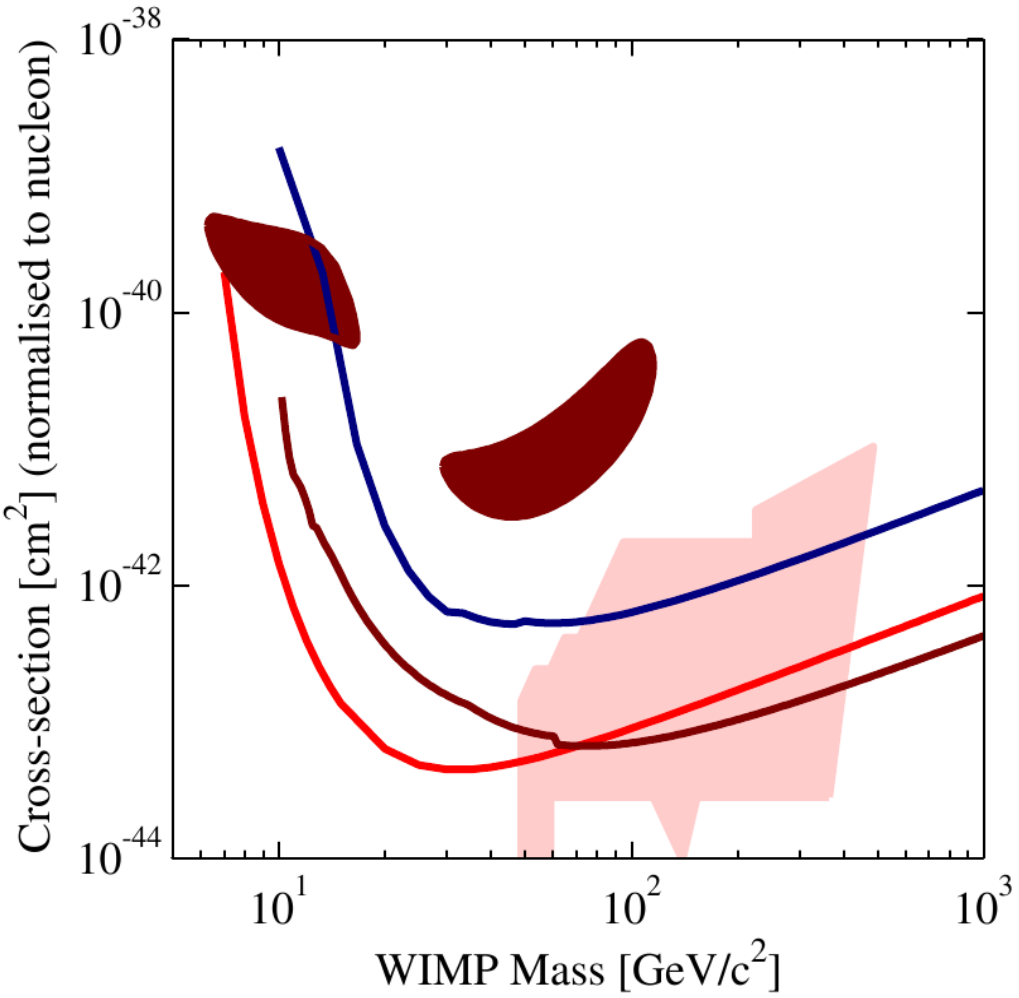

Figure 9.5: The excluded cross sections of various experiments are shown. The results from CRESST–II [38] is displayed in blue, from XENON [39] in red and from CDMS–II [36] in brown. The DAMA [34] evidence corresponds to the brown colored "islands". The light red shaded area on the bottom is a possible parameter space for a Supersymmetric Model [70]. The direct Dark Matter search experiments begin to give boundary conditions for a realization of these models. The plot is created with the database of Ref. [71].

Chapter 10

Basic Methods for Statistical Data Analysis

To quantify the error in a measurement is as important as the resulting value itself. There are two kinds of errors, the statistical and the systematical one. The last one is a result of uncertainties like the limited knowledge on the exact dimensions of the devices or the influence of a minor source of disturbance. These effects can only be estimated or a limit to their influence can be given. The statistical error gives an indication how certain the same result would come out of the same experiment in case of a repetition. E.g. for low count numbers the error on the measured count number can be given by the Poisson statistic. In case of low event rates, like the Dark Matter experiments, the statistical error is high compared to the value itself. Here we try to minimize that error by including the expected time or energy distribution of the measured events and not only their rate. One analytic ansatz is the Erlang distribution introduced in section 10.2.

10.1 Poisson Distribution

The analysis of the statistical error of data with a method quantified by an analytical expression has the advantage that it is fast to calculate and has an exact result. The Poisson distribution is the most basic method. It describes the probability distribution of resulting values with a known true average value λ. The inverted task has to be done to conclude for the true value if only a few measurements are accessible. As this correlation is not unique, since a measured value can belong to different true values λ, the construct of a Confidence Level (CL) is introduced. The CL is the probability in which extend one can be sure that the result belongs to a range of true values and

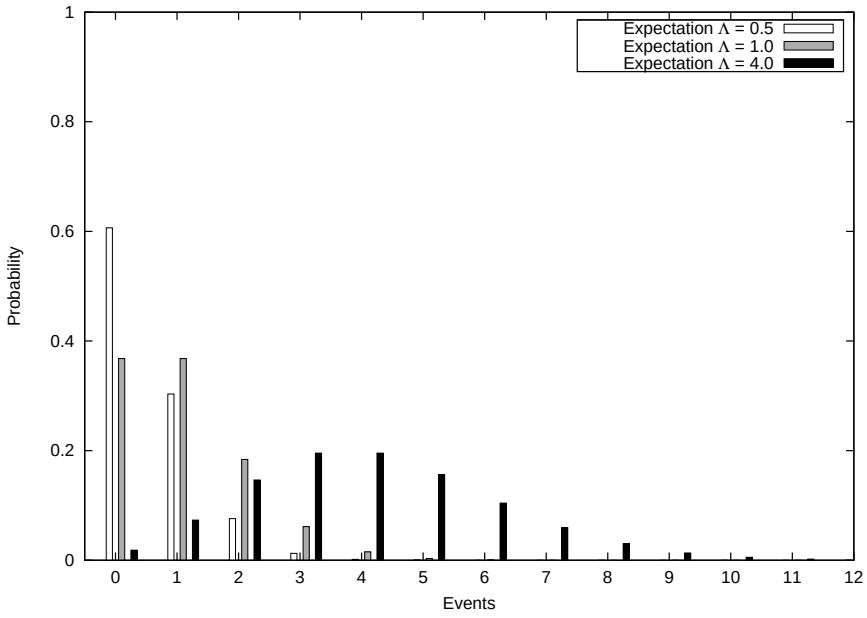

Figure 10.1: Here one sees the development of the Poisson probability distributions with increasing mean values. The Poisson distribution gives the probability that for a mean value a certain integer value is realized. The mean value Λ is often unknown before the measurement and a limit to the allowed range of Λ can be obtained as a result of the measurement.

is not a statistical outlier. In the Dark Matter search community results are usually given to a 90 % confidence (90 % CL).

The Poisson distribution describes the probability to measure k events as the result of an experiment with an average event rate λ after the measuring time t is:

$$Poi(k;\lambda t) = \frac{e^{-\lambda t}(\lambda t)^k}{k!} \tag{10.1}$$

Some example distributions for different values of the expected events $\Lambda = \lambda \cdot t$ are displayed in Fig. 10.1. The Poisson distribution gives a prediction if the average value is known. But in a real measurement the problem is the opposite way around: One has a result and wants to know the mean value or at least in which range the unknown mean value is.

This can be done by some simple simulations: For example, if an upper limit to the number of expected events Λ of an experimental result of k_m

measured counts is the focus. Then one has to add up all Poisson probabilities for k from zero to k_m for an assumed Λ. The sum is called confidence level CL.

$$1 - CL = \sum_{n=0}^{n=k_m} Poi(n, \Lambda) \tag{10.2}$$

It gives the probability to have an experiment with k_m or less counts, if the true value is Λ. The value of Λ is increased until at $\Lambda = \Lambda_{CL}$ the sum CL reaches a predefined value CL_{wanted}. Then one can say that the measurement excludes with at least the probability CL_{wanted} all values for Λ smaller than Λ_{CL}. The upper limit is reasonable if one always want to include zero as a possible result.

In principle one is free to define a both–sided limit, meaning the rest probability $(1-CL_{wanted})$ can arbitrarily be divided to the lower and the higher side from the measured value. Very common is the both–sided symmetrical limit where the rest probability is divided in equal parts to both sides. This case will further be called both–sided limit. It is defined like the following:

$$\sum_{n=0}^{n=k_m} Poi(n, \Lambda_{high}) = CL_{high} = \frac{1 - CL}{2} \tag{10.3}$$

and

$$\sum_{n=k_m}^{n=\infty} Poi(n, \Lambda_{low}) = CL_{low} = 1 - \frac{1 - CL}{2} \tag{10.4}$$

Some results for values of k_m between zero and twenty are shown in Tab. 10.1. The 90 % upper limit is shown in the second column. The lower and the upper bound, Λ_{min} and Λ_{max}, of the both–sided limit is listed in the third respectively forth column and the difference between this values is the width of the allowed range in this case, which is displayed in the last column. The values are illustrated in Fig. 10.2.

The Dark Matter community always give results in form of an upper limit[1]. The reason to do this is the careful handling of background. There might be a not–understood class of background events. One cannot be sure that the k_m observed events came from the source one is looking for. They might also be background. The source causes in the realistic scenario between 0 and k_m counts. If one is sure that k'_m events, with $0 < k'_m < k_m$, really caused by the source, then at some point change to a both–sided limit to narrow the range

[1]Except the DAMA Experiment [34] which follows a different strategy than the event–by–event based measurement of Dark Matter. They measure an annual fluctuation of their background — further details in Sec. 3.4.

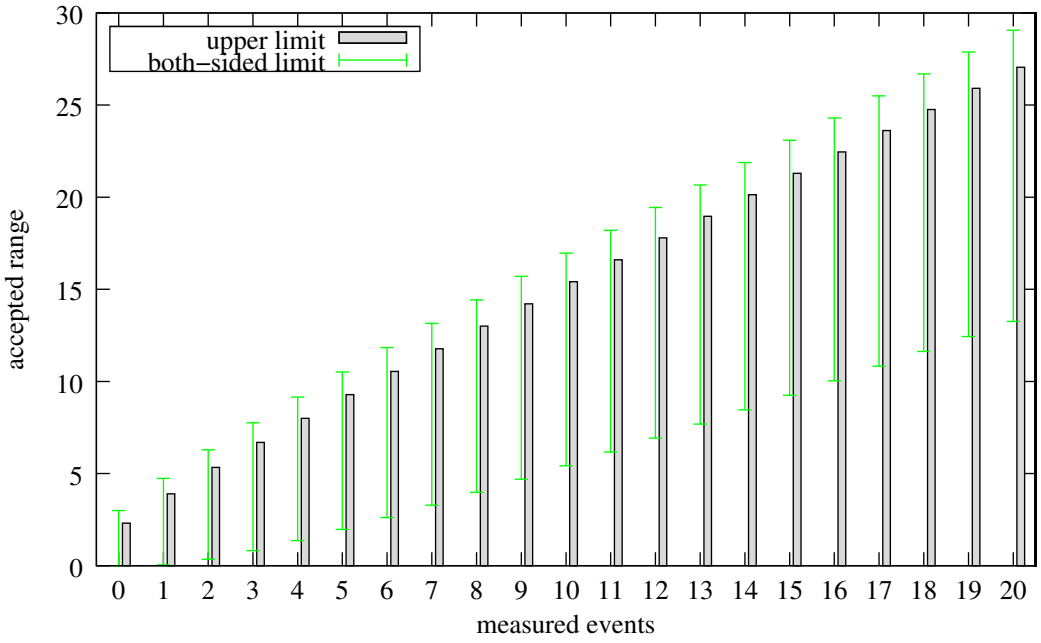

Figure 10.2: Values from Tab 10.1 in a graphical illustration. If the measured events are sure to be only signal, it is advisable to switch above three measured events to a both–sided limit in the case of a Confidence Level (CL) of 90 %, if one want to select the smallest range of resulting values. With this criterion the result has always the minimal possible uncertainty in the light of absolute values. Only if a criterion like this for switching from one– to both–sided limit is predefined the value of CL is exact [72].

measured events	event rate			range
	90% CL	95% lower CL	95% upper CL	both–sided limit with 90% CL (col4-col3)
0	2.302	0	2.995	2.995
1	3.889	0.051	4.743	4.692
2	5.322	0.355	6.295	5.940
3	6.680	0.817	7.753	6.936
4	7.993	1.366	9.153	7.787
5	9.274	1.970	10.513	8.543
6	10.532	2.613	11.842	9.229
7	11.770	3.285	13.148	9.863
8	12.994	3.980	14.434	10.454
9	14.205	4.695	15.705	11.010
10	15.406	5.425	16.962	11.537
11	16.598	6.169	18.207	12.038
12	17.781	6.924	19.442	12.518
13	18.957	7.689	20.668	12.979
14	20.128	8.463	21.886	13.423
15	21.292	9.246	23.097	13.851
16	22.451	10.035	24.301	14.266
17	23.606	10.832	25.499	14.667
18	24.756	11.634	26.691	15.057
19	25.902	12.441	27.879	15.438
20	27.045	13.254	29.062	15.808

Table 10.1: This table displays the excluded count rate for the 90 % Confidence Level (CL) for the Poisson distribution for different measured event numbers. Table was built with the $poi\_List(20)$ command from App. G.2.2

for the experimental result. A criterion for the point of change is given in the paper of Feldman and Cousins [72]. They solve that problem for the case of a known background rate. In Dark Matter search the background rate is not known and therefore this method cannot be applied.

As you see in Tab. 10.1 the one–sided upper limit is always slightly lower than the upper side of a both–sided limit with the same CL. The difference is that the one–sided upper limit approximately grows linear with the measured counts as one side is per definition fixed to zero. The allowed range of a both–sided limit grows only with the square–root of the measured counts. The range above three measured counts gets smaller than the allowed range from the upper limit due to the rising lower limit (see Fig. 10.2).

The Poisson method only takes the number of events and not their distribution. One might have additional information of the expectation of the event distribution in time or energy. With this additional information, for example from the energy spectrum of chapter 9, one could decide by the spectral distribution weather it is more likely to be background or signal.

10.2 Erlang Distribution

The Erlang distribution gives the probability that Poisson distributed events with the event rate λ produce k events within the time t. In data analysis it is used to find an optimized upper limit to the count rate. The additional information about the time distribution is used. For example, if in a year long data taking period there are two events in the last minute (and no events at other times), one can calculate the probability for the empty period (one year minus one minute). This is only slightly higher than the limit for one whole empty year, but much lower than the limit for one whole year with two events. The slight worsening to higher limits is mainly due to the correct statistical treatment of choosing the "optimal" measuring period (see Sec. 11.3).

With the formula for the Erlang distribution one can determine the probability of k events within the time period t with an event rate of λ:

$$Erl(t; k, \lambda) = \frac{\gamma(k, \lambda t)}{\Gamma(k)}$$

where $\Gamma(k)$ is the gamma function (for integers equal to the factorial) and $\gamma(k, \lambda t)$ corresponds to the incomplete gamma function:

$$\gamma(k, \lambda t) = \int_0^{\lambda t} x^{k-1}\, e^{-x}\, dx$$

In Fig. 10.3 the Erlang distribution is shown for the example of $\lambda = 1$. The plot is done for $k = 1, 2, 5$. The Erlang distribution predicts, when the first or any other event should happen. A deviation from that behavour can be quantified. Usage of this knowledge leads to an improvement of an analysis, which relies only on the total count number and uses the Poisson method.

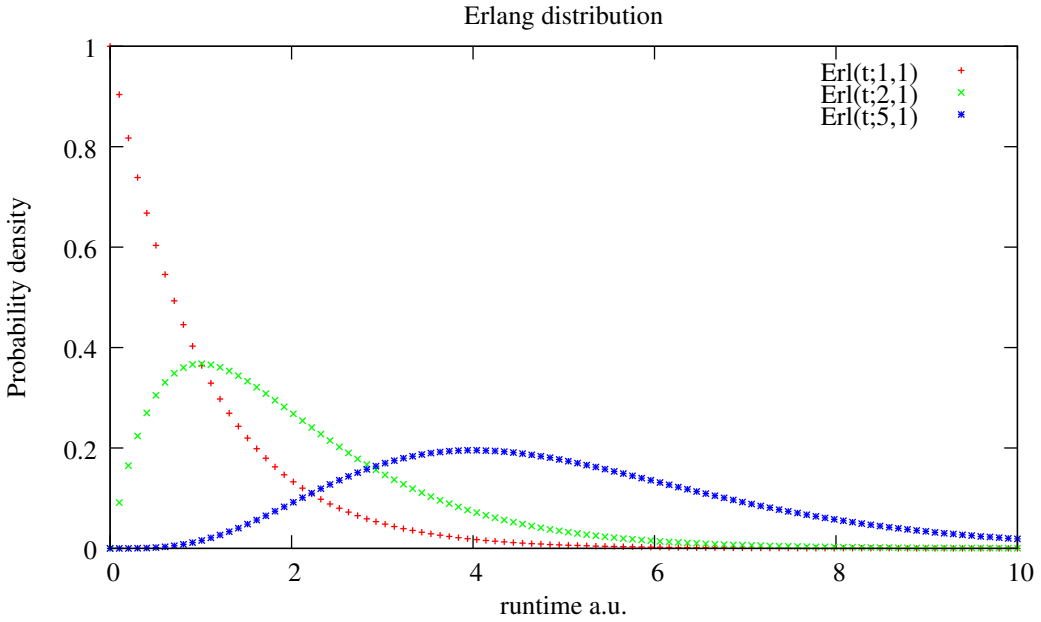

Figure 10.3: Examples of the probability density distributions for different measured event numbers. For the case of $k = 1$, the first measured event, the probability density function is identical to a exponential function. The second event can only happen after the first, so for the start at $t = 0$ the probability density is also zero.

In Fig. 10.4 the probability of measuring k counts is plotted for $k = 0$, 1, 2 over time t. This total probability is the integral of the probability density function of Fig. 10.3. For $t = 1$ the upper limit of the count rate is identical to the Poisson result. The advantage of using the Erlang distribution is that the probability of intermediate states (like two counts in the last minute of a year measuring time) can be calculated[2]. In this way every kind of background with spectral properties different to the expectation in respect to the variable t will have less impact onto the upper limit.

All values for the variable t have to be equally probable to apply the

[2]To a good approximation the result would be in our example the mean value λ which fulfills the $CL = 90\%$ criterion for the slightly shorter time. For a correct calculation one has to follow the steps of Sec. 11.3.

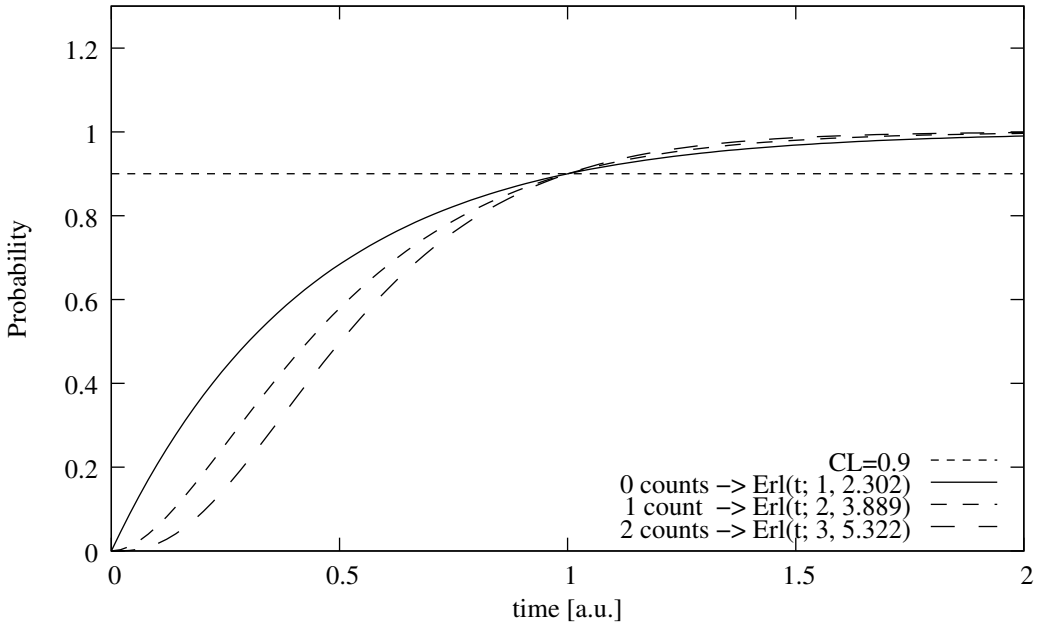

Figure 10.4: Examples of the probability distribution for different measured event numbers. At the time equal to one, the Erlang limit is identical to the Poisson limit from the previous section. The difference is that the Erlang limit can account for the distribution of the events. With the Poisson method the calculated count rate is only affected by the total count number.

Erlang method. This property is easily fulfilled for the time. If one wants to use it for another variable y where the values are not equally likely one can rescale to another variable y' according to their probability distribution. All values of y' have to be then equally likely. Then the Erlang distribution holds also for that new variable y'. For example from chapter 9 about the expected WIMP signal the energy spectrum is known and one can rescale to a "new" energy variable E'_R such that the spectrum in this variable is flat. The details of the rescaling procedure is topic of section 11.1.

The principle of using additional information for the upper limit calculation, like the Erlang method does, is also the idea in the next chapter. As the determination of the upper limit value with this method gets more complex, an analytial calculation is not possible any longer. The needed calculations will be introduced in the next chapters step by step.

Chapter 11

Yellin Method

The Yellin method [57] is introduced to find the optimum upper limit of experiments which may have a contribution of unknown background. The discrimination is done via the likelihood of a certain gap in the spectrum of the measured data of any parameter. The author of Ref. [57] provides a FORTRAN program for this task. After implementing the "standard" Yellin method in a C++ based software the results of both will be compared. The combination of different experimental results is focused on in the last section.

11.1 Transformation of the Variable

For the universality of a spectrum based method like the Yellin method, the probability distribution of the occurrence of the specified parameter x' should be flat. The values of x' should vary within zero and one. If one investigates the distribution in the time the first condition is usually fulfilled. The second condition is easily obtained by normalizing all times to the duration of the measurement.

If the variable for the limit calculation does not have a flat probability distribution one has to think of a more advanced normalization. The transformation of the variable x with the probability distribution $p(x)$ to the new variable x' with a flat probability distribution is done for a certain x_a by the formula:

$$x'(x_a) = \frac{\int_{x_{low}}^{x_a} p(x)\mathbf{d}x}{\int_{x_{low}}^{x_{high}} p(x)\mathbf{d}x} \tag{11.1}$$

An example for such a transformation is shown in Fig. 11.1 for the energy variable. The probability density function in this case is an assumed WIMP energy recoil spectrum. In the figure the transformation is plotted for two

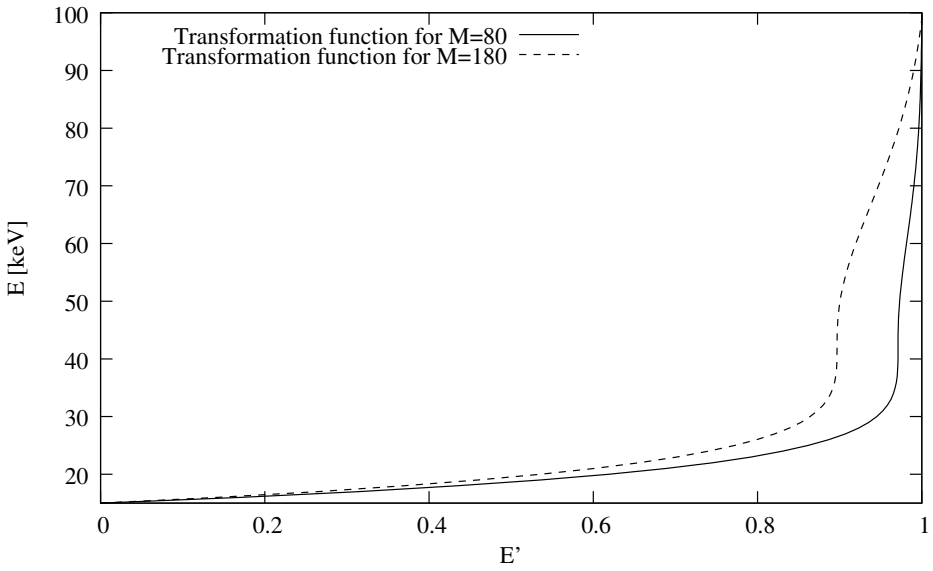

Figure 11.1: Shown are the positions of a 1 keV grid of the recoil Energy E in the new variable E'. The energy spectrum of elastic scattering and an experimental lower energy threshold of 15 keV is assumed. The probability distribution of the transformation is the expected recoil spectrum shown in Fig. 9.3 for the WIMP mass $M_\chi = 80\,\frac{GeV}{c^2}$. The dashed line is the transformation function for $M_\chi = 180\,\frac{GeV}{c^2}$. In the transformation function all physics input is included. Within the normalized new Yellin variable E' only the statistics influences the result of R_{obs} in Eq. 9.11.

WIMP masses. The expectation determines the position of an event in the new variable E'.

In the following it is assumed that the transformation into the new variable x' is already done. Only the statistical method to analyze the event distribution in x' itself will be in the focus. The spectral based statistic check the hypothesis if the event distribution follows $p(x)$. If the measured distribution follows the assumed spectrum $p(x)$, the events then should be homogenously distributed in x'. Any deviation from the homogenous distribution in x' gives information to give a better limit on the occurence of $p(x)$. If the measured distribution and $p(x)$ are different, a lower upper limit can be obtained with the Poisson method. A good performance of a statistical method is therefore stated in this work, if a method results on average in a lower limit. Then the optimum advantage of the spectral information is gained.

11.2 Maximum Gap Method

The maximum gap method of Yellin is a natural way of implementing a spectrum based upper limit calculation: The largest gap in an experimental result is compared to the probability such a large gap appearing in the expectation. These probabilities can be calculated by simulations. To simplify the understanding, this section will lead to the construction of a lookup table for the upper limit value in dependence of the largest empty gap of a measurement. The intermediate results of the computer simulations will be discussed in detail as the maximum gap method is the basis of the methods later discussed.

11.2.1 Largest Gap Spectra

To formulate an expectation for the occurrence of a certain largest gap it is necessary to simulate experiments, so–called Monte Carlo (MC) studies. A single experiment consists of N counts. The events are distributed homogeneously in the whole parameter space, which can always be achieved with a transformation $y \to y'$ following the rules of the previous section. The largest empty gap for every experiment is calculated. The distribution of the largest gaps with zero containing counts in an experiment with N measured counts is stored in a histogram. Such a histogram of the gap distribution is called LG^0_N. The index "0" refers to the zero events in the gap. The index N refers to the total number count number N in each single experiment.

The spectra LG^0_N are histograms of the largest gap containing zero counts, called $\Delta x'_0$. For each integer N the spectra have to be calculated. In this work they are calculated via MC and up to $N = 100$. Some examples are shown in Fig. 11.2. The minimal possible value $\Delta x'_{0,\,min}$ in LG^0_N is $\Delta x'_{0,\,min} = \dfrac{1}{N+1}$ and corresponds to an equidistant event distribution. All entries in LG^0_0 are exact one as the empty gap is always the whole range of the interval from zero to one.

The $LG^0_1(\Delta x'_0)$ histogram is exactly a step function. If there is one count, either the gap on the right or on the left of the event is the largest empty gap of the experiment. It depends on the position of the count. Is it smaller than $x' = 0.5$ the largest gap is on its right side and vice versa. The position distribution of the counts is by construction homogeneous. Because of these two properties together the LG^0_1 is equal to the mentioned step function with the step at $\Delta x'_0 = 0.5$.

For values of $N \geq 3$ the shape of the probability distribution of the largest gap remains similar. The maximum shifts to lower values of $\Delta x'_0$

and the distribution becomes narrower. This trend could be used to save the calculation time for MCs while extending the Yellin method for limit calculations of experiments with high count rates. However, in this work all LG-Spectra are obtained with MC studies.

11.2.2 Gap Distribution for a known True Value

In a comparison of a measurement to an expectation one has to take into account that even a fixed given value for the average rate, called True Value Λ, leads to a variation of the number of measured counts for different experiments. The probability for the realization of a certain count number k is described by the Poisson distribution of Sec. 10.1.

To obtain the gap distribution $GD^0(\Lambda_{ass},\, \Delta x'_0)$ of the largest empty gap $\Delta x'_0$ for a assumed True Value Λ_{ass}, one has to add up all relevant spectra LG^0_N accordingly. The different LG^0_N spectra have to be weighted with the probability of their occurrence. Therefore the formula of the spectrum $GD^0(\Lambda_{ass},\, \Delta x'_0)$ can be written as:

$$GD^0(\Lambda_{ass},\, \Delta x'_0) = \sum_{i=0}^{N_{max}} Poi(i, \Lambda_{ass}) LG^0_i(\Delta x'_0) \tag{11.2}$$

The weighting factors in case of $GD^0(3.0)$ are shown in Tab. 11.1 to illustrate the procedure. N_{max} in principal is infinity. But as N and Λ_{ass} are very different, the weight gets very low. So one can ignore all N for which

$$Poi(N, \Lambda_{ass}) < \epsilon \tag{11.3}$$

Here ϵ is chosen to be 0.0001, because the influence of other spectra is negligible. The sum over all included Poisson probability functions is this way greater than 0.9990. In the worst case sum spectrum GD contains one per mill less events than the corresponding LGs. This condition defines a N_{max} being the highest value of N with $Poi(N, \Lambda_{ass}) > \epsilon = 0.0001$.

In the previous section the LG^0_N are calculated up to $N = 100$. This limits the calculation of the $GD^0(\Lambda_{ass},\, \Delta x'_0)$ to values of $\Lambda_{ass} \leq 70.1$. Because in the sum needed for $GD^0(70.2,\, \Delta x'_0)$ the $LG^0_{101}(\Delta x'_0)$ would has to be included as $Poi(101, 70.2) = 0.000104 > 0.0001$. All calculations in this work stop for this reason at a value of $\Lambda = 70.0$.

In the rest of this work the parameter $\Delta x'_0$ is not explicitly mentioned in the gap distribution functions $GD^0(\Lambda_{ass},\, \Delta x'_0)$ and $LG^0_N(\Delta x'_0)$. For better readability the shorter implicit definitions $GD^0(\Lambda_{ass})$ and LG^0_N will be used instead. Λ_{ass} is from here on simply called Λ.

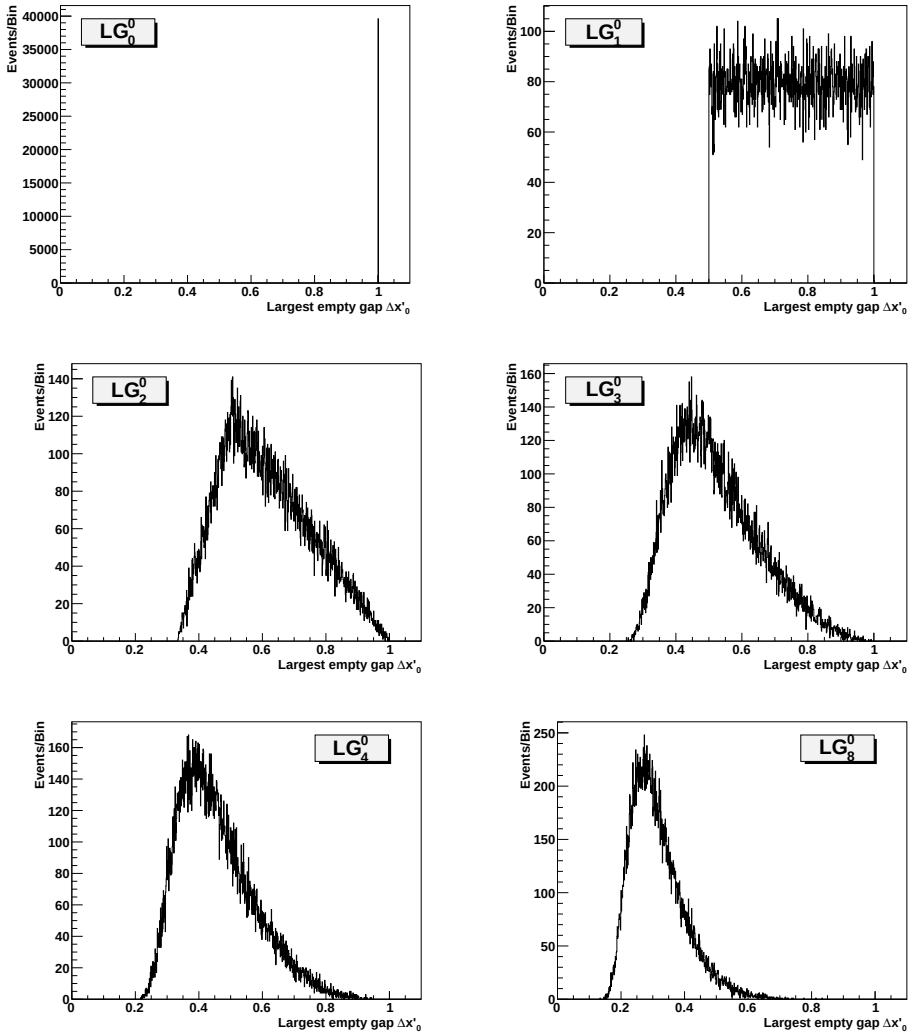

Figure 11.2: Examples of simulated "Largest Gap"–Spectra $LG_N^0(\Delta x_0')$ with zero events in the gap and N from zero to four and $N = 8$. The lowest entry always occurs in the case the events are distributed homogeneously. The spectrum for N events has therefore the lowest entry at $\Delta x_0' = \dfrac{1}{N+1}$. Above $N = 3$ the spectral shape remains similar, but the maximum occurs a lower values and the spread of the distribution becomes smaller.

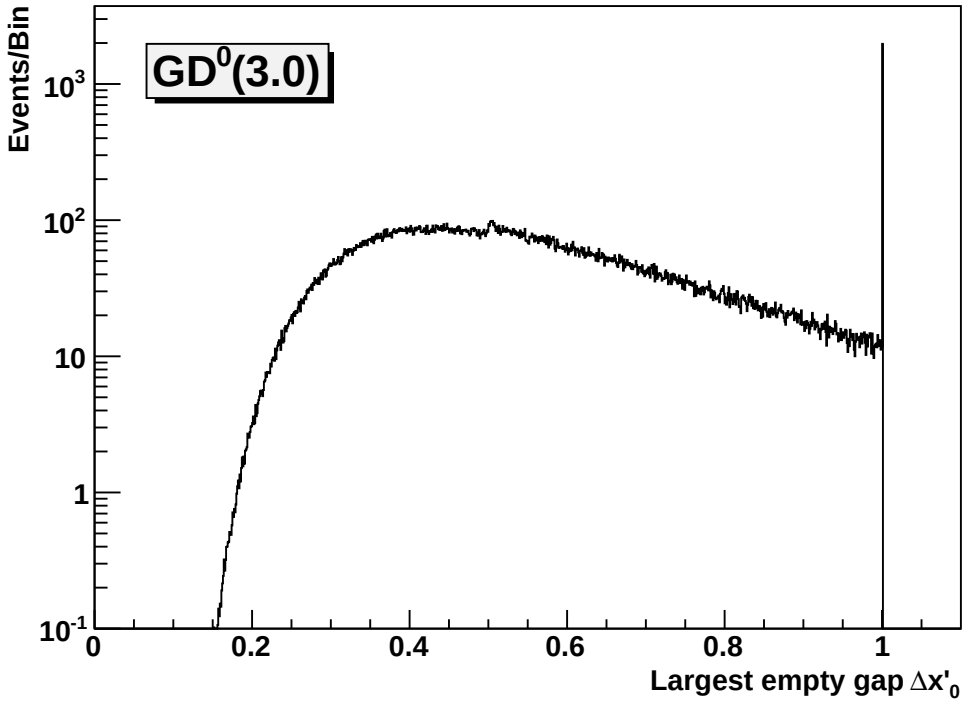

Figure 11.3: Spectrum of the gap distribution in the case of $\Lambda = 3.0$ is shown on a logarithmic scale. The spectrum is the sum of different LG^0 spectra which are added together. The single spectra are weighted according to the values of Tab. 11.1. The feature of $GD^0(3.0)$ at the position of $\Delta x'_0 = 0.5$ is for example due to the contribution of the step function LG^0_1, the peak at $\Delta x'_0 = 1$ due to LG^0_0.

N	$Poi(N, 3.0)$	$\sum_N Poi(N, 3.0)$
0	0.04979	0.04979
1	0.14936	0.19915
2	0.22404	0.42319
3	0.22404	0.64723
4	0.16803	0.81526
5	0.10082	0.91608
6	0.05041	0.96649
7	0.02160	0.98810
8	0.00810	0.99620
9	0.00270	0.99890
10	0.00081	0.99971
11	0.00022	0.99993

Table 11.1: The weighting factors in case of $\Lambda = 3.0$ are shown. In the third column the sum over all factors of column two are displayed. The sum at the end is 0.99993 meaning that the contribution of the other, not included spectra, is negligible.

11.2.3 Confidence Level and Lookup Table

The knowledge of the gap distribution $GD^0(\Lambda)$ allows the comparison of a measurement with the simulated expectation. The fraction of the $GD^0(\Lambda)$ distribution with a smaller $\Delta x'_0$ than the measurement is the confidence level (CL) for a certain Λ. In that sense, the confidence level is a function $CL(\Lambda, \Delta x'_0)$ of Λ and $\Delta x'_0$.

In data analysis the problem is turned around: The CL is fixed, in Dark Matter search experiments to $CL = 90\,\%$, and the $\Delta x'_0$ is measured. So one has to find the corresponding Λ. Therefore the function $\Delta x'_{0,\,CL=0.9}(\Lambda)$ is calculated.

For every $\Lambda < 70$ the $\Delta x'_0$ with $CL = 0.9$ is found by integrating the $GD^0(\Lambda)$ numerically from zero to $\Delta x'_{0,\,CL=0.9}$. This step is shown schematically in Fig. 11.4. The position[1] of $x'_{CL=0.9}$ is marked with a red line in the spectra $GD^0(5.0)$, $GD^0(4.0)$, $GD^0(3.0)$ and $GD^0(2.3)$. This correlation between Λ and $\Delta x'_{0,\,CL=0.9}$ is noted in a lookup table $LT^0_{CL=0.9}(\Delta x'_{0,\,CL=0.9})$.

The lookup table LT^0 includes all relevant information for a data analysis.

[1]Formally the position is defined by an integral equation:

$$0.9 = \int_0^{x'_{0,\,CL=0.9}} GD^0(\Lambda,\, \Delta x'_0)\, \mathbf{d}\Delta x'_0 \tag{11.4}$$

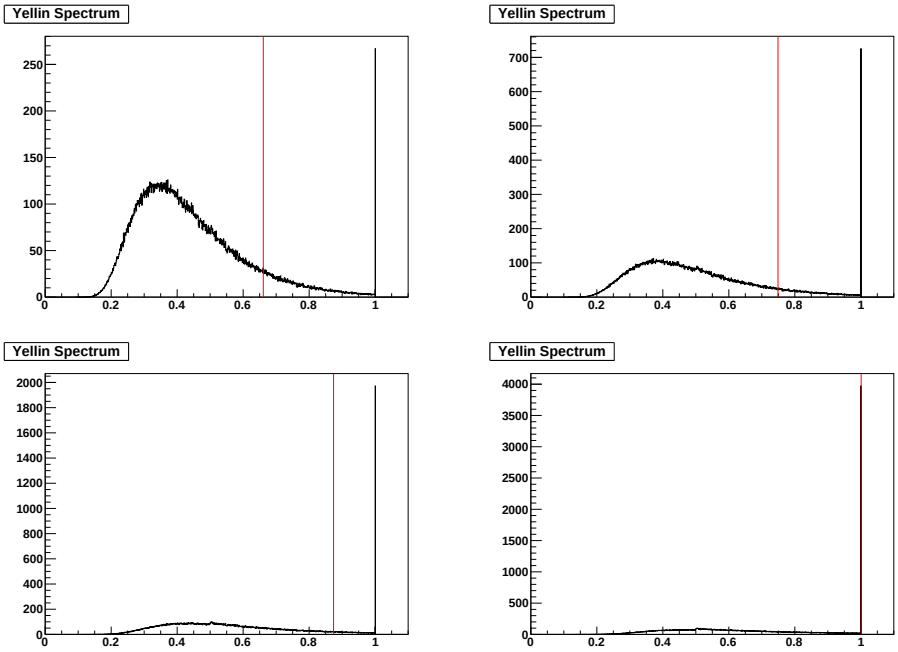

Figure 11.4: Example spectra of the gap distribution of the True Values Λ of $5.0, 4.0, 3.0$ and 2.3 are plotted. At the position where $90\,\%$ of the gaps are smaller than $\Delta x'_0$, a red line is displayed. This correlation between Λ and $\Delta x'_0$ is used in the limit calculation.

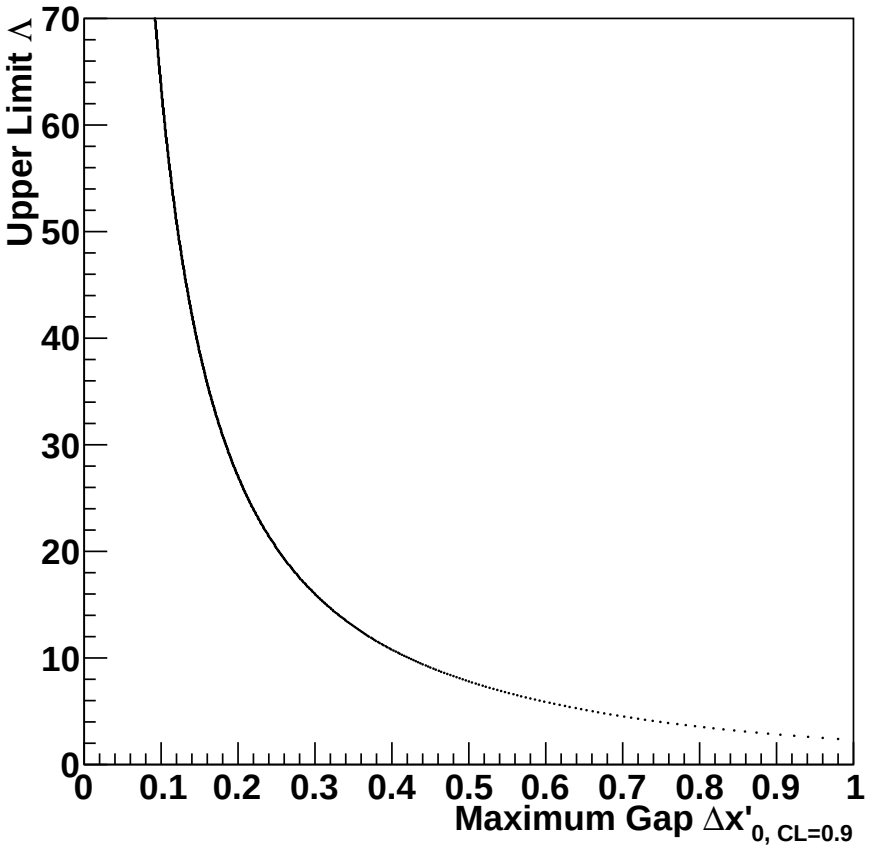

Figure 11.5: The lookup table $LT^0_{CL=0.9}(\Delta x'_{0,\,CL=0.9})$ is plotted. It is obtained by the integration over the $GD^0(\Lambda)$ as it is shown in Fig. 11.4. The position of the red line marks the relevant $\Delta x'_{0,\,CL=0.9}$ there.

After selecting the largest empty gap $\Delta x'_0$ in the measurement of the variable x' the upper limit with 90 % CL can be read. A penalty for the a posteriori selection process of the "best" range $\Delta x'_0$ is automatically included. The achieved upper limit value Λ is the correct final result result. As it is a limit to the count number, it has to be devided through the whole measurement time to get the observed rate R_{obs}. The limit of $\Delta x'_0 = 1$ is exactly the Poisson limit for zero counts: $\Lambda = 2.3$. This behavior gives confidence in the Yellin method.

11.3 Optimum Gap Method

Besides the mentioned advantages, the maximum gap method has a big disadvantage: There are event constellations, where the maximum gap method performs badly. For example in the case of two equidistant events ($x'_1 = 0.33$ and $x'_2 = 0.66$). The limit calculated with the maximum gap method is $\Lambda_{MG} = 14.1$. The Poisson limit $\Lambda_{Poi} = 5.32$ is much lower. One would tend to use the better method, which is however a not allowed a posteriori decision. To avoid this the "optimum gap" method is introduced: All maximum gaps containing j counts are analyzed and not only the maximum empty gap with $j = 0$. The method with this choosing of the number of counts in the gap is called the optimum gap method. It introduces a mechanism for a guaranteed upper limit performance at least as good as the Poisson limit.

11.3.1 Calculation of the Spectra

To formulate the expectation of the occurrence of a certain gap with j containing counts, MC simulations have to be done. Similar to the case of $j = 0$, which is identical to the maximum gap method, all spectra LG_i^j are to be calculated. For $j \geq i$ the entries $\Delta x'_j$ in LG_i^j are always one. The value $\Delta x'_j = 1$ is the maximum of $\Delta x'_j$ and can never be lower for $j \geq i$. All spectra of that kind are identical to LG_0^0, displayed in Fig. 11.2.

The simulation done in this work, analyzed a MC experiment with i counts for all $j < i$ simultaneously. An increase of the time for MC simulations could therefore be kept small, compared to the maximum gap method. This procedure in principle could lead to a statistical dependence of the different spectra. But this dependence is negligible for the large number of simulated experiments here.

The gap distribution $GD^j(\Lambda)$ for a certain assumed value of Λ can be calculated again by the Eq. 11.2. The pre–factors are independent of the chosen j and such are always identical to the ones for the maximum gap method. With the knowledge of the $GD^j(\Lambda)$ the lookup tables LT^j can be achieved according to section 11.2.3.

11.3.2 Choosing the Optimum LT Branch

The procedure of the previous section leads to the individual lookup tables $LT^j(\Delta x'_j)$ for a certain value for the allowed counts in a gap j. The result is displayed in Fig. 11.6. Each branch corresponds to a j. The value of LT^j at the position of $\Delta x'_j = 1$ is again the Poisson upper limit for j counts.

Now one checks for a measurement with given $\Delta x'_{measured}$, which value of j results in the lowest upper limit Λ_{best}, which is the minimum of $LT^j(\Delta x'_{j,\,CL=0.9} = \Delta x'_{measured})$ for all values of j. For the example of two equidistant events the corresponding limits are shown in Fig. 11.6. The lowest value is reached for $j = 2$. The result for $\Delta x'_2 = 1$ corresponds to the Poisson upper limit for two counts, which is expected, since an equidistant distribution indicates that the assumed $p(x)$ is realized in the measurement. This automatic choice removes the disadvantage of the maximum gap method in automatically leading to the Poisson limit, in case it is best. However, there is still an a posteriori choice of the best branch. This choice has to be compensated by a certain penalty, which is the topic of the next section.

11.3.3 Calculation of the Correct CL_{Single} Function

Each of the LT branches of Fig. 11.6 are calculated with 90 % CL. The optimum gap method like it is introduced at the moment allows a free choice of the optimum LT^j branch. One can imagine that a penalty has to be taken into account for this selection process. The combined CL of the method as a whole has not to be the same than the CL_{single} of the single LT^j branches.

A simple example for the higher CL_{single} is the connection of three ropes with two knots. If the single knot would have a probability of 90 % to hold, then the combination of the ropes would have only 81 %. The probability of a single knot corresponds to CL_{single}, the probability of the whole rope to CL. The single knot has to have a stability probability of about 94.9 % that the rope is to 90 % "secure". In a Yellin like method the right CL_{single} has to be determined via computer simulations.

The correct CL_{single} value is a function of the assumed Λ. This parameter determines how many branches are possible to choose from. A large number of MC simulations have to be performed for each value of Λ to calculate the fraction of experiments, where the calculated upper limit is greater or equal as the assumed value of Λ. This fraction is by definition the confidence level CL_{real} for the upper limit calculation. Due to the a posteriori choice of the best branch of the Yellin method CL_{real} can be lower than $CL_{single} = 90\,\%$. The value of CL_{single} was used for the calculation of the lookup tables. The calculation of CL_{real} is now repeated with a higher CL_{single}. For any new value of CL_{single} the lookup tables LT^j have to be recalculated. The step width taken in this work is $\Delta CL_{single} = 0.2\,\%$. If CL_{real} reaches 90 % the right value of CL_{single} for this individual Λ is found.

Practically this step was done in this work by calculating all possible $LT^j_{CL_{single}}(\Lambda)$ in a first step. In the second step 100 000 MC experiments with homogeneously distributed events are done and analyzed. The count number

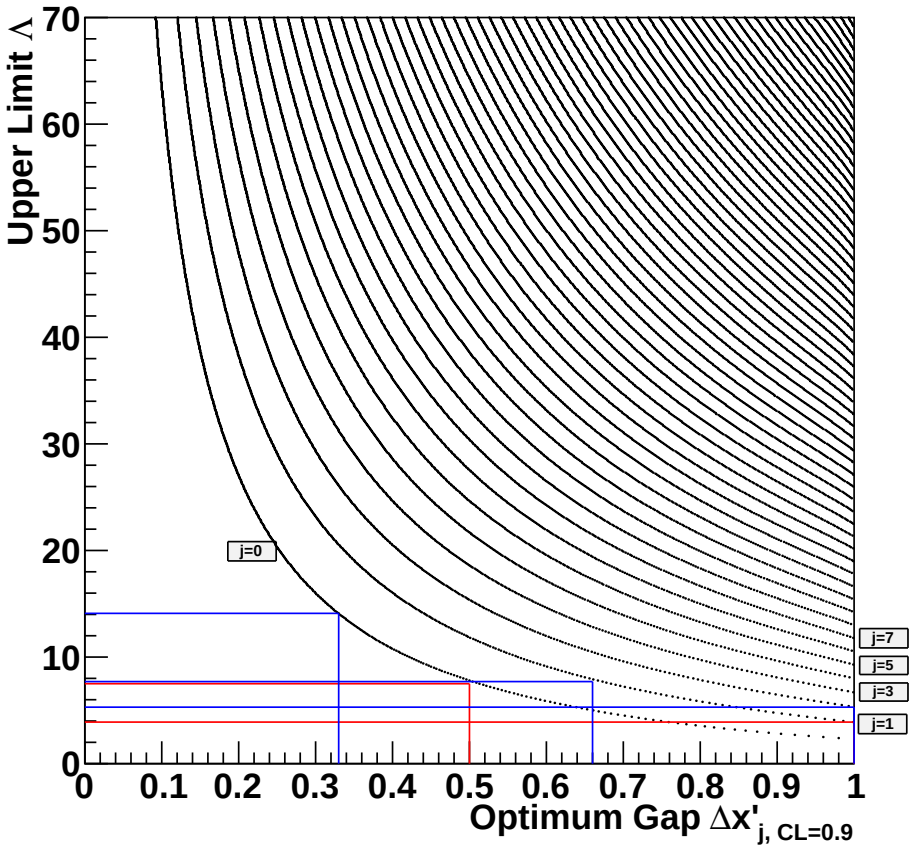

Figure 11.6: Here the same plot as in Fig. 11.5 is shown, but the calculation is now made not only for the maximum gap with zero counts in its range, but also for some counts therein. One can see for example a result with one count in the middle (red) of its measurement range would have a better upper limit value, if it takes the largest gap with one count therein. In this example that would be identical to the Poisson limit for one count. The similar scenario for two equidistant events is plotted in blue.

in a single experiment follows a Poisson distribution around the value of Λ. The value of Λ was increased in steps of 0.1 for a constant CL_{single} until the CL_{real} drops below 88 %. Then Λ was set to a value where CL_{real} was the last time equal or bigger than 91 %. At the beginning of the calculation, where $CL_{single} \leq 0.91$, the value of Λ is always set again to its start value of 2.3. For all values of Λ one obtains such at least two values of CL_{single}. One result has $CL_{real} > 0.9$ and one $CL_{real} < 0.9$. It was linearly interpolated between the two values of the corresponding CL_{single} to obtain the final value for CL_{single}, where $CL_{real} = 0.9$.

The function of CL_{single} over Λ is displayed in Fig. 11.7. Up to a value of $\Lambda = 3.9$, there is no choice for the LT^j branch, as only LT^0 has Λ values below it. As a consequence the CL_{single} is exactly 0.9. Strictly speaking the function is not defined below $\Lambda = 2.3$, the end point of the LT^0 branch, as there is no LT branch at all. $\Lambda = 2.3$ is the $CL = 0.9$ Poisson limit, if 0 counts are measured.

11.3.4 Final Optimum Gap Method LT

The CL_{single} function has to be accounted for in the individual LT^j. The lookup tables are now calculated with the correct CL_{single} for each different upper limit Λ. The result of this procedure is displayed in Fig. 11.8. For an easy comparison the $LT^0_{CL=0.9}$ of the maximum gap method is also shown in red. The LT^j_{opt} are shifted commonly to higher upper limit values, which is the penalty for the choice of the optimum j. On the positions of the steep increases of LT^j_{opt} the $CL_{single}(\Lambda)$ function has its step positions.

The shifted LT^j_{opt} leads also to higher fallback values in the optimum gap method compared to the Poisson method. Due to the allowed selection of the optimal gap j the CL_{single} is in general higher than 90 %. The Poisson limit is always calculated with $CL = 90\,\%$. This small performance loss is unavoidable and is the price for the choice of the optimum interval.

With the lookup table the upper limit determination for the optimum gap method can be done in four steps:

- Rescale the physical unit of the measurement to the normalized space with flat probability density function via an expected spectrum.
- Calculate for all integer j lower or equal the measured count number the largest gap $\Delta x'_j$ of the measurement.
- Lookup the upper limit value Λ_j for the corresponding gap on the $LT^j(\Delta x'_j)$ branch of Fig. 11.8.

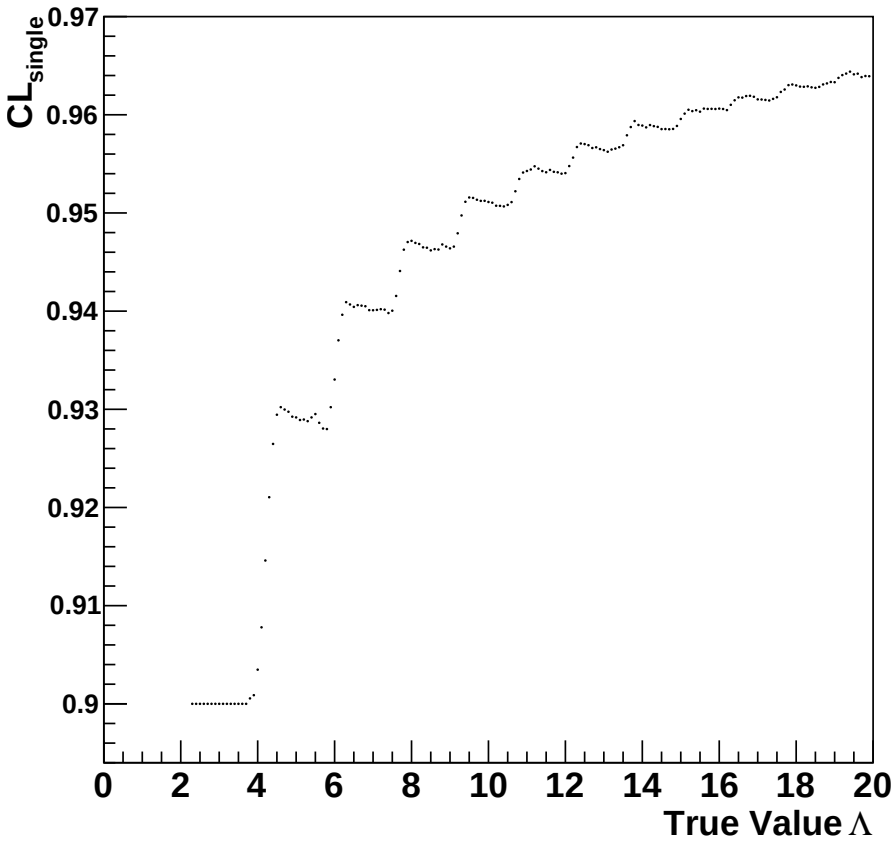

Figure 11.7: The function of CL_{single} over the value of Λ is shown. The function increases quickly at the positions of the True Value Λ where a new branch LT^j can be chosen. Below $\Lambda = 2.3$ the function is not defined.

- Select the lowest Λ_j as the final upper limit.

All described steps of the optimum gap method, starting from the calculation of the LG_j^i spectra to the selection of the best Λ_j value from an array of experimentally found largest gaps can be done with the software provided in App. G.2.2. The next section will compare the implementation of the optimum gap method of this work with the one provided in Ref. [57].

11.3.5 Software Check

The implementation of the 1D Yellin method presented in this work is now checked by the original FORTRAN–Software of Ref. [57]. There are 5000 MC experiments done and then analyzed with both software implementations. The result of of the upper limit of the simulated experiments with a True Value of $\Lambda = 5.0$ is summarized in Tab. 11.2. The average upper limit value as well as the RMS of the value spread are very consistent. But if one compares not only the average of the 5000 experiments but one compares them individually a tiny difference is obvious as Fig. 11.9 reveals: Upper limit values of both methods, which are very close to the steps in the CL_{single} function differ up to 0.6 units in Λ. This behavior can be understood by the way the CL_{single} function is calculated. In Ref. [57] some critical True Values are chosen and the CL_{single} value is calculated exactly there. True Values in between are interpolated linearly. The approach of the implementation in this work is to really calculate all CL_{single} values individually for each position of Λ. Therefore small differences between Ref. [57] and this work in the CL_{single} functions occur. They are responsible for the different results close to the steep increases of the CL_{single} function. As the behavior of the CL_{single} function is not intuitive, the ansatz of this work seems to be more conservative.

After the good agreement of both implementations could be proven, the newly developed implementation will be used to further develop the limit calculation method beyond what is known in literature.

11.4 Combining different Results

In the field of Dark Matter Search it is important to have multiple experiments to crosscheck the results. However, the technical realizations of the combination of different results within the Yellin method is problematic. Every experiment has a measured (energy) spectrum. The critical issue is the order of the variable transformation and the adding of the different results. Or in other words, if one adds the different results in a parameter space normalized

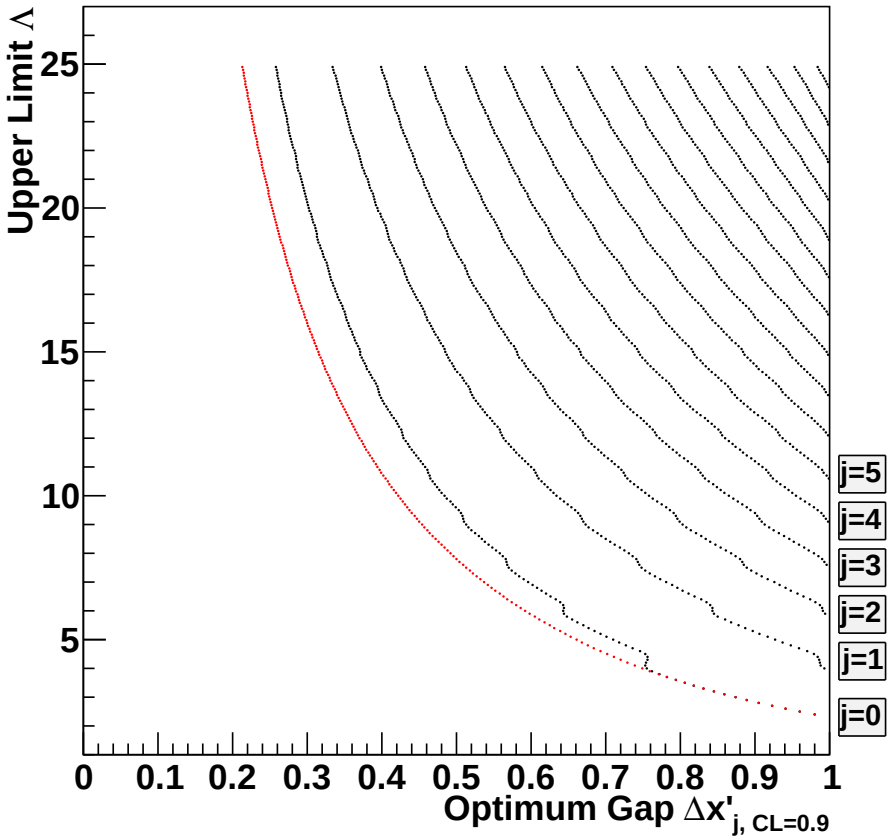

Figure 11.8: A comparison between the maximum (red) and the optimum (black) gap method. The possibility of choosing the optimal gap has to be accounted via a higher probability in the confidence level CL_{single}. This circumstance explains the difference between the red and the lowest black $j = 0$ exclusion line. With the help of this lookup "table" the upper limit to a experiment can easily be obtained for an experiment with a given set of $\Delta x'_j$. All issues like for example the CL_{single} function are accounted for. One has just to compare the upper limit values for all possible j and select among them the lowest value Λ_j.

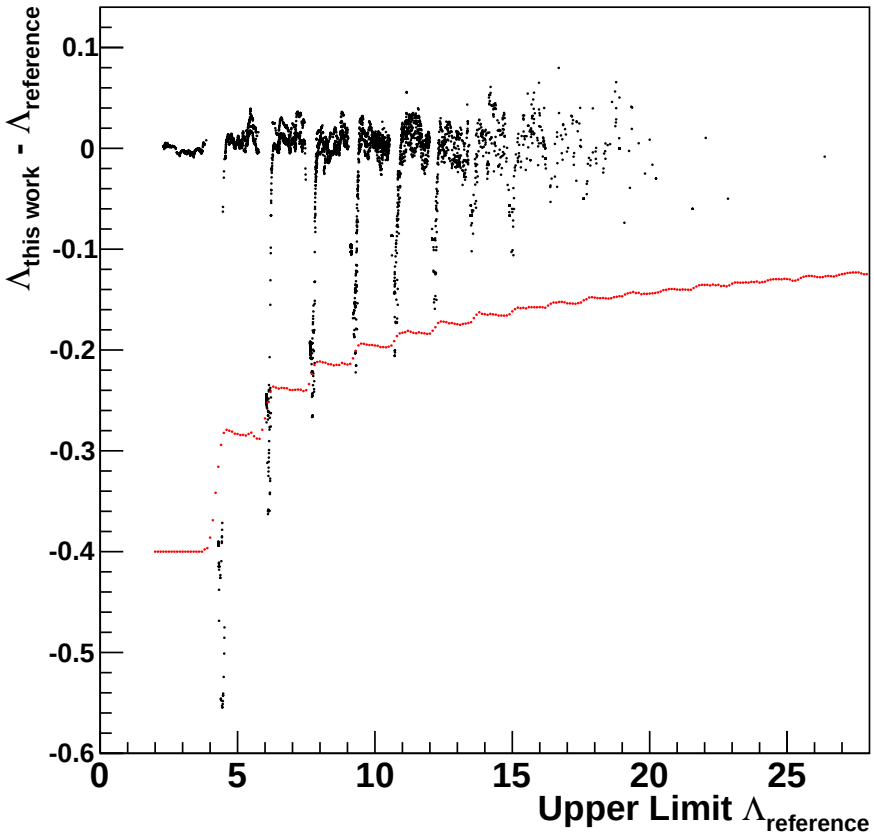

Figure 11.9: The difference (black) of the upper limit values of the original software of Ref. [57] and of this thesis are directly compared on a individual basis for all 5000 MC experiments. Over a wide range the results agree within 0.05 units for the upper limit value. At certain values for the resulting upper limit the difference becomes wider. These positions are identical to the positions where a step in the CL_{single} function (red line, arbitrary units) occurs. The two implementations of the optimum gap method would further converge, if the same CL_{single} function would be used. In Ref. [57] a linear interpolation between the minimum and the maximum of a step in the CL_{single} function is used, whereas the CL_{single} function in this work was calculated with the help of MC on all positions directly. Therefore they can be assumed to be more accurate.

Method	Average	RMS
This work	9.15	3.40
Ref.[57]	9.20	3.38

Table 11.2: The result of the calculated upper limit value of 5000 simulated experiments with a True Value of 5.0. On average the software of Yellin [57] provides a little bit worse limit values. This can be explained with the different determination of the CL_{single} function. But altogether the limit values are in good agreement, as one can see on the event–by–event analysis of Fig. 11.9.

to one or in the physical units. Each order has obvious advantages, which will be highlighted in the following discussion.

The most natural ansatz, if there are two similar experiments, seems to be the summarizing of the measured spectra in the physical units, e.g. the energy scale. After that one transforms them together in the normalized Yellin variable for further analysis. The situation of different similar experiments can be realized by multiple experiments having the same target nucleus. Strictly speaking it is also realized in every experiment with a modular detector design. Then the different modules have to be added together to obtain a result for the whole experimental setup.

Small individual parameters, like a different data taking time, different module mass or a different lower energy threshold have to be taken into account in the expected sum spectrum for the variable transformation. A physical background at a certain energy range could be suppressed efficiently with this procedure. On the other hand this order is not sufficient of adding results of different target detector materials. For a general solution the revers order is better.

The transformation is made for each individual experiment or experiment detector module first. Then the different experiments are added together in the normalized Yellin variable. This procedure works in every combination of target materials, different detector thresholds or different energy regions. In addition it suppresses the influence of detector effects which are always at the same position of the detector measurement range and not a spesific physical position. Such an effect could be a leakage from electro magnetic background events at the lower energy threshold of the detector in a CRESST–like experiment. The detector measurement times are added together and can be taken as total measurement time for the combined system. This second procedures are favored at the moment by the Dark Matter community due to its flexibility.

Chapter 12

Extension to more Dimensions

The method described in the previous chapter is limited to one single parameter. In Dark Matter Search usually the recoil energy is used for this purpose as the expected spectrum can be modelled in detail. But all direct detection experiments have in addition a discrimination parameter, that indicates the kind of interaction of a event. For CRESST this is the light yield, which indicates if the interaction was electro magnetic or a nuclear recoil. The discrimination is in general dependent on the deposited recoil energy. Due to this dependency one would like to have a method, which can handle the spectral information of two parameters simultaniously.

In this work the Yellin method is extended to 2 dimensions. To extend the one–dimensional Yellin method to a second dimension dedicated computer simulations were done in the framework of this thesis. the extension to a second dimension is not possible by an unique rule. The pendant to a 1D gap, the $\Delta x'$, in 2D can be defined in different ways. Here three well motivated possibilities are introduced. After the definition of the method the same steps as in section 11.3 have to be simulated.

Namely the steps are the calculation of the LG^i_j spectra followed by the determination of the $GD^j(\Lambda)$. Thereafter the calculation of the lookup tables $LT^j_{CL_{single}}$ for all possible values of CL_{single} has to be done. From this array of lookup tables the CL_{single} function is calculated with help of a large number of MC simulations. Finally a lookup table $LT^j_{CL=0.9}$ can be obtained for each possible count number j in the 2D "gap".

All these calculations have to be done for each presented method. The methods differ only in the algorithm how they determine the largest 2D "gap", the so–called optimum area. The performance of the methods in compare in the next chapter.

Before one can apply such a 2D method to a measurement, one has to transform the physical parameters, here x and y, to the normalized space.

This can be done by first rescale x to x' at each y. the distribution of events then depends only on y and not x' as after the transformation they are homogeneously distributed. Then on transfers y t y' as in the 1D case. Therefore the rule of Sec. 11.1 has to be followed to end up with x' and y', the normalized parameter. One can revers the order, i.e. first transform y toy' at each x and then transform x to x'. Both methods lead to a homogenous distribution. This rescaled parameters can be directly compared to the simulated results.

12.1 Best of x and y 1D–limit (B–1D)

For the B–1D method the optimum area is defined by the 1D optimum gap either of the x'– or y'–coordinate. This is obviously an advantage if the events have a large empty 1D–gap in at least one of the coordinates. The B–1D method selects automatically the gap resulting in the lowest limit, independently of the coordinate. So the optimum gap for $j = 0$ included counts can be in the other coordinate than the optimum gap with $j = 1$.

The algorithm for the largest gap search needs only a slight modification: After the search of the largest gap in each coordinate, the values of the largest gap are compared for each possible j. The larger value of $\Delta x'_j$ and $\Delta y'_j$ is stored as final result of this method. However, this changed algorithm for the determination of the largest gap changes the LG^i_j spectra as the probability for the occurrence of different largest gap values changes as you see in Fig. 12.1 in comparison to Fig. 11.2.

The numerical values for the Yellin 1D gaps and the largest area of the B–1D method are the same as the second parameter is always set to one. The two following 2D methods have not this restriction. There the optimum area is selected while finding the combined optimum in both parameters simultaneously.

12.2 Patch Method (P–2D)

In contrast to the previous way for a multi–dimensional extension, the patch method is the most general form of an extension. It was suggested by Yellin [73], but so far there is no implementation.

The algorithm of the P–2D method searches for the largest rectangular patch. A rectangular is limited by a event on a edge or a corner. It also may not leave the maximum parameter space. The maximum parameter space can alway be rescaled to a unit square, analog to the 1D case, so the total

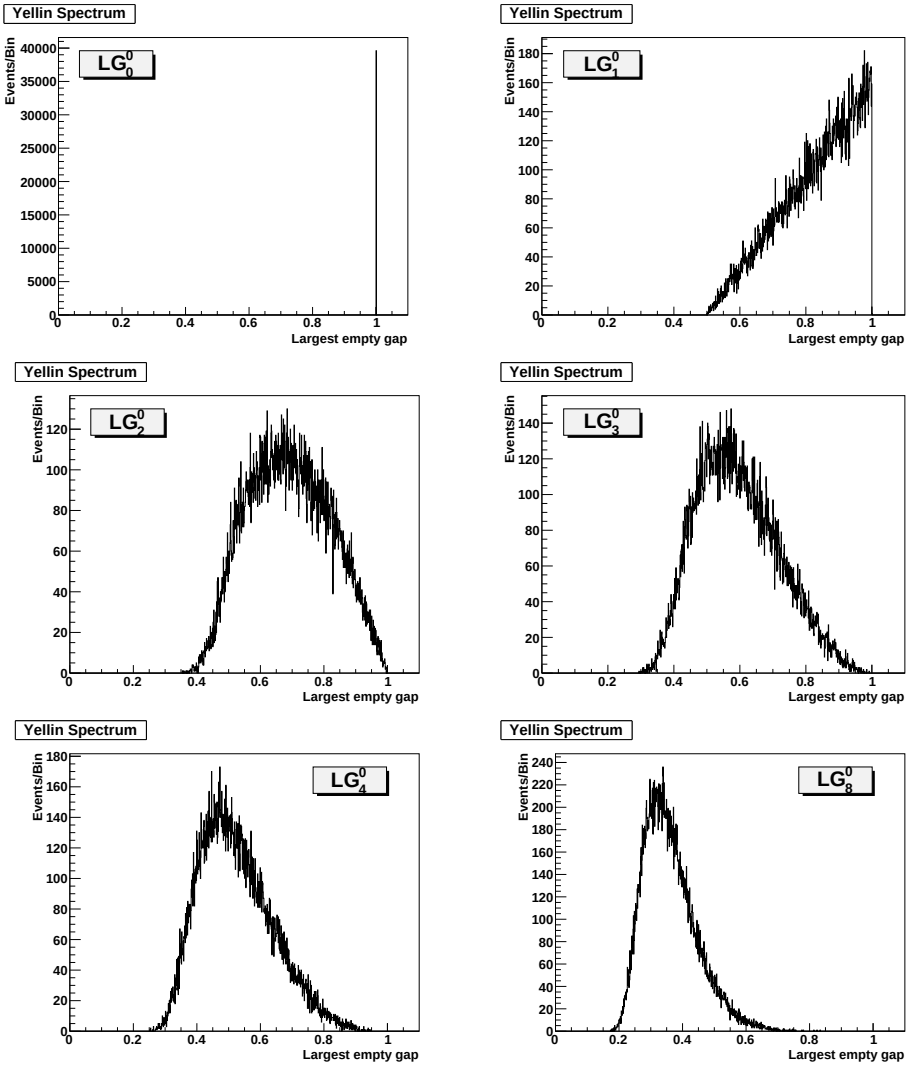

Figure 12.1: The same kinds of the LG^i_jspectra than in Fig. 11.2 are shown for the B–1D method. Due to the change in these spectra the GD spectra also changing and all Lookup tables have to be recalculated with the new CL_{single} function.

area is equal to one. The analogon to the optimum gap $\Delta x'_j$ in 1D is now the optimum area A_j. This number is the input of the LG spectra.

All possible configurations of the rectangle have to be checked in an analysis. This leads to a very extensive maximum patch search for higher count numbers. Every count could in principle limit the x'–parameter on the lower or the higher border as well as the y'–parameter and has to be combined with any other count of the measurement. Such the calculation of th LG spectra take most time of all methods of this work. Once the LG spectra are obtained the next simulation steps are equal complex as in the other methods.

Interestingly the CL_{single} function is rather similar as in the optimum gap method of the 1D case as shown in Fig. 12.2. If this similarity would be taken as criterium for the best extension to a further dimension, the P–2D method would be the optimum choice.

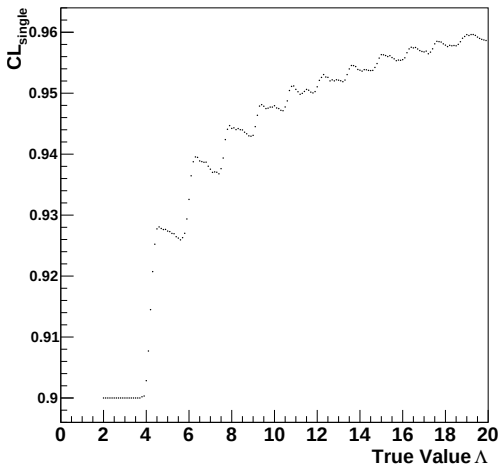

Figure 12.2: The CL_{single} function in the P–2D method is very similar to the 1D one of Fig. 11.7. Its steps are a little bit lower, but the falling behavior of the function until it reaches the next step is remarkably similar. In that sense it is the most natural extension of the 1D Yellin method.

12.3 Corner Method (C–2D)

The C–2D method should be described by a simple algorithm for the selection of the optimum rectangle, which must not always to be the perfect choice in the light of area, like it is done in the P–2D method.

The chosen algorithm searches rectangles like they are defined in a drawing program: Two points in opposite corners define a box there. In our case every event is checked for the area in connection with every other event. The event number contained in the rectangle is also counted. The points at the corner of the total parameter space are included as possible partners. They are needed, for example, in the case of one measured event to define the second corner. In contrast to the P–2D method there is no possibility that a measured event defines the position of the edge of the rectangle.

In the next section there are two examples to illustrate the principle of the both 2D algorithms, P–2D and C–2D.

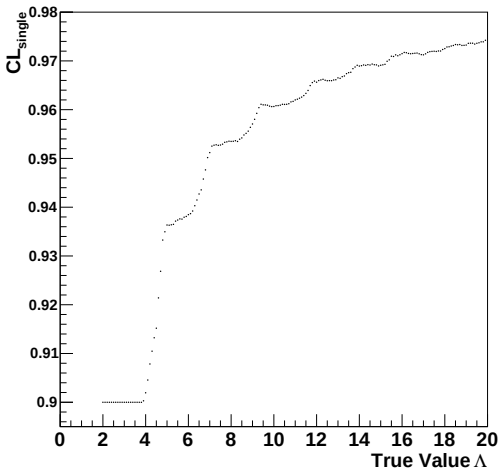

Figure 12.3: The CL_{single} function for the C–2D method has a much steeper rising. The steps at the True Value positions where a new branch can be selected are still there, but they are by far not that dominant like in Fig. 12.2.

12.4 Example events analyzed with P–2D and C–2D

To give a deeper insight into the working principle of the two 2D methods some extreme event cases will be presented in this section. The first one in Fig. 12.4 with 10 measured counts has a huge gap in the y' coordinate and a group of events as well as on the top and on the bottom, each about in the middle of the x' coordinate. It is obvious that the events distribution is very different from the expectation, which after the transformation $y \to y'$ should lead to a homogenious distribution in y'. This adds information to

improve the limit. Here the P–2D method easily chooses the gap with zero events in the y' coordinate and calculates an upper limit of about 5.1 counts, even if the measurement has 10 counts. The C–2D algorithm can only select a rectangle with an event or the corners of the parameter space in its corners. The best choice made with this restriction is the blue marked box containing one event, but that only leads to an upper limit of about 14.1.

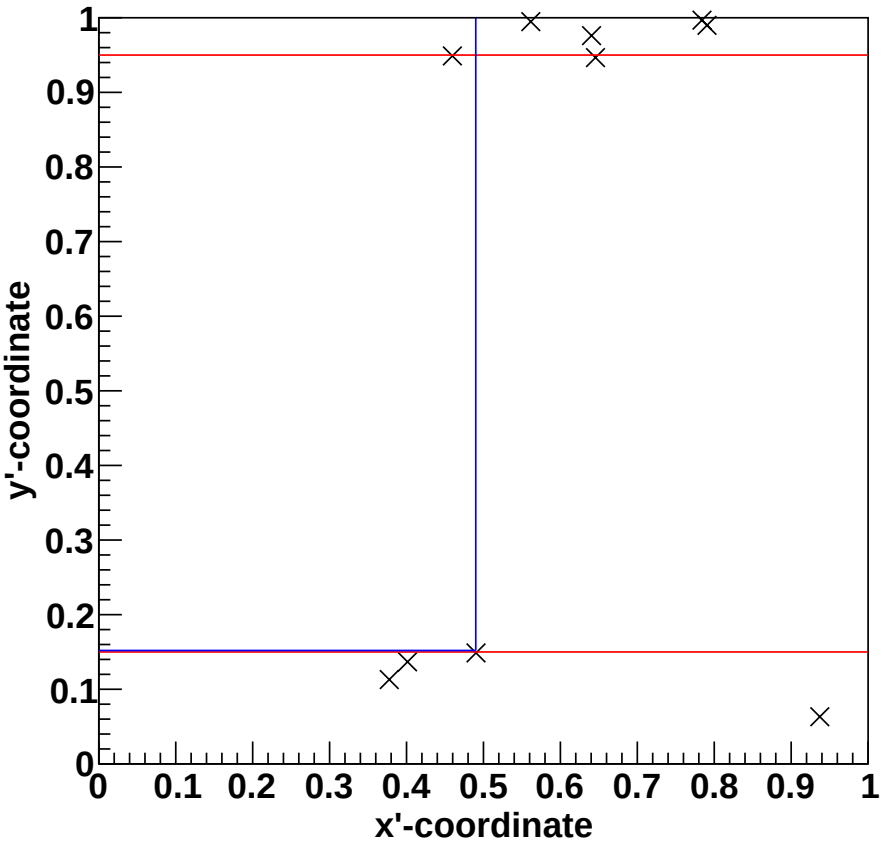

Figure 12.4: Example for an event constellation where one naturally would select the large gap in the y' coordinate — marked in red — for the optimum area. But the algorithm of the C–2D method is not able to select such an area, because there is no event at the borders of the x' coordinate and therefore this natural box cannot be selected. The best choice for the C–2D algorithm is the blue box which includes one event.

On the other hand the C–2D method has an advantage against the P–2D method. If both methods arrive at the same value for the optimum Area,

the P–2D method results at relatively high values due to its steep exclusion curve, shown in Fig. 12.5. An example for the constellation of events, where this property is dominant is shown in Fig. 12.6. Both methods can only select an area which is similar in the size. However, in the C–2D method this corresponds to an upper limit value of 11.4 in contrast the P–2D method where that area corresponds to 18.5. The P–2D method is normally able to find larger optimum areas than the C–2D method within the same event constallation. Here both methods end up with the same optimum area, which results in a worse upper limit for P–2D.

The P–2D method has the property, that always the largest possible area is found. This positive property on the one side leads to a bad performance of the P–2D method in the cases when it is not possible to find an large rectangle due to the event constellation. The second example illustrates this behavior in more detail. In other words the P–2D method is used to find large gaps due to the testing of all possible rectangles. Mathematically this behavior can be expressed through a steep raise of the LT function, shown in red in Fig. 12.5.

It cannot be said a priori which advantage, the guaranteed selection of the biggest optimum area of the P–2D method or the flatter LT function of the C–2D method, is of more impact to the excluded upper limit. Therefore the methods are tested in different background scenarios in the next chapter. The performance of the methods will be a criterion which method is suitable for a real measurement analysis.

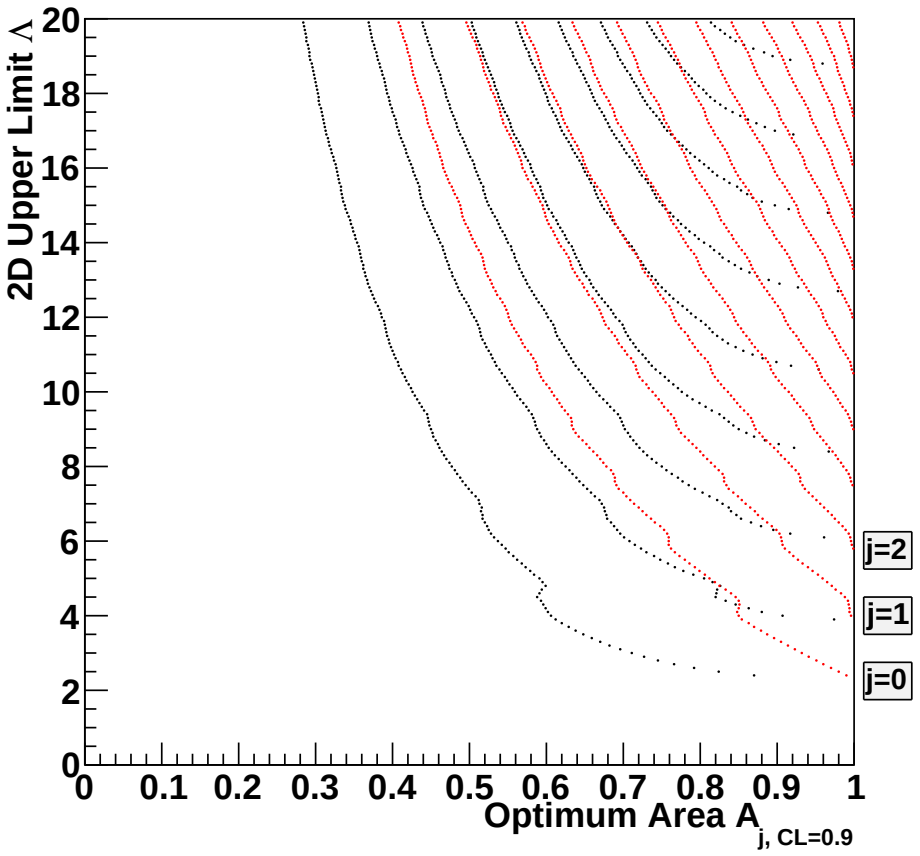

Figure 12.5: The Upper Limit is plotted versus the optimum Area for the C–2D (black) and the P–2D (red) method. For event distributions like in Fig. 12.6, where the two methods arrive at about the same optimum area, the C–2D method arrives due to the flatter LT curve at a remarkably better limit. The P–2D method is normally able to find larger optimum areas than the C–2D method within the same event constallation.

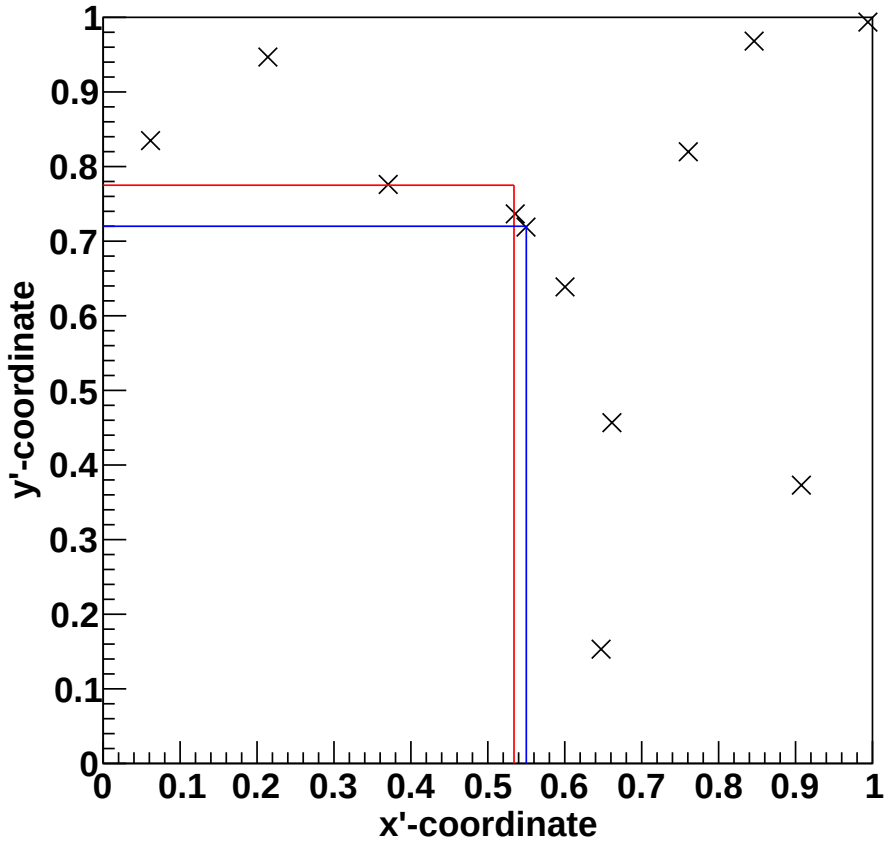

Figure 12.6: Example for an event constellation where both of the 2D methods would arrive at about the same optimum Area. In such cases the P–2D method results in a worse Upper Limit value, as it has a very steep LT curve (compare Fig. 12.5).

Chapter 13

Study of the new 2D Methods in Presence of an Unknown Background

To simulate the effects of an unknown background seems to be ridiculous in the first place, as an unknown background is by definition 'unknown'. But one can think of a possible dangerous background for the experiment. This hypothetical background behaves with respect to the WIMP distribution somehow different and the consequences of these differences will be quantified. Two models are introduced in the first section and will be compared with the scenario of a background–free experiment. Thereafter the results of the 1D and 2D methods of the previous section will be compared and are analyzed for their results in the different background scenarios.

13.1 The Background Models

The detailed models of a possible background of low rate experiments should take into account how a signal from different background sources would look like. In this work three scenarios are studied in detail. They are introduced in the first part and analyzed thereafter.

First the optimum case is modeled: An experiment where only the searched signal is measured and no unknown background occurs. Thereafter a background for the performance test of spectral methods is defined. All measured events lie only in a finite region of the signal area. In the last case of the background distribution a most realistic contamination for the CRESST experiment is modeled. The signal region has a contamination from the upper side, which is extended to the lower end of the abscissa. A leakage from the

electro–magnetic population into the band of the nuclear recoil events could cause such a behavior in the energy to light yield diagram.

13.1.1 Signal–like Distributed Background (SDB)

An event population with a flat probability density in the whole signal region is indistinguishable from the signal. That might be due to the signal itself. All methods of chapter 10 are tested with such an event sample. An illustrative example is shown in Fig. 13.1. A deviation from that event distribution results in combination with the spectral analysis in a better upper limit than it is expected from a simple Poisson approach.

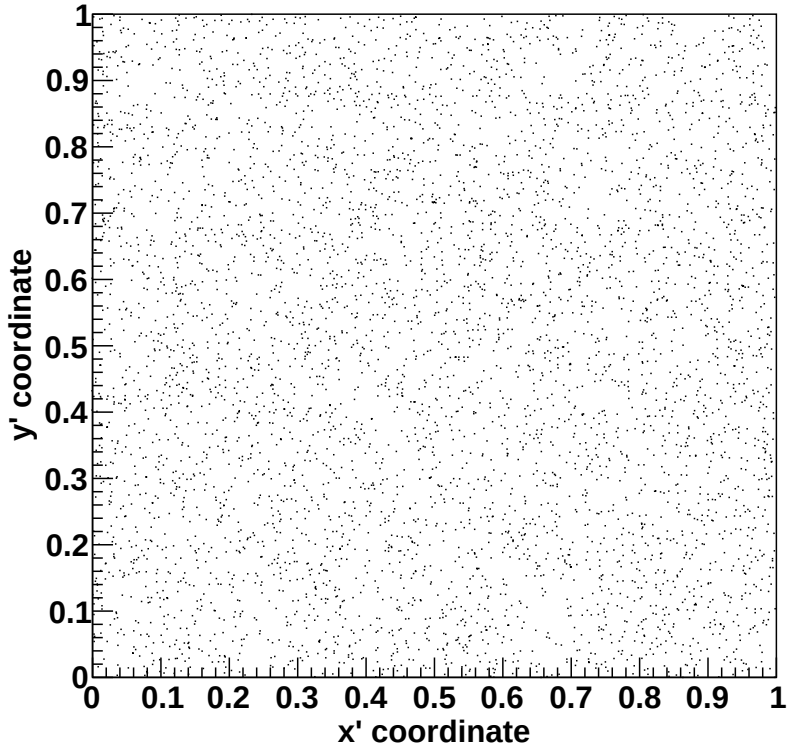

Figure 13.1: An event distribution of a signal–like, homogenous background (SDB) in the x'– and y'–coordinate is shown. This kind of event distribution is expected if the signal is distributed exactly like the assumption without a contribution from an unknown source is measured. However, a source with exact the same spectral shape than the expected WIMP recoil spectrum would be indistinguishable.

13.1.2 One Quarter Background (OQB)

To demonstrate the positive effect of his new method, Yellin used in Ref. [57] for his one dimensional Optimal Gap method a background scenario consisting of 50 % of the events in the range between $[0; 0.5]$ and the rest of the events distributed between $[0; 1]$. The two dimensional analogon is that 50 % of the events are arranged in a quarter of the whole region like it is shown in Fig. 13.2. In principle the ratio between the signal part, represented via the SDB, and the 'unknown background' can vary. Therfore a number after the type of background indicates the relative amount, e.g. OQB50 refers to the above mentioned scenario with 50 % background contribution. In figure 13.2 an example of the pure OQB100 case is shown.

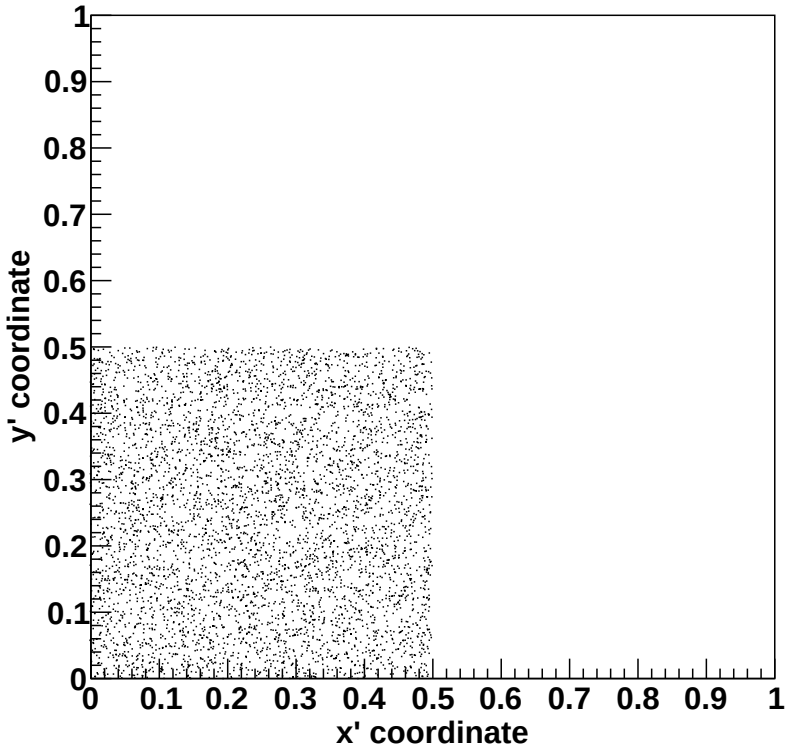

Figure 13.2: An Event distribution of the Quarter Background (QB) is displayed for the whole signal area of the x'– and y'–coordinates. The amount of QB to all the signal is 100 %, therefore that case is referred as QB100. In a more realistic scenario it should be mixed with a certain level of SDB, which simulates the signal one really wants to measure.

13.1.3 Circular Leakage Background (CLB)

Typically data of direct Dark Matter search experiments is presented in form of a two dimensional histogram where a discrimination parameter is plotted over the recoil energy. For CRESST the discrimination parameter is the light yield and a typical result plot looks like Fig. 13.3. The discrimination becomes worse towards low energies and the event class of the electro–magnetic interaction leaks into the WIMP recoil band.

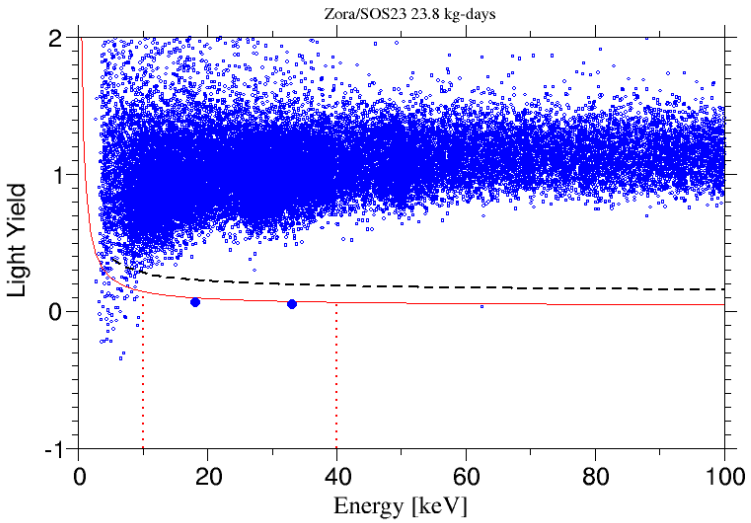

Figure 13.3: The published result plot of the commissioning run of CRESST–II of Ref. [38]. Shown is the discrimination parameter, light yield, over the recoil energy. The discrimination becomes worse at low energies and electro–magnetic events leak into the region of interest for WIMP search beneath the red line. This behavior is modeled with the CLB background.

An approximation of this leaking, expressed in the transformed variable (see Sec 11.1), is done here while the events are distributed randomly in the x'–coordinate, but the allowed range in the y'–coordinate depends from the x–position via a circular boundary limit:

$$y' \in \left[\sqrt{1-(1-x')^2}; 1\right] \tag{13.1}$$

Within this range the events are spread with the same probability for any position. In Fig. 13.4 a pure CLB distribution is shown. But similar to the OQB case, the CLB scenario can be mixed with the SDB "signal". To illustrate such a mixed population a CLB30 is displayed in Fig. 13.5.

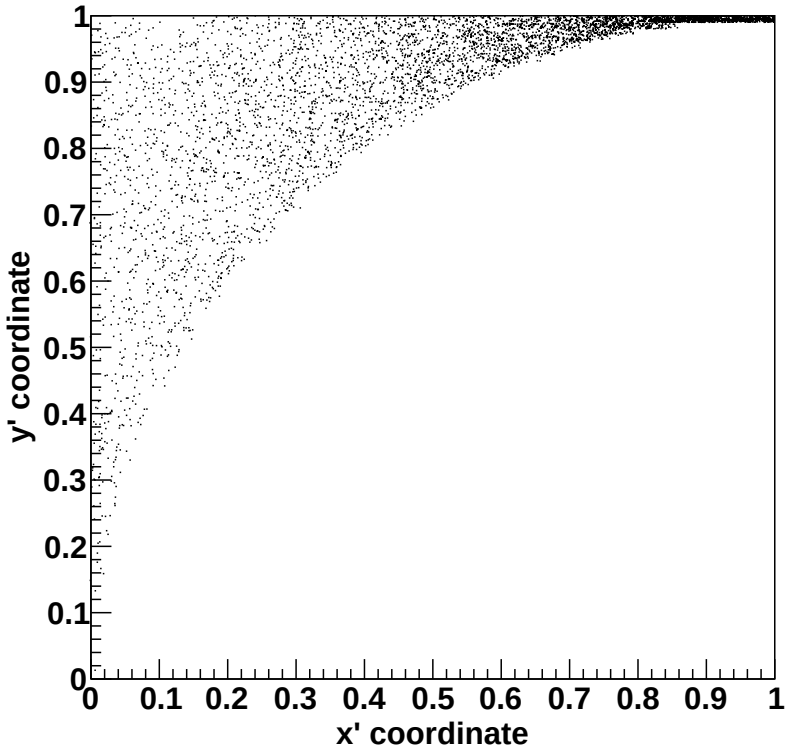

Figure 13.4: An event distribution of Circular Leakage background (CLB). They have an equal probability for every x'–position, but the allowed range for the y'–coordinate is dependent of x' via the Eq. 13.1. In the allowed y'–range they have a random position.

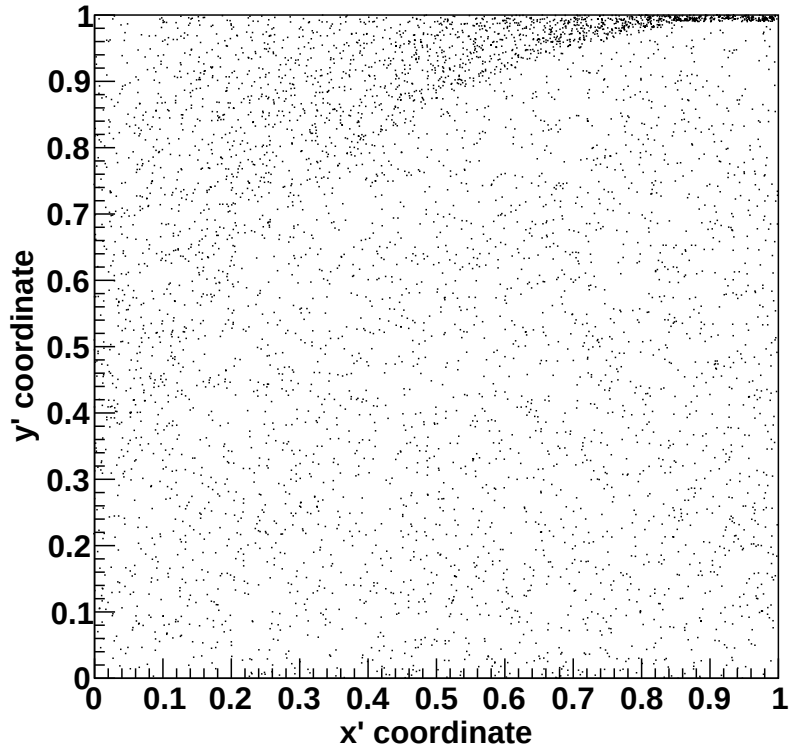

Figure 13.5: An event distribution of a combination of 30 % Circular Leakage (CLB) and 70 % homogeneously distributed events (SDB) is shown. Such a combined scenario is a very challenging test for all methods.

13.2 Comparison of the 2D Methods in various Background Scenarios

To compare the performance of the presented methods, especially the performance at low rates, a special test procedue has to be applied. This procedure is introduced in the first section. However, the performance is dependent on the background model. Therefore the different analysis methods are tested with the various kinds of background introduced in the last section to give a recommendation for the data analysis of low statistic experiments.

13.2.1 The Comparison Procedure

For the comparison of the methods it was chosen to scan over a reasonable range of assumed True Values. For every of the True Values five thousand experiments were simulated. The counts in a single experiment are determined by the Poisson distribution with a mean Value which corresponds to the True Value. The counts are distributed according to the background modells of the previous section. Each single experiment is then analyzed with the methods B–1D, P–2D and C–2D. As a result one has an upper limit for every of the 5000experiments for each True Value like in Fig. 13.6, which is calculated with a True Value of 5 in presence of the CLB30. The red line marks the values of equal results of the two methods. One can see the results have the tendency to higher limits for the C–2D method. The average value of all limit values is taken as indicator for the performance.

Therefore for every assumed True Value and every method in any background model the average value for the resulting upper limit is plotted to illustrate which method has a better performance on average. But, once again, due to the statistical spread, it is not guaranteed that a method is in all cases better than another. For this reason, a smaller spread is an advantage of a method. This aspect is highlighted in Sec. 13.2.5.

13.2.2 Statistical Performance with a pure Signal (SDB)

For the case of a SDB, which is indistinguishable from a real signal, it is a priori not clear, whether the methods perform the same. To test the performance 5000 simulated experiments were analyzed for the different True Values with the different methods. In Fig. 13.7 the performance of the different methods is shown as a function of the true values. All methods are comparable as they more or less yield in the same limits. The C–2D method is a little bit worse than all other methods. In the SDB scenario it makes no difference if one

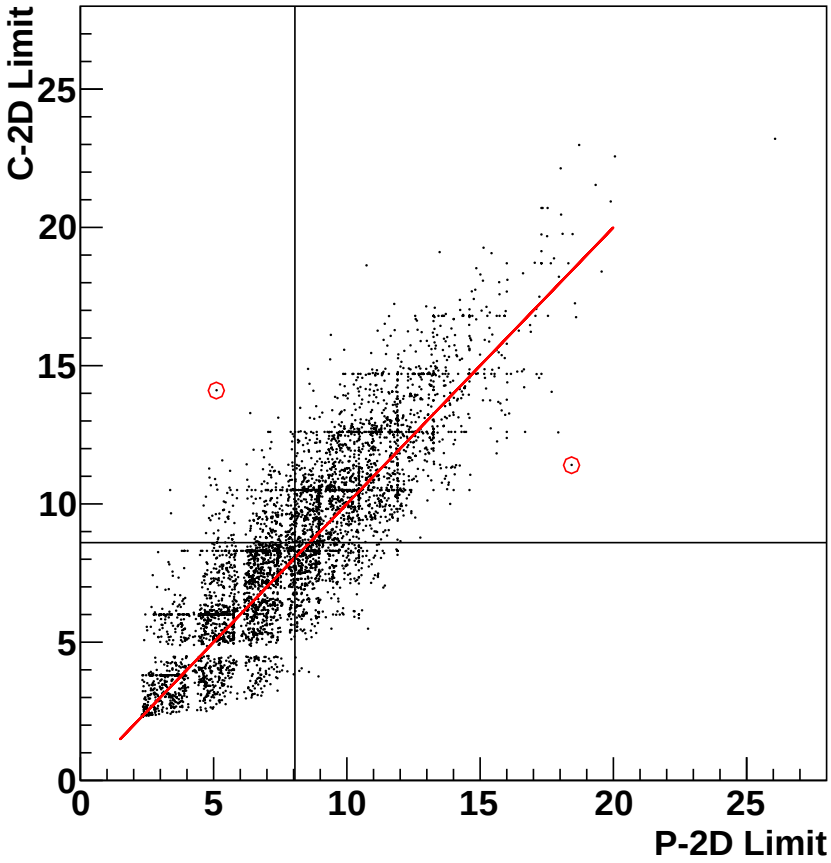

Figure 13.6: The result of 5000 simulated experiments with a assumed average rate of 5 is analyzed with the two 2D methods individually. The red line marks the position of equal performance. The points are shifted a little bit to higher resulting limits for the C–2D method. This shift corresponds to a higher average value (black line), which is now used to compare the performance of the various statistical methods. The previously discussed example events of section 12.4 are marked with a red circle.

analyses the data in 1D or 2D. The spread of the individual result around the average value is measured in terms of the root–mean–square value (RMS). The RMS for all five methods is about the same, compare with Fig. 13.8, so the influence of the chosen method on the result in case of a pure signal population is negligible.

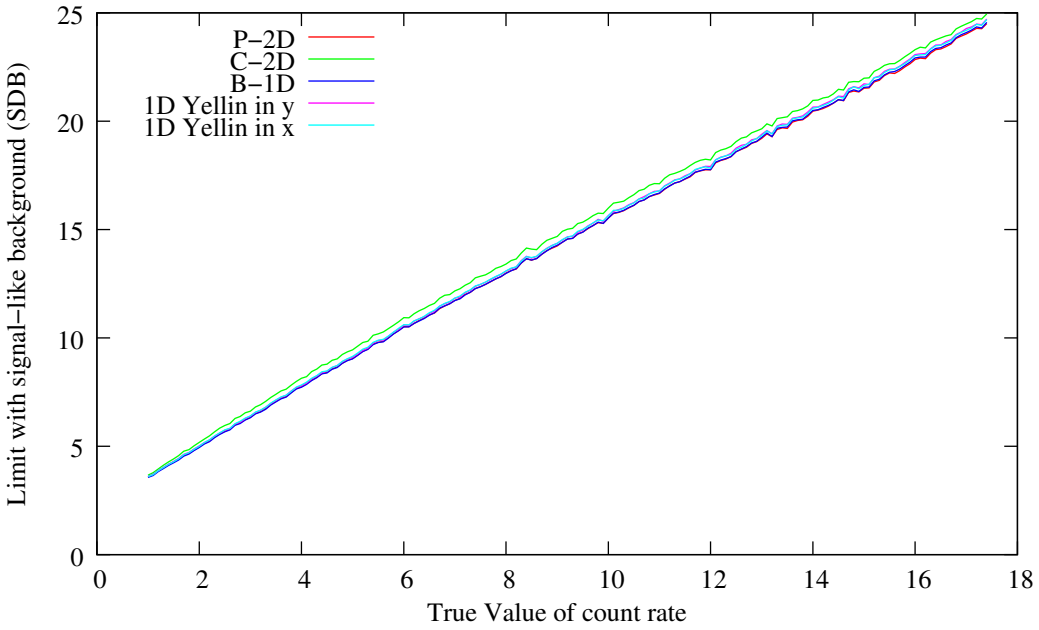

Figure 13.7: All five methods search with different approaches of section 11.3 and chapter 12 for the upper limit in a statistically distributed events group at various assumed "True Values". Within a very tiny variation all methods result at the same value. The RMS–spread of the different methods is comparable, but individual results may vary a lot, like it is displayed in Fig. 13.6.

13.2.3 Statistical Performance Test with OQB

A background of this type is used in Ref. [57] to show the better performance of the 1D Yellin method. Although it is not a very realistic assumption to have a sharply bounded background model, the ansatz of the OQB100 has the advantage that one expects for higher and higher count rates the methods to approach at a saturation value which refers to the optimum gap respectively optimum area of the size 0.5. This behavior can be observed in Fig. 13.9 for all investigated methods. The expected saturation values are listed in Tab. 13.1. Qualitatively one can see that the two 1D methods and the combined 1D method, B–1D, approach rather quickly at their saturation.

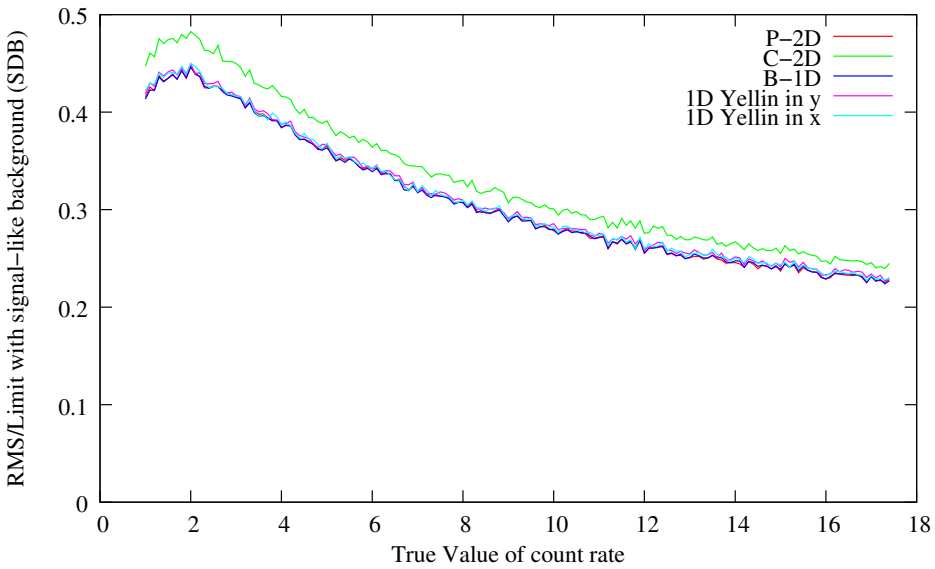

Figure 13.8: The relative root mean square (RMS) spread of the results is plotted over the true value of the 5000 experiments. All methods have about the same relative spread. The C–2D method is a little bit worse than the others.

The two 2D methods, P–2D and C–2D, seem to have a slower saturation. This property makes them the better choice for a data analysis in Dark Matter search. They can suppress background much more efficiently than the others as they approach the saturation slower. The lower resulting values are an advantage of the C–2D method. Although only the C–2D method rises over the saturation value of $j = 0$. As there has to be the events directly in the corner, it is sometimes of advantage to take the area with $j = 1$. The C–2D method ends up with an effective saturation value somewhere in between the expected value for $j = 0$ and $j = 1$.

Method	Saturation value $j = 0$	$j = 1$
Yellin 1D	9.5	-
B–1D	11.0	-
P–2D	14.3	-
C–2D	7.3	12.2

Table 13.1: In the above table the saturation values for the different methods of data analysis are shown. The saturation value for the OQB is the $LT^0(0.5)$ value. Only for the C–2D method the brunch of LT^1 influences the saturation due to the sub-optimal algorithm, compared to the P2D.

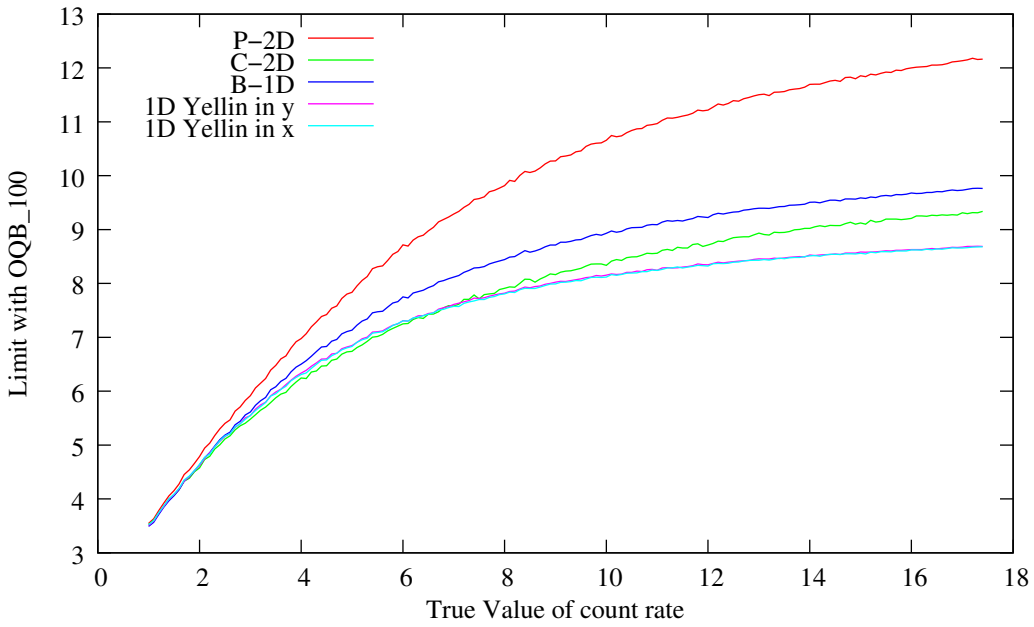

Figure 13.9: In this background scenario all methods converge against a saturation value of Tab. 13.1, which corresponds to a largest gap of 0.5 with zero counts in it. It is a qualitative characteristic of the two 2D methods, that they converge very slowly against that value as they are still able to find a non–trivial gap at higher event rates. However, the 1D methods have a smaller saturation value in that background case.

In the next situation the OQB is mixed to equal parts with a signal. So no saturation value for the upper limit can be expected any more. Only the direct comparison of the results from other methods are possible. The first impression of the results of Fig. 13.10 is that all five investigated methods perform similarly. The P–2D method is about 5 % worse on average than the 1D methods. The B–1D and C–2D methods achieve an even slightly better result, but summarized one can state that in this background case the methods are more or less equal in respect to the achieved upper limit value.

13.2.4 Realistic CRESST–like Test with CLB

The CLB scenario is designed to imitate a likely possibility in Dark Matter search experiments like CRESST. One has a flat probability distribution in the energy coordinate (here x) and a discrimination parameter (e.g. light yield, here y) which becomes worse for low energies, where the background is leaking in.

First the example of no signal and only that type of background is

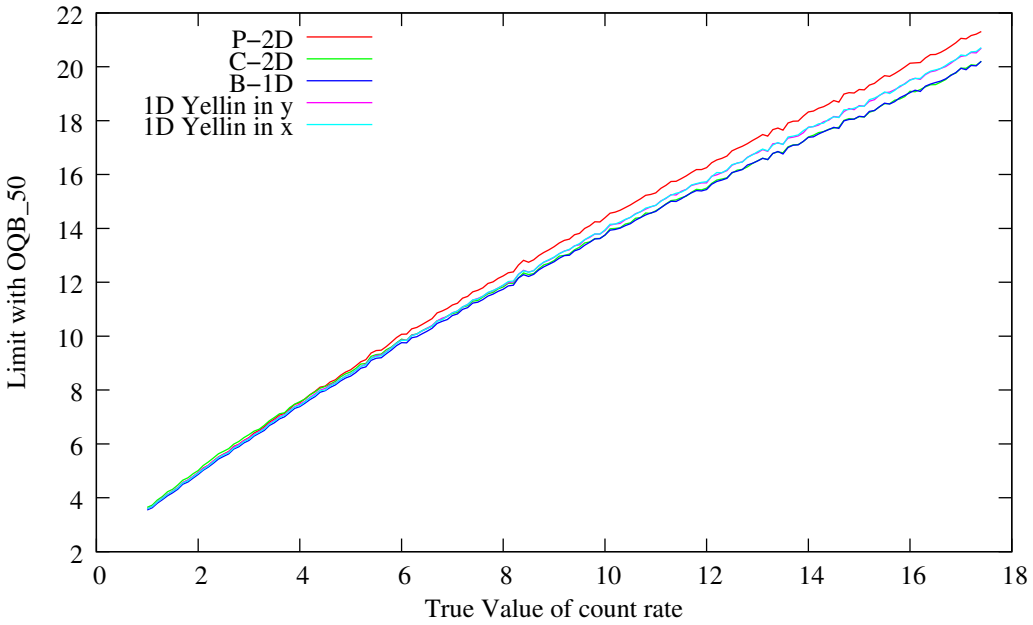

Figure 13.10: Here, in the background case where OQB and "signal" (SDB) are mixed equally, the P-2D method is worse than any other possibility. Even the 1D methods perform about 5 % better. The best solutions for that background scenario are the B–1D and the C–2D methods with an even better performance than the 1D methods. Both of the B–1D and the C–2D methods have almost identical upper limit values.

investigated. In Fig. 13.11 one sees that, as expected, the 1D Yellin method of the energy coordinate is not sufficient anymore. Every other method is at least twice as good in the upper limit. The C–2D method performs again extremely good with its low saturation value for high count rates, but at lower rates it is not the best choice. The B–1D and the P–2D method are better up to a rate of about four counts. The Yellin 1D method in the y coordinate performs well, but is no real option, because that would mean, that one chooses the analyzing method after obtaining the measurement. This method is only displayed for comparison.

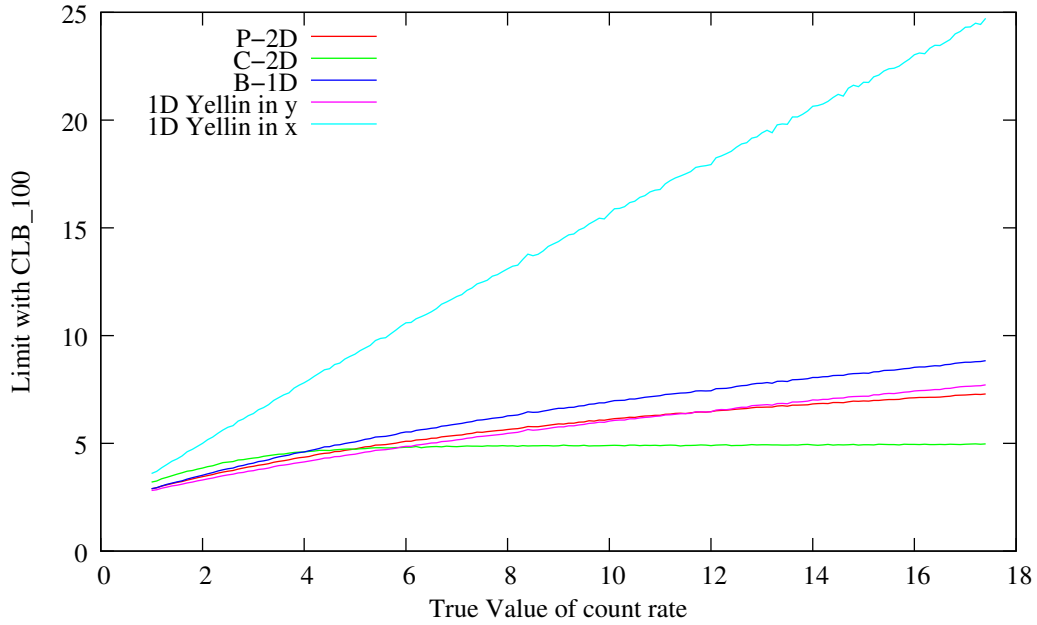

Figure 13.11: The methods for data analysis are tested against a pure leakage background, which becomes worse for low energies. As expected, every method in this case performs much better than the 1D Yellin method, which as no ability to use the information of the discrimination parameter. Very promising for high leakage rates is the C-2D method. The flat LT function and the event free parameter space in the CLB100 scenario lead to a low saturation value. For True Values smaller than four the other 2D methods perform a little bit better.

Within the scenario of CLB the situation also becomes more complicated in a mixed case of signal and background. There are 30 % of background within the signal, but still the improvement of every 2D extension over the standard 1D Yellin method in the x–coordinate is significant. On average a factor of 1.2 is gained in the upper limit value rather independently of the

chosen method. The C–2D and the B–1D method perform slightly worse than the P–2D method. Remarkably the 1D Yellin of the y–coordinate results at the same performance than the advanced 2D methods. Therefore the 2D methods are the best choice for every experiment having the possibility of a mixed event population consisting of some background and the real signal.

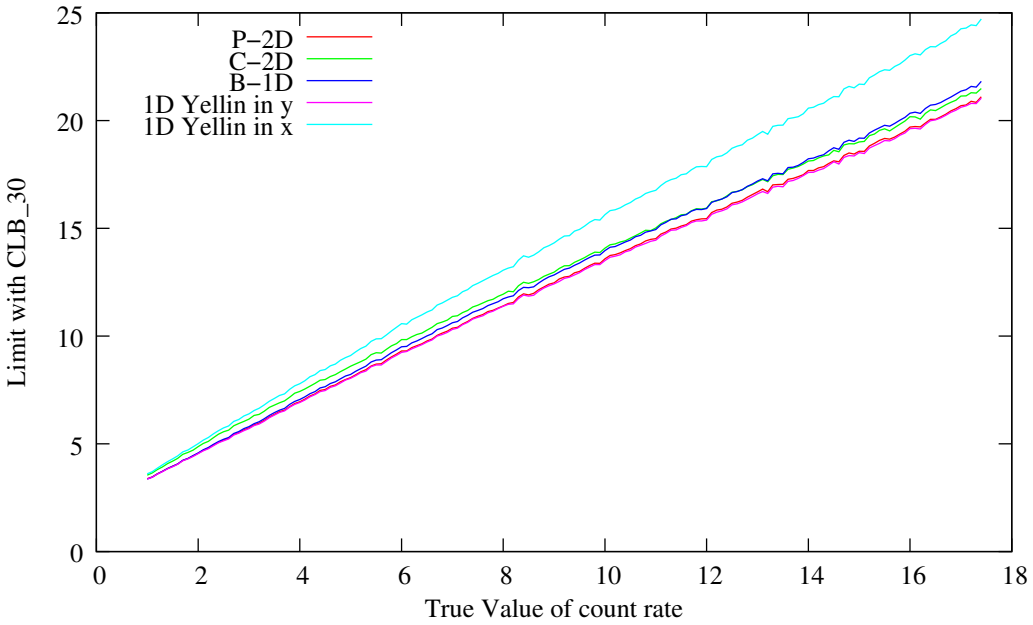

Figure 13.12: The worst case scenario in the Dark Matter search is reconstructed in this background scenario, where one has in addition to the signal (SDB) a contribution of 30 % leakage background (CLB). Surprisingly the 1D Yellin method for the y–coordinate (e.g. light yield) is one of the best in that scenario together with the P–2D method. The B–1D and the C–2D method have an average result which is only a few percent worse. All methods perform about a factor of 1.2 better than the 1D method in the x (here energy) parameter.

13.2.5 Spread of the results

The spread of the single events around the average value is an indicator of the significance of the result. If the spread is too high, the result based on only a few measurements has a high probability to differ from the result based on many single measurements. So the spread has to be taken into account to give a suitable advice for the optimum statistiacal method.

The spread is defined in this work as the root mean square (RMS) value of all single measurement results defined as:

$$RMS = \sqrt{\frac{\sum_{i=1}^{N} \left(\Lambda_i - \bar{\Lambda}\right)^2}{N}} \tag{13.2}$$

were $\bar{\Lambda}$ is the average resulting limit value of all single measurements. If the spread of one method is higher than from another it would mean that the result of one single measurement has a larger uncertanty. As the Dark Matter Search experiment have to calculate their results on a low statistical basis, the spread should be as low as possible.

In Fig. 13.13 the ratio of the spread to the average result value is plotted versus the true average value of the simulated experiments. The spread at lower values around 2 is relatively low, as the single results have a lower limit. No value can be lower than the Poissonian limit. Due to this limitation the spread is also limited. Towards higher true values the relative spread decreases again. There the single experiments are likly to measure multiple events and result in a more presice limit value. The relative spread of the red P–2D method is systematically lower than the relative spread of the C–2D method.

This difference between the two advanced 2D methods is a clear advantage of the P–2D method. The spread of this method is in all background scenarios lower. This means that the results calculated with the P–2D method are more fixed around a true value which one wants to obtain.

13.2.6 Result of the Statistical Tests

It is also worth mentioning, that if there is only a pure signal (SDB) it does not matter what method is chosen. Here also the 1D and 2D implementations of the Yellin method arrive at the same conclusion. As soon as there is a signal in combination with background it is advantageous to choose a 2D method. The C–2D and the B–1D implementation are on average also better than the 1D method in a realistic CRESST–like background case, but their performance is a little bit worse in the interesting region of low rates compared to the P–2D scenario. In the study of the CLB30 case it was found that the gain by changing into the 2D parameter space is about a factor 1.2 and one still analyzes the data without any bias.

The computer studies show that for future data analysis of CRESST a 2D analysis would be of advantage. Even if there is only 30 % contribution from leakage background to the signal, the result for the upper limit gains from the 2D information about a factor of 1.2. Whether the C–2D or the

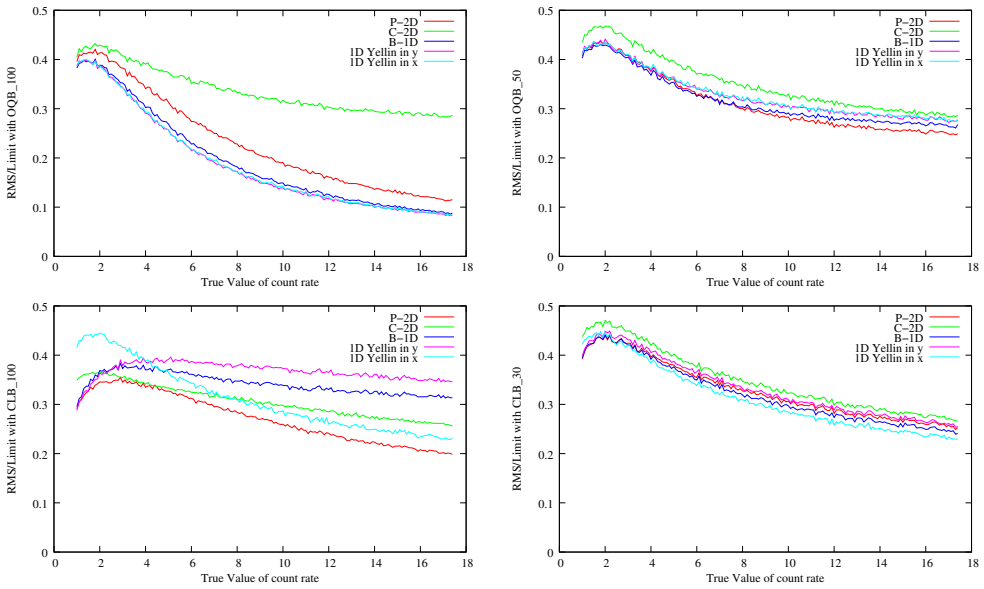

Figure 13.13: The relative RMS spread of the results of the background scenarios is plotted versus the True Value of the simulated experiments. The decrease towards lower True Values is due to the lower boundary of the upper limit. It cannot be lower than 2.3, the Poissonian limit for an experiment with zero measured counts.

P–2D perform in all situations better than the other. The recommendation of the author would be the P–2D method as it is less sensitive to unlucky event constellations. It also has a much smaller RMS spread within the single results. However, the C–2D method is only slightly worse in performance and reaches within the clear background scenarios, OQB100 and CLB100, in the lower saturation values.

Chapter 14

Summary of Part III

In the third part of this work all steps of the upper limit calculation for a low rate experiment were critically investigated.

The calculation of the recoil spectrum is important for the translation of the measurement result into the normalized parameter space [0;1] where the limit calculation is done. The errors of the translation were found to be 20 % for the elastic scattering. For the inelastic scattering model the result becomes highly dependent on cosmic parameters as well as on nuclear physics parameter. The comparison between the experiments is very difficult.

To find the optimum upper limit in presence of unknown background the method of Yellin was introduced and checked with an independently developed new software. The method was extended in different ways to a second dimension.

To test the performance of the different 2D extensions different background scenarios were developed. The methods are tested with these background scenarios. The performance of the 2D methods was proven to be better than in the 1D case. Which 2D method is best, depends of the background scenario, which is not known in a real measurement. Therefore the patch method (P–2D) is recommend for future data analysis, because of the good performance in the realistic background case and its smaller spread of the single results around the average value.

Part IV

Appendix

Appendix A

Circuit Diagram of the Fast Analog Sum Builder

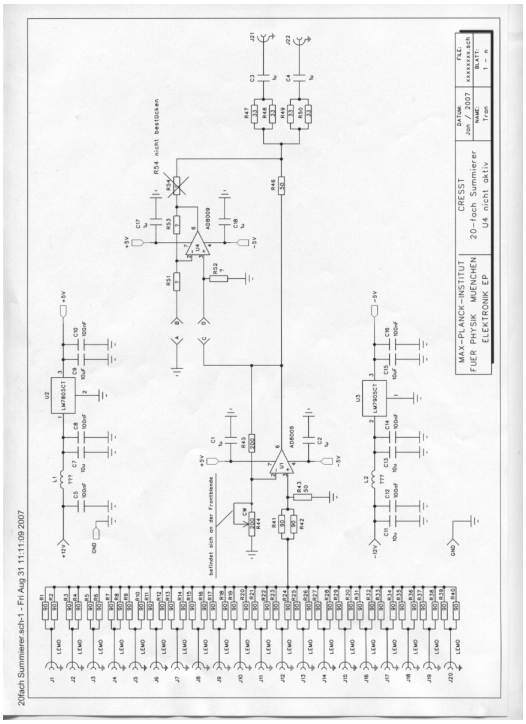

Figure A.1: The fast FIFO (FanIn–FanOut) from [74]. This device was developed in the framework of this thesis. It can add the analog signals of all twenty panels of the muon veto very fast. The output is created in less than 1 ns. This property made it possible to treat the analog sum signal like any other channel of the veto system without additional delay lines.

Appendix B

Muon Veto Data

Here the fit result of all panels is presented. First the histograms of the pulse hight of the CME group for all twenty panels were fitted like in Fig.7.2. Afterwards the effect of the different cuts are shown like in Fig.7.3 for each panel seperately. The yellow histogram displays the AME group. In red the CME group is displayed. The black histogram contains the DVE group which is taken for the coincidence data analysis. Last but not least the distributions for the three event groups is shown in the sum energy parameter.

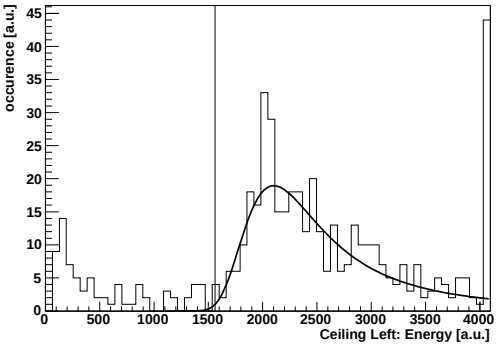
occurence [a.u.]
Ceiling Left: Energy [a.u.]

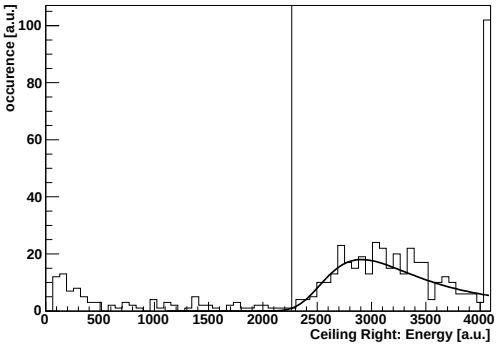
occurence [a.u.]
Ceiling Right: Energy [a.u.]

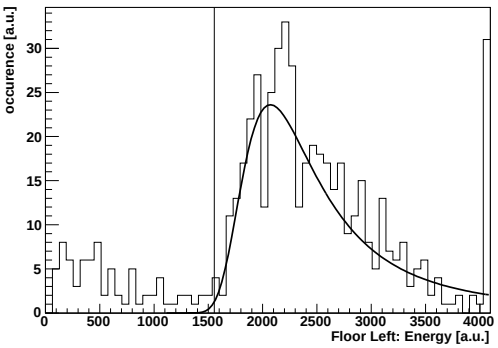
occurence [a.u.]
Floor Left: Energy [a.u.]

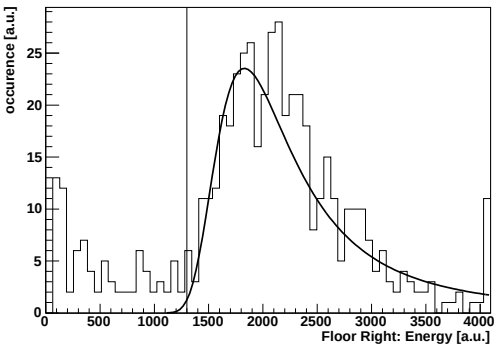
occurence [a.u.]
Floor Right: Energy [a.u.]

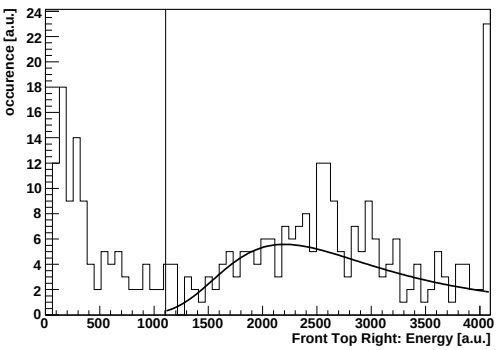
occurence [a.u.]
Front Top Right: Energy [a.u.]

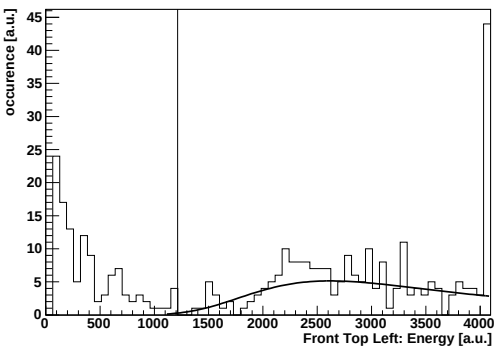
occurence [a.u.]
Front Top Left: Energy [a.u.]

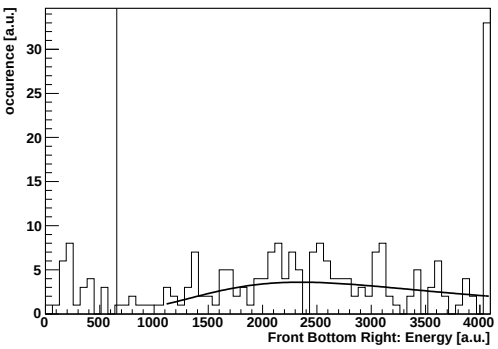
occurence [a.u.]
Front Bottom Right: Energy [a.u.]

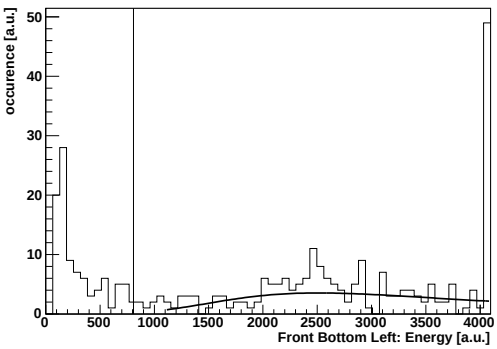
occurence [a.u.]
Front Bottom Left: Energy [a.u.]

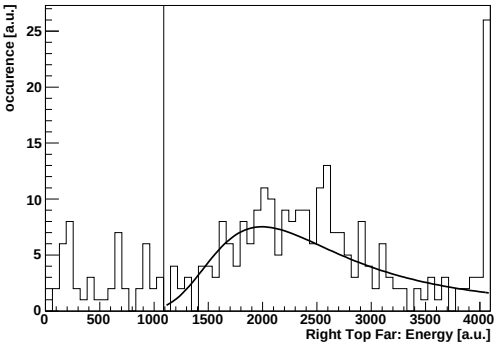
occurence [a.u.]
Right Top Far: Energy [a.u.]

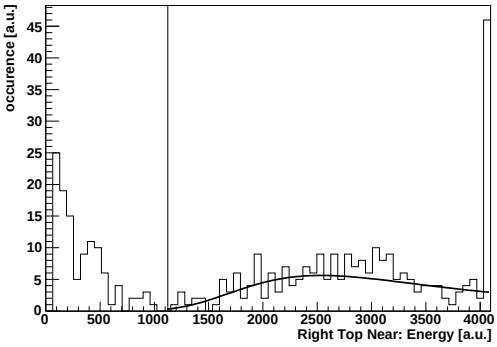
occurence [a.u.]
Right Top Near: Energy [a.u.]

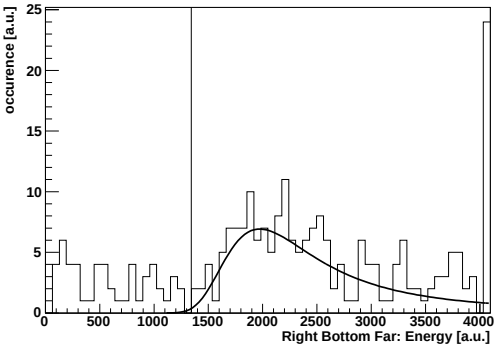
occurence [a.u.]
Right Bottom Far: Energy [a.u.]

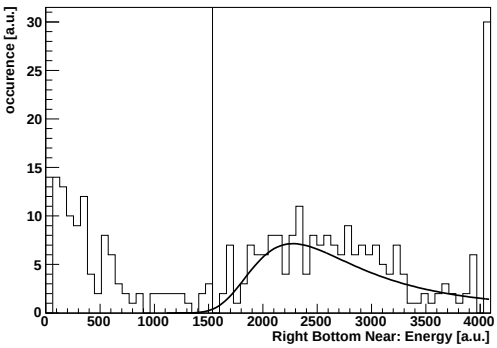
occurence [a.u.]
Right Bottom Near: Energy [a.u.]

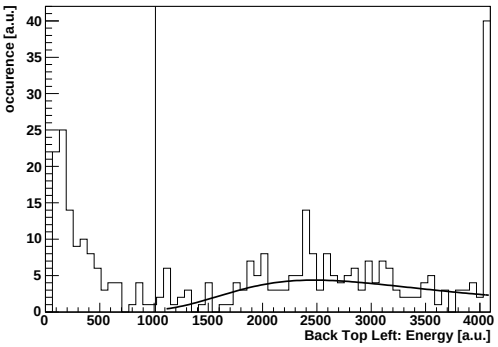
occurence [a.u.]
Back Top Left: Energy [a.u.]

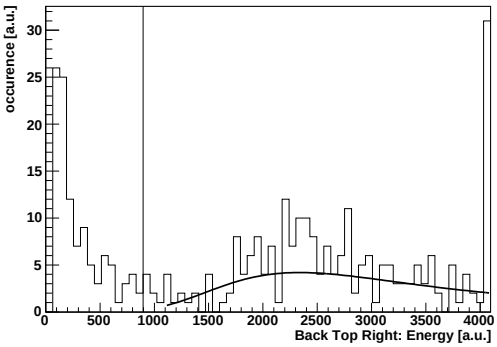
occurence [a.u.]
Back Top Right: Energy [a.u.]

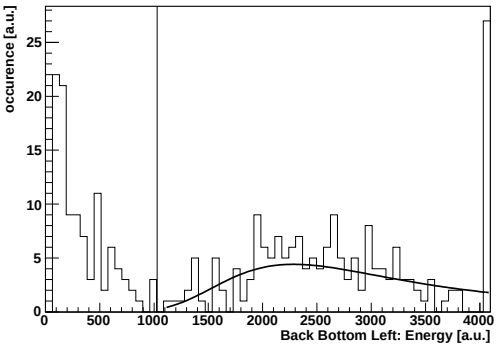
occurence [a.u.]
Back Bottom Left: Energy [a.u.]

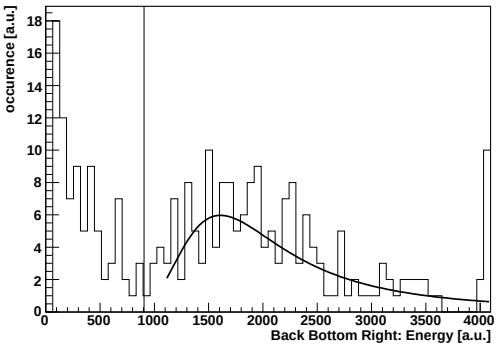
occurence [a.u.]
Back Bottom Right: Energy [a.u.]

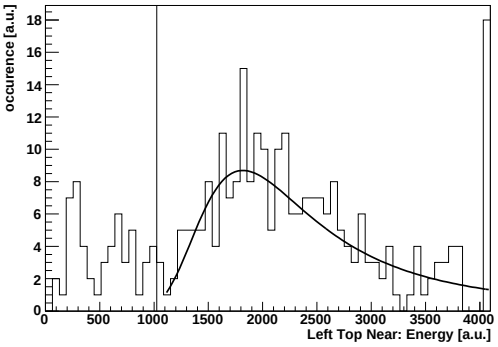
occurence [a.u.]
Left Top Near: Energy [a.u.]

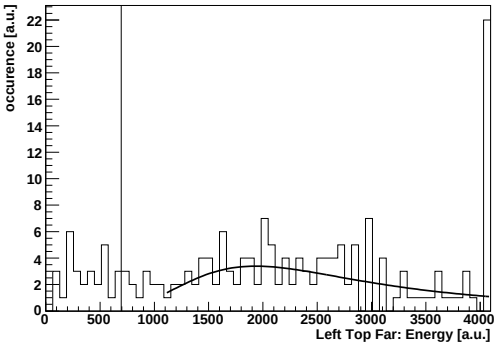
occurence [a.u.]
Left Top Far: Energy [a.u.]

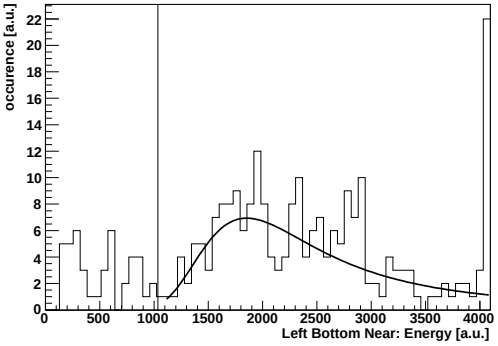
occurence [a.u.]
Left Bottom Near: Energy [a.u.]

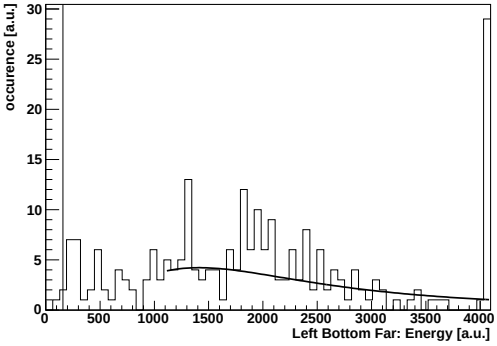
occurence [a.u.]
Left Bottom Far: Energy [a.u.]

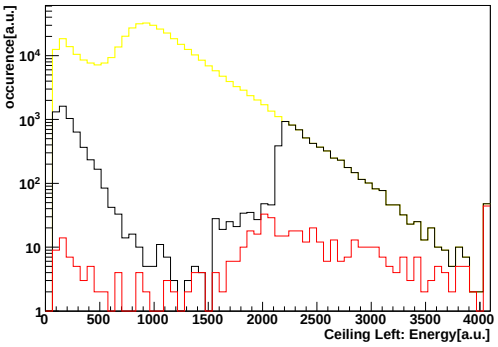
occurence[a.u.]
Ceiling Left: Energy[a.u.]

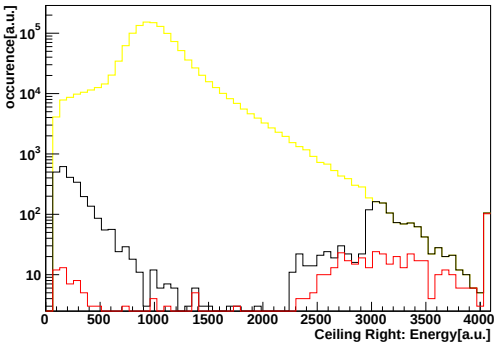
occurence[a.u.]
Ceiling Right: Energy[a.u.]

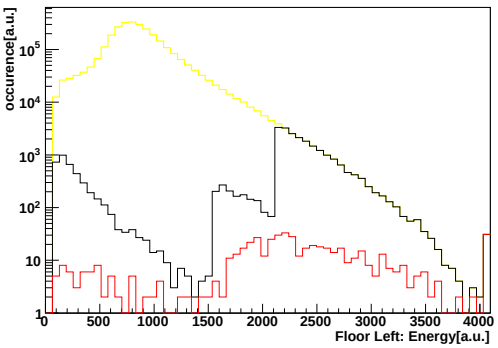
occurence[a.u.]
Floor Left: Energy[a.u.]

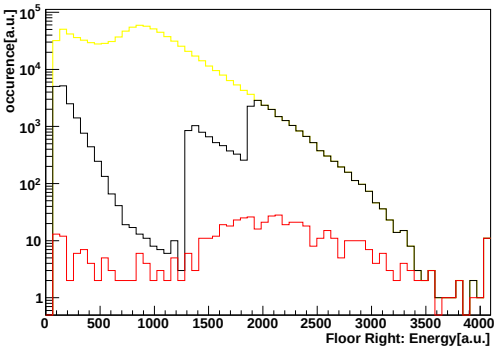
occurence[a.u.]
Floor Right: Energy[a.u.]

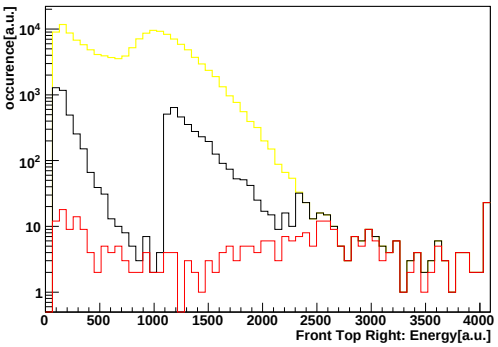
occurence[a.u.]
Front Top Right: Energy[a.u.]

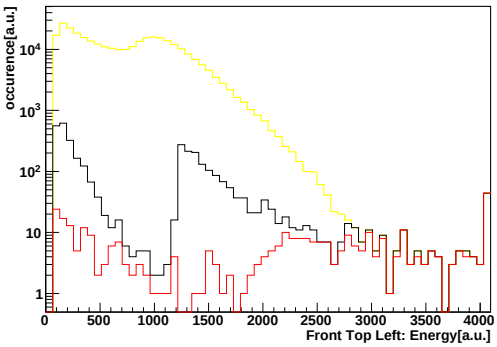
occurence[a.u.]
Front Top Left: Energy[a.u.]

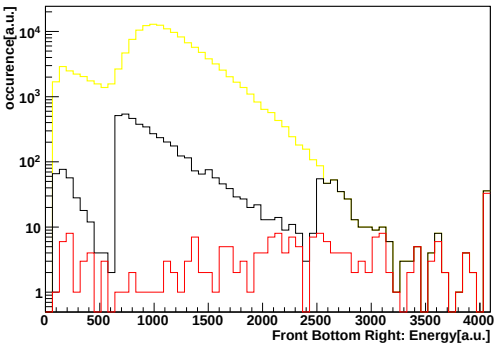
occurence[a.u.]
Front Bottom Right: Energy[a.u.]

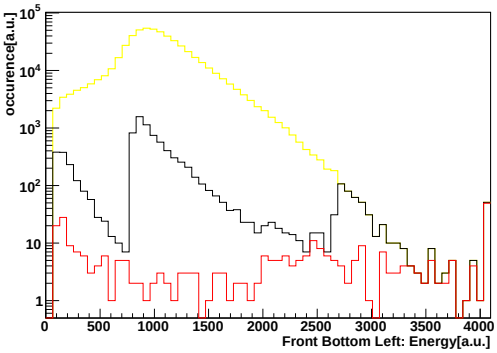
occurence[a.u.]
Front Bottom Left: Energy[a.u.]

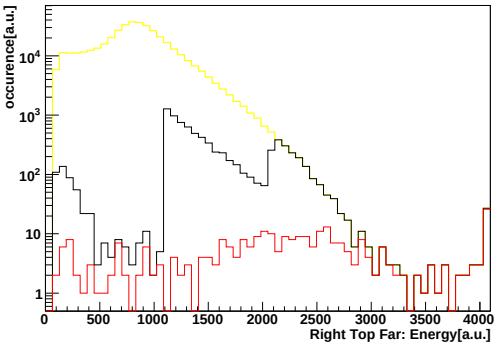
occurence[a.u.]
Right Top Far: Energy[a.u.]

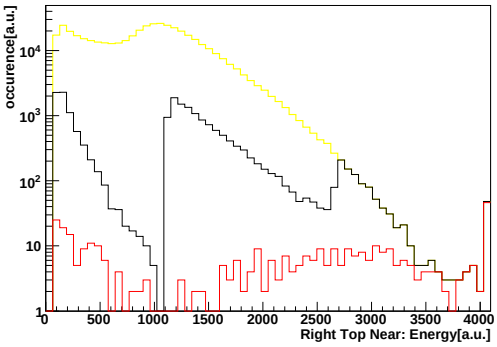
occurence[a.u.]
Right Top Near: Energy[a.u.]

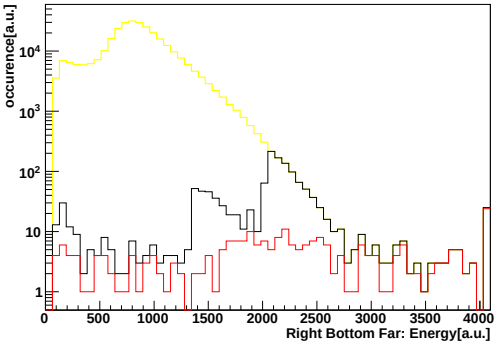
occurence[a.u.]
Right Bottom Far: Energy[a.u.]

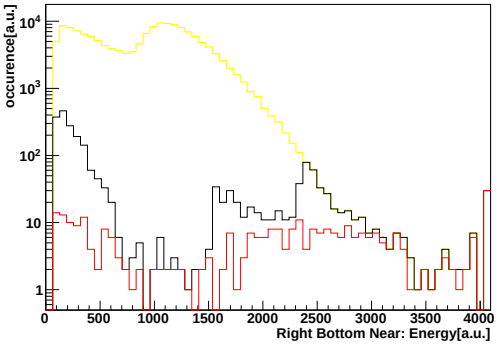
occurence[a.u.]
Right Bottom Near: Energy[a.u.]

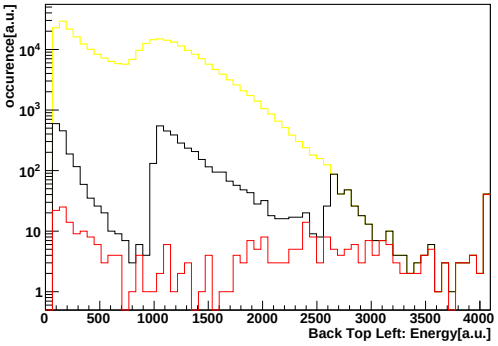
occurence[a.u.]
Back Top Left: Energy[a.u.]

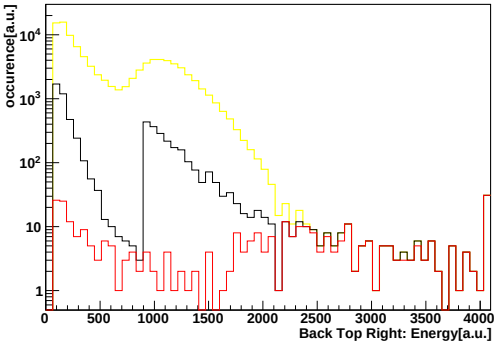
occurence[a.u.]
Back Top Right: Energy[a.u.]

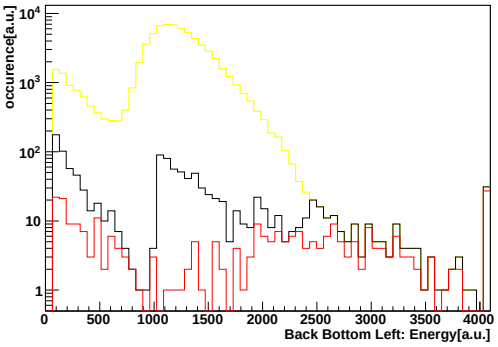
occurence[a.u.]
Back Bottom Left: Energy[a.u.]

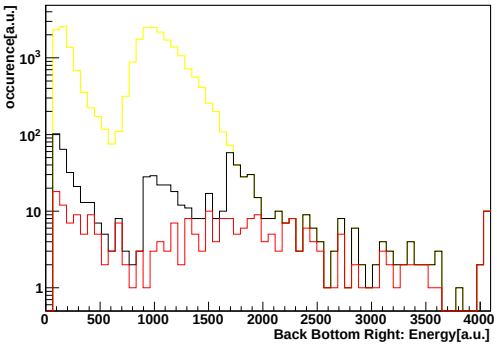
occurence[a.u.]
Back Bottom Right: Energy[a.u.]

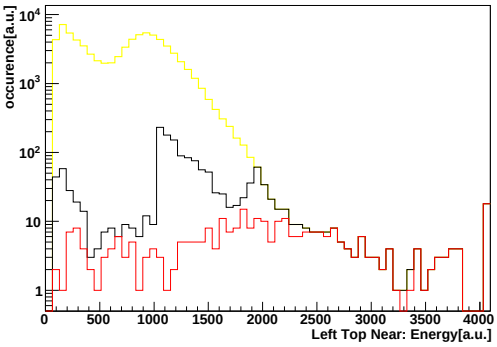
occurence[a.u.]
Left Top Near: Energy[a.u.]

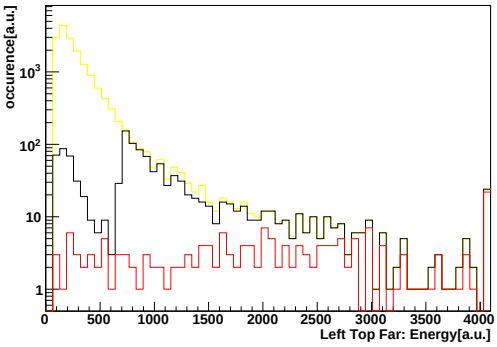
occurence[a.u.]
Left Top Far: Energy[a.u.]

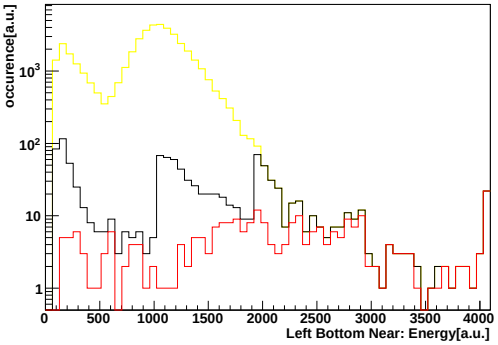
occurence[a.u.]
Left Bottom Near: Energy[a.u.]

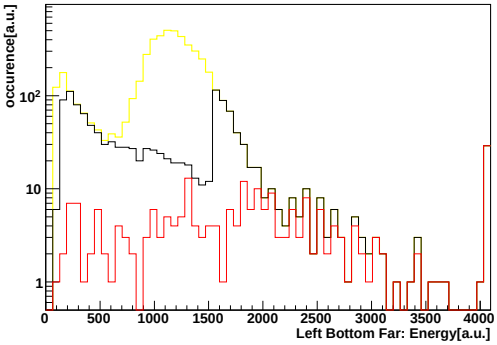
occurence[a.u.]
Left Bottom Far: Energy[a.u.]

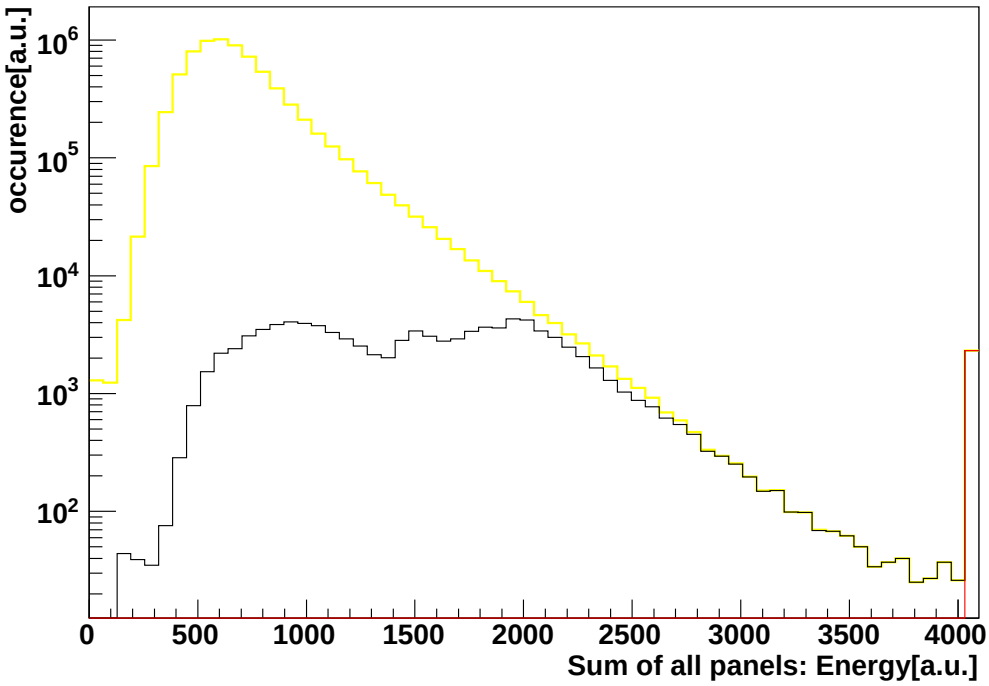
occurence[a.u.]
10^6
10^5
10^4
10^3
10^2
0
500
1000
1500
2000
2500
3000
3500
4000
Sum of all panels: Energy[a.u.]

Appendix C

Landau Function

The Landau function describes the energy loss of a minimal ionizing particle in matter. This distribution fits very good the deposited energy of a muon in the CRESST veto panels. As the Landau distribution can not be given analytically it is difficult to illustrate. However, for the purpose of this thesis the Landau–Vavilov approximation for the Landau distribution will provide a feeling for the used parameters. The approximation has the following form:

$$vav(sig, MPV, x) = \sqrt{\exp\left[-\frac{x - MPV}{\sigma} - \exp\left(-\frac{x - MPV}{\sigma}\right)\right]}$$

, here the MPV gives the mean peak value and the σ is a parameter for the width of the distribution. In Fig C.1 are some example functions with different combinations of MPV and σ plotted.

For the data analysis purpose of chapter 7 the even better approximation of the software package ROOT is taken to provide a result as realistic as possible, but the principal behaviour of the Landau distribution is described well within the Landau–Vavilov approximation.

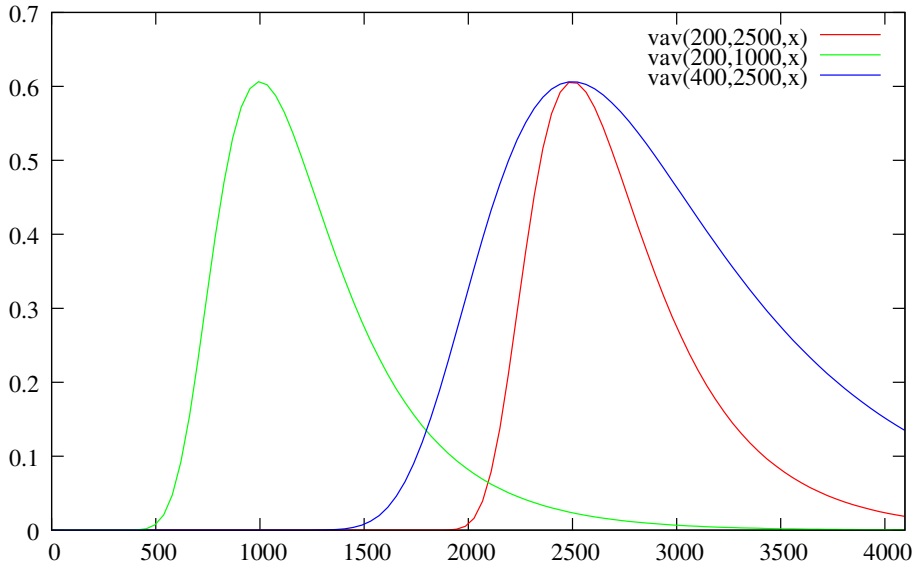

Figure C.1: The Landau–Vavilov function for a combination of typical parameters. The σ is a parameter for the width of the distribution and MPV determines the mean peak value. In the Fits for the data analysis the more sophisticated application of the Landau distribution is taken, which was provided by the software package ROOT.

Appendix D

Shell–Code

D.1 Coldtrap

`www.pit.physik.uni-tuebingen.de/~kimmerle/diss/script`

In this printed version, the code is not provided explicitly. It is available online via the above link.

D.2 Data Quality Monitoring

`www.pit.physik.uni-tuebingen.de/~kimmerle/diss/DQM_script`

In this printed version, the code is not provided explicitly. It is available online via the above link.

D.3 Gnuplot Fitting of the Quenching Factor

`www.pit.physik.uni-tuebingen.de/~kimmerle/diss/gnuplot_n_cal`

In this printed version, the code is not provided explicitly. It is available online via the above link.

D.4 Calculation of the Quenching Factor and its Error

`www.pit.physik.uni-tuebingen.de/~kimmerle/diss/qf_calc_n_cal`

In this printed version, the code is not provided explicitly. It is available online via the above link.

Appendix E

Perl–Code

E.1 Mixing.pl

`www.pit.physik.uni-tuebingen.de/~kimmerle/diss/mixing.pl`

In this printed version, the code is not provided explicitly. It is available online via the above link.

E.2 Extract.pl

`www.pit.physik.uni-tuebingen.de/~kimmerle/diss/extract_xyz.pl`

In this printed version, the code is not provided explicitly. It is available online via the above link.

Appendix F

C–Code

F.1 SimLight: Border Definition

`www.pit.physik.uni-tuebingen.de/~kimmerle/diss/Rand.01`

In this printed version, the code is not provided explicitly. It is available online via the above link.
`www.pit.physik.uni-tuebingen.de/~kimmerle/diss/Rand.02`

In this printed version, the code is not provided explicitly. It is available online via the above link.

F.2 SimLight: Source Positioning

`www.pit.physik.uni-tuebingen.de/~kimmerle/diss/Quellen.c`

In this printed version, the code is not provided explicitly. It is available online via the above link.

Appendix G

C++–Code

G.1 Data Analysis Part

G.1.1 Muon Veto Calibration

Plotting 2D Maps

`www.pit.physik.uni-tuebingen.de/~kimmerle/diss/Darstellen_top_panel.C`

In this printed version, the code is not provided explicitly. It is available online via the above link.

Overlap Histo

`www.pit.physik.uni-tuebingen.de/~kimmerle/diss/ascii_hist.C`

In this printed version, the code is not provided explicitly. It is available online via the above link.

G.1.2 Muon Analysis Root–Macro

`www.pit.physik.uni-tuebingen.de/~kimmerle/diss/VetoCheck3.C`

In this printed version, the code is not provided explicitly. It is available online via the above link.

G.1.3 Landau Integral

`www.pit.physik.uni-tuebingen.de/~kimmerle/diss/Landau.C`

In this printed version, the code is not provided explicitly. It is available online via the above link.

G.1.4 Time Difference Root–Macro

`www.pit.physik.uni-tuebingen.de/~kimmerle/diss/time_diff_muon.C`

In this printed version, the code is not provided explicitly. It is available online via the above link.

G.2 Limit Calculation

G.2.1 Dark Matter Cross Section ROOT–Macro

`www.pit.physik.uni-tuebingen.de/~kimmerle/diss/WIMP_Spekt.C`

In this printed version, the code is not provided explicitly. It is available online via the above link.

G.2.2 Yellin method ROOT–Macro

`www.pit.physik.uni-tuebingen.de/~kimmerle/diss/statistics.C`

In this printed version, the code is not provided explicitly. It is available online via the above link.

List of Figures

1.1 Pioneer 10 . . . 7
1.2 NGC3198 in False Colors . . . 8
1.3 NGC3198 Rotation Curve . . . 9
1.4 Bullet Cluster in Light of X–Ray . . . 11
1.5 MS1054: X–Ray Distribution . . . 13
1.6 MS1054: Gravitational Centers . . . 14
1.7 Formation of a Supernova Ia . . . 16
1.8 Distance–Redshift Relation . . . 18
1.9 Modification of the Hubble Law . . . 20
1.10 Supernova Result for Matter Content . . . 21
1.11 CMB Map from the WMAP Satellite . . . 23
1.12 CMB Power–Spectrum . . . 24
1.13 Time–Line of the Universe . . . 25

2.1 GRT Experiment . . . 30
2.2 Laboratory Test of Newton's 2nd Law . . . 32

3.1 Table of Elements . . . 34
3.2 Table of Isotopes . . . 35
3.3 Muon Decay . . . 37
3.4 Z0 Decay . . . 38
3.5 Distribution of Light Elements in the Universe . . . 43
3.6 DAMA Result . . . 45
3.7 CDMS II Result . . . 46

5.1 LNGS Site . . . 52
5.2 Shielding Factor for Muons . . . 53
5.3 Setup of the CRESST Experiment . . . 56
5.4 Detector Module of the CRESST II Experiment . . . 57

6.1 Muon Veto Setup . . . 60
6.2 Cabling of the Muon Veto . . . 62

6.3 Comparison of the Results for the Top Panel 67
6.4 Comparison of the Results for the Side Panel 68
6.5 Comparison of the Results for the Bottom Panel 69
6.6 Overlap between Gamma and Muon Population 70

7.1 Sum Signal of Veto System 73
7.2 Muon Spectrum of a Example Panel 74
7.3 Spectrum of Example Panel after Cuts Applied 76
7.4 Simulated and Measured Multiplicities of Muon Veto System . 79
7.5 "Clear Muon Event" Group Investigation 81
7.6 Muon Candidate Rate 82
7.7 Standard Pulse 87
7.8 Test Pulse 88
7.9 Scatter Plot from Neutron Calibration 91
7.10 Quenching Factor 92
7.11 Quenching Factor Comparison 93
7.12 Time Difference between Zora Detector and Veto System . . . 95
7.13 Time Difference versus Pulse Height 96

9.1 Simple Recoil Spectrum 105
9.2 Form Factor of Tungsten 109
9.3 Recoil Spectra of Elastic Scattering from WIMPs 111
9.4 Recoil Spectrum of Inelastic Scattering from WIMPs 112
9.5 Cross Section Limit 114

10.1 Poisson Distribution 116
10.2 Both– vs. One– Sided Limit 118
10.3 Erlang Distribution 121
10.4 Erlang Integral Distribution 122

11.1 Variable Transformation of an Energy Spectrum 126
11.2 Examples of Simulated "Largest Gap"–Spectra 129
11.3 Gap Distribution in case of Lambda = 3.0 130
11.4 Examples of the CL calculation 132
11.5 Lookup Table for CL=0.9 and Maximum Gap 133
11.6 Exclusion over Maximum Gap Size for Various Count Numbers 136
11.7 Confidence Level function 138
11.8 Comparison of Maximum and Optimal Gap Method 140
11.9 Difference between the SW Implementations vs. Upper Limit . 141

12.1 LG spectra for the B-1D method 145
12.2 Input Confidence Level for P–2D 146

12.3 Input Confidence Level for C–2D 147
12.4 Example for Failure of C–2D Method 148
12.5 Comparison of 2D Exclusions 150
12.6 Example for Failure of P–2D Method 151

13.1 Event Distribution of Signal-like Background 154
13.2 Event Distribution of Quarter Background 155
13.3 Discrimination Parameter Plot of CRESST 156
13.4 Event Distribution of Circular Leakage 157
13.5 Event Distribution of 30 % Circular Leakage 158
13.6 Calculation for CLB30 with True Value 5 160
13.7 Methods Tested with SDB 161
13.8 RMS Spread in SDB 162
13.9 Methods Tested with OQB100 163
13.10Methods Tested with OQB50 164
13.11Methods Tested with CLB100 165
13.12Methods Tested with CLB30 166
13.13RMS Spread of the methods 168

A.1 Fast Analog Sum (FIFO) 175

C.1 Landau Function 186

List of Tables

3.1 Fermion like Particles of the Standard Model 40
3.2 Boson like Particles of the Standard Model 40
3.3 Possible Candidates for a Dark Matter Particle 42

6.1 Veto Panels 60

7.1 Muon Veto Fit Parameter 75
7.2 Measured Quenching Factor 91

9.1 Radius Parameterization for Helm Form Factor 108

10.1 Poisson Exclusion 119

11.1 Weight factors in case of Lambda = 3.0 131
11.2 Comparison of the 1D Yellin Method Implementations 142

13.1 Comparison of Saturation Values 162

Bibliography

[1] Viktor T. Toth and Slava G. Turyshev. Pioneer anomaly: Evaluating newly recovered data. *arxiv*, 2007. 12 pages, 15 figures, invited talk at the "III Mexican Meeting on Mathematical and Experimental Physics," Mexico City, Mexico, 10-14 September 2007, `http://arxiv.org/pdf/0710.2656v1`, abstract: The Pioneer 10/11 spacecraft yielded the most precise navigation in deep space to date. However, their radio-metric tracking data received from the distances between 20–70 astronomical units from the Sun consistently indicated the presence of a small, anomalous, Doppler frequency drift. The drift is a blue frequency shift that can be interpreted as a sunward acceleration of $a_P = (8.74 \pm 1.33) \times 10^{-10} m/s^2$ for each particular spacecraft. This signal has become known as the Pioneer anomaly; the nature of this anomaly remains unexplained. New Pioneer 10 and 11 radio-metric Doppler data recently became available. The much extended set of Pioneer Doppler data is the primary source for new upcoming investigation of the anomaly. We also have almost entire records of flight telemetry files received from the the Pioneers. Together with original project documentation and newly developed software tools, this additional information is now used to reconstruct the engineering history of both spacecraft. To that extent, a thermal model of the Pioneer vehicles is being developed to study possible contribution of thermal recoil force acting on the two spacecraft. In addition, to improve the accuracy of orbital reconstruction, we developed a new approach that uses actual flight telemetry data during trajectory analysis of radio-metric Doppler files. The ultimate goal of these efforts is to investigate possible contributions of the thermal recoil force to the detected anomalous acceleration.

[2] John D. Anderson, Philip A. Laing, Eunice L. Lau, Anthony S. Liu, Michael Martin Nieto, and Slava G. Turyshev. Indication, from pioneer 10/11, galileo, and ulysses data, of an apparent anomalous, weak, long-range acceleration. *Phys.Rev.Lett. 81*, pages 2858–2861, 1998. Revtex, 4 pages and 1 figure. Minor changes for publication; `http://arxiv.org/`

pdf/gr-qc/9808081v2; abstract: Radio metric data from the Pioneer 10/11, Galileo, and Ulysses spacecraft indicate an apparent anomalous, constant, acceleration acting on the spacecraft with a magnitude $\sim 8.5 \times 10^{-8}$ cm/s^2, directed towards the Sun. Two independent codes and physical strategies have been used to analyze the data. A number of potential causes have been ruled out. We discuss future kinematic tests and possible origins of the signal.

[3] Nasa. Pioneer nasa. http://www.nasa.gov/externalflash/NASA45/21/; 21_pioneer_83hc357.jpg.

[4] M. Moniez. Review of results from eros microlensing search for massive compact objects. *Arxiv*, 2009. IDM2008 - identification of dark matter 2008, Stockholm : Suède (2008); http://arxiv.org/pdf/0901.0985v2; abstract: We present the results of the EROS2 search for the hidden galactic matter of the halo through the gravitational microlensing of stars in the Magellanic clouds. Microlensing was also searched for and found in the Milky-Way plane, where foreground faint stars are expected to lens background stars. A total of 67 million of stars were monitored over a period of about 7 years. Hundreds of microlensing candidates have been found in the galactic plane, but only one was found towards the subsample of bright –well measured– Magellanic stars. This result implies that massive compact halo objects (machos) in the mass range $10^{-7}M_\odot < M < 5M_\odot$ are ruled out as a major component of the Milky Way Halo.

[5] wikipedia. All pictures from that site: http://commons.wikimedia.org and free under this licence:
Permission is granted to copy, distribute and/or modify this document under the terms of the GNU Free Documentation License, Version 1.2 or any later version published by the Free Software Foundation; with no Invariant Sections, no Front-Cover Texts, and no Back-Cover Texts. A copy of the license is included in the section entitled "GNU Free Documentation License".
More details can be found here: http://en.wikipedia.org/wiki/GNU_Free_Documentation_LicenseSome pictures refer to the public domain in the US, but were found on wiki common:This work is in the public domain in the United States because it is a work of the United States Federal Government under the terms of Title 17, Chapter 1, Section 105 of the US Code.

[6] K. G. Begeman. H i rotation curves of spiral galaxies. *Astronomy and Astrophysics*, pages 47–60, 1989. found at `http://adsabs.harvard.edu/abs/1989A%26A...223...47B`.

[7] Douglas Clowe, Marusa Bradac, Anthony H. Gonzalez, Maxim Markevitch, Scott W. Randall, Christine Jones, and Dennis Zaritsky. A direct empirical proof of the existence of dark matter. *arxiv*, 2006. Accepted for publication in ApJL, `http://arxiv.org/pdf/astro-ph/0608407v1`, abstract: We present new weak lensing observations of 1E0657-558 (z=0.296), a unique cluster merger, that enable a direct detection of dark matter, independent of assumptions regarding the nature of the gravitational force law. Due to the collision of two clusters, the dissipationless stellar component and the fluid-like X-ray emitting plasma are spatially segregated. By using both wide-field ground based images and HST/ACS images of the cluster cores, we create gravitational lensing maps which show that the gravitational potential does not trace the plasma distribution, the dominant baryonic mass component, but rather approximately traces the distribution of galaxies. An 8-sigma significance spatial offset of the center of the total mass from the center of the baryonic mass peaks cannot be explained with an alteration of the gravitational force law, and thus proves that the majority of the matter in the system is unseen.

[8] M. J. Jee, R. L. White, H. C. Ford, J. P. Blakeslee, G. D. Illingworth, D. A. Coe, and K. V. H. Tran. Hst/acs weak-lensing and chandra x-ray studies of the high-redshift cluster ms 1054-0321. *arxiv*, 2005. Accepted for publication in apj. Full-resolution version can be downloaded from `http://acs.pha.jhu.edu/~mkjee/ms1054.pdf`, `http://arxiv.org/pdf/astro-ph/0508044v1`, abstract: We present Hubble Space Telescope/Advanced Camera for Surveys (ACS) weak-lensing and Chandra X-ray analyses of MS 1054-0321 at z=0.83, the most distant and X-ray luminous cluster in the Einstein Extended Medium-Sensitivity Survey (EMSS). The high-resolution mass reconstruction through ACS weak-lensing reveals the complicated dark matter substructure in unprecedented detail, characterized by the three dominant mass clumps with the four or more minor satellite groups within the current ACS field. The direct comparison of the mass map with the Chandra X-ray image shows that the eastern weak-lensing substructure is not present in the X-ray image and, more interestingly, the two X-ray peaks are displaced away from the hypothesized merging direction with respect to the corresponding central and western mass clumps, possibly because of ram pressure. In addition, as observed in our previous weak-lensing

study of another high-redshift cluster CL 0152-1357 at $z = 0.84$, the two dark matter clumps of MS 1054-0321 seem to be offset from the galaxy counterparts. We examine the significance of these offsets and discuss a possible scenario, wherein the dark matter clumps might be moving ahead of the cluster galaxies. The non-parametric weak-lensing mass modeling gives a projected mass of $M(r < 1Mpc) = (1.02 + -0.15)x10^{15}$ solar mass, where the uncertainty reflects both the statistical error and the cosmic shear effects. Our temperature measurement of $T = 8.9^{+1.0}_{-0.8}\,keV$ utilizing the newest available low-energy quantum efficiency degradation prescription for the Chandra instrument, together with the isothermal beta description of the cluster ($r_c = 16" + -15"$ and $beta = 0.78 \pm 0.08$), yields a projected mass of $M(r < 1Mpc) = (1.2 + -0.2)x10^{15}$ solar mass, consistent with the weak-lensing result.

[9] Walter F. Brisken, John M. Benson, A. J. Beasley, Edward B. F omalont, W. M. Goss, and S. E. Thorsett. Measurement of the parallax of psr b0950+08 using the vlba. *The Astrophysical Journal*, 2000. `http://stacks.iop.org/0004-637X/541/i=2/a=959`; abstract: A new technique has been developed to remove the ionosphere's distorting effects from low-frequency VLBI data. By fitting dispersive and nondispersive components to the phases of multifrequency data, the ionosphere can be effectively removed from the data without the use of a priori calibration information. This technique, along with the new gating capability of the VLBA correlator, was used to perform accurate astrometry on pulsar B0950+08, resulting in a much improved measurement of this pulsar's proper motion ($\mu_\alpha = -1.6 \pm 0.4masyr^{-1}$, $\mu_\delta = 29.5 \pm 0.5masyr^{-1}$) and parallax ($\pi = 3.6 \pm 0.3mas$). This puts the pulsar at a distance of $280 \pm 25pc$, about twice as far as previous estimates, but in good agreement with models of the electron density in the Local Bubble.

[10] P. A. Mazzali, F. K. Roepke, S. Benetti, and W. Hillebrandt. A common explosion mechanism for type ia supernovae. *Arxiv*, 2007. 8 pages, 2 figures; `http://arxiv.org/pdf/astro-ph/0702351v1`; abstract: Type Ia supernovae, the thermonuclear explosions of white dwarf stars composed of carbon and oxygen, were instrumental as distance indicators in establishing the acceleration of the universe's expansion. However, the physics of the explosion are debated. Here we report a systematic spectral analysis of a large sample of well observed type Ia supernovae. Mapping the velocity distribution of the main products of nuclear burning, we constrain theoretical scenarios. We find that all supernovae have low-velocity cores of stable iron-group elements. Outside this core, nickel-

56 dominates the supernova ejecta. The outer extent of the iron-group material depends on the amount of nickel-56 and coincides with the inner extent of silicon, the principal product of incomplete burning. The outer extent of the bulk of silicon is similar in all SNe, having an expansion velocity of $\sim 11000 km/s$ and corresponding to a mass of slightly over one solar mass. This indicates that all the supernovae considered here burned similar masses, and suggests that their progenitors had the same mass. Synthetic light curve parameters and three-dimensional explosion simulations support this interpretation. A single explosion scenario, possibly a delayed detonation, may thus explain most type Ia supernovae.

[11] S. Bailey, G. Aldering, P. Antilogus, C. Aragon, C. Baltay, S. Bongard, C. Buton, M. Childress, N. Chotard, Y. Copin, E. Gangler, S. Loken, P. Nugent, R. Pain, E. Pecontal, R. Pereira, S. Perlmutter, D. Rabinowitz, G. Rigaudier, K. Runge, R. Scalzo, G. Smadja, H. Swift, C. Tao, R. C. Thomas, and C. Wu. Using spectral flux ratios to standardize sn ia luminosities. *arxiv*, 2009. 6 pages, 3 figures, 2 tables; accepted by A&A Letters; v2 fixed typos of literature SNe redshifts in table 2, final language and formatting edits, small improvements to literature SNe comparison, `http://arxiv.org/pdf/0905.0340v2`, abstract: We present a new method to standardize Type Ia supernova (SN Ia) luminosities to $\sim< 0.13$ magnitudes using flux ratios from a single flux-calibrated spectrum per SN. Using Nearby Supernova Factory spectrophotomery of 58 SNe Ia, we performed an unbiased search for flux ratios which correlate with SN Ia luminosity. After developing the method and selecting the best ratios from a training sample, we verified the results on a separate validation sample and with data from the literature. We identified multiple flux ratios whose correlations with luminosity are stronger than those of light curve shape and color, previously identified spectral feature ratios, or equivalent width measurements. In particular, the flux ratio R(642/443) = F(642 nm) / F(443 nm) has a correlation of 0.95 with SN Ia absolute magnitudes. Using this single ratio as a correction factor produces a Hubble diagram with a residual scatter standard deviation of $0.125 \pm 0.011 mag$, compared with $0.161 \pm 0.015 mag$ when fit with the SALT2 light curve shape and color parameters x1 and c. The ratio R(642/443) is an effective correction factor for both extrinsic dust reddening and instrinsic variations such as those of SN 1991T-like and SN 1999aa-like SNe. When combined with broad-band color measurements, spectral flux ratios can standardize SN Ia magnitudes to $\sim 0.12 mag$. These are the first spectral metrics that improve over the standard normalization methods based upon light curve shape and color and they

provide among the lowest scatter Hubble diagrams ever published.

[12] Saul Perlmutter and Brian P. Schmidt. Measuring cosmology with supernovae. *arxiv*, 2003. In Supernovae & Gamma Ray Bursts, K. Weiler, Ed., Springer, Lecture Notes in Physics (in press), 24 pages, 7 figs,`http://arxiv.org/pdf/astro-ph/0303428v1`, abstract: Over the past decade, supernovae have emerged as some of the most powerful tools for measuring extragalactic distances. A well developed physical understanding of type II supernovae allow them to be used to measure distances independent of the extragalactic distance scale. Type Ia supernovae are empirical tools whose precision and intrinsic brightness make them sensitive probes of the cosmological expansion. Both types of supernovae are consistent with a Hubble Constant within 10% of $H_0 = 70 km/s/Mpc$. Two teams have used type Ia supernovae to trace the expansion of the Universe to a look-back time more than 60% of the age of the Universe. These observations show an accelerating Universe which is currently best explained by a cosmological constant or other form of dark energy with an equation of state near w = p/rho = -1. While there are many possible remaining systematic effects, none appears large enough to challenge these current results. Future experiments are planned to better characterize the equation of state of the dark energy leading to the observed acceleration by observing hundreds or even thousands of objects. These experiments will need to carefully control systematic errors to ensure future conclusions are not dominated by effects unrelated to cosmology.

[13] Adam G. Riess, Louis-Gregory Strolger, John Tonry, Stefano Casertano, Henry C. Ferguson, Bahram Mobasher, Peter Challis, Alexei V. Filippenko, Saurabh Jha, Weidong Li, Ryan Chornock, Robert P. Kirshner, Bruno Leibundgut, Mark Dickinson, Mario Livio, Mauro Giavalisco, Charles C. Steidel, Narciso Benitez, and Zlatan Tsvetanov. Type ia supernova discoveries at z>1 from the hubble space telescope: Evidence for past deceleration and constraints on dark energy evolution. *Arxiv*, 2004. Accepted Astrophysical Journal, to Appear June 2004 72 pages, 17 Figures; `http://arxiv.org/pdf/astro-ph/0402512v2`; abstract: We have discovered 16 Type Ia supernovae (SNe Ia) with the Hubble Space Telescope (HST) and have used them to provide the first conclusive evidence for cosmic deceleration that preceded the current epoch of cosmic acceleration. These objects, discovered during the course of the GOODS ACS Treasury program, include 6 of the 7 highest-redshift SNe Ia known, all at $z > 1.25$, and populate the Hubble diagram in unexplored ter-

ritory. The luminosity distances to these and 170 previous SNe Ia are provided. A purely kinematic interpretation of the SN Ia sample provides evidence at the $> 99\%$ confidence level for a transition from deceleration to acceleration or similarly, strong evidence for a cosmic jerk. Using a simple model of the expansion history, the transition between the two epochs is constrained to be at $z = 0.46 \pm 0.13$. The data are consistent with the cosmic concordance model of $\Omega_M \sim 0.3$, $\Omega_\Lambda \sim 0.7 (\chi^2_{dof} = 1.06)$, and are inconsistent with a simple model of evolution or dust as an alternative to dark energy. For a flat Universe with a cosmological constant. When combined with external flat-Universe constraints we find $\omega = -1.02 + 0.13 - 0.19$ (and $\omega < -0.76$ at the 95% confidence level) for an assumed static equation of state of dark energy, $P = \omega/\rho c^2$. Joint constraints on both the recent equation of state of dark energy, ω_0, and its time evolution, $d\omega/dz$, are a factor of ~ 8 more precise than its first estimate and twice as precise as those without the SNe Ia discovered with HST. Our constraints are consistent with the static nature of and value of w expected for a cosmological constant (i.e., $\omega_0 = -1.0, d\omega/dz = 0$), and are inconsistent with very rapid evolution of dark energy. We address consequences of evolving dark energy for the fate of the Universe.

[14] D. N. Spergel, R. Bean, O. Doré, M. R. Nolta, C. L. Bennett, J. Dunkley, G. Hinshaw, N. Jarosik, E. Komatsu, L. Page, H. V. Peiris, L. Verde, M. Halpern, R. S. Hill, A. Kogut, M. Limon, S. S. Meyer, N. Odegard, G. S. Tucker, J. L. Weiland, E. Wollack, and E. L. Wright. Wilkinson microwave anisotropy probe (wmap) three year results: Implications for cosmology. *Arxiv*, 2006. 91 pgs, 28 figs. Accepted version of the 3-year paper as posted to `http://lambda.gsfc.nasa.gov/product/map/dr2/map_bibliography.cfm` in January 2007; `http://arxiv.org/pdf/astro-ph/0603449v2`; abstract: A simple cosmological model with only six parameters (matter density, $\Omega_m h^2$, baryon density, $\Omega_b h^2$, Hubble Constant, H_0, amplitude of fluctuations, σ_8, optical depth, τ, and a slope for the scalar perturbation spectrum, n_s) fits not only the three year WMAP temperature and polarization data, but also small scale CMB data, light element abundances, large-scale structure observations, and the supernova luminosity/distance relationship. Using WMAP data only, the best fit values for cosmological parameters for the power-law flat LCDM model are $(\Omega_m h^2, \Omega_b h^2, h, n_s, \tau, \sigma_8) = 0.1277 + 0.0080 - 0.0079, 0.02229 \pm 0.00073, 0.732 + 0.031 - 0.032, 0.958 + -0.016, 0.089 + -0.030, 0.761 + 0.049 - 0.048$). The three year data dramatically shrink the allowed volume in this six dimensional parameter space. Assuming that the primordial fluctuations are adiabatic with a power law spectrum, the

WMAP data alone require dark matter, and favor a spectral index that is significantly less than the Harrison-Zel'dovich-Peebles scale-invariant spectrum ($n_s = 1, r = 0$). Models that suppress large-scale power through a running spectral index or a large-scale cut-off in the power spectrum are a better fit to the WMAP and small scale CMB data than the power-law LCDM model; however, the improvement in the fit to the WMAP data is only $\Delta\chi^2 = 3$ for 1 extra degree of freedom. The combination of WMAP and other astronomical data yields significant constraints on the geometry of the universe, the equation of state of the dark energy, the gravitational wave energy density, and neutrino properties. Consistent with the predictions of simple inflationary theories, we detect no significant deviations from Gaussianity in the CMB maps.

[15] Ralf Aurich, Holger S. Janzer, Sven Lustig, and Frank Steiner. Do we live in a "small universe"? *Arxiv*, 2007. abstract: We compute the effects of a compact flat universe on the angular correlation function, the angular power spectrum, the circles-in-the-sky signature, and the covariance matrix of the spherical harmonics coefficients of the cosmic microwave background radiation using the full Boltzmann physics. Our analysis shows that the Wilkinson Microwave Anisotropy Probe (WMAP) three-year data are well compatible with the possibility that we live in a flat 3-torus with volume $\sim 5x10^3 Gpc^3$. ; `http://arxiv.org/pdf/0708.1420v2`.

[16] WMAP Collaboration. Results of the wmap satalite, 2009. `http://map.gsfc.nasa.gov`.

[17] Slava G. Turyshev. Experimental tests of general relativity. *Annu. Rev. Nucl. Part. Sci. 58, 207-248*, 2008. revtex4, 30 pages, 10 figures, `http://arxiv.org/pdf/0806.1731v2`, abstract: Einstein's general theory of relativity is the standard theory of gravity, especially where the needs of astronomy, astrophysics, cosmology and fundamental physics are concerned. As such, this theory is used for many practical purposes involving spacecraft navigation, geodesy, and time transfer. Here I review the foundations of general relativity, discuss recent progress in the tests of relativistic gravity in the solar system, and present motivations for the new generation of high-accuracy gravitational experiments. I discuss the advances in our understanding of fundamental physics that are anticipated in the near future and evaluate the discovery potential of the recently proposed gravitational experiments.

[18] Particle Data Group. Particle data group and w.m. yao et al. *J. Phys. G 33,205*, 2006.

[19] Albert Einstein. Sitzungsberichte der preussischen akademie der wissenschaften zu berlin. *Annalen der Physik 49,146*, 1916.

[20] Steven Weinberg. Gravitation and cosmology. *Rev. Mod. Phys. 61*, 1989.

[21] Robert H. Sanders and Stacy S. McGaugh. Modified newtonian dynamics as an alternative to dark matter. *Ann.Rev.Astron. & Astrophys. 40*, pages 263–317, 2002. To be published in volume 40 of Annual Reviews of Astronomy & Astrophysics. 36 pages plus 12 figures and 1 table, `http://arxiv.org/pdf/astro-ph/0204521v1`, abstract: Modified Newtonian dynamics (MOND) is an empirically motivated modification of Newtonian gravity or inertia suggested by Milgrom as an alternative to cosmic dark matter. The basic idea is that at accelerations below $a_0 \approx 10^{-8} cm/s^2 \approx cH_0/6$ the effective gravitational attraction approaches $\sqrt{g_N * a_0}$ where gN is the usual Newtonian acceleration. This simple algorithm yields flat rotation curves for spiral galaxies and a mass-rotation velocity relation of the form $M \propto V^4$ that forms the basis for the observed luminosity-rotation velocity relation– the Tully-Fisher law. We review the phenomenological success of MOND on scales ranging from dwarf spheroidal galaxies to superclusters, and demonstrate that the evidence for dark matter can be equally well interpreted as evidence for MOND. We discuss the possible physical basis for an acceleration-based modification of Newtonian dynamics as well as the extension of MOND to cosmology and structure formation.

[22] M. B. Gerrard and T. J. Sumner. The effect of a fifth large-scale space-time dimension on orbital dynamics. *arxiv*, 2007. 15 pages, 9 figures Updated to include Pioneer Anomaly - 1 additional figure, `http://arxiv.org/pdf/gr-qc/0605080v2`, abstract: A model based on simple assumptions about 4-dimensional space-time being closed and isotropic, and embedded in a 5th large-scale dimension, r, representing the radius of curvature of space-time, has been used in an application of Newton's Second Law to describe a system with angular momentum. It has been found that the equations of MOND used to explain the rotation curves of galaxies appear as a limit within this derivation and that there is a universal acceleration constant, ao, with a value, again consistent with that used by MOND. This approach does not require modification of Newtonian dynamics, only its extension into a fifth large-scale dimension. The transition from the classical Newtonian dynamics to the MOND

regime emerges naturally and without the introduction of arbitrary fitting functions, if this 5-dimensional model is adopted. The paper also includes the derivation of an effect in 5-dimensional orbital dynamics which is in reasonable agreement with the observed Pioneer Anomaly.

[23] M. B. Gerrard and T. J. Sumner. Earth flyby and pioneer anomalies. *arxiv*, 2008. 10 pages, 3 figures. Updated with clarified angle definitions and formatting, `http://arxiv.org/pdf/0807.3158v2`, abstract: Applying Newtonian dynamics in five dimensions rather than four, to a universe that is closed, isotropic and expanding, suggests that under certain circumstances an additional and previously unidentified acceleration can arise affecting the four dimensional motion of spacecraft. The reported acceleration anomalies from several Earth flybys and from the Pioneer spacecrafts are in reasonable agreement with the predicted values of this additional acceleration. Equations governing this additional acceleration have been derived from first principles, without the introduction of free parameters or new constants and without amendment to the law of gravity.

[24] Silvia Behar and Moshe Carmeli. Derivation of the tully-fisher law from general relativity theory: Doubts about the existence of halo dark matter. *Int.J.Theor.Phys. 39*, pages 1397–1404, 2000. `http://arxiv.org/pdf/astro-ph/9907244v1`, abstract: Observations show that for disk galaxies the fourth power of the circular velocity of stars around the core of the galaxy is proportional to the luminosity L. This is known as the Tully-Fisher law. Since L is proportional to the mass M of the galaxy, it follows that the fourth power of the circular velocity is proportional to M. Newtonian mechanics, however, tells that the square of the circular velocity is proportional to M. In order to rectify this big difference, astronomers assume the existence of halo dark matter. In this paper we show that general relativity theory yields a term of the Tully-Fisher form. This puts doubts about the necessity and existence of halo dark matter for galaxies.

[25] et. al. J. H. Gundlach. Laboratory test of newton's second law for small accelerations. *Phys.Rev.Lett. 98*, 2007. `http://link.aps.org/doi/10.1103/PhysRevLett.98.150801`; abstract: We have tested the proportionality of force and acceleration in Newton's second law, $F = ma$, in the limit of small forces and accelerations. Our tests reach well below the acceleration scales relevant to understanding several current astrophysical puzzles such as the flatness of galactic rotation curves, the

Pioneer anomaly, and the Hubble acceleration. We find good agreement with Newton's second law at accelerations as small as $5 \times 10^{-14} m/s^2$.

[26] Matthias Schädel and Andreas Türler. Ein platz für schwergewichte. *Physik Journal*, Juni 2009. Abstract: Modernen Alchemisten gleich haben Forscher in den vergangenen Jahrzehnten das Periodensystem wiederholt um neue Elemente erweitert. Obwohl sich in den Experimenten immer höchstens ein einzelnes Atom der superschweren Elemente befindet, das innerhalb von Sekunden zerfällt, ist es gelungen, chemische Verbindungen zu erzeugen und zu untersuchen.

[27] Matthew Colless. Cosmological results from the 2df galaxy redshift survey. *arxiv*, 2003. 11 pages, to appear in Carnegie Observatories Astrophysics Series, Vol.2: Measuring and Modeling the Universe, ed. W.L. Freedman (Cambridge: Cambridge University Press); full-colour, full-resolution version at http://www.mso.anu.edu.au/2dFGRS/Public/Publications, `http://arxiv.org/pdf/astro-ph/0305051v1`, abstract: The 2dF Galaxy Redshift Survey (2dFGRS) has produced a three-dimensional map of the distribution of 221,000 galaxies covering 5% of the sky and reaching out to a redshift z=0.3. This is first map of the large-scale structure in the local Universe to probe a statistically representative volume, and provides direct evidence that the large-scale structure of the Universe grew through gravitational instability. Measurements of the correlation function and power spectrum of the galaxy distribution have provided precise measurements of the mean mass density of the Universe and the relative contributions of cold dark matter, baryons, and neutrinos. The survey has produced the first measurements of the galaxy bias parameter and its variation with galaxy luminosity and type. Joint analysis of the 2dFGRS and cosmic microwave background power spectra gives independent new estimates for the Hubble constant and the vacuum energy density, and constrains the equation of state of the vacuum.

[28] M. L. Perl and et. al. Evidence for anomalous lepton production in e^+-e^- annihilation. *Phys.Rev.Lett. 35*, 1975. `http://prola.aps.org/abstract/PRL/v35/i22/p1489_1` ; DOI: doi:10.1103/PhysRevLett.35.1489.

[29] Christine Sutton. Meet the family: the leptons. *J J THOMSON'S ELECTRON*. `http://www.iop.org/EJ/article/0031-9120/32/4/017/pe7404.pdf?request-id=8d241913-50bf-4f1c-bcc8-2a3fd1d668c1`.

[30] Frank Daniel Steffen. Dark matter candidates - axions, neutralinos, gravitinos, and axinos. *Eur.Phys.J.*, 2008. 31 pages, 14 figures, abstract: The existence of dark matter provides strong evidence for physics beyond the Standard Model. Extending the Standard Model with the Peccei-Quinn symmetry and/or supersymmetry, compelling dark matter candidates appear. For the axion, the neutralino, the gravitino, and the axino, I review primordial production mechanisms, cosmological and astrophysical constraints, experimental searches, and prospects for experimental identification. `http://arxiv.org/pdf/0811.3347v1`.

[31] C. A. Baker, D. D. Doyle, P. Geltenbort, K. Green, M. G. D. van der Grinten, P. G. Harris, P. Iaydjiev, S. N. Ivanov, D. J. R. May, J. M. Pendlebury, J. D. Richardson, D. Shiers, and K. F. Smith. An improved experimental limit on the electric dipole moment of the neutron. *Phys.Rev.Lett. 97*, 2006. `http://arxiv.org/pdf/hep-ex/0602020v3`; abstract: An experimental search for an electric-dipole moment (EDM) of the neutron has been carried out at the Institut Laue-Langevin (ILL), Grenoble. Spurious signals from magnetic-field fluctuations were reduced to insignificance by the use of a cohabiting atomic-mercury magnetometer. Systematic uncertainties, including geometric-phase-induced false EDMs, have been carefully studied. Two independent approaches to the analysis have been adopted. The overall results may be interpreted as an upper limit on the absolute value of the neutron EDM of $d_n \leq 2.9x10^{-26} e \cdot cm$ (90% CL).

[32] Gianfranco Bertone, Dan Hooper, and Joseph Silk. Particle dark matter: Evidence, candidates and constraints. *arxiv*, 2004. 144 pages, 46 figures, submitted to Physics Reports, `http://arxiv.org/pdf/hep-ph/0404175v2`, abstract: In this review article, we discuss the current status of particle dark matter, including experimental evidence and theoretical motivations. We discuss a wide array of candidates for particle dark matter, but focus on neutralinos in models of supersymmetry and Kaluza-Klein dark matter in models of universal extra dimensions. We devote much of our attention to direct and indirect detection techniques, the constraints placed by these experiments and the reach of future experimental efforts.

[33] Brian Fields and Subir Sarkar. Big-bang nucleosynthesis (particle data group mini-review). *W.-M. Yao et al., J. Phys. G33*, page 1, 2006. 11 pages, 1 (new) figure; from Review of Particle Physics 2006 (`http://pdg.lbl.gov/`), `http://arxiv.org/pdf/astro-ph/0601514v2`, abstract: A critical review is given of the current status of cosmological

nucleosynthesis. In the framework of the Standard Model with 3 types of relativistic neutrinos, the baryon-to-photon ratio, η, corresponding to the inferred primordial abundances of deuterium and helium-4 is consistent with the independent determination of η from WMAP observations of anisotropies in the cosmic microwave background. However the primordial abundance of lithium-7 inferred from observations is significantly below its expected value. Taking systematic uncertainties in the abundance estimates into account, there is overall concordance in the range $\eta = (4.7 - 6.5)x10^{-10}$ @ 95% c.l. (corresponding to a cosmological baryon density $\Omega_B h^2 = 0.017$ - 0.024). The D and He-4 abundances, together with the CMB determination of η, provide the bound $N_\nu = 3.24 \pm 1.2$ @ 95% c.l. on the effective number of neutrino species. Other constraints on new physics are discussed briefly.

[34] R. Bernabei, P. Belli, F. Cappella, R. Cerulli, C. J. Dai, A. d'Angelo, H. L. He, A. Incicchitti, H. H. Kuang, J. M. Ma, F. Montecchia, F. Nozzoli, D. Prosperi, X. D. Sheng, and Z. P. Ye. First results from dama/libra and the combined results with dama/nai. *arxiv*, 2008. 40 pages, 21 figures, 6 tables, `http://arxiv.org/pdf/0804.2741v1`, abstract:The highly radiopure $\simeq$ 250 kg NaI(Tl) DAMA/LIBRA set-up is running at the Gran Sasso National Laboratory of the I.N.F.N.. In this paper the first result obtained by exploiting the model independent annual modulation signature for Dark Matter (DM) particles is presented. It refers to an exposure of 0.53 ton$\times$yr. The collected DAMA/LIBRA data satisfy all the many peculiarities of the DM annual modulation signature. Neither systematic effects nor side reactions can account for the observed modulation amplitude and contemporaneously satisfy all the several requirements of this DM signature. Thus, the presence of Dark Matter particles in the galactic halo is supported also by DAMA/LIBRA and, considering the former DAMA/NaI and the present DAMA/LIBRA data all together (total exposure 0.82 ton$\times$yr), the presence of Dark Matter particles in the galactic halo is supported at 8.2 σ C.L..

[35] V. A. Kudryavtsev, M. Robinson, and N. J. C. Spooner. The expected background spectrum in nai dark matter detectors and the dama result. *Arxiv*, 2009. `http://arxiv.org/pdf/0912.2983v1`; abstract: Detailed Monte Carlo simulations of the expected radioactive background rates and spectra in NaI crystals are presented. The obtained spectra are then compared to those measured in the DAMA/NaI and DAMA/LIBRA experiments. The simulations can be made consistent with the measured DAMA spectrum only by assuming higher than reported concentrations

of some isotopes and even so leave very little room for the dark matter signal. We conclude that any interpretation of the annual modulation of the event rate observed by DAMA as a dark matter signal, should include full consideration of the background spectrum. This would significantly restrict the range of dark matter models capable of explaining the modulation effect.

[36] The CDMS Collaboration and Z. Ahmed. Results from the final exposure of the cdms ii experiment. *arxiv*, 2009. `http://arxiv.org/pdf/0912.3592v1`; abstract: We report results from a blind analysis of the final data taken with the Cryogenic Dark Matter Search experiment (CDMS II) at the Soudan Underground Laboratory, Minnesota, USA. A total raw exposure of 612 kg-days was analyzed for this work. We observed two events in the signal region; based on our background estimate, the probability of observing two or more background events is 23
data set an upper limit on the Weakly Interacting Massive Particle (WIMP)-nucleon elastic-scattering spin-independent cross-section of $7.0x10^{-44}cm^2$ for a WIMP of mass $70GeV/c^2$ at the 90
level. Combining this result with all previous CDMS II data gives an upper limit on the WIMP-nucleon spin-independent cross-section of $3.8x10^{-44}cm^2$ for a WIMP of mass $70GeV/c^2$. We also exclude new parameter space in recently proposed inelastic dark matter models.

[37] Joachim Kopp, Thomas Schwetz, and Jure Zupan. Global interpretation of direct dark matter searches after cdms-ii results. *arxiv*, 2009. `http://arxiv.org/pdf/0912.4264v1`; abstract: We perform a global fit to data from Dark Matter (DM) direct detection experiments, including the recent CDMS-II results. We discuss possible interpretations of the DAMA annual modulation signal in terms of spin-independent and spin-dependent DM-nucleus interactions, both for elastic and inelastic scattering. We find that in the spin-dependent inelastic scattering off protons a good fit to all data is obtained. We present a simple toy model realizing such a scenario. In all the remaining cases the DAMA allowed regions are disfavored by other experiments or suffer from severe fine tuning of DM parameters with respect to the galactic escape velocity. Finally, we also entertain the possibility that the two events observed in CDMS-II are an actual signal of elastic DM scattering, and we compare the resulting CDMS-II allowed regions to the exclusion limits from other experiments.

[38] G. Angloher, M. Bauer, I. Bavykina, A. Bento, A. Brown, C. Bucci, C. Ciemniak, C. Coppi, G. Deuter, F. von Feilitzsch, D. Hauff, S. Henry,

P. Huff, J. Imber, S. Ingleby, C. Isaila, J. Jochum, M. Kiefer, M. Kimmerle, H. Kraus, J. C. Lanfranchi, R. F. Lang, B. Majorovits, M. Malek, R. McGowan, V. B. Mikhailik, E. Pantic, F. Petricca, S. Pfister, W. Potzel, F. Proebst, W. Rau, S. Roth, K. Rottler, C. Sailer, K. Schaeffner, J. Schmaler, S. Scholl, W. Seidel, L. Stodolsky, A. J. B. Tolhurst, I. Usherov, and W. Westphal. Commissioning run of the cresst-ii dark matter search. *Astroparticle Physics 31, pp. 270-276*, 2009. `http://arxiv.org/pdf/0809.1829v2`; abstract: The CRESST cryogenic direct dark matter search at Gran Sasso, searching for WIMPs via nuclear recoil, has been upgraded to CRESST-II by several changes and improvements.We present the results of a commissioning run carried out in 2007. The basic element of CRESST-II is a detector module consisting of a large ($300g$)$CaWO_4$ crystal and a very sensitive smaller ($2g$) light detector to detect the scintillation light from the $CaWO_4$.Information from light-quenching factor studies allows the definition of a region of the energy-light yield plane which corresponds to tungsten recoils. A neutron test is reported which supports the principle of using the light yield to identify the recoiling nucleus. Data obtained with two detector modules for a total exposure of 48 kg-days are presented. Judging by the rate of events in the "all nuclear recoils" acceptance region the apparatus shows a factor ten improvement with respect to previous results, which we attribute principally to the presence of the neutron shield. In the "tungsten recoils" acceptance region three events are found, corresponding to a rate of 0.063 per kg-day. Standard assumptions on the dark matter flux, coherent or spin independent interactions,then yield a limit for WIMP-nucleon scattering of $4.8 \times 10^{-7} pb$, at M_{WIMP} $50GeV$.

[39] J. Angle, E. Aprile, F. Arneodo, L. Baudis, A. Bernstein, A. Bolozdynya, P. Brusov, L. C. C. Coelho, C. E. Dahl, L. DeViveiros, A. D. Ferella, L. M. P. Fernandes, S. Fiorucci, R. J. Gaitskell, K. L. Giboni, R. Gomez, R. Hasty, L. Kastens, J. Kwong, J. A. M. Lopes, N. Madden, A. Manalaysay, A. Manzur, D. N. McKinsey, M. E. Monzani, K. Ni, U. Oberlack, J. Orboeck, G. Plante, R. Santorelli, J. M. F. dos Santos, P. Shagin, T. Shutt, P. Sorensen, S. Schulte, C. Winant, M. Yamashita, and for the XENON Collaboration. First results from the xenon10 dark matter experiment at the gran sasso national laboratory. *arxiv*, 2008. accepted for publication in Phys. Rev. Lett, `http://arxiv.org/pdf/0706.0039v2`, abstract: The XENON10 experiment at the Gran Sasso National Laboratory uses a 15 kg xenon dual phase time projection chamber (XeTPC) to search for dark matter weakly interacting massive particles (WIMPs). The detector measures simultaneously the scintillation and the ionization

produced by radiation in pure liquid xenon, to discriminate signal from background down to 4.5 keV nuclear recoil energy. A blind analysis of 58.6 live days of data, acquired between October 6, 2006 and February 14, 2007, and using a fiducial mass of 5.4 kg, excludes previously unexplored parameter space, setting a new 90
for the WIMP-nucleon spin-independent cross-section of 8.8 $\times 10^{-44} cm^2$ for a WIMP mass of 100 GeV/c^2, and 4.5 $\times 10^{-44} cm^2$ for a WIMP mass of 30 GeV/c^2. This result further constrains predictions of supersymmetric models.

[40] CDMS Collaboration. A search for wimps with the first five-tower data from cdms. *arxiv*, 2008. `http://arxiv.org/pdf/0802.3530v2`, abstract: We report first results from the Cryogenic Dark Matter Search (CDMS II) experiment running with its full complement of 30 cryogenic particle detectors at the Soudan Underground Laboratory. This report is based on the analysis of data acquired between October 2006 and July 2007 from 15 Ge detectors (3.75 kg), giving an effective exposure of 121.3 kg-d (averaged over recoil energies 10–100 keV, weighted for a weakly interacting massive particle (WIMP) mass of 60 Gev). A blind analysis, incorporating improved techniques for event reconstruction and data quality monitoring, resulted in zero observed events. This analysis sets an upper limit on the WIMP-nucleon spin-independent cross section of 6.6×10^{-44} cm^2 (4.6×10^{-44} cm^2 when combined with previous CDMS Soudan data) at the 90% confidence level for a WIMP mass of 60 GeV. By providing the best sensitivity for dark matter WIMPs with masses above 42 GeV/c^2, this work significantly restricts the parameter space for some of the favored supersymmetric models.

[41] EDELWEISS Collaboration. Sensitivity of the edelweiss wimp search to spin-dependent interactions. *Physics Letter B*, June 2005. `http://dx.doi.org/10.1016/j.physletb.2005.04.052`.

[42] Lngs website. `www.lngs.infn.it`.

[43] J. Gascon. Direct search for wimp dark matter. *Dans Astroparticles and cosmology, Frontier Group*, pages (2004) 91–107, 2005. abstract: We will review the experimental aspects of the direct search for WIMP dark matter. In thin search, one looks in a terrestrial target for nuclear recoils produced by the impacts with WIMPs from the galatic halo. After describing the different search strategies and review the currently running experiments and the prospects of future experiments.
`http://arxiv.org/pdf/astro-ph/0504241v1`.

[44] R. F. Lang, G. Angloher, M. Bauer, I. Bavykina, A. Bento, A. Brown, C. Bucci, C. Ciemniak, C. Coppi, G. Deuter, F. von Feilitzsch, D. Hauff, S. Henry, P. Huff, J. Imber, S. Ingleby, C. Isaila, J. Jochum, M. Kiefer, M. Kimmerle, H. Kraus, J. C. Lanfranchi, M. Malek, R. McGowan, V. B. Mikhailik, E. Pantic, F. Petricca, S. Pfister, W. Potzel, F. Pröbst, S. Roth, K. Rottler, C. Sailer, K. Schäffner, J. Schmaler, S. Scholl, W. Seidel, L. Stodolsky, A. J. B. Tolhurst, I. Usherov, and W. Westphal. Discrimination of recoil backgrounds in scintillating calorimeters. *arxiv*, 2009. 5 pages, 9 figures.

[45] B. Majorovits, S. Henry, and H. Kraus. Development of superconducting contacts for the cresst ii 66-channel superconducting quantum interference device readout system. *Review of Scientific Instruments*, 2007. `http://link.aip.org/link/?RSI/78/073301/1`.

[46] Sabine Roth. Sputtered tungsten thin films and composite detectors for the application in the dark matter experiments cresst and eureca, 2007. TU München; `http://www.e15.physik.tu-muenchen.de/fileadmin/downloads/thesis/dipl/2007_Sabine_Roth.pdf`.

[47] Michael Kiefer, Franz Pröbst, Godehard Angloher, Irina Bavykina, Dieter Hauff, and Wolfgang Seidel. Glued cawo4 detectors for the cresst-ii experiment. *Proceeding Cryoscint*, 2008. To appear in the proceedings of CryoScint08 (`http://cryoscint08.in2p3.fr`), Univ. Lyon 1, France, June 6th 2008, P. Di Stefano (IPN Lyon) and F. Petricca (MPP Munich) eds. 6 pages, 10 figures Version 2: Added I. Bavykina to the authors list; abstract: The Cryogenic Rare Event Search with Superconducting Thermometers Phase II (CRESST-II) at the L.N.G.S in Italy is searching for Dark Matter using low-temperature calorimeters. These detectors allow to discriminate different particles by simultaneous measurement of phonons and scintillation light. The sensors used consist of superconducting tungsten thin-film thermometers, which measure the thermal effect of the phonons created in an attached absorber crystal. It has been observed that the scintillation of the CaWO4 absorber degrades during the process of depositing the tungsten film. In order to prevent this, a new technique for producing the detectors was investigated. This technique might also be valuable by expanding the range of scintillator materials suitable for producing a Dark Matter detector. `http://arxiv.org/pdf/0809.4975v2`.

[48] H. Wulandari, J. Jochum, W. Rau, and F. von Feilitzsch. Neutron background studies for the cresst dark matter experiment. *arxiv*, 2004. 15

pages, 6 figures, http://arxiv.org/pdf/hep-ex/0401032v1, abstract: The new detection concept applied for the direct WIMP search experiment CRESST II, which enables a clear discrimination between electron recoils and nuclear recoils, will leave neutrons as the main background. This background will soon limit the sensitivity of the experiment and therefore become an important issue for the next phase of CRESST. We have performed a study based on Monte Carlo simulations to investigate how neutrons from different origins affect CRESST and which measures have to be taken to reach the projected sensitivity.

[49] J. C. Lanfranchi, C. Ciemniak, C. Coppi, F. von Feilitzsch, A. Gütlein, H. Hagn, C. Isaila, J. Jochum, M. Kimmerle, S. Pfister, W. Potzel, W. Rau, S. Roth, K. Rottler, C. Sailer, S. Scholl, I. Usherov, and W. Westphal. Neutron scattering facility for characterization of cresst and eureca detectors at mk temperatures. *Arxiv*, 2008. 6 pages, 7 figures, To appear in the proceedings of CryoScint08 (http://cryoscint08.in2p3.fr), Univ. Lyon 1, France, June 6th 2008, P. Di Stefano (IPN Lyon) and F. Petricca (MPP Munich) edshttp://arxiv.org/pdf/0810.0132v1, abstract: CRESST (Cryogenic Rare Event Search with Superconducting Thermometers) is an experiment located at the Gran Sasso underground laboratory and aimed at the direct detection of dark matter in the form of WIMPs. The setup has just completed a one year commissioning run in 2007 and is presently starting a physics run with an increased target mass. Scintillating $CaWO_4$ single crystals, operated at temperatures of a few millikelvin, are used as target to detect the tiny nuclear recoil induced by a WIMP. The powerful background identification and rejection of α, e^- and γ events is realized via the simultaneous measurement of a phonon and a scintillation signal generated in the $CaWO_4$ crystal. However, neutrons could still be misidentified as a WIMP signature. Therefore, a detailed understanding of the individual recoil behaviour in terms of phonon generation and scintillation light emission due to scattering on Ca, O or W nuclei, respectively, is mandatory. The only setup which allows to perform such measurements at the operating temperature of the CRESST detectors has been installed at the Maier-Leibnitz-Accelerator Laboratory in Garching and is presently being commissioned. The design of this neutron scattering facility is such that it can also be used for other target materials, e.g. $ZnWO_4$, $PbWO_4$ and others as foreseen in the framework of the future multitarget tonne-scale experiment EURECA (European Underground Rare Event Calorimeter Array).

[50] M. Kimmerle. *Muon Veto Guide*, 2008. http://www.pit.physik.

uni-tuebingen.de/~kimmerle/Vetoguide/userguide.pdf.

[51] D. Nicolodi. Calibration system for the muon veto scintillators employed in the cresst-ii dark matter search experiment., 2006. http://www.pit.physik.uni-tuebingen.de/diplom/nicolodi.pdf.

[52] Jens Leypoldt. Simlight, 1994. http://www.pit.physik.uni-tuebingen.de/simlight/simlight.html.

[53] J. Jochum. Private communication, 2006.

[54] R. F. Lang, G. Angloher, M. Bauer, I. Bavykina, A. Bento, A. Brown, C. Bucci, C. Ciemniak, C. Coppi, G. Deuter, F. von Feilitzsch, D. Hauff, S. Henry, P. Huff, J. Imber, S. Ingleby, C. Isaila, J. Jochum, M. Kiefer, M. Kimmerle, H. Kraus, J. C. Lanfranchi, B. Majorovits, M. Malek, R. McGowan, V. B. Mikhailik, E. Pantic, F. Petricca, S. Pfister, W. Potzel, F. Pröbst, S. Roth, K. Rottler, C. Sailer, K. Schäffner, J. Schmaler, S. Scholl, W. Seidel, L. Stodolsky, A. J. B. Tolhurst, I. Usherov, and W. Westphal. Electron and gamma background in cresst detectors. *Astroparticle Physics*, 2009. http://arxiv.org/pdf/0905.4282v1; abstract: The CRESST experiment monitors $300\,g$ $CaWO_4$ crystals as targets for particle interactions in an ultra low background environment. In this paper, we analyze the background spectra that are recorded by three detectors over many weeks of data taking. Understanding these spectra is mandatory if one wants to further reduce the background level, and allows us to cross-check the calibration of the detectors. We identify a variety of sources, such as intrinsic contaminations due to primordial radioisotopes and cosmogenic activation of the target material. In particular, we detect a $3.6\,keV$ X-ray line from the decay of 41-Ca with an activity of $(26 \pm 4)\mu Bq$, corresponding to a ratio $41 - Ca/40 - Ca = (2.2 \pm 0.3) \times 10^{-16}$.

[55] R. F. Lang, G. Angloher, M. Bauer, I. Bavykina, A. Bento, A. Brown, C. Bucci, C. Ciemniak, C. Coppi, G. Deuter, F. von Feilitzsch, D. Hauff, S. Henry, P. Huff, J. Imber, S. Ingleby, C. Isaila, J. Jochum, M. Kiefer, M. Kimmerle, H. Kraus, J. C. Lanfranchi, M. Malek, R. McGowan, V. B. Mikhailik, E. Pantic, F. Petricca, S. Pfister, W. Potzel, F. Pröbst, S. Roth, K. Rottler, C. Sailer, K. Schäffner, J. Schmaler, S. Scholl, W. Seidel, L. Stodolsky, A. J. B. Tolhurst, I. Usherov, and W. Westphal. Scintillator non-proportionality and gamma quenching in cawo4. *Arxiv*, 2009. http://arxiv.org/pdf/0910.4414v1; abstract: We measure and explain scintillator non-proportionality and gamma quenching of CaWO4

at low energies and low temperatures. Phonons that are created following an interaction in the scintillating crystal at temperatures of 15mK are used for a calorimetric measurement of the deposited energy, and the scintillation light is measured with a separate cryogenic light detector. Making use of radioactivity intrinsic to the scintillating crystal, the scintillator non-proportionality is mapped out to electron energies <5keV. The observed behavior is in agreement with a simple model based on Birks' law and the stopping power dE/dx for electrons. We find for Birks' constant $k_B = (18.5 \pm 0.7)$nm/keV in CaWO4. Gamma lines allow a measurement of the reduced light yield of photons with respect to electrons, as expected in the presence of scintillator non-proportionality. In particular, we show that gamma-induced events in CaWO4 give only about 90 percent of the light yield of electrons, at energies between 40keV and 80keV.

[56] Klaus Eitel. Investigation of ambient and μ-induced neutron background in lsm. *Journal of Physics*, 2010. `http://www.iop.org/EJ/article/1742-6596/203/1/012027/jpconf10_203_012027.pdf`, abstract: A good particle candidate for Cold Dark Matter (CDM) is the supersymmetric neutralino or more generally a weakly interacting massive particle (WIMP). The expected interaction rate of WIMPs with the detector medium in the direct detection experiments is below 0.01 events/kg/day. This makes a good knowledge of the background conditions highly important, especially with ever increasing sensitivity of the detectors. One major component of the background is related to energetic neutrons induced by cosmic muons. However, the flux of low energy and thermal neutrons typically from (α; n) reactions in the rock surrounding underground experiments gives also valuable information about the overall environmental activity. Detailed studies carried out in the framework of the Edelweiss experiment are presented with first identification of muon-induced neutron candidates in Ge bolometers.

[57] S. Yellin. Finding an upper limit in the presence of unknown background. *Phys.Rev. D66*, page 032005, 2002. 8 pages, 5 figures (eps), revtex4, amsmath.sty. Paper reorganized to improve readability, `http://arxiv.org/pdf/physics/0203002v2`, abstract: Experimenters report an upper limit if the signal they are trying to detect is non-existent or below their experiment's sensitivity. Such experiments may be contaminated with a background too poorly understood to subtract. If the background is distributed differently in some parameter from the expected signal, it is possible to take advantage of this difference to get a stronger limit

than would be possible if the difference in distribution were ignored. We discuss the "Maximum Gap" method, which finds the best gap between events for setting an upper limit, and generalize to "Optimum Interval" methods, which use intervals with especially few events. These methods, which apply to the case of relatively small backgrounds, do not use binning, are relatively insensitive to cuts on the range of the parameter, are parameter independent (i.e., do not change when a one-one change of variables is made), and provide true, though possibly conservative, classical one-sided confidence intervals.

[58] J. D. Lewin and P.F.Smith. Review of mathematics, numerical factors, and corrections for dark matter experiments based on elastic nuclear recoil. *Astropart.Phys. 6, 87*, 1996.

[59] F. Donato, N. Fornengo, and S. Scopel. Effects of galactic dark halo rotation on wimp direct detection. *Astropart.Phys. 9*, pages 247–260, 1998. 14 pages, 7 figures included as PS files, `http://arxiv.org/pdf/hep-ph/9803295v1`, abstract: The effects of a possible rotation of the galactic dark halo on the calculation of the direct detection rates for particle dark matter are analyzed, with special attention to the extraction of the upper limits on the WIMP–nucleon scalar cross section from the experimental data. We employ a model of dark halo rotation which describes the maximal possible effects. For WIMP masses above 50 GeV, the upper limit exclusion plot is modified by less than a factor of two when rotation is included. For lighter masses the effect can be stronger, suggesting the necessity to develop specific models of halo rotation in order to provide more accurate conclusions.

[60] Martin C. Smith and et. al. The rave survey: constraining the local galactic escape speed. *Monthly Notices of the Royal Astronomical Society*, pages 755–772, 2007. `http://dx.doi.org/10.1111/j.1365-2966.2007.11964.x`; abstract: We report new constraints on the local escape speed of our Galaxy. Our analysis is based on a sample of high-velocity stars from the RAVE survey and two previously published data sets. We use cosmological simulations of disc galaxy formation to motivate our assumptions on the shape of the velocity distribution, allowing for a significantly more precise measurement of the escape velocity compared to previous studies. We find that the escape velocity lies within the range $498 < v_{esc} < 608 km/s$ (90 per cent confidence), with a median likelihood of $544 km/s$. The fact that v_{esc}^2 is significantly greater than $2v_{circ}^2$ (where $v_{circ} = 220 km/s$ is the local circular velocity) implies that there must be a significant amount of mass exterior to the solar circle, that is, this

convincingly demonstrates the presence of a dark halo in the Galaxy. We use our constraints on v_{esc} to determine the mass of the Milky Way halo for three halo profiles. For example, an adiabatically contracted NFW halo model results in a virial mass of $1.42^{+1.14}_{-0.54}10^{12}M_{\odot}$ and virial radius of $305^{+66}_{-45}kpc$ (90 per cent confidence). For this model the circular velocity at the virial radius is $142^{+31}_{-21}km/s$. Although our halo masses are model dependent, we find that they are in good agreement with each other.

[61] G. Belanger, F. Boudjema, A. Pukhov, and A. Semenov. Dark matter direct detection rate in a generic model with micromegas2.2. *Arxiv*, 2008. `http://arxiv.org/pdf/0803.2360v2`; abstract: We present a new module of the micrOMEGAs package for the calculation of WIMP-nuclei elastic scattering cross sections relevant for the direct detection of dark matter through its interaction with nuclei in a large detector. With this new module, the computation of the direct detection rate is performed automatically for a generic model of new physics which contains a WIMP candidate. This model needs to be implemented within micrOMEGAs2.1.

[62] Sofia Sivertsson and Joakim Edsjo. Accurate calculations of the wimp halo around the sun and prospects for its gamma ray detection. *Arxiv*, 2009. 16 pages, 7 figures, latex; `http://arxiv.org/pdf/0910.0017v1`; abstract: Weakly interacting massive particles (WIMPs) can be captured by heavenly objects, like the Sun. Under the process of being captured by the Sun, they will build up a population of WIMPs around it, which will eventually sink to the core. It has been suggested that this halo of WIMPs around the Sun could be a gamma ray source, possibly distinct enough to have nice detectable signature for WIMP dark matter. We here revisit this problem using detailed Monte Carlo simulations and detailed composition and structure information about the Sun to estimate the size of the gamma ray flux. Compared to earlier simpler estimates, we find that the gamma ray flux from WIMP annihilations in the Sun halo would be negligible; no current or planned detectors would be able to detect this flux.

[63] Manuel Drees and Chung-Lin Shan. Model-independent determination of the wimp mass from direct dark matter detection data. *Arxiv*, 2008. 30 pages, 15 figures, typos fixed, one reference added, `http://arxiv.org/pdf/0803.4477v3`, abstract: Weakly Interacting Massive Particles (WIMPs) are one of the leading candidates for Dark Matter. We develop a model-independent method for determining the mass m_{χ} of the WIMP by using data (i.e., measured recoil energies) of direct detection experiments.

Our method is independent of the as yet unknown WIMP density near the Earth, of the form of the WIMP velocity distribution, as well as of the WIMP-nucleus cross section. However, it requires positive signals from at least two detectors with different target nuclei. In a background-free environment, $m_\chi \sim 50$ GeV could in principle be determined with an error of $\sim 35\%$ with only 2×50 events; in practice upper and lower limits on the recoil energy of signal events, imposed to reduce backgrounds, can increase the error. The method also loses precision if m_χ significantly exceeds the mass of the heaviest target nucleus used.

[64] R. Helm. ? *Phys. Rev. 104 1466*, 1956.

[65] Gintaras Duda, Ann Kemper, and Paolo Gondolo. Model independent form factors for spin independent neutralino-nucleon scattering from elastic electron scattering data. *arxiv*, 2006. 20 pages, 8 figures, `http://arxiv.org/pdf/hep-ph/0608035v2`, abstract: Theoretical calculations of neutralino-nucleon interaction rates with various nuclei are of great interest to direct dark matter searches such as CDMS, EDELWEISS, ZEPLIN, and other experiments since they are used to establish upper bounds on the WIMP-proton cross section. These interaction rates and cross sections are generally computed with standard, one or two parameter model-dependent nuclear form factors, which may not exactly mirror the actual form factor for the particular nucleus in question. As is well known, elastic electron scattering can allow for very precise determinations of nuclear form factors and hence nuclear charge densities for spherical or near-spherical nuclei. We use charge densities derived from elastic electron scattering data to calculate model independent, analytic form factors for various target nuclei important in dark matter searches, such as Si, Ge, S, Ca and others. We have found that for nuclear recoils in the range of 1-100 keV significant differences in cross sections and rates exist when the model independent form factors are used: at 30 keV nuclear recoil the form factors squared differ by a factor of 1.06 for ^{28}Si, 1.11 for ^{40}Ca, 1.27 for ^{70}Ge, and 1.92 for ^{129}Xe. We show the effect of different form factors on the upper limit on the WIMP-proton cross section obtained with a hypothetical ^{70}Ge detector during a 100 kg-day effective exposure. Helm form factors with various parameter choices differ at most by 10–20% from the best (Fourier Bessel) form factor, and can approach it to better than 1% if the parameters are chosen to mimic the actual nuclear density.

[66] B. Krusche. Nuclear mass form factors from coherent photoproduction of π^0 mesons. *Eur.Phys.J. A26*, pages 7–18, 2005. Accepted for publica-

tion in Eur. Phys. J. A, http://arxiv.org/pdf/nucl-ex/0509003v1, abstract: Data for coherent photoproduction of π^0 mesons from nuclei (^{12}C, ^{40}Ca, ^{93}Nb, ^{nat}Pb), recently measured with the TAPS detector at the Mainz MAMI accelerator, have been analyzed in view of the mass form factors of the nuclei. The form factors have been extracted in plane wave approximation of the $A(\gamma, \pi^0)A$ reaction and corrected for final state interaction effects with the help of distorted wave impulse approximations. Nuclear mass rms-radii have been calculated from the slope of the form factors for $q^2 \to 0$. Furthermore, the Helm model (hard sphere form factor folded with Gaussian) was used to extract diffraction radii from the zeroes of the form factor and skin thicknesses from the position and height of its first maximum. The diffraction radii from the Helm model agree with the corresponding charge radii obtained from electron scattering experiments within their uncertainties of a few per cent. The rms-radii from the slope of the form factors are systematically lower by up to 5% for PWIA and up to 10% for DWIA. Also the skin thicknesses extracted from the Helm model are systematically smaller than their charge counter parts.

[67] Spencer Chang, Graham D. Kribs, David Tucker-Smith, and Neal Weiner. Inelastic dark matter in light of dama/libra. *Phys. Rev. D*, 2009. http://prd.aps.org/abstract/PRD/v79/i4/e043513; abstract: Inelastic dark matter, in which weakly interacting massive particle (WIMP)-nucleus scatterings occur through a transition to an excited WIMP state ∼100 keV above the ground state, provides a compelling explanation of the DAMA annual modulation signal. We demonstrate that the relative sensitivities of various dark matter direct detection experiments are modified such that the DAMA annual modulation signal can be reconciled with the absence of a reported signal at CDMS-Soudan, XENON10, ZEPLIN, CRESST, and KIMS for inelastic WIMPs with masses O(100 GeV). We review the status of these experiments, and make predictions for upcoming ones. In particular, we note that inelastic dark matter leads to highly suppressed signals at low energy, with most events typically occurring between 20 and 45 keV(unquenched) at xenon and iodine experiments, and generally no events at low (∼10 keV) energies. Suppressing the background in this high-energy region is essential to testing this scenario. The recent CRESST data suggest seven observed tungsten events, which is consistent with expectations from this model. If the tungsten signal persists at future CRESST runs, it would provide compelling evidence for inelastic dark matter, while its absence should exclude it.

[68] R. Lemrani and et.al. Dark matter tool. `http://pisrv0.pit.physik.uni-tuebingen.de/darkmatter/`.

[69] Brian Feldstein, A. Liam Fitzpatrick, and Emanuel Katz. Form factor dark matter. *Arxiv*, 2009. 23 pages, 7 figures, refs added; `http://arxiv.org/pdf/0908.2991v2`; abstract: We present a dynamical alternative to inelastic dark matter as a way of reconciling the modulating signal seen at DAMA with null results at other direct detection experiments. The essential ingredient is a new form factor which introduces momentum dependence in the interaction of dark matter with nuclei. The role of the form factor is to suppress events at low momentum transfer. We find that a form factor approach is most likely not viable in the context of the standard halo model, however it is consistent with halo models suggested by recent Via Lactea simulations. As an example of possible form factors, we present a class of models where the necessary momentum dependence arises from interference of GeV mass gauge bosons coupling the dark matter to nuclei. At energies relevant for direct detection experiments these models contain one or two additional parameters beyond the case of a standard WIMP.

[70] E. A. Baltz and P. Gondolo. Implications of muon anomalous magnetic moment for supersymmetric dark matter. *arxiv*, 2001. `http://arxiv.org/pdf/hep-ph/0102147v2`; abstract: The anomalous magnetic moment of the muon has recently been measured to be in conflict with the Standard Model prediction with an excess of 2.6 sigma. Taking the excess at face value as a measurement of the supersymmetric contribution, we find that at 95% confidence level it imposes an upper bound of 500 GeV on the neutralino mass and forbids higgsinos as being the bulk of cold dark matter. Other implications for the astrophysical detection of neutralinos include: an accessible minimum direct detection rate, lower bounds on the indirect detection rate of neutrinos from the Sun and the Earth, and a suppression of the intensity of gamma-ray lines from neutralino annihilations in the galactic halo.

[71] Vuk Mandic Rick Gaitskell and Jeff Filippini. Direct detection of wimp dark matter, sensitivity plots, 2010. `http://dmtools.berkeley.edu/limitplots/`.

[72] Gary J. Feldman and Robert D. Cousins. A unified approach to the classical statistical analysis of small signals. *Phys.Rev. D57.3873*, 1999. 40 pages, 15 figures. Changes 15-Dec-99 to agree more closely with published version. A few small changes, plus the two substantive changes we made

in proof back in 1998: 1) The definition of "sensitivity" in Sec. V(C). It was inconsistent with our actual definition in Sec. VI. 2) "Note added in proof" at end of the Conclusion; abstract: We give a classical confidence belt construction which unifies the treatment of upper confidence limits for null results and two-sided confidence intervals for non-null results. The unified treatment solves a problem (apparently not previously recognized) that the choice of upper limit or two-sided intervals leads to intervals which are not confidence intervals if the choice is based on the data. We apply the construction to two related problems which have recently been a battle-ground between classical and Bayesian statistics: Poisson processes with background, and Gaussian errors with a bounded physical region. In contrast with the usual classical construction for upper limits, our construction avoids unphysical confidence intervals. In contrast with some popular Bayesian intervals, our intervals eliminate conservatism (frequentist coverage greater than the stated confidence) in the Gaussian case and reduce it to a level dictated by discreteness in the Poisson case. We generalize the method in order to apply it to analysis of experiments searching for neutrino oscillations. We show that this technique both gives correct coverage and is powerful, while other classical techniques that have been used by neutrino oscillation search experiments fail one or both of these criteria. ; `http://arxiv.org/pdf/physics/9711021v2`.

[73] S. Yellin. Extending the optimum interval method. *arxiv*, 2007. `http://arxiv.org/pdf/0709.2701v1`; abstract: The optimum interval method for finding an upper limit of a one-dimensionally distributed signal in the presence of an unknown background is extended to the case of high statistics. There is also some discussion of how the method can be extended to the multiple dimensional case.

[74] Trung-Si Tran. private communication, 2007.

Acknowledgment

Vielen Dank an alle, die diese Arbeit durch Tatkraft oder motivierende Worte unterstützt haben. Dabei möchte ich besonders die folgenden Personen hervorheben:

Meinen Eltern danke ich für ihre permanente Unterstützung während meiner gesamten Ausbildung. Diese Grundlage und Euer Rückhalt haben diese Dissertation möglich gemacht.

Meiner Frau Sonja danke ich für ihre Geduld, ihr Verständnis und die Freude auf eine gemeinsame Zukunft, die die Fertigstellung dieser Arbeit erleichtert haben. Es war nicht immer einfach, aber wir haben es zusammen geschafft!

Meinen Betreuern, meiner Frau und allen Kollegen, die Teile der Arbeit Korrektur gelesen haben, danke ich herzlich für die Vorschläge zu neuen Formulierungen und die Behebung von Rechtschreibfehlern. Prof. Jochum danke ich darüber hinaus ganz besonders für die umfangreiche Ausbildung der letzen Jahre.

Meinen Tübinger Kollegen, meinen Freunden und den Mitgliedern der CRESST Kollaboration danke ich für die vielen schönen Erinnerungen abseits der Wissenschaft und natürlich auch für die lehrreiche Zeit bei der gemeinsamen[1] Forschung.

[1]Den Freunden und Kollegen mit denen ich nicht gemeinsam geforscht habe, danke ich statt dessen umso mehr für den gemeinsamen Spaß zwischen und/oder nach der Forschung.